

INFORMATION TO USERS

This manuscript has been reproduced from the microfilm master. UMI films the text directly from the original or copy submitted. Thus, some thesis and dissertation copies are in typewriter face, while others may be from any type of computer printer.

The quality of this reproduction is dependent upon the quality of the copy submitted. Broken or indistinct print, colored or poor quality illustrations and photographs, print bleedthrough, substandard margins, and improper alignment can adversely affect reproduction.

In the unlikely event that the author did not send UMI a complete manuscript and there are missing pages, these will be noted. Also, if unauthorized copyright material had to be removed, a note will indicate the deletion.

Oversize materials (e.g., maps, drawings, charts) are reproduced by sectioning the original, beginning at the upper left-hand corner and continuing from left to right in equal sections with small overlaps.

Photographs included in the original manuscript have been reproduced xerographically in this copy. Higher quality 6" x 9" black and white photographic prints are available for any photographs or illustrations appearing in this copy for an additional charge. Contact UMI directly to order.

**ProQuest Information and Learning
300 North Zeeb Road, Ann Arbor, MI 48106-1346 USA
800-521-0600**

UMI[®]

University of Alberta

**Investigation of Existing and Proposed Modulation
Formats in Fiber-Optic Communication Systems**

by

Kwok-sing Cheng



A thesis submitted to the Faculty of Graduate Studies and Research in partial fulfillment
of the requirements for the degree of Doctor of Philosophy

Department of Electrical and Computer Engineering

Edmonton, Alberta

Fall 2001



**National Library
of Canada**

**Acquisitions and
Bibliographic Services**

**395 Wellington Street
Ottawa ON K1A 0N4
Canada**

**Bibliothèque nationale
du Canada**

**Acquisitions et
services bibliographiques**

**395, rue Wellington
Ottawa ON K1A 0N4
Canada**

Your file Votre référence

Our file Notre référence

The author has granted a non-exclusive licence allowing the National Library of Canada to reproduce, loan, distribute or sell copies of this thesis in microform, paper or electronic formats.

The author retains ownership of the copyright in this thesis. Neither the thesis nor substantial extracts from it may be printed or otherwise reproduced without the author's permission.

L'auteur a accordé une licence non exclusive permettant à la Bibliothèque nationale du Canada de reproduire, prêter, distribuer ou vendre des copies de cette thèse sous la forme de microfiche/film, de reproduction sur papier ou sur format électronique.

L'auteur conserve la propriété du droit d'auteur qui protège cette thèse. Ni la thèse ni des extraits substantiels de celle-ci ne doivent être imprimés ou autrement reproduits sans son autorisation.

0-612-68918-2

Canada

UNIVERSITY OF ALBERTA
LIBRARY RELEASE FORM

Name of Author: KWOK-SING CHENG

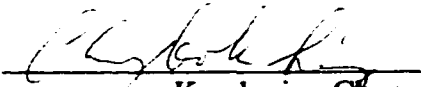
Title of Thesis: INVESTIGATION OF EXISTING AND PROPOSED MODULATION
FORMATS IN FIBER-OPTIC COMMUNICATION SYSTEMS

Degree: DOCTOR OF PHILOSOPHY

Year this Degree Granted: 2001

Permission is hereby granted to the University of Alberta Library to reproduce single copies of this thesis and to lend or sell such copies for private, scholarly, or scientific research purposes only.

The author reserves all other publication rights in association with the copyright in the thesis, and except as hereinbefore provided, neither the thesis nor any substantial portion thereof may be printed or otherwise reproduced in any material form whatever without the author's prior written permission.


Kwok-sing Cheng
7C, Block 4, Melody Garden
Tuen Mun, N. T
Hong Kong

Date: July 17, 2001

“And behold, the LORD was passing by! And a great and strong wind was rending the mountains and breaking in pieces the rocks before the LORD; but the LORD was not in the wind. And after the wind and earthquake, but the LORD was not in the earthquake. After the earthquake a fire, but the LORD was not in the fire; and after the fire a sound of a gentle blowing.”

[I Kings 19:11-12]


UNIVERSITY OF ALBERTA


FACULTY OF GRADUATE STUDIES AND RESEARCH


The undersigned certify that they have read, and recommend to the Faculty of Graduate Studies and Research for acceptance, a thesis entitled

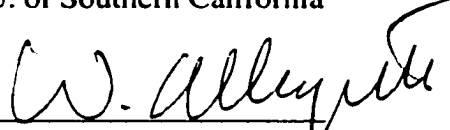
“Investigation of Existing and Proposed Modulation Formats in Fiber-Optic Communication Systems “

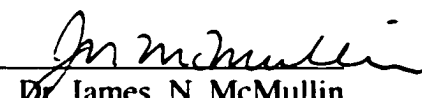
submitted by KWOK-SING CHENG in partial fulfillment of the requirements for the degree of DOCTOR OF PHILOSOPHY.

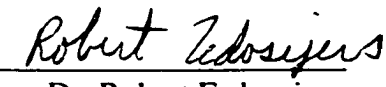

Dr. Jan Conradi
Co-supervisor


Dr. Bruce Cockbrun
Co-supervisor


Dr. Alan E. Willner
U. of Southern California


Dr. Walter Allegretto
Mathematics


Dr. James N. McMullin
Elec. and Comp. Eng.


Dr. Robert Fedosejevs
Elec. and Comp. Eng

May 18, 2001

Dedicated to My Parents

Cheng Pei Cheung and Cheng Cheung Yuk Kam

for their love and support

Abstract

This thesis evaluates several alternative transmission formats to determine their potential for different types of WDM fiber systems. The research contributions involve four different parts: (1) construction of a new simulation software package that accurately models the optical fiber. Various nonlinear effects and chromatic dispersion modeling were incorporated into the new software; (2) comparison of the duobinary and OSSB transmission formats with the commonly used NRZ OOK format; (3) examination of the compatibility of different SSB formats with the duobinary format, for the possibility of combining the OSSB and duobinary formats; (4) comparison of the performance of three different alternative RZ formats, namely, bipolar RZ (BP-RZ), duobinary RZ (D-RZ) and modified duobinary RZ (MD-RZ), with the commonly used RZ format.

Acknowledgements

I would like to express my deepest appreciation to my mentor Dr. Jan Conradi (now director of Corning), for his tremendous help throughout the entire research. I would also like to thank my supervisor Dr. Bruce Cockburn, for his guidance in the thesis writing and encouragement throughout the second half of my research.

I would also like to thank Corning Inc. and TRILabs for their financially support, friendly and stimulating research environment and state-of-the-art research facilities.

I am also in debt to many people both in Corning Inc. and TRILabs; especially Dr. Roger Peterson and David Clegg in TRILabs; Dr. Shiva Kumar, Dr. Ulrik Gliese, Dr. Liming Wang, Dr. Sergi Burtsev, Dr. Kim Jepsen, Jason Hurley and Becki Morgan in Corning Inc..

Also, I want to thank all my friends in TRILabs for their help, support and encouragement throughout my research, especially, Kay Wee Ang, Sik Heng Foo, Clarence Kan, William Kwong, Chee Yoon Lee, Robert Novak, Ernest Siu, Yan Xin, Endymion Yeung, and Horace Yu.

I want to thank my family for their patience and support. Throughout these many years of studies, my parents supported and encouraged me, and provided necessary financial assistance without any hesitation.

Last but not least, I want to thank my God, my personal Savior, for giving me all these people to help me finish my research, and for walking with me through many difficult times. I give glory and honor to my Highest God who showed me His mercy and love.

Table of Contents

1. INTRODUCTION.....	1
1.1. SONET SYSTEMS	1
1.2. LIMITATION ON THE TRANSMISSION RATE DUE TO CHROMATIC DISPERSION	3
1.2.1 Cause of Chromatic Dispersion and Its Effect	3
1.2.2 Modulation Methods that Compensate for Chromatic Dispersion	4
1.2.3 Electrical Compensation for Chromatic Dispersion	5
1.2.4 Optical Compensation for Chromatic Dispersion	6
1.3. WAVELENGTH DIVISION MULTIPLEXING	7
1.3.1 The Need for WDM.....	7
1.3.2 Applications of WDM to Different Levels of the Communication Network	9
1.3.3 Brief Description of WDM-based SONET Networks	10
1.3.4 Limit to of the WDM Network Capacity	14
1.3.5 Increase in WDM Capacity	15
1.3.6 Increase in Transmission Length.....	16
1.4. RESEARCH CONTRIBUTIONS OF THIS THESIS	17
1.5. THESIS OUTLINE	19
2. MODELING OF THE FIBER OPTIC SYSTEM.....	21
2.1. INTRODUCTION	21
2.2. BRIEF DESCRIPTION OF VARIOUS FIBER DISTORTIONS	21
2.2.1 Chromatic Dispersion.....	22
2.2.2 Kerr Effect for Self-Phase Modulation (SPM), Cross-Phase Modulation (XPM) and Four Wave Mixing (FWM).....	26
2.2.3 Stimulated Brillouin Scattering (SBS) and Stimulated Raman Scattering (SRS).....	27
2.2.4 Polarization Mode Dispersion (PMD)	30
2.3. THE NONLINEAR SCHRODINGER EQUATION	31
2.3.1 NLSE: Including only Chromatic Dispersion	34
2.3.2 NLSE: Including only SPM.....	35
2.3.3 Coupled NLSEs: Including Chromatic Dispersion, SPM and XPM	36
2.3.4 Coupled NLSEs: Including Chromatic Dispersion, SPM, XPM and FWM	38
2.4. NUMERICAL SIMULATION	40
2.5. VERIFICATION OF THE SIMULATION PROGRAM	44
2.6. CALCULATION OF THE Q FACTOR	50
3. THEORETICAL AND NUMERICAL COMPARISON OF THE NRZ, DUOBINARY AND OSSB FORMATS.....	56
3.1. INTRODUCTION	56
3.2. MODELING OF OPTICAL SIGNALS.....	57
3.2.1 Transmitter Modeling for Different Formats.....	58
3.2.2 Optimization of the Duobinary Filter	62
3.3. CHROMATIC DISPERSION AND THE EYE CLOSURE PENALTY	67
3.4. LINEAR CROSS TALK	72
3.4.1 Cross Talk in an Optical Cross Connect	72
3.4.2 Cross Talk due to Close Channel Spacing and Optical Demultiplexing Filter	77
3.5. SELF-PHASE MODULATION	81
3.6. CROSS-PHASE MODULATION	89
3.7. FOUR WAVE MIXING	100
3.8. FULL-SCALE SHORT-HAUL SIMULATIONS.....	113
3.9. FULL-SCALE TERRESTRIAL SYSTEM SIMULATIONS	123
3.10. OC-768 LINE-RATE SIMULATIONS	128

3.11. SUMMARY.....	134
4. EXPERIMENTAL COMPARISON OF THE THREE TRANSMISSION FORMATS	136
4.1. INTRODUCTION	136
4.2. TRANSMITTER SETUP.....	136
4.2.1 <i>Duobinary Signal</i>	136
4.2.2 <i>OOK and OSSB Signals</i>	139
4.2.3 <i>Signal Spectra and Eye Diagrams</i>	145
4.3. CHANNEL CROSS TALK.....	147
4.4. XPM MEASUREMENT.....	151
4.5. FWM MEASUREMENT	155
4.6. SINGLE-SPAN SYSTEM EXPERIMENTS	158
4.7. MULTI-SPAN TERRESTRIAL SYSTEM EXPERIMENTS.....	162
4.8. SUMMARY.....	170
5. OPTICAL SINGLE SIDEBAND DUOBINARY TRANSMISSION.....	171
5.1. INTRODUCTION	171
5.2. OPTICAL SINGLE SIDEBAND TRANSMISSION	171
5.2.1 <i>Conventional Single-sideband Signal</i>	172
5.2.2 <i>Compatible Single-sideband Signal</i>	173
5.2.3 <i>Approximated Single-sideband Signal</i>	175
5.3. COMPATIBILITY PROBLEMS OF SINGLE-SIDEBAND SIGNALS WITH DUOBINARY SIGNALS.....	176
5.4. TRANSMITTER MODULE FOR A SINGLE-SIDEBAND DUOBINARY SIGNAL	177
5.5. SINGLE-SIDEBAND TO DOUBLE-SIDEBAND CONVERSION	179
5.6. SINGLE-CHANNEL SIMULATIONS AND ANALYSIS.....	184
5.7. SUMMARY.....	187
6. INVESTIGATION OF DIFFERENT RZ FORMATS	188
6.1. INTRODUCTION	188
6.2. SIGNAL GENERATION.....	191
6.3. PERFORMANCE COMPARISON	193
6.4. ANALYSIS	196
6.5. SUMMARY.....	199
7. CONCLUSION	200
7.1. RESEARCH SUMMARY.....	200
7.2. FUTURE WORK	203

List of Tables

Table 1.1: SONET Optical Line Rates	3
Table 2.1: BERs for Certain Q Factor Values	54
Table 3.1: Typical Fiber Characteristics.....	82
Table 3.2: Average Q over 32 Channels (1 span, SSMF, 50 GHz spacing).....	117
Table 3.3: Average Q over 32 Channels (1 span, NZDSF, 50 GHz spacing)	119
Table 3.4: Average Q over 32 Channels (1 span, SSMF, 25 GHz spacing).....	121
Table 3.5: Average Q Over 32 Channels (1 span, NZDSF, 25 GHz spacing)	123
Table 3.6: Average Q over 32 Channels (5 span, SSMF, 50 GHz spacing).....	125
Table 3.7: Average Q over 32 Channels (5 spans, NZDSF, 50 GHz spacing).....	126
Table 3.8: Average Q over 32 Channels (5 span, SSMF, 25 GHz spacing).....	127
Table 3.9: Average Q over 32 Channels (5 span, NZDSF, 25 GHz spacing)	128
Table 3.10: Average Q over 32 Channels (1 span, SSMF, 100 GHz spacing).....	130
Table 3.11: Average Q over 32 Channels (1 span, NZDSF, 100 GHz spacing)	132
Table 3.12: Average Q Over 32 Channels (5 span, SSMF, 100 GHz spacing).....	133
Table 3.13: Average Q over 32 Channels (5 span, NZDSF, 100 GHz spacing)	134
Table 6.1: Fiber Parameters.....	194

List of Figures

Figure 1.1: Growth in the number of Internet Users (source [3])	2
Figure 1.2: Top 15 Nations in Internet Use at Year-End 2000 [4]	2
Figure 1.3: A Single-Channel System with Dispersion Compensation	7
Figure 1.4: Progress in Fiber-Optic System Capacity [26]	8
Figure 1.5: SONET Rings in a Multi-level WDM System (Source [31])	9
Figure 1.6: Schematic Diagram of a Fiber Optic System with OADMs	13
Figure 1.7: Proposed Programmable Optical Add/drop Multiplexer (source [27])	13
Figure 2.1: Co-ordinate System for Electromagnetic Wave Propagation in Fiber..	23
Figure 2.2: Dispersion Profile of Different Fibers	26
Figure 2.3: Pulse Spreading due to PMD	31
Figure 2.4: Pulse Spreading of a Gaussian Pulse	35
Figure 2.5: Spreading of the Signal Spectrum due to SPM	36
Figure 2.6: Amplitude Distortion of a Continuous-wave Channel due to XPM	38
Figure 2.7: Effects of FWM and Channel Allocation for 4-channel WDM systems	39
Figure 2.8: Flow Chart for Split-Step Fourier Method Solving the Schrodinger Equation	43
Figure 2.9: Comparison of Analytical and Simulated Results for Gaussian Pulse Propagation Including Only the Chromatic Dispersion Effect	45
Figure 2.10: Comparison of Analytical and Simulated Results for Gaussian Pulse Propagation including only the nonlinear effects	46
Figure 2.11: Comparison of Analytical and Simulated Results for Soliton Transmission Including Both Chromatic Dispersion and Nonlinear Effects	48
Figure 2.12: Comparison of Analytical and Simulated Results for Four-Wave- Mixing (solid line-analytical, bubble - simulated)	50
Figure 2.13: Receiver for an Optical-Fiber System	51
Figure 2.14: Noise Distribution of ‘1’s of a Received Optical Signal	52
Figure 2.15: BER versus Decision Threshold Curves	54
Figure 3.1: Transmitter Schematics for the Three Transmission Formats	59
Figure 3.2: Comparison between the Amplitude Response of the Delay-and-Add Circuit and Bessel Filter (solid line-delay-and-add circuit, dashed line-Bessel filter)	63
Figure 3.3: Maximum Eye Opening at Different Distances of Received Duobinary Signals with Different Bessel Filter Order and Their Corresponding 3dB Bandwidth	64
Figure 3.4: Comparison of the Maximum Eye Opening for Two Different Modulation-depth Cases and the Corresponding 3dB Bandwidth (without electrical filtering)	66
Figure 3.5: Comparison of the Maximum Eye Opening for Two Different Modulation-depth Cases (with electrical filtering)	66
Figure 3.6: Real and Imaginary Parts of a Spreading Gaussian Pulse after Increasing Propagation Distances (real part- light dash, imaginary part- thin solid, absolute amplitude- thick solid)	70
Figure 3.7: Comparison of Eye Opening as a Function of Fiber Length under the Influence of only Chromatic Dispersion	71

Figure 3.8: Illustration of an Optical Cross Connect.....	73
Figure 3.9: Comparison of the Eye Opening of the Three Formats With and Without Same-Wavelength Cross Talk (first case).....	74
Figure 3.10: Illustration of the Amplitude and Phase Profiles of the OSSB Signals With and Without Cross talk.	76
Figure 3.11: Eye Opening Degradation as a Function of Optical Cross Talk.....	77
Figure 3.12: Eye Degradation due to Optical Filtering Effect.....	78
Figure 3.13: Eye Degradation due to 3-Channel Cross Talk using different Optical Filters.....	79
Figure 3.14: Eye Degradation Due to 3-Channel Cross Talk for OSSB Signaling with Different Modulation Depths.....	80
Figure 3.15: Eye Opening and the Corresponding Residual Dispersion under the Influence of SPM (SSMF, 160 km).....	83
Figure 3.16: Eye Opening and the Corresponding Residual Dispersion under the Influence of SPM (NZDSF, 160 km).....	83
Figure 3.17: Eye Opening and the Corresponding Residual Dispersion under the Influence of SPM (SSMF, 5x90 km).....	84
Figure 3.18: Eye Opening and the Corresponding Residual Dispersion under the Influence of SPM (NZDSF, 5x90 km).....	84
Figure 3.19: Illustration of the Iterative Approximation Method for Evaluating the SPM Distortion.....	86
Figure 3.20: Comparison of the simulated and approximated eyes of the Three Formats under the Influence of Chromatic Dispersion and SPM.....	87
Figure 3.21: Evolution of the SPM Distortion for the Three Formats.....	88
Figure 3.22: Two-Channel XPM System Setup.....	89
Figure 3.23: Successive Components of XPM Noise Generation.....	92
Figure 3.24: Comparison of the Two-channel XPM Simulation Results with the Analytical Approximation for the Three Formats (solid line--Simulation; Bubble- Analytic).....	93
Figure 3.25: Comparison of Normalized Standard Deviation between Simulations and Analytic Approximations (solid line-simulation; bubble-approximation) due to XPM.	94
Figure 3.26: Comparison of Normalized Standard Deviation between the Three Formats with Different Channel Spacing Resulting from XPM Effect (channel spacing : top 50 GHz, middle 70 GHz, bottom 90 GHz).....	96
Figure 3.27: Comparison of the Frequency Spectra of the Absolute-Square of the Optical Signals between the Three Formats.....	97
Figure 3.28: Comparison of the Normalized Standard Deviation between the Three Formats in Single-Span 50 GHz Spacing 5-Channel Configuration Resulting from XPM Effect.	97
Figure 3.29: Renormalized Standard Deviation versus Residual Dispersion for a 5-Span Configuration.....	99
Figure 3.30: Comparison of the XPM noise of the Three Formats in Terrestrial System Configuration.....	100
Figure 3.31: Schematic Diagram of the 3-Channel System for Examining the FWM Penalty.....	101

Figure 3.32: Comparison between Simulations and Approximated Analysis for 3-Channel FWM Systems	103
Figure 3.33: Comparison between the Simulations and Approximate Analysis for 3-Channel FWM Systems (each point is average over 20 simulation runs).....	104
Figure 3.34: Comparison of the FWM Penalty between the Three Formats	104
Figure 3.35: Difference in the FWM Triplets between the Three Formats	106
Figure 3.36: Illustration of the Two Degenerate FWM Triplets Mainly Responsible for the FWM Distortion in a 5-Channel WDM System using NZDSF	108
Figure 3.37: Comparison of the 5-Channel FWM Induced Standard Deviation for Different Numbers of Spans (the power under each diagram denotes the average launch power per channel).....	109
Figure 3.38: Illustration of the Sinusoidal-Modulation when the Channel Spacing is Not Exact for the 5-channel System.....	111
Figure 3.39: Comparison of the Square-detected CW Channel under the Influence of the FWM Triplets for Exact and Slightly-off Channel Spacing (top-exact spacing, bottom-slightly-off spacing).....	111
Figure 3.40: Comparison of 5-Channel FWM Penalty for Different Numbers of Spans with Detuned Carrier Frequencies (power under each diagram denotes the average launch power per channel).....	112
Figure 3.41: Schematic Diagram of the Single-span 32-Channel Simulations.....	114
Figure 3.42: Comparison of the Average Amplitude of the ‘1’s and ‘0’s in 3-bit Patterns (1 span, 50 GHz spacing, SSMF, 6 dBm average launched power) ..	115
Figure 3.43: Comparison of the Normalized Standard Deviation of the ‘1’s and ‘0’s in 3-bit Patterns (1 span, 50 GHz spacing, SSMF, 6 dBm average launched power).....	115
Figure 3.44: Comparison of Q value at Different Average Launched Power Level (1 Span, 50 GHz spacing, SSMF) [top 2dBm, middle 4 dBm, bottom 6 dBm]	116
Figure 3.45: Comparison of the Standard Deviation of Q at Three Different Average Launched Power Levels (1 Span, 50 GHz spacing, SSMF) [top 2 dBm, middle 4 dBm, bottom 6 dBm]	117
Figure 3.46: Comparison of the Normalized Standard Deviation of the ‘1’s and ‘0’s in 3-bit Patterns (1 span, 50 GHz spacing, NZDSF, 6dBm average launched power).....	118
Figure 3.47: Comparison of the Q Values at Different Average Launched Power Levels (1 Span, 50 GHz spacing, NZDSF) [top 0 dBm, middle 2 dBm, bottom 4 dBm]	119
Figure 3.48: Comparison of the Normalized Standard Deviation of the ‘1’s and ‘0’s in 3-bit Patterns (1 span, 25 GHz spacing, SSMF, 6 dBm average launched power).....	120
Figure 3.49: Comparison of Q values at Different Average Launched Power Levels (1 Span, 25 GHz spacing, SSMF) [top 2dBm, middle 4 dBm, bottom 6 dBm] ..	121
Figure 3.50: Comparison of the Normalized Standard Deviation of the ‘1’s and ‘0’s in 3-bit Patterns (1 span, 25 GHz spacing, NZDSF, 6 dBm average launched power).....	122
Figure 3.51: Comparison of the Q Value at Different Average Launched Power Levels (1 Span, 25 GHz spacing, NZDSF) [top 0 dBm, bottom 2 dBm].....	123

Figure 3.52: Comparison of Q Values at Different Average Launched Power Levels (5 Span, 50 GHz spacing, SSMF) [top 0 dBm, middle 2 dBm, bottom 4 dBm]	124
Figure 3.53: Comparison of Q value at Different Average Launched Power Levels (5 Span, 50 GHz spacing, NZDSF) [top 0 dBm, middle 2 dBm, bottom 4 dBm].	126
Figure 3.54: Comparison of Q Values at Different Average Launched Power Levels (5 Span, 25 GHz spacing, SSMF) [top 0 dBm, middle 2 dBm, bottom 4 dBm]	127
Figure 3.55: Comparison of the Q Values at Different Average Launched Power Levels (5 Span, 25 GHz spacing, NZDSF) [top 0 dBm, middle 2 dBm]	128
Figure 3.56: Comparison of Q Values at Different Average Launched Power Levels (1 Span, 100 GHz spacing, SSMF) [top 2 dBm, middle 4 dBm, bottom 6 dBm]	130
Figure 3.57: Comparison of Q Values at Different Average Launched Power Levels (1 Span, 100 GHz spacing, NZDSF) [top 2dBm, middle 4dBm, bottom 6dBm]	131
Figure 3.58: Comparison of Q Values at Different Average Launched Power Levels (5 Span, 100 GHz spacing, SSMF) [top 2 dBm, middle 4 dBm, bottom 6 dBm]	132
Figure 3.59: Comparison of Q Values at Different Average Launched Power Levels (5 Span, 100 GHz spacing, NZDSF) [top 2 dBm, middle 4 dBm, bottom 6 dBm]	133
Figure 4.1: Schematic Diagram of the Duobinary Transmitter	137
Figure 4.2: Frequency Response of the Bessel Filter for the Duobinary Conversion	138
Figure 4.3: Experimental Three-Level Duobinary Eyes	139
Figure 4.4: Schematic Diagram of the OOK Transmitter	141
Figure 4.5: Schematic Diagram of the OSSB Transmitter	142
Figure 4.6: Schematic Diagram of the Hilbert Transform Circuit	142
Figure 4.7: Measured Output of the Hilbert Transform Circuit	143
Figure 4.8: Schematic Diagram for the Heterodyne Method for Measuring the Optical Spectrum of the Signal	143
Figure 4.9: Composite Spectrum obtained from the Heterodyne Method (on the left-optical spectrum, on the right box-square-law-detected spectrum)	144
Figure 4.10: Frequency Spectra of the Three Transmission Formats	145
Figure 4.11: Comparison of the Back-to-Back Eye Diagrams of the Duobinary and OOK Signals.	146
Figure 4.12: Schematic Diagram of the Optical Receiver	146
Figure 4.13: Evolution of the Square-law-detected Duobinary Eye with Different Lengths of SMF	147
Figure 4.14: Schematic Diagram for the Cross Talk Measurement Set-up	148
Figure 4.15: Example of the BER versus Threshold Voltage Curve	149
Figure 4.16: Q versus Channel Spacing from Experimental Results	149
Figure 4.17: Simulated Eye Opening of OOK and OSSB Formats with Different Channel Spacing under Three Different Conditions	150
Figure 4.18: Experimental Setup for the 2-Channel XPM Measurement	151
Figure 4.19: Normalized Standard Deviation versus Launched Power for Three Different Channel Spacings (SMF)	152

Figure 4.20: Normalized Standard Deviation versus the Launched Power for three Different Channel Spacings (NZDSF)	153
Figure 4.21: Experimental and Simulation XPM Distortion for Duobinary Format	154
Figure 4.22: Experimental and Simulated XPM Distortion Results (solid - simulation, dots- experiment)	155
Figure 4.23: Experimental Set-up for the 2-channel FWM Measurement	156
Figure 4.24: Experimental Setup for 2-channel FWM Measurement	157
Figure 4.25: FWM Ratio between the Original Signal and the FWM-generated Signal	157
Figure 4.26: Experimental Setup for Full-scale Single-span Experiment	159
Figure 4.27: FWM-generated Distortion as a Function of the Launched Power for Duobinary Signaling	161
Figure 4.28: Eye diagram after 170 km of Propagation for the Duobinary Format	161
Figure 4.29: Q Comparison of the Three Formats in Single-span Configuration ..	162
Figure 4.30: Experimental Setup for Multi-span Experiment using SMF	163
Figure 4.31: Optical Output from the Re-circulating Loop	164
Figure 4.32: Experimental Setup for Multi-span Experiment using NZDSF	166
Figure 4.33: Illustration of the Build-up of the ASE-noise Sidelobe	167
Figure 4.34: Illustration of Gain Tilt Effect	168
Figure 4.35: Q Values for Multi-span System using SMF	169
Figure 4.36: Q Measurement for OOK signal after circulating 6-loops with NZDSF	170
Figure 5.1: Conventional Optical SSB Signal Generator (solid line-electrical path, dotted line-optical path)	172
Figure 5.2: CSSB Signal Generator for a Fiber Optic System (solid line-electrical path, dotted line-optical path)	175
Figure 5.3: Phase Cancellation Method for Generating the OSSB-Duobinary Signal	178
Figure 5.4: Field Spectrum of the Single-sideband Duobinary Signal using an Optimized 5-tap Transversal Filter to Realize the Hilbert Transform	178
Figure 5.5: Single Sideband-to-Double-Sideband Converter	180
Figure 5.6: Plot of the X and Y Terms from Equation (5.22) and the Resulting Eye Opening of the Simulated SSB-to-DSB Signal	184
Figure 5.7: Received signal eye opening versus fiber length for Perfect OSSB Duobinary	186
Figure 5.8: Received signal eye opening versus fiber length for VSB Duobinary ...	186
Figure 6.1: Illustration of XPM-induced Chirping of Two-channel Cases (thick solid line - pulse of channel 1, dashed line - pulse of channel 2, light solid line-induced chirp from channel 1) (adapted from Fig. 7.11 [12])	190
Figure 6.2: Illustration of the Situation where the FWM is Close to a Minimum for the RZ Format	191
Figure 6.3: Schematic Diagram for Generating Different Types of RZ Signals	192
Figure 6.4: Optical Spectra of Four Different RZ Formats	193
Figure 6.5: Received Signal Eyes with 9 dBm Average Launched Channel Power	195

Figure 6.6: Eye Opening Penalty (1 channel, dash lines) and Average Q (8 channels, solid lines) versus Average Launched Channel Power	196
Figure 6.7: Pulse Evolution at 2, 4 and 8 km of SMF (light solid line 2 km, dark solid line 4 km, dark dashed line 8 km).....	198
Figure 6.8: Suppression of Ghost Pulses in both D-RZ and MD-RZ	198

List of Symbols and Abbreviations

AC	Alternating current
AOM	Acousto-optic modulator
ASE	Amplified spontaneous emission
BER	Bit-error ratio
CSSB	Compatible single-sideband
CW	Continuous-wave
DC	Direct current
DCF	Dispersion compensating fiber
DCM	Dispersion compensating module
DMF	Dispersion-managed fiber
EDF	Erbium-doped fiber
EDFA	Erbium-doped fiber amplifier
FOCS	Fiber optics communication system
FWM	Four-wave mixing
GVD	Group velocity dispersion
LAN	Local area network
MAN	Metropolitan area network
MZM	Mach-Zehnder modulator
NE	Node element
NLSE	Nonlinear Schrodinger equation
NRZ	Non-return-to-zero
NZDSF	Non-zero dispersion shifted fiber
OADM	Optical add drop multiplexer
OC-N	Optical carrier – N
OSNR	Optical signal-to-noise ratio
OSSB	Optical single-sideband
OOK	On-off keying
OSA	Optical communication analyzer
OCA	Optical communication analyzer
PDH	Plesiochronous digital hierarchy
PMD	Polarization mode dispersion

PRBS	Pseudo-random bit sequence
RZ	Return-to-zero
SBS	Stimulated Brillouin scattering
SSMF	Standard single-mode fiber
SNR	Signal-to-noise ratio
SOA	Semi-conductor optical amplifier
SONET	Synchronous optical network
SPM	Self-phase modulation
SRS	Stimulated Raman scattering
STS-N	Synchronous transport signal-N
TDM	Time division multiplexer
VSF	Vestigial single-sideband
WAN	Wide area network
WDM	Wavelength division multiplexer
XPM	Cross-phase modulation
A_{eff}	Effective core area
c	Speed of light
f	Frequency
g	Gain parameter
I_p	Intensity of a pump wave
I_s	Intensity of a signal wave
n_{eff}	Effective refractive index
P_{in}	Input power
P_o	Output power
Q	Q factor (performance measure)
T	Retarded time frame
T_0	Unit time delay
x,y	Spatial co-ords
z	Propagation direction
α	Fiber attenuation
α_p	Fiber attenuation for the pump wave
α_s	Fiber attenuation for the signal wave

β	Propagation constant
β_n	nth derivative of the propagation constant
ϵ	Electric permittivity
ϵ_0	Electric permittivity of a vacuum
ϕ_{nl}	Nonlinear phase change
σ_0	Standard deviation of 'Space'
σ_1	Standard deviation of 'Mark'
μ_0	Mean of 'Space'
μ_1	Mean of 'Mark'
ω	Angular frequency
χ	Susceptibility of a material

1. Introduction

1.1. SONET systems

Since the first test conducted back in 1976 [1], the fiber optic communication system (FOCS) has emerged as the most viable solution for high-speed data exchange for both metropolitan and long-haul data networks. The first generation of FOCSs operated in an asynchronous mode: the transmitting side and receiving side were operated using unsynchronized clocks (the so-called Plesiochronous Digital Hierarchy, or PDH). Such asynchronous operation creates a number of system management problems and high complexity in the required high-speed electronic network equipment. As a result, the industry gradually concluded that the asynchronous mode should be replaced by a synchronous mode of operation. After two decades of rapid development, the first generation network has largely been replaced by a second-generation network technology, which in North America is called Synchronous Optical Network (SONET). The main purpose of this second-generation standard included greater inter-operability for system equipment manufactured by different vendors, simpler synchronous networking, enhanced OAM&P (operations, administration, maintenance, and provisioning), and compatibility with any service mix including both traditional circuit-switched voice calls and new services such as Asynchronous Transfer Mode (ATM) [2].

Today SONET provides the backbone of most high-speed, data-communication-related services such as video teleconferencing, LAN (local-area network) and WAN (wide-area network) connectivity, long-distance telephone services, cable television broadcasting and Internet access [7]. The demand for higher transmission capacity continues to be very strong. A report shows that the number of North American Internet users increased from less than 2 million in 1994 to close to 21 million in 1998 [3], as shown in **Figure 1.1**. A more recent report shows that during the last two years, the number of North American Internet users increased by about seven times, as shown in **Figure 1.2**. At the end of 2000, the worldwide Internet population was close to 400 million. A similar growth trend has also been seen in other countries around the world. In North America the relaxation of telecommunications laws has also permitted cable

companies to enter various new fields such as multimedia, Internet access and even phone and wireless services [5]. This, in turn, has stimulated demand for higher capacity for their metropolitan and nationwide optical-fiber backbones [6]. To stay competitive with their existing competitors and the emerging cable-based service providers, telecommunication companies are constantly striving for ever more efficient and faster fiber optic technologies [7].

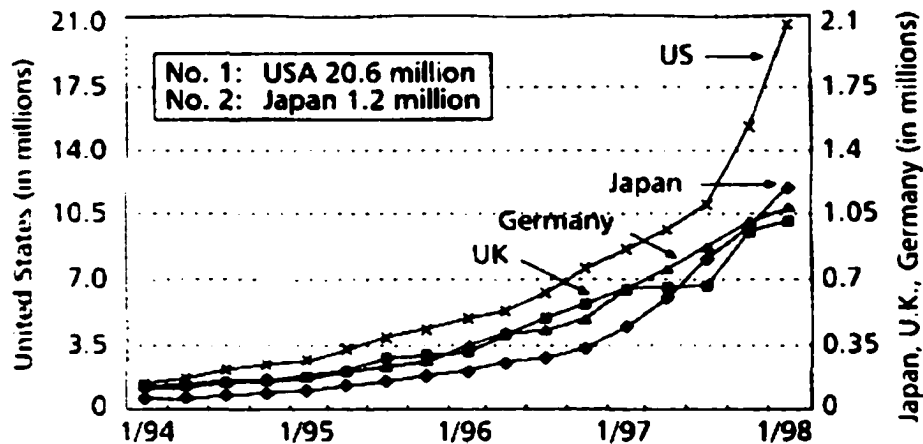


Figure 1.1: Growth in the number of Internet Users (source [3])

Rank	Nation	Internet Users (Millions)	World Share (%)
1	United States	135.7	36.2
2	Japan	26.9	7.18
3	Germany	19.1	5.10
4	UK	17.9	4.77
5	China	15.8	4.20
6	Canada	15.2	4.05
7	South Korea	14.8	3.95
8	Italy	11.6	3.08
9	Brazil	10.6	2.84
10	France	9.0	2.39
11	Australia	8.1	2.16
12	Russia	6.6	1.77
13	Taiwan	6.5	1.73
14	Netherlands	5.4	1.45
15	Spain	5.2	1.39
	Worldwide Total	374.9	100

Figure 1.2: Top 15 Nations in Internet Use at Year-End 2000 [4]

1.2. Limitation on the Transmission Rate due to Chromatic Dispersion

1.2.1 Chromatic Dispersion and Its Effect

Until recently, the time-division multiplexing (TDM) technique was used to increase SONET system capacity. A higher bit-rate SONET signal is formed by multiplexing a number of electrically equivalent synchronous transport signals (STSs). The capacity is therefore determined by the number of STSs contained in a SONET signal. For instance, a SONET OC-3 signal combines 3 STS-1 signals and an OC-12 signal combines 12 STS-1 signals, where OC stands for optical carrier. The standard SONET line rates and the equivalent STS formats are shown in **Table 1.1**.

Optical Carrier Level	Electrical Equivalent	Line Rate (Mbits/second)	Number of Voice Calls
OC-1	STS-1	51.84	672
OC-3*	STS-3	155.52	2016
OC-12*	STS-12	622.08	8064
OC-24	STS-24	1244.16	16,128
OC-48*	STS-48	2488.32	32,256
OC-192*	STS-192	9953.28	129,024

* denotes those rates that are widely supported.

Table 1.1: SONET Optical Line Rates

For transmission rates up to OC-48, the approach of using TDM to increase the SONET capacity is largely limited by the upper frequency limitations of the required microwave and optoelectronics components and the inherent noise present in the FOCSs. For higher transmission rates, the optical fiber itself becomes one of the major limitations. A great amount of research has been required to push the capacity beyond OC-48.

As the transmission rate increases, the corresponding bandwidth of the optical signal also increases. The large optical bandwidth creates a serious problem when the line rate reaches OC-192 [17-21]. The problem occurs because of an inherent optical fiber property called chromatic dispersion. Chromatic dispersion causes the different

frequency components of the signal to travel at different group velocities. A consequence of this phenomenon is pulse spreading, which causes intersymbol interference (ISI) and, subsequently, drastically increases the bit-error-ratio (BER). Because of chromatic dispersion, a FOCS implemented with standard single-mode fibers (SSMFs) can only transmit signals as far as 100 km at the OC-192 rate if the system lacks compensation against dispersion. Over the previous few years, tremendous effort has been spent solving the chromatic dispersion problem. The various compensation methods can be grouped into three categories, namely, modulation methods, electrical compensation methods, and optical compensation methods.

1.2.2 Modulation Methods that Compensate for Chromatic Dispersion

Common bandwidth efficient modulation methods include M-ary, duobinary, optical single-sideband (OSSB) and soliton. The aim of the M-ary and duobinary modulation methods is to reduce the frequency spectrum of the optical signal, thereby reducing the effects of chromatic dispersion. The M-ary signal is generated by weighting the amplitude of the binary tributaries (two or more STSs) and then summing them together. The resulting signal carries more information in one symbol period and therefore a lower transmission rate (narrower optical spectrum) can be used to transmit the same amount of information as an uncompensated signal. However, an M-ary signal is significantly more sensitive to noise and it has been found that M-ary signaling is not a practical solution for chromatic dispersion [9]. Duobinary signaling, on the other hand, does not increase the amount of information carried by the same symbol period, but rather simply reduces the optical bandwidth. It has been proven experimentally and theoretically that duobinary signaling is a practical way of extending the transmission distance to more than 250 km [9,10].

The rationale for OSSB signaling comes from phase-cancellation theory [11]. The benefit of this modulation format is that essentially only one optical sideband is present in the signal spectrum (as opposed to the two sidebands in the conventional

frequency-translated baseband transmission format). Because of this single-sidedness, the transmitted signal has less bandwidth and hence less distortion after square-law detection. For the conventional NRZ modulation method, the square-law detection creates more distortion due to the back-folding of the optical spectrum from the carrier frequency to the baseband. Experiments have already shown that transmission distances of up to 320 km are possible using OSSB [11].

Soliton transmission exploits the interaction between the chromatic dispersion and nonlinear self-phase modulation in the fiber [12]. In most cases the nonlinear effect deteriorates the system performance. In principle, the pulse spreading caused by the chromatic dispersion can be exactly compensated for by the pulse compression resulting from self-phase modulation and hence the pulse shape of the optical signal can be maintained. In practice, soliton transmission requires that the optical power of the signal be tightly maintained at a certain value throughout the optical link. Also, return-to-zero (RZ) coding is required to avoid bit-to-bit interaction which, in turn, generates a larger signal spectrum. Nevertheless, with these requirements, a 400 Gbits/s (i.e., 20 channels at 20 Gbits/s, combined using wavelength-division multiplexing) transmission has been demonstrated recently in a controlled laboratory environment [13].

1.2.3 Electrical Compensation for Chromatic Dispersion

To achieve electrical compensation, microstrip lines [14], microwave waveguides [15] and transversal filters [16] have all been used in attempts to compensate for chromatic dispersion. Compensating devices were placed after the detector in the receiver side of the system, where the optical signal is converted to an electrical signal. The resulting compensation is only marginal because the linear signal distortion caused by the chromatic dispersion becomes nonlinear after the square-law detection, and thus it cannot be effectively compensated by any linear compensation methods. The compensation can be improved by using the OSSB transmission format, because the linear dispersion characteristics of the optical signal are largely retained after square-law

detection. In this case, a transversal filter should perform better than either microstrip lines or microwave waveguides because the latter devices can only approximately reverse the dispersion, whereas the transversal filter can be optimized to almost fully reverse the dispersion.

1.2.4 Optical Compensation for Chromatic Dispersion

In recent years many optical compensating methods have been proposed to solve the dispersion problem. These methods include signal prechirping [17], mid-system spectral inversion [18], a differential time delay method [19], a Chebyshev-polynomial optical compensation circuit [20], dispersion-compensating fiber (DCF) [21], and a chirped fiber Bragg grating [22]. Among these schemes, signal prechirping, DCF and chirped Bragg grating are the more widely used.

Signal prechirping is usually generated at the Mach-Zehnder (MZ) modulator during the amplitude modulation of the optical carrier by an electrical signal. Prechirping occurs when the modulated optical signals propagating in the two optical paths inside a MZ modulator are almost complementary to each others, but with slight difference in magnitude. When these two signals combine, the resulting signal is not just amplitude modulated, but is also phase modulated. As a result, prechirping adds phase modulation to the signal, modulation that is proportional to the instantaneous power of the signal itself. For any practical two-arm MZ modulator, chirping always exists [8, p 149]. With proper control, the chirping can counteract pulse spreading in the propagating signal because it has the effect of compressing the time-domain shape of the optical signal as the signal travels through the fiber. With this method, the transmission distance can be increased up to 150 km [8, p.154].

Both DCFs and chirped Bragg gratings have dispersion characteristics that is opposite to that of the transmission fibers; therefore they can largely reverse dispersion distortion. In current commercial systems, both DCFs and chirped Bragg gratings are commonly used for dispersion compensation [23, pp. 457-459]. The DCF and chirped Bragg grating are inserted at the receiving end of each fiber span to compensate for chromatic dispersion during optical propagation and to suppress the nonlinear effects of the fiber (more details in Chapter 3). For long-haul systems, an entire fiber link consists

of several fiber spans— typically each span is from 80 km to 120 km long. **Figure 1.3** shows a simple single-span single-channel system with either a DCF or a Bragg grating fiber (BGF) to overcome fiber attenuation. The transmission distance can be extended to more than 500 km with the use of in-line optical amplifiers [23, pp. 414–415].

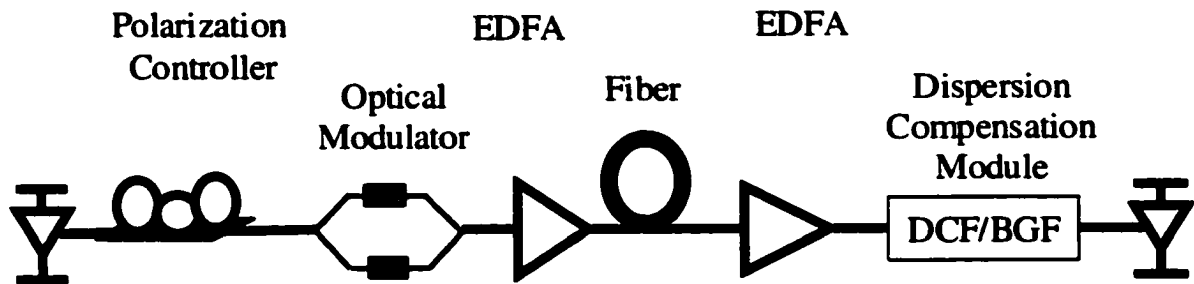


Figure 1.3: A Single-Channel System with Dispersion Compensation

1.3. Wavelength Division Multiplexing

1.3.1 The Need for WDM

Even though the deleterious effects of chromatic dispersion can be significantly reduced using the above compensation methods, it is still difficult to further increase the system capacity beyond OC-192 using TDM with a single optical carrier. The bandwidth limitation of the microwave and optoelectronics components is one major cause of this difficulty. **Figure 1.4** shows the increase in fiber-optic system capacity during the last twenty years using various technologies. Two types of TDM (electrical TDM [ETDM] and optical TDM [OTDM]) are shown on the figure. OTDM multiplexes information signals in the optical domain instead of in the electrical domain, in ETDM. More complex optical components are required to implement OTDM. As shown on **Figure 1.4**, OTDM has never been used in commercial systems, even though it has been demonstrated experimentally that OTDM can increase the capacity above 100 Gbits/s. As for ETDM, only 40 Gbits/s capacity has been experimentally demonstrated, but it is only now being applied to commercial systems. **Figure 1.4** shows that as of the end of 1999, the OC-192 transmission rate is the highest that was available for commercial

systems. However, it is expected that OC-768 (40 Gbits/s) commercial systems will be available in the near future [32].

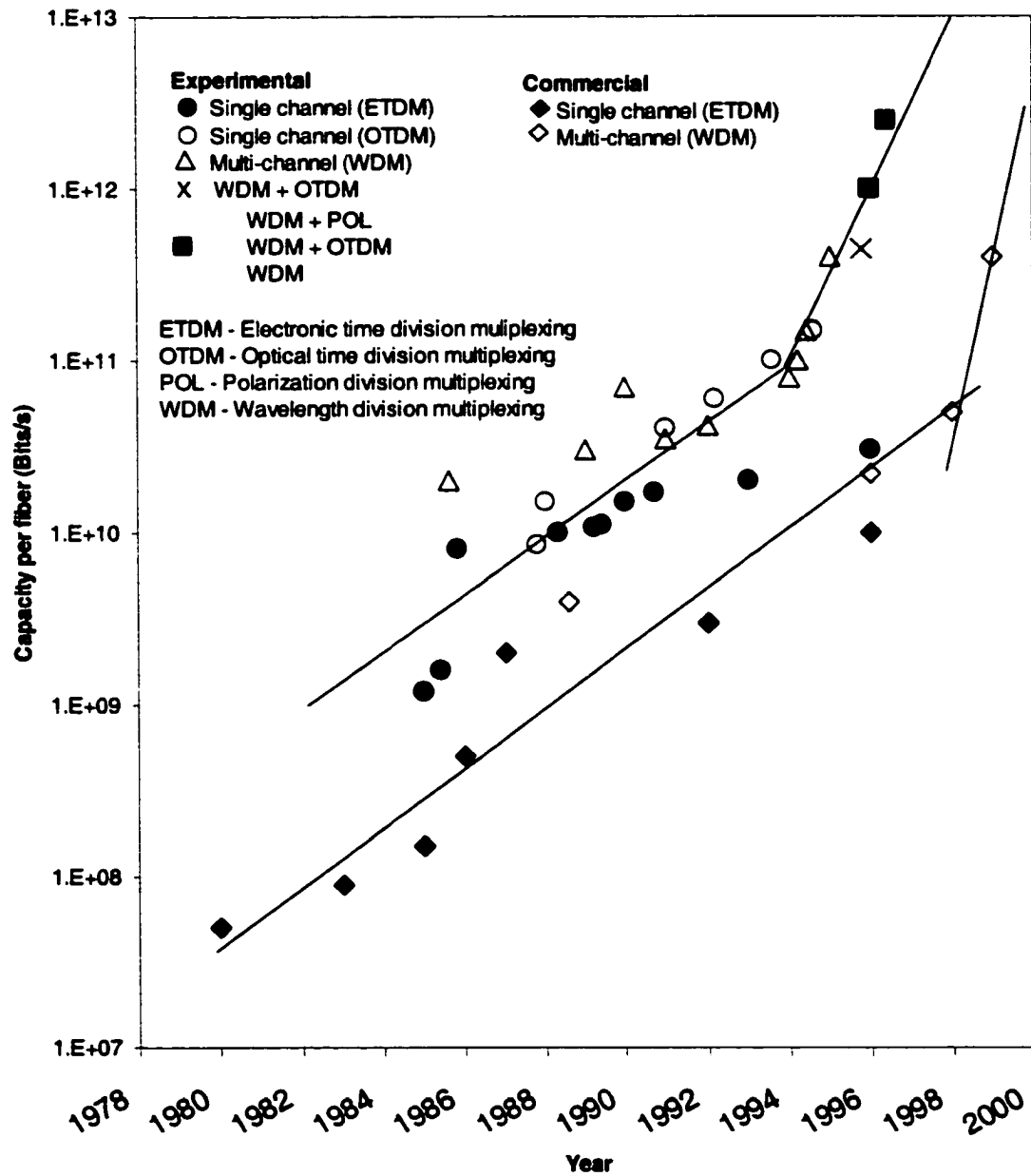


Figure 1.4: Progress in Fiber-Optic System Capacity [26]

To further increase the transmission capacity, **Figure 1.4** shows that the most viable known solution is to adopt wavelength division multiplexing (WDM). Instead of

using one optical carrier (a single wavelength) for transmission, the information bit stream can be carried by many optical carriers with different optical wavelengths. This way, while the bandwidth of each channel can remain the same, the overall capacity can be increased. Commercially available WDM systems can already achieve a total capacity that is higher than what can be achieved by OTDM in the laboratory. The transmission record by the end of 2000 was set by NEC, which demonstrated WDM transmission with a total capacity of 6.4 terabits/s (160 OC-768 channels) [29]. Alcatel also demonstrated a WDM system that has a total capacity of 5.2 terabits/s [28]. Optisphere (a subsidiary of Siemens) claimed that their WDM system had a total capacity of 7.02 terabits/s [30].

Commercial SONET systems using WDM technology are now being deployed. Currently, Nortel Networks offers a wide range of SONET systems that aggressively exploit the WDM technology [24]. The start-of-the-art Nortel system, OPTera, can multiplex 160 OC-192 channels and can possibly transmit to as far as 4000 km with multiple spans [25].

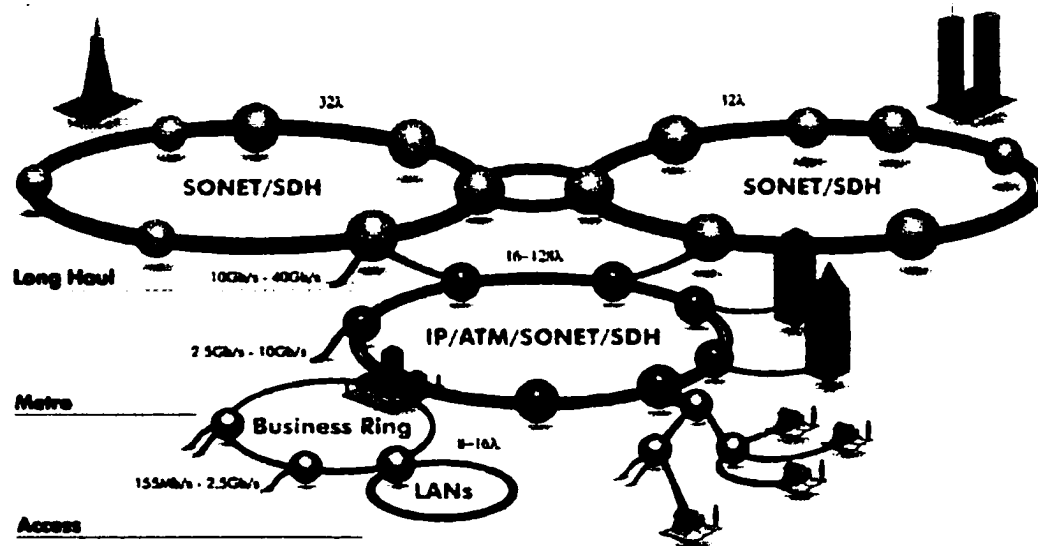


Figure 1.5: SONET Rings in a Multi-level WDM System (Source [31])

1.3.2 Applications of WDM to Different Levels of the Communication Network

Figure 1.5 shows a network map that illustrates the role SONET systems play at different levels of the telecommunication network. Besides their well-known role as the backbone of long-haul communication systems, SONET rings are also useful in metropolitan area networks. A recent report indicates that the WDM technology is not

only beneficial to nationwide and international long-haul systems, it is also a very practical method to scale up a metropolitan network [27]. As seen in **Figure 1.5**, a metropolitan network typically connects to many local area networks. The required traffic capacity for these LANs varies depending on the nature of the network applications: some might operate at the OC-3 rate while others are operating at the OC-12 rate. WDM can allow individual LANs to be upgraded to a transmission rate more suitable for metropolitan networking, simply by increasing the transmission rate of the particular optical channel (or, if necessary, by assigning an extra optical channel). The major benefit of WDM technology lies in the fact that no extra optical fiber is required to increase a system's capacity. Any existing FOCS can be upgraded simply by replacing the terminal equipment and the in-line optical amplifiers in the optical link.

1.3.3 Brief Description of WDM-based SONET Networks

A basic WDM optical network (e.g. a SONET ring) consists of a number of network elements (NEs) including optical amplifiers, wavelength division multiplexers, optical add/drop multiplexers, optical monitoring equipment, optical fiber, optical sources, optical modulators and detectors.

The function of an optical modulator is to transform an incoming information signal from the electrical domain to the optical domain (optical field) to be suitable for fiber-optic transmission. Once in the optical domain, the information signal then propagates through optical fibers (transmission media) to reach the destination.

If the transmission distance is long, optical amplifiers are required to periodically amplify the propagating optical signal to maintain an acceptable signal-to-noise ratio at the destination. Currently, the most widely-used optical amplifiers are Erbium-doped Fiber amplifier (EDFA). Basically, the process of amplification in an EDFA begins with up-conversion where ions in the Erbium-doped fiber (EDF) from a lower-energy level are excited to a higher energy level by means of a pump laser. The energy difference between the higher energy and the lower energy levels is chosen to be roughly equal to the energy of the photons forming the optical signal to be amplified. When an optical signal to be amplified enters an EDFA, its photons will stimulate the up-converted ions to make transitions to the lower energy level. During this down conversion process, a new

photon with the same energy with a coherent electromagnetic field is emitted and hence amplification of the incoming optical signal is achieved. The ions in the higher energy level can also undergo a down conversion spontaneously without any means of external simulations. This down conversion also emits a photon with a non-coherent electromagnetic field. This is referred to as spontaneous emission. A spontaneously-generated photon can, in turn, stimulate an ion in the higher energy level to emit a photon. This process repeats throughout the entire EDFA; it is called amplified spontaneous emission (ASE). ASE is the major noise source in an EDFA, that distorts the information signal [23, p. 366].

Another type of optical amplifier is the Raman amplifier. Similar to the EDFA, the Raman amplifier has a wide amplification spectrum. The major difference between the Raman amplifier and EDFA is that the gain peak (in wavelength) of the Raman amplifier is tunable whereas EDFA has fixed gain peak (more details will be given in later chapters).

Upon its arrival at the destination, the information signal is then transformed back to the electrical domain through an optical detector. An optical detector is usually referred to as a square-law detector. In such a detector, a photo-current (the transformed electrical-domain signal) generated by the detector is proportional to the optical power of the detected optical signal. The optical power, in turn, is proportional to the square of the electromagnetic field of the optical signal, and thus an optical detector is called a square-law detector.

For a multi-channel WDM signal, the destinations of individual channels may be different; therefore, different channels maybe dropped and detected at different nodes along a SONET system. Also, individual channels that form the WDM signal may originate from different nodes. Therefore, add/drop multiplexers are required in a SONET system. **Figure 1.6** depicts a simplified fiber optic system connecting two nodes inside a SONET system. In this example, each node is capable of adding and dropping one or more optical channels. For the “add” operation, information is first modulated into each designated optical channel through an optical modulator (usually of the Mach-Zehnder type). These new optical channels are then combined using an add/drop multiplexer with the existing channels carried by the composite optical channel

propagating in the optical link. For the “drop” operation, the drop channels are separated from the multiplexed optical signal through the add-drop multiplexer. Each of these channels is then detected separately by a photodetector as requested by the SONET node.

One proposed add/drop multiplexer is shown in **Figure 1.7**. In this figure, there is a series of tunable fiber Bragg gratings placed between two optical circulators. These Bragg gratings are designed as ‘notch’ filters, which allow all WDM channels except one to pass through. The channel that does not pass through the grating is reflected backward. The optical circulators have three ports: input, output and reflection. When a signal enters from the input port, it will exit from the output port. If, however, a signal enters from the output port, it will be re-directed to exit from the reflection port, but not the input port. An optical circulator cascaded with a fiber Bragg grating can be used for the ‘drop’ operation in an add/drop multiplexer. As shown in **Figure 1.7**, the left circulator allows a multi-channel WDM signal to enter from the input port and exit from the output port. The WDM signal then propagates through a fiber Bragg grating, where a channel located at wavelength, λ_α , is reflected. The reflected channel is re-directed to the de-multiplexer through the reflection port of the left circulator and the ‘drop’ operation is completed. The add/drop multiplexer can drop multiple channels simply by cascading more fiber Bragg grating (designed to reflect other WDM channels) with the grating just mentioned.

The ‘add’ operation of the add/drop multiplexer is similar to the ‘drop’ operation. As shown in **Figure 1.7**, a fiber Bragg grating is cascaded with a circulator on the right side of the add/drop multiplexer. The circulator is configured to allow the WDM signal leaving the ‘drop’ section of the add/drop multiplexer to enter from the “output port” and exit from the reflection port. A channel located at wavelength, λ_β , is inserted at the input port of the circulator. This channel then exits from the output port and arrives at the Bragg grating. The Bragg grating is designed to reflect the signal located at λ_β . Thus, the channel at λ_β is reflected from the grating and is combined with the WDM signal. The resulting signal then exits from the reflection port of the circulator and the ‘add’ operation is completed. More channels can be added by putting more Bragg gratings in front of the grating just described and inserting a wavelength multiplexer in front of the input port of the right circulator to combine all ‘add’ channels.

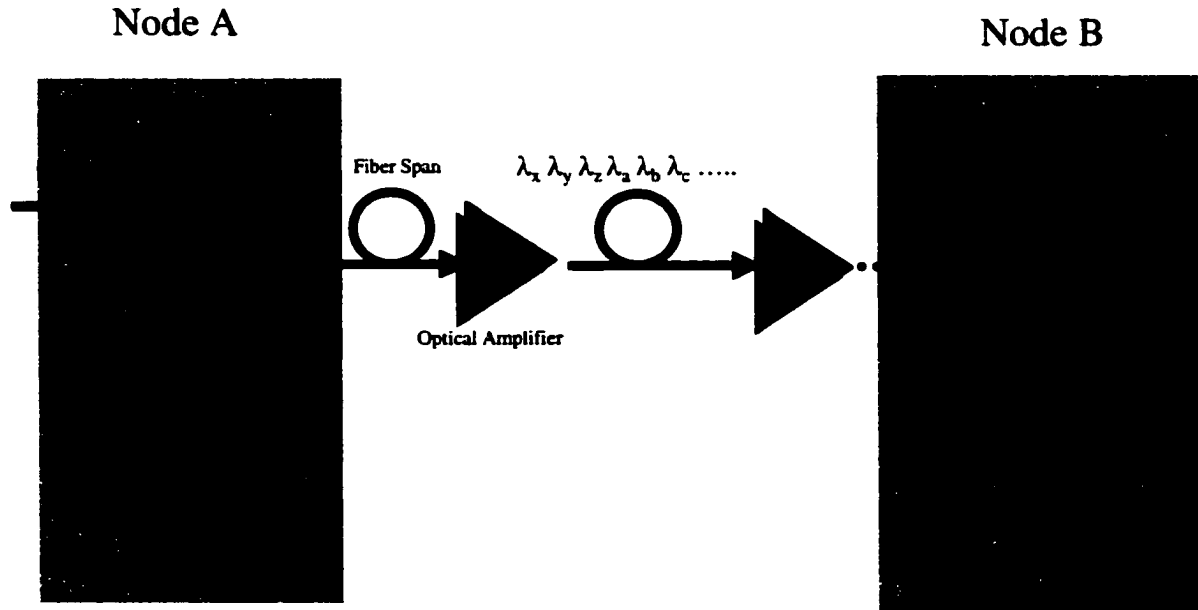


Figure 1.6: Schematic Diagram of a Fiber Optic System with OADMs

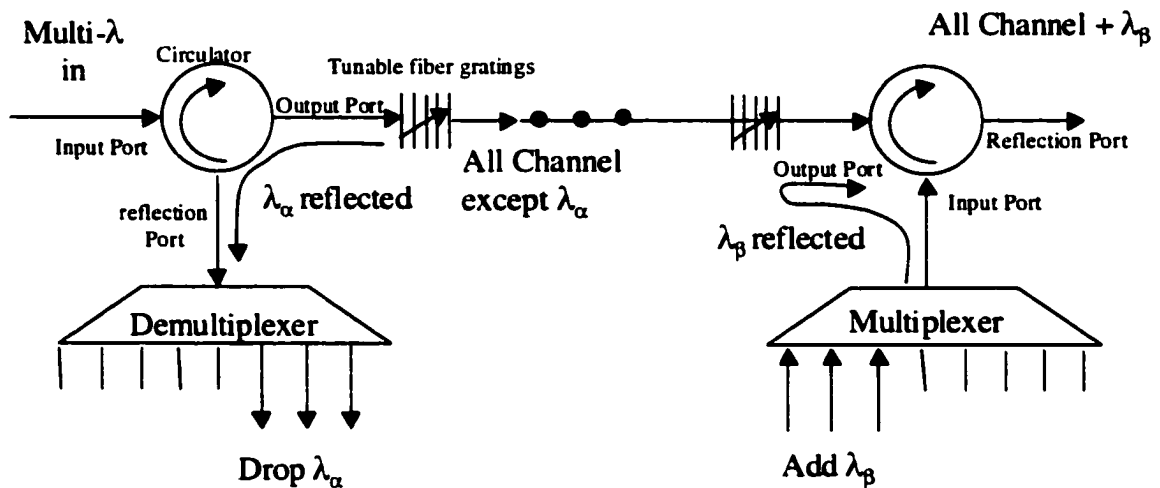


Figure 1.7: Proposed Programmable Optical Add/drop Multiplexer (source [27])

The combined WDM signal output from node A in **Figure 1.6** propagates through the optical link that consists of possibly several fiber spans before reaching node B. Between two consecutive fiber spans is the inline amplifier module. A state-of-the-art EDFA not only consists of EDF, but also includes gain flattening filters to compensate for the uneven gain characteristics of the EDF. Typical EDFA has a gain peak at around 1533 nm and the useful bandwidth can be extended to about 1600 nm which is the L band

(1570-1600nm) [33]. The flattening filter is essential to maintain an even power distribution among the optical channels along the entire optical link. Nowadays, the inline optical amplifier module is designed in such a way that the chromatic dispersion compensation module can be easily cascaded. As mentioned above, the compensation module can be either a DCF or a chirped fiber Bragg grating. The advantage of the fiber grating is its ability to adjust the compensation for each individual optical channel (the chromatic dispersion changes slightly from one channel to the other one because of the dispersion slope; more details will be given in Chapter 2). The shortcoming of the fiber grating is its inband amplitude ripple, a characteristic that is hard to predict before fabrication. Also, a nonlinear phase change is another problem for the fiber Bragg grating. On the other hand, this characteristic of the DCF can be much more accurately predicted. A packaged DCF is sometimes called a dispersion-compensating module (DCM).

1.3.4 Limit the WDM Network Capacity

The ultimate capacity limit of a single-fiber WDM system is determined by the transmission rate of each optical channel and the number of optical channels that can be fit into one fiber. The number of WDM channels is determined by (i) the effective gain bandwidth of the optical amplifier (research is attempting to increase the possible gain bandwidth); (ii) the carrier frequency spacing between channels (the allowed carriers on the International Telecommunications Union [ITU] grid are based on a constant frequency separation); and (iii) the transmission rate of individual optical channels.

The minimum frequency spacing between channels is partly determined by the filter bandwidth of the add/drop demultiplexer, the wavelength stability of each laser, and the stability of the demultiplexer when staying at individual carrier wavelengths [27]. The second important factor is the signal distortion caused by the chromatic dispersion and various nonlinear effects of the fiber (more details will be given in Chapter 2). Nonlinear fiber effects occur because one or more fiber parameters are not constants, but depend on optical power (e.g., the higher the optical power, the stronger the fiber nonlinear effect). The strength of the chromatic dispersion and the nonlinear effects depends on many factors including: the bandwidth of each channel, the spacing between

channels, the number of channels, the optical power of each channel, the length of the optical link and, especially, the type of optical fiber [12, Chapter2].

Three types of single-mode fibers are commercially available: non-dispersion shifted single-mode fiber (often called standard single-mode fiber or SSMF), dispersion shifted fiber (DSF) and non-zero dispersion shifted fiber (NZDSF). SSMF was widely used in the past decade: millions of kilometers of SSMF have been buried underground in North America and around the world. The dispersion-shifted fiber was subsequently invented to overcome the problem of chromatic dispersion that exists in SSMF. However, this type of fiber was found to be unsuitable for WDM applications because of a nonlinear effect called Four-Wave-Mixing (FWM). Consequently DSF is not commonly used in fiber systems. To deal with FWM, manufacturers developed a third generation fiber, commonly called non-zero dispersion-shifted fiber. This type of fiber is engineered to overcome chromatic dispersion and to suppress FWM.

1.3.5 Increase in WDM Capacity

Researchers are seeking ways to reduce the channel spacing in order to fit more channels into the available EDFA bandwidth and hence increase the system capacity. For example, researchers are investigating alternative transmission formats to the commonly used NRZ format that can reduce the channel bandwidth without greatly increasing the signal distortion. Another benefit of reduced channel bandwidth is that the design tolerance of the demultiplexer can be relaxed. It should be noted that the filtering bandwidth of the demultiplexer should be as close as possible to that of the optical channel to minimize the accumulated noise from the amplifier and to minimize the cross talk between neighboring channels. Both the duobinary and OSSB transmission formats have these desired characteristics. They both require less bandwidth than the conventional transmission format; and therefore they might be capable of reducing the combined distortion from chromatic dispersion and nonlinear fiber effects. A recent journal article discusses the potential of duobinary transmission [34]. A total of 132 OC-384 duobinary channels were tightly fit into a 35 nm wavelength band (using both polarizations) and were successfully transmitted through more than 100 km of optical fiber. A 2^7-1 pseudorandom bit sequence (PRBS) generated the information bits.

Another way to increase the transmission capacity of WDM systems is to increase the transmission rate of individual channels. The advantages of a higher transmission rate can be seen from a simple example. Assume that the bandwidth of the optical amplifier is 3.75 THz (30 nm). For an OC-192 (10 Gb/s per channel) system with 50 GHz channel spacing, it is possible to fit in 75 channels to achieve a total capacity of 750 Gbits/s. For an OC-768 (40 GHz per channel) system with 100 GHz channel spacing, it is possible to fit in 38 channels to achieve a total capacity of 1520 Gbits/s. The capacity of the OC-768 system is double that of the OC-192 system but the channel spacing is halved. The wider channel spacing eases the fabrication tolerance of expensive system devices. The smaller number of channels reduces the required number of system components and hence minimize the cost of the system.

Higher transmission-rate systems (i.e. optical channels) are clearly a very promising method for increasing WDM capacity. A better measure of the capacity of the system is its spectral efficiency, which is defined as the ratio of the channel transmission rate to the channel spacing. For an OC-192 system with 50 GHz spacing, the spectral efficiency is 20%; on the other hand, an OC-768 system with 100 GHz spacing has 40% spectral efficiency. For NRZ signals, the signal bandwidth (where most of the signal power is contained) is close to double of the transmission frequency. For example, the optical power of a conventional OC192 signal is contained within the 20GHz region centered at the carrier frequency. Because of this, the signal overlapping becomes gradually more severe as the spectral efficiency is increased beyond 50%. The main problems of higher transmission-rate systems, as mentioned above, are the expense and availability of technology for the large scale fabrication of the required components: Recent research shows that, for OC-768 at least, the technology has reached a mature state of development.

1.3.6 Increase in Transmission Length

Fiber optic systems can be divided into three different categories based on the transmission distance. Systems with a transmission length of less than 200 km are usually called short-haul systems. With advances in optical amplifier technology, it is now economical to transmit WDM signals through a short-haul system with only a single

span. Many short-haul systems are also single-span systems. Terrestrial fiber systems transmit signals among a number of major cities. The typical length of terrestrial systems ranges up to around 600 kilometers. Usually, terrestrial systems consist of a number of fiber spans with the typical length of each fiber span being around 80-120 km. The third type of system transmits signals between continents via submarine fiber-optic cables laid on the ocean floor. The typical transmission length of these submarine systems is in the order of 10,000 km. The typical fiber span length for these systems is 40 km. The reason for the shorter fiber spans is that these optical systems need to operate at lower power in order to suppress the build up of nonlinear fiber effects. To maintain a sufficiently high signal-to-noise ratio (SNR), the gain of the optical amplifiers needs to be low for noise reduction. Therefore, the loss of each fiber span (span loss) needs to be small and hence the fiber spans need to be kept shorter.

It has been found that for ultra-long submarine systems, the return-to-zero (RZ) format performs much better than the non-return-to-zero (NRZ) format [36]. This is due to the fact that the RZ format is less susceptible to nonlinear fiber effects (more detail will follow in later chapters). Nonlinear fiber effects are proportional to the signal power, which means the RZ format can safely operate at a higher power than the NRZ formats. The higher operating power permits longer fiber spans. This is because the SNR reduction due to the increase in span loss can be compensated by an increase in signal power, which maintains the SNR. As a result, the RZ format is also being introduced into terrestrial systems either to reduce the number of spans or to increase the SNR with the existing span length. Today, it is possible for terrestrial spans to reach to several thousands of kilometers in length with the aid of Raman amplifiers.

1.4. Research Contributions of This Thesis

This thesis evaluates several alternative transmission formats to determine their potential for different types of WDM fiber systems. The research contributions involve four different parts.

(1) To evaluate the performance of different alternative transmission formats, the fastest and most economical way is to use computer simulations. Also, computer simulations can evaluate systems before they can be implemented with current

technologies. A simulation software package was developed previously at TR Labs [8, Chapter 7]. It is capable of performing system-level evaluation including the modeling of essential optoelectronic and optical components used in a typical fiber optic system. However, the program uses only a simple model for the optical fiber that takes into account only the linear chromatic dispersion effect, but no nonlinear fiber effects. This older package is therefore not adequate for simulating WDM systems, where nonlinear fiber effects cannot be ignored. Thus, an important contribution of this research is to create a new simulation software package that accurately models the optical fiber. Various nonlinear effects and chromatic dispersion modeling were incorporated into the new software.

(2) Another main contribution of this research is the comparison of the duobinary and OSSB transmission formats with the commonly used NRZ OOK format. Our research group at TR Labs has previously investigated both alternative transmission formats in a single-channel configuration. The new research extends the investigation to evaluate the performance of these two transmission formats in a WDM configuration. Specifically, this research systematically compares the performance of the OOK, duobinary and OSSB formats in both short-haul and terrestrial systems that are significantly influenced by the combined effect of fiber nonlinearities and chromatic dispersion. Since both the duobinary and OSSB formats have the potential to further reduce the channel spacing of a WDM system, this research also examines potential WDM systems with channel spacing that is narrower than available in current commercial systems. The performance evaluation of these three formats was based on theoretical analyses, simulations and experiments. The theoretical analyses systematically examine the impact of individual nonlinear effects and chromatic dispersion on the three formats. The findings from the theoretical analysis were then confirmed by simulations using the improved simulation tools. As for the experimental part, laboratory testbeds were constructed for each transmission format to measure their performance in different types of fiber systems. To our knowledge no previous research has examined the impact of fiber nonlinear effects on the OSSB format. Similarly, it appears that no previous research has done a systematic examination of the impact of fiber nonlinear effects on the duobinary format. Published work has suggested the

potential benefit of the duobinary format for overcoming nonlinear fiber effects, but without given any evidence or proof [37].

(3) Knowing that both the duobinary and OSSB formats are capable of reducing the signal bandwidth by 50%, another contribution of this research is to examine the possibility of combining these two formats to further reduce the signal bandwidth. There are few types of single-sideband (SSB) formats that can be implemented readily in fiber systems. This part of the research examines the compatibility of each of these SSB formats with the duobinary format. Also, an optical device that is capable of converting a SSB signal back to double-sideband is examined. No previous research has demonstrated that this optical device has this capability. This device is required to combine the OSSB and duobinary formats. Single-channel simulations were performed to evaluate the performance of the resulting combined format.

(4) The fourth contribution of this research is to compare the performance of three different alternative RZ formats, namely, bipolar RZ (BP-RZ), duobinary RZ (D-RZ) and modified duobinary RZ (MD-RZ), with the commonly used RZ format. Miyamoto et al. showed that BP-RZ performs better than RZ. Their study used simulations and experiments, but they did not clearly explain their conclusions [38]. By examining the other two alternative RZ formats along with the BP-RZ and RZ formats, this research attempts to explain the cause of the performance improvement of the alternative RZ formats. The ultimate goal of this part of the research is to examine the feasibility of the three alternative RZ formats for extending the fiber span length in terrestrial WDM systems. The investigations were based on both simulations and theoretical analyses.

1.5. Thesis Outline

The rest of this thesis is organized as follows: Chapter 2 discusses various fiber distortions and possible methods for simulating signal propagation through an optical fiber. The verification of the accuracy of the resulting simulation tool is also presented. Chapter 3 compares the OOK, OSSB and duobinary formats using simulations and theoretical analysis. Chapter 4 presents the experimental results of the comparison of the performance of these three formats. Chapter 5 discusses a method of combining the duobinary and OSSB formats to further reduce the bandwidth of the signal spectrum.

Simulation results are presented to show the performance of this hybrid OSSB duobinary format. Chapter 6 compares the conventional RZ format with three other alternative RZ formats, namely, duobinary RZ, modified-duobinary RZ and bi-polar RZ. The main objective of this comparison is to examine whether or not the various alternative RZ formats are capable of increasing the fiber span for typical terrestrial systems. Finally, the main findings of this research are summarized in Chapter 7. Directions for future follow-up research are also proposed.

2. Modeling of the Fiber Optic System

2.1. Introduction

This chapter provides details of the simulation algorithms used to model signal propagation down the optical fiber. Along with other existing simulation subroutines, the entire simulation tool is capable of evaluating system performance using a technique called Q-factor estimation (more details in section 2.6). In Section 2.2, we briefly introduce various non-ideal effects found in fibers. Section 2.3 discusses how the various fiber effects can be modeled mathematically. The simulation program based on this model is described in Section 2.4. The procedures used to verify the accuracy of the simulation program are described in Section 2.5. Finally, Section 2.6 describes how we performed Q-factor estimation of the detected signal at the receiving end.

2.2. Brief description of various fiber distortions

The major nonlinear effects that exist in optical fiber include self-phase modulation (SPM), cross-phase modulation (XPM), four-wave mixing (FWM), stimulated Brillouin scattering (SBS), stimulated Raman scattering (SRS), and polarization-mode dispersion (PMD). Among these nonlinear effects, only SPM and PMD exist in single-channel (as well as multi-channel) systems; all of the other effects require more than one channel in the system.

For a single-channel fiber optic system of short length (< 100 km), the linear model (which models only chromatic dispersion) is sufficient to simulate accurately signal propagation in the optical fiber because the nonlinear effects of the fiber are not significant [8]. For longer distances, the fiber model must also include the nonlinear effects. As will be shown later, the strengths of the nonlinear fiber effects are directly proportional to the power of the propagating signal. As mentioned in Chapter 1, a typical terrestrial system is formed by several fiber spans connected by inline EDFAs. At the output of each inline EDFA, the signal power is restored to the original launched level. Therefore, unlike in single-span systems, where the nonlinear effects are only strong at the launching end of the optical link, propagating signals in long-distance systems are

distorted repeatedly by the nonlinear effects. Thus the accumulated nonlinear distortion can be much stronger for long-distances systems and hence a model of the nonlinear effects must be included in the simulation.

With respect to WDM systems, both chromatic dispersion and nonlinear effects must be taken into account even for short optical links. As mentioned above, the nonlinear effects are proportional to the signal power. A typical WDM signal usually consists of several tens of optical channels. Thus, the total launched power of a composite WDM signal is many times higher than that of a single-channel signal, and the resulting nonlinear effects could be important even over a short propagation distance.

The following sub-sections will describe the physical origins of each individual nonlinear fiber effect.

2.2.1 Chromatic Dispersion

As for other phenomena in optical communications, the equations governing the linear (e.g. only chromatic dispersion) and nonlinear (chromatic dispersion along with other fiber effects) aspects of signal propagation in optical fiber are derived from Maxwell's equation listed below [12, p. 29].

$$\nabla \times E = -\frac{\partial B}{\partial t} \quad (2.1)$$

$$\nabla \times H = J_f + \frac{\partial D}{\partial t} \quad (2.2)$$

$$\nabla \cdot D = \rho_f \quad (2.3)$$

$$\nabla \cdot B = 0 \quad (2.4)$$

where t is time; E and H are the electric and magnetic field vectors, respectively; and D and B are the corresponding electric and magnetic flux densities. The electric and magnetic fields carry the information signal from one end of the optical link to the other. The current density vector J_f and the scalar charge density ρ_f represent the sources for the electromagnetic field. In a medium, such as optical fiber, that has no free charge, $J_f=0$ and $\rho_f=0$ (i.e. no electric field source). The flux densities D and B arise in response to

the electric and magnetic fields E and H propagating inside the medium and are related to them through the following constitutive relations,

$$D = \epsilon_0 E + P \quad (2.5)$$

$$B = \mu_0 H + M \quad (2.6)$$

where ϵ_0 is the vacuum permittivity, μ_0 is the vacuum permeability, and P and M are the induced electric and magnetic polarizations. For a nonmagnetic medium, such as optical fiber, $M = 0$.

A linear wave propagation equation can be derived by assuming that the flux density, D , is directly proportional to both the propagating electric field and the induced electric polarization in each frequency. The resulting wave equation can be written as,

$$\nabla^2 \bar{E} + n^2(\omega) \frac{\omega^2}{c^2} \bar{E} = 0 \quad (2.7)$$

where ω is the angular frequency; n is commonly known as the refractive index, which is related to the permittivity of the medium [12, p30-31]; and \bar{E} is the Fourier transform of the electric field.

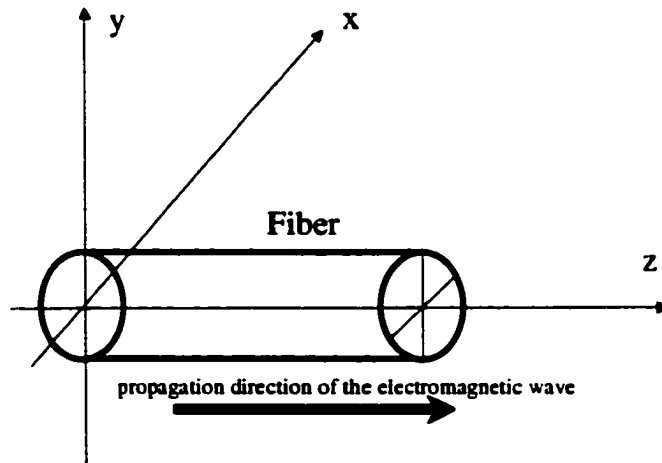


Figure 2.1: Co-ordinate System for Electromagnetic Wave Propagation in Fiber

With a few approximations [12, p35], the solution to (2.7) can be written as,

$$\bar{E} = A(\omega) F(x, y) \exp[-i\beta(\omega)z] \quad (2.8)$$

where $F(x,y)$ is the cross-sectional mode distribution and is assumed to be constant throughout the length of the entire optical fiber. Coordinates x and y are orthogonal to each other and to the coordinate z along the direction of propagation. The optical field propagates in the z direction, as described by the $\exp(-j\beta z)$ term, where β is the propagation constant which is related to the refractive index of the fiber. This coordinate system is graphically illustrated in **Figure 2.1**. $A(\omega)$ is the Fourier transform of the amplitude of the optical field $A(t)$, which encodes the information to be transmitted. For on-off keying (OOK) modulation, A consists of unit and zero pulses that represent '1' and '0' bits in the time domain. As will be shown later, in the nonlinear propagation regime, A is a function of both time and propagation direction. The details of the calculation of these parameters can be found in [12, p32-35]. This section only focuses on the effects of chromatic dispersion.

Equation (2.8) shows that for linear propagation, the electric field is only modified by the propagation constant, β , through the last term in the equation. In general, β is a function of frequency, and can therefore be expanded into a Taylor series as follows,

$$\beta(\omega) = \beta_0 + \beta_1\omega + \frac{\beta_2}{2!}\omega^2 + \frac{\beta_3}{3!}\omega^3 + \dots \quad (2.9)$$

where ω is the angular frequency relative to the angular frequency, ω_0 , of the optical carrier (or the laser); β_0 is the propagation constant at ω_0 , and for $n>0$, $\beta_n = \left. \frac{d^n \beta}{d\omega^n} \right|_{\omega=\omega_0}$.

If only the β_0 term in (2.9) is important, then the propagating electric field is only modified by a complex constant according to (2.8). If both the β_0 and β_1 terms are included, then according to the properties of the Fourier transform, the electric field is just time shifted. The corresponding behaviors in the time domain for these two cases are,

$$A(\omega)F(x, y)\exp(-i\beta_0 z) \xrightarrow{\text{inverse Fourier transform}} A(t)F(x, y)\exp(-i\beta_0 z) \quad (2.10)$$

$$A(\omega)F(x, y)\exp(-i\beta_0 z)\exp(-i\beta_1\omega z) \xrightarrow{\text{inverse Fourier transform}} A(t - \beta_1 z)F(x, y)K \quad (2.11)$$

where K is a complex constant.

The second case, where both the zero and first derivatives of β are significant, (2.11) shows that at a propagation distance, z_1 , the signal travels by ' $\beta_1 z_1$ ' in time. The speed of the traveling signal is, thus, equal to $z_1/\beta_1 z_1 = 1/\beta_1 = V_g$. V_g is known as the group velocity of the signal.

The effects of higher-order derivatives of the propagation constant β are not simply to add a constant or time-shift to the signal; they also change the phase relationship between different frequency components in the signal spectrum. The rate of phase change affecting a frequency component in the signal increases as the frequency increases. The increase in phase change is equivalent to an increase in the propagation speed. Thus, high frequency components travel faster than low frequency components. This phenomenon is known as the chromatic dispersion. For optical fiber, the fourth-order or higher derivatives are very small and can be neglected [23, pp. 39-46]. As will be shown in a later section and in Chapter 3, the effect of chromatic dispersion is pulse spreading, which increasingly causes intersymbol interference at the receiver as the propagation distance lengthens. The dispersion caused solely by the second derivative β_2 of the propagation constant is referred to as the group-velocity dispersion (GVD).

The strength of the chromatic dispersion is mostly determined by the physical properties of the optical fiber, the relative refractive index difference between the core and the cladding, the cross-sectional refractive index profile, and the wavelength of the optical carrier. It is possible to manipulate the index profile of the fiber to adjust the zero-dispersion wavelength and to modify the dispersion characteristics of the fiber as a function of frequency. The zero-dispersion wavelength is the wavelength where the second order derivative of the propagation constant β is equal to zero. Both the dispersion-flattened fiber (DFF) and the dispersion-shifted fiber (DSF) are good examples of commercially-available dispersion-modified fibers [40]. The DFF is engineered to suppress the third-order derivative of β to keep the GVD small throughout a wide-range of frequencies. The DSF is made to shift the dispersion-zero wavelength to a desired wavelength. **Figure 2.2** illustrates the dispersion profiles for different fibers.

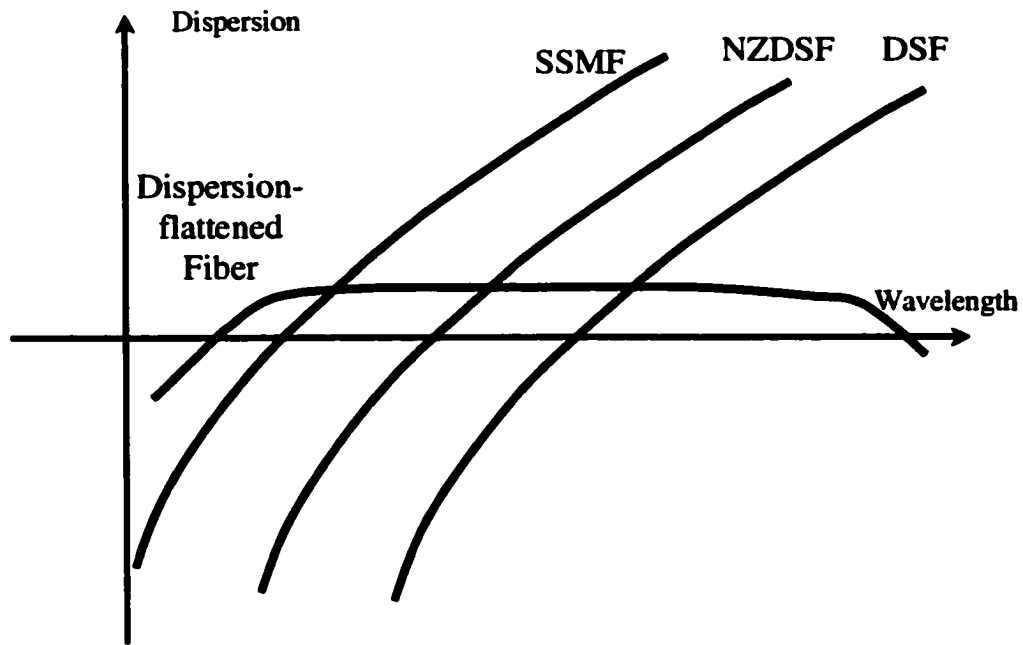


Figure 2.2: Dispersion Profile of Different Fibers

2.2.2 Kerr Effect for Self-Phase Modulation (SPM), Cross-Phase Modulation (XPM) and Four Wave Mixing (FWM)

SPM, XPM and FWM have similar origins. All three effects are caused by the nonlinear response of the propagation medium when it interacts with the optical field. As in other nonlinear optical media, the induced polarization of the fiber is not simply proportional to the incoming optical field. The induced polarization results from the interaction of the incoming electromagnetic (EM) wave with the molecules of the fiber, an interaction that induces a dipole moment. The dipole moment, in turn, generates a secondary EM wave and thus the total wave propagation in the fiber is the sum of the incoming wave and the secondary wave. Since the dipole moment is not, in general, linearly proportional to the incoming electromagnetic wave, the secondary wave generated by the dipole moment will not be a scaled replica of the primary incoming wave: it will contain signal components at the same frequency as the primary wave as well as new harmonics at higher frequencies. Because of this, the secondary wave effectively adds distortion to the propagating signal.

In optical fiber, the nonlinear component of the response is relatively small and can be treated as a small perturbation. Because of this, the induced polarization can be separated into linear and nonlinear parts. The linear part of the polarization is directly proportional to the optical field at a given optical frequency. The nonlinear part of the induced polarization is described by the third-order susceptibility of the glass from which the fiber is made, $\chi^{(3)}$. This is known as the Kerr effect [41, p. 699]. Since the optical fiber can be treated as an isotropic material, the second-order susceptibility can be ignored [41, p. 699]. If the transmission rate of each optical channel in the WDM system is less than terabits (10^{12}) per second [12, p. 38], the nonlinear polarization can be related to $\chi^{(3)}$ by

$$P_{NL} = \epsilon_0 \chi^{(3)} E^3 \quad (2.12)$$

where ϵ_0 is the vacuum electric permittivity and E is the optical field strength. Equation (2.12) implies that if the optical field consists of multiple signals located at different frequencies, the signals will mix multiplicatively with each other. This process is called four-wave mixing (FWM). If the signals are equally spaced in the frequency domain, some of the mixing terms at new frequencies will overlap with existing signals (usually referred to as optical channels in a communication system) in the frequency domain and will cause signal distortion.

As will be shown in section 2.3, both the self-phase modulation (SPM) and cross-phase modulation (XPM) effects are also due to nonlinear polarization in the optical medium. As the name suggests, the effect of SPM is to modulate the phase of the optical field according to its instantaneous power. In the case of XPM, the phase distortion is proportional to the instantaneous power of other optical channels present in the WDM system.

2.2.3 Stimulated Brillouin Scattering (SBS) and Stimulated Raman Scattering (SRS)

SRS and SBS are very similar processes. From the quantum mechanical point of view, these two scatterings can be understood as the process whereby the incoming optical field is scattered by the molecules of the optical fiber. The consequence of the

scattering is the generation of phonons (vibrational quanta) and a secondary optical field. Due to the conservation of energy, the photon energy of the secondary field must be less than that of the original field (i.e. the pump wave); therefore the frequency of the secondary field is less than the pump wave. Usually, this secondary optical field is called the Stoke wave. The major difference between SRS and SBS is the frequency of the phonons. With respect to SBS, the frequency of the phonons ranges from a few megahertz to tens of megahertz; therefore these scattering-induced phonons are usually classified as acoustic phonons. In contrast, the frequency of SRS is much higher, typically up to a few terahertz (about 12.5 THz for commercial fiber); therefore, these phonons are usually called optical phonons. Another major difference between these two processes is the propagation direction of the Stoke wave. The Stoke wave generated by SBS can only travel in the direction opposite to that of the pump wave; on the other hand the stoke wave created from SRS can travel in both directions in a manner similar to the amplified spontaneous emission (ASE) of photons in Erbium-doped fiber amplifiers.

Mathematically, the two scattering processes can be described by the following pair of equations [12, p. 237]:

$$\frac{dI_s}{dz} = \pm g I_p I_s \mp \alpha_s I_s \quad (2.13)$$

$$\frac{dI_p}{dz} = -g I_p I_s - \alpha_p I_p \quad (2.14)$$

where g is the gain parameter for either the SRS or SBS processes; I_p and I_s are the intensities of the pump and stoke waves, respectively; and α_p and α_s are the attenuation factors for the pump and stoke waves, respectively. The upper and lower sets of signs in (2.13) are for SRS and SBS, respectively. If one can assume that the pump wave is an unmodulated optical signal and is not depleted by the stoke wave, and the power drop in the pump wave is mostly due to fiber attenuation (non-depleted pump), and not power transfer to the stoke wave, (2.13) can be approximately solved and has the solution as follows,

$$I_s(z) = I_s(0) \exp\left\{\left[\pm g I_p(0) \mp \alpha_s\right] z\right\} \quad (2.15)$$

From (2.15) we note that the power of the stoke wave increases exponentially along the propagation direction.

These scattering processes do occur in WDM systems where a higher frequency channel pumps a channel at a lower frequency. The scattering becomes important if the pump power exceeds a certain level. This threshold for SBS is usually above 10 dBm (10 mW) [12], which is above the operating point of any commercial system. Thus the effect of SBS can be safely ignored. SRS has a much higher threshold than SBS, typically more than 100 mW [43]; therefore for single-channel systems, SRS can also be ignored. With the higher signal powers in a WDM system, however, SRS could cause considerable distortion. The reason is that the frequency of the phonons generated by SRS can be as high as a few terahertz, which means that the gain spectrum of the stoke waves is of the same magnitude. If the WDM system contains many channels, the channels located at the shorter wavelength can generate stoke waves which overlap with the channels at longer wavelengths. In particular, if the entire WDM spectrum lies within the SRS gain spectrum, the last channel located at the longest wavelength will be affected by the stoke waves generated by all other channels. However, for this research, the simulation bandwidth was limited to about 1.6 terahertz. Within this bandwidth, SRS is not a significant contribution to overall distortion.

The preceding discussion has described the two scattering processes as adverse effects on the fiber-optic system. In practice, both of these processes can be exploited as an essential component of a fiber system. Before EDFAs became popular, stimulated Raman amplification was considered one promising method of optical amplification [42]. Similar to the EDFA gain spectrum, the gain spectrum of the Raman amplification is also wide, with a gain peak occurring 100 nm (12.5 THz) longer than the pump wavelength. Thus, it is possible to amplify an optical signal in the 1550 nm window by placing a high-power laser at around 1450 nm. The major advantage of Raman amplification is that its gain spectrum can be wavelength-tunable, unlike the fixed Erbium gain spectrum [42]. Thus, it can amplify a signal that is outside the gain spectrum of the EDFA. Another advantage of Raman amplification is its distributed nature. Unlike in an EDFA, Raman amplification can be performed in the transmission fiber simply by launching the pump light from the opposite end of the fiber into which the signal is launched. Signal

amplification occurs throughout the transmission fiber and hence it is a distributed form of amplification. Consequently, the noise from the Raman amplification can be lower than in an EDFA because the gain occurs at a signal power level much higher than with the EDFA. As a result, the Raman amplifier has been the subject of tremendous research in recent years [42]. A similar application can also be found for the SBS process. However, due to its narrow gain spectrum, the Brillouin effect is not commonly used in the WDM system [23, pp. 385-391].

2.2.4 Polarization Mode Dispersion (PMD)

In a single-mode fiber, there exist two orthogonal propagation modes. If the fiber is perfectly circular, these two modes will have exactly the same mode distribution and propagation constant [12]. In this case, the two modes are degenerate and hence the signals carried by these separate modes can be treated as one signal. Nevertheless, in real optical fiber, the fiber core is not perfectly circular. Because of this, the two modes will actually have different propagation constants and mode distributions. It has been shown that the variation of the mode distribution is negligibly small for most practical situations and therefore can be ignored. PMD occurs because the two orthogonal modes travel at different speeds, and power is coupled back and forth between the modes (mode coupling) during the signal propagation. Even without mode coupling, the pulse spreading due to PMD would occur because the two modes arrive at the receiver at different times. This is graphically illustrated in **Figure 2.3**.

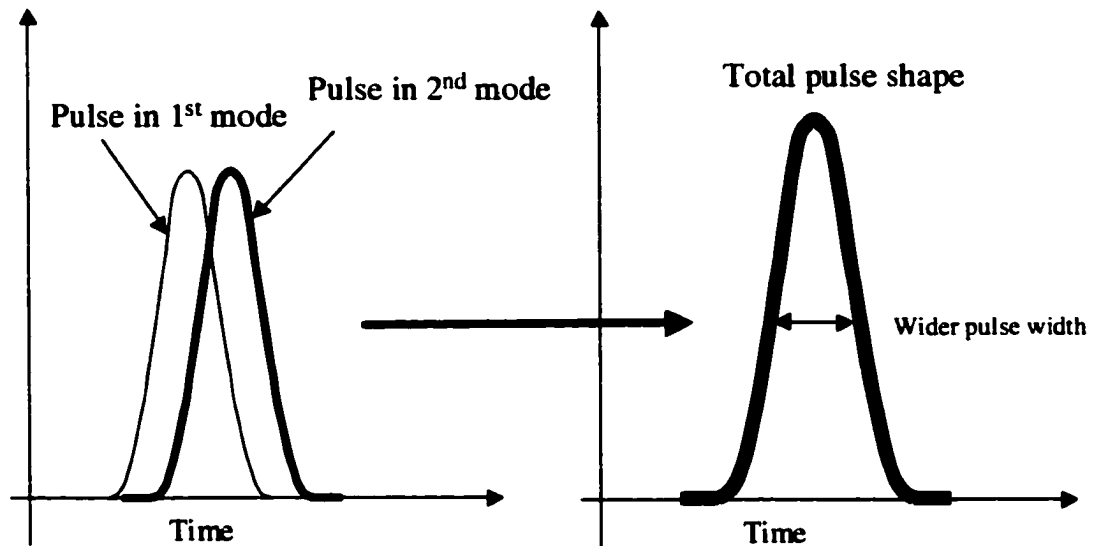


Figure 2.3: Pulse Spreading due to PMD

In the last 10 years, fabrication techniques for optical fiber have greatly improved, thus greatly reducing PMD for all types of fiber. For a fiber link length of less than 1000 km of currently manufactured fiber, PMD can simply be ignored for OC-192 system [44]. This research deals mainly with OC-192 systems; therefore it is reasonable to ignore the effects of PMD in our simulations.

2.3. The Nonlinear Schrodinger Equation

Chromatic dispersion and most of the nonlinear effects (including SPM, XPM FWM, and SRS) can be modeled accurately by the nonlinear Schrodinger equation (NLSE). A detailed derivation of the nonlinear Schrodinger equation can be found in [12]. This section only discusses the derivation results and related explanations. Since SRS can be ignored in our simulations, the terms that account for SRS are excluded in the equations discussed below. The following paragraphs will first explain the assumptions made in the derivation, then various forms of the nonlinear Schrodinger equation will be discussed.

As mentioned in the last section, light actually propagates in two orthogonal modes along single-mode fiber. The nonlinear Schrodinger equation assumes that the two modes are degenerate. In other words, the two modes are assumed to have exactly the same cross-sectional mode distribution and propagation speed. Second, the nonlinear

part of the induced polarization is assumed to be proportional to the cube of the optical field amplitude. This is due to the fact that the nonlinear response of the optical fiber is relatively fast and can be treated as an instantaneous effect when the transmission rate of each channel is less than terabits per second [12]. Third, it is assumed that the optical field consists of both fast and slowly varying fields. This is true because the frequency of the optical carrier (the laser) in an optical communication system is in the hundreds of terahertz (the fast varying portion); by contrast, the bandwidth of the information carried by the optical carrier is only in the tens of giga (10^9) hertz (the slowly varying portion).

With the above assumptions, the optical field can be written in the form

$$E = \frac{1}{2} \left[A(t, z) F(x, y) e^{-j\beta z} e^{j\omega_b t} + c.c \right] \quad (2.16)$$

where *c.c* denotes the complex conjugate of the first term in the expression; $\exp(j\omega_b t)$ is the rapidly varying field; and ω_b is the angular frequency of the optical carrier. The first three factors in the first term describe the slowly varying part of the optical signal. $F(x, y)$ is the cross-sectional mode distribution and is assumed to be constant throughout the entire optical fiber. Coordinates x and y are orthogonal to each other and to the coordinate z along the direction of propagation. The optical field propagates in the z direction, as described by the $\exp(-j\beta z)$ term, where β is the propagation constant as discussed in the previous section. $A(t, z)$ is the amplitude of the optical field which encodes the information to be transmitted.

The nonlinear Schrodinger equation [12, p. 45] describes how $A(t, z)$ varies over space and time as the light signal propagates through the fiber. It can be expressed as:

$$\frac{\partial A}{\partial z} = i \frac{\beta_2}{2} \frac{\partial^2 A}{\partial T^2} + \frac{\beta_3}{6} \frac{\partial^3 A}{\partial T^3} - \frac{\alpha}{2} A - i\gamma |A|^2 A \quad (2.17)$$

where $\gamma = \frac{2\pi n_2}{\lambda_0 A_{eff}}$; $n_2 = \frac{3}{8n} \chi^{(3)}$, where n_2 is the nonlinear refractive index and n is the

linear refractive index; $A_{eff} = \left[\int \int_{-\infty}^{\infty} |F(x, y)|^2 dx dy \right]^2 / \int \int_{-\infty}^{\infty} |F(x, y)|^4 dx dy$ is the effective core area; $i = (-1)^{1/2}$; α is the power attenuation factor; $T = t - z/V_g$; and V_g is the group velocity which equals to $1/\beta_1$. The first two terms on the right side of the equation

describe the chromatic dispersion. The third term takes into account the fiber attenuation. Typical values for the fiber attenuation range between 0.20 - 0.25 dB/km [45]. The last term on the right side of the equation describes the nonlinear effects of the fiber. In the derivation, the instantaneous power of the optical signal is set equal to $|A|^2$. Equation (2.17) can be used to model either the evolution of a single optical channel or the evolution of a composite signal that contains more than one channel propagating through the fiber.

It should be noted that equation (2.17) is derived by assuming that the Fourier transform is defined in the conventional way as

$$F(\omega) = \int_{-\infty}^{\infty} f(t)e^{-j\omega t} dt \quad (2.18)$$

If the minus sign in the exponential term is absent from (2.18), the signs of some of the terms in (2.17) will be different (for details refer to [12]).

Inherently, the use of the discrete Fourier transform in the numerical simulation assumes that A is periodic, i.e., the information sequence is repeated after a certain period of time. In the actual experiments, the Bit-Error-Ratio Tester (BERT) indeed generated a periodic signal which modulated the optical carrier; therefore the nonlinear Schrodinger equation provides a good model for our experiments. It is convenient to define a modified time frame, T , that moves synchronously along with the optical signal. Such a T is usually called the retarded frame [12, p 45]. At different locations along the fiber, such a time frame is offset by the time required for the optical signal to travel from the input of the fiber to the particular location at the group velocity, V_g . In other words, time in this time frame is expressed relative to the moving center of the signal.

Factors β_2 and β_3 in Schrodinger's equation are usually expressed in terms of the measurable dispersion parameter, D , as follows [12, p. 10]:

$$\beta_2 = \frac{d\beta_1}{d\omega} = \frac{d\beta_1}{d\lambda} \frac{d\lambda}{d\omega} = \frac{-\lambda_0^2}{2\pi c_0} D \quad (2.19)$$

$$\beta_3 = \frac{\lambda_0^3}{(2\pi c_0)^2} \left(2D + \lambda_0 \frac{dD}{d\lambda} \right) \quad (2.20)$$

where $D = \frac{d\beta_1}{d\lambda}$ is in units of ps/(nm km).

The following sub-sections discuss different forms of the NLSE. The linear form of the NLSE will be described in section 2.3.1. Then, the nonlinear form of the NLSE including only the SPM is described in section 2.3.2. Section 2.3.3 discusses another more detailed form of the NLSE that include chromatic dispersion , SPM and XPM effects. Section 2.3.4 discusses the most detailed form of the NLSE that includes chromatic dispersion, SPM, XPM and FWM.

2.3.1 NLSE: Including only Chromatic Dispersion

By ignoring the last term in equation (2.17) which is responsible for nonlinear effects, the nonlinear Schrodinger equation simplifies to

$$\frac{\partial A(T, z)}{\partial z} = i \frac{\beta_2}{2} \frac{\partial^2 A(T, z)}{\partial T^2} + \frac{\beta_3}{6} \frac{\partial^3 A(T, z)}{\partial T^3} - \frac{\alpha}{2} A(T, z) \quad (2.21)$$

which describes only the linear chromatic dispersion effect. This simplified equation has an analytical solution, which is obtained by transforming the equation into the frequency domain (using the Fourier transform) [12]. The solution is as follows:

$$A(\omega, z + \Delta z) = A(\omega, z) \exp \left\{ i \left[\frac{-\beta_2}{2} \omega^2 - \frac{\beta_3}{6} \omega^3 \right] \Delta z \right\} \exp \left(-\frac{\alpha}{2} \Delta z \right) \quad (2.22)$$

where Δz is the incremental distance. This equation is widely used to model chromatic dispersion.

As seen from (2.22), the chromatic dispersion (i.e. the β_2 term in the exponential expression) increases the phase in quadratic fashion as the absolute frequency increases. The result of this phase change in the frequency domain is pulse spreading, which causes intersymbol interference (ISI). **Figure 2.4** shows the change in the width of a Gaussian pulse propagating through a SSMF (ignoring attenuation). In the figure, the pulses are captured at a traveling interval of 100 km. The pulse at 0 km has the highest amplitude and gradually decreases for increasing displacements in either direction.

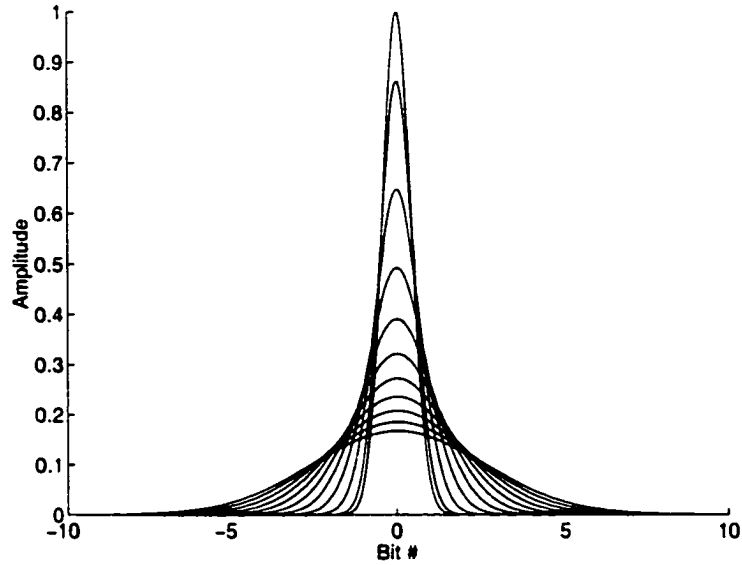


Figure 2.4: Pulse Spreading of a Gaussian Pulse

2.3.2 NLSE: Including only SPM

If both the dispersion and attenuation terms on the right side are ignored, (2.17) can be simplified to

$$\frac{\partial A(T, z)}{\partial z} = -i\gamma |A(T, z)|^2 A(T, z) \quad (2.23)$$

The analytical solution for this equation is

$$A(T, z + \Delta z) = A(T, z) \exp\left[-i\gamma |A(T, z)|^2 \Delta z\right] \quad (2.24)$$

For single-channel systems, (2.24) describes SPM, which has the effect of modulating the instantaneous phase of the optical signal. The phase distortion is proportional to the instantaneous power $|A(T, z)|^2$ of the signal. For multi-channel systems, this equation models SPM, XPM and FWM together. Without chromatic dispersion, SPM alone would not cause any distortion to the signal because the additional phase term would be removed by the square-law detector at the receiver. The effect of SPM can be clearly illustrated by the signal spectrum spread of a Gaussian pulse while propagating through an optical fiber, as shown in **Figure 2.5**. Both fiber attenuation and chromatic dispersion were ignored when calculating these signal spectra. The peak power of the Gaussian pulse was set at 10 mW. The nonlinear refractive index and effective core area were set at $2.3 \times 10^{-20} \text{ m}^2/\text{W}$ and $85 \text{ } \mu\text{m}^2$, respectively. The spectra were captured within a traveling

interval of 20 km. The spectrum at 0 km has the largest peak magnitude and narrowest width. The signal bandwidth then gradually widens as the propagation distance increases. In the time domain, however the Gaussian shape of the pulse does not change at all.

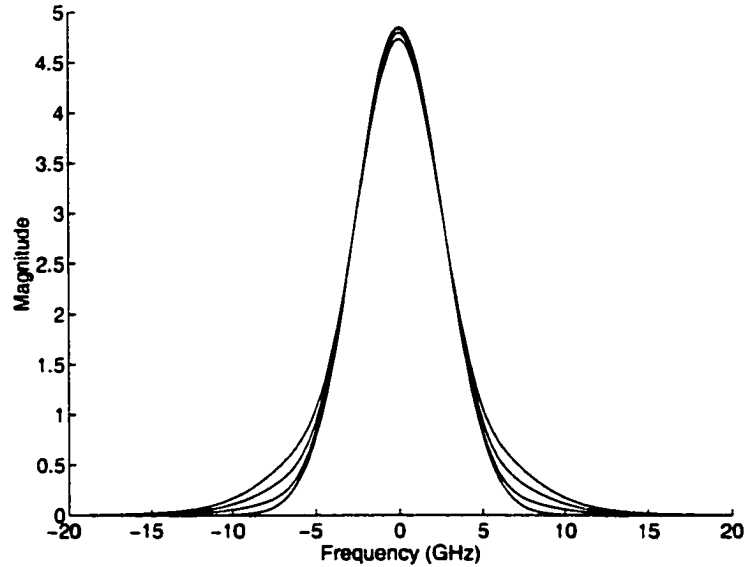


Figure 2.5: Spreading of the Signal Spectrum due to SPM

2.3.3 Coupled NLSEs: Including Chromatic Dispersion, SPM and XPM

It is not possible to see the separate influences of the three previously mentioned nonlinear effects in the current form of the nonlinear Schrodinger equation. The reason is that equation (2.17) treats a group of channels as one signal and hence it describes the change of all channels together. It is not possible to isolate one single channel and then predict its propagation evolution from (2.17).

In order to examine the individual influences of the three non-linear effects, a set of coupled nonlinear Schrodinger equations can be derived using a similar approach as for (2.17). The optical field is assumed to have the form [12, p. 239],

$$E = \frac{1}{2} \left[\sum_{n=1}^N A_n(t, z) F(x, y) e^{-j\beta^n z} e^{j\omega_{bn} t} + c.c \right]$$

where β^n and ω_{bn} are the propagation constant and the angular frequency of the optical carrier for the n^{th} channel, respectively. These coupled Schrodinger equations are

accurate only if the frequency spectra of the optical channels are sufficiently well separated from each other.

To include only the SPM and XPM effects, the derivation ignores all mixing terms in the induced nonlinear polarization except for those that contain the instantaneous power, $|A_j|^2$, of the optical channels (refer to the nonlinear polarization equation mentioned in the previous section). Each of the coupled Schrodinger equations has the following form [12, p. 242]:

$$\frac{\partial A_j}{\partial z} = -\Delta\beta_{1j} \frac{\partial A_j}{\partial T} + i \frac{\beta_{2j}}{2} \frac{\partial^2 A_j}{\partial T^2} + \frac{\beta_{3j}}{6} \frac{\partial^3 A_j}{\partial T^3} - \frac{\alpha}{2} A_j - i\gamma |A_j|^2 A_j - 2i\gamma A_j \sum_{n=1, n \neq j}^N |A_n|^2 \quad (2.25)$$

$$\beta_{3j} = \beta_3$$

$$\beta_{2j} = \beta_2 + \beta_3(\omega_{0j} - \omega_{ref})$$

$$\Delta\beta_{1j} = \beta_{1j} - \beta_{1,ref} = \beta_2(\omega_{0j} - \omega_{ref}) + \beta_3(\omega_{0j} - \omega_{ref})^2 / 2$$

where ω_{ref} is the reference angular frequency for which the D parameter is measured; N is the number of optical channels present in the system; and j denotes the channel number.

Compared to (2.17), (2.25) has an extra term (the last term) describing XPM. An approximate analytical solution describing only the SPM and XPM effects can be obtained by ignoring the dispersion terms as follows:

$$A_j(T, z + \Delta z) = A_j(T, z) \exp\left[i\gamma |A_j(T, z)|^2 \Delta z\right] \exp\left[2i\gamma \sum_{n=1, n \neq j}^N |A_n(T, z)|^2 \Delta z\right] \quad (2.26)$$

Equation (2.26) shows that XPM adds an extra phase distortion to the optical channel. For each channel, the additional distortion is proportional to the sum of the instantaneous power of all the other channels.

In the presence of the chromatic dispersion, the phase distortion caused by XPM is converted into amplitude distortion. A good example of a fiber system that shows the XPM effect is a system that consists of two channels where one of them is a continuous-wave signal while the other is modulated. Without the XPM effect, the continuous-wave channel would have constant amplitude in the time domain for the entire propagation distance. However, with the XPM effect, an amplitude fluctuation would appear. This is illustrated in **Figure 2.6**. In the figure, the diagram on the right side that shows the

amplitude distortion due to XPM effect is actually obtained experimentally with the ASE noise removed. A 90 km length of NZDSF was used in the experiment. The average launched powers of both channels were set at 6 dBm.

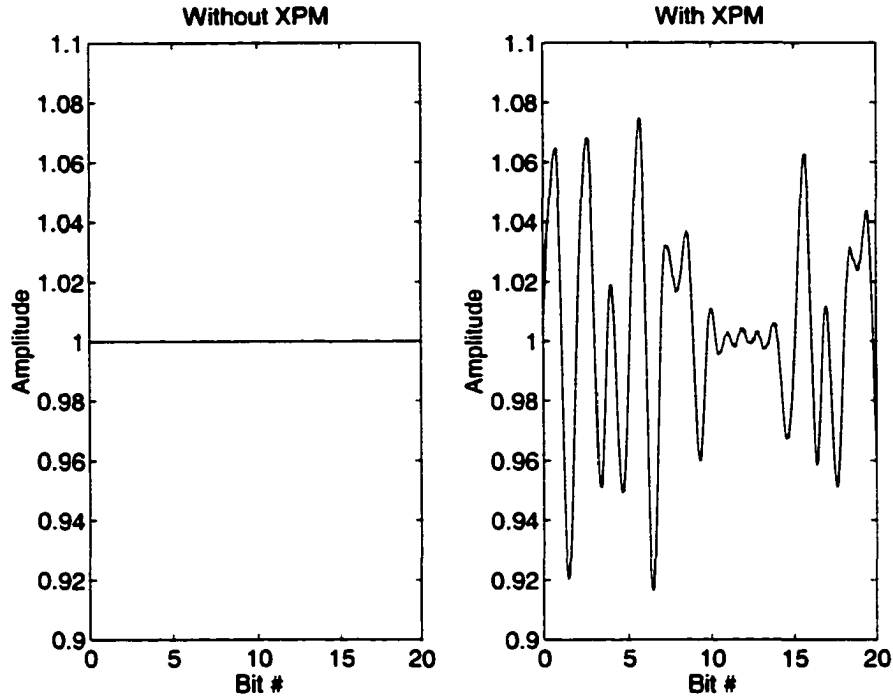


Figure 2.6: Amplitude Distortion of a Continuous-wave Channel due to XPM

2.3.4 Coupled NLSEs: Including Chromatic Dispersion, SPM, XPM and FWM

To account for FWM, the derivation of the coupled equations must include all mixing terms of the induced nonlinear polarization except for those terms that are far away from the original frequency spectrum. The ignored mixing terms are located at frequencies that are roughly three times those of the frequency of the original signal; therefore they can be safely ignored for optical fiber. A four-channel WDM system can be fully described by four coupled equations as follows [12, p.408]:

$$\begin{aligned} \frac{\partial A_1}{\partial z} = & i \frac{\beta_{21}}{2} \frac{\partial^2 A_1}{\partial T^2} + \frac{\beta_{31}}{6} \frac{\partial^3 A_1}{\partial T^3} - \frac{\alpha}{2} A_1 - i\gamma |A_1|^2 A_1 - 2i\gamma A_1 \sum_{n=2}^4 |A_n|^2 \\ & - i\gamma A_2^2 A_3^* \exp(i\Delta\beta_{2231} z) - 2i\gamma A_2 A_3 A_4^* \exp(i\Delta\beta_{2341} z) \end{aligned} \quad (2.27)$$

$$\begin{aligned} \frac{\partial A_2}{\partial z} = & -\Delta\beta_{12} + i \frac{\beta_{22}}{2} \frac{\partial^2 A_2}{\partial T^2} + \frac{\beta_{32}}{6} \frac{\partial^3 A_2}{\partial T^3} - \frac{\alpha}{2} A_2 - i\gamma |A_2|^2 A_2 - 2i\gamma A_2 \sum_{n=1, n \neq 2}^4 |A_n|^2 \\ & - i\gamma A_3^2 A_4^* \exp(i\Delta\beta_{3342} z) - 2i\gamma A_1 A_3 A_2^* \exp(i\Delta\beta_{1322} z) - 2i\gamma A_1 A_4 A_3^* \exp(i\Delta\beta_{1432} z) \end{aligned} \quad (2.28)$$

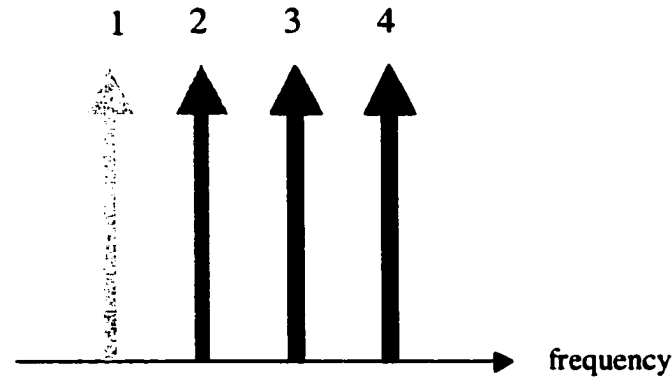
$$\frac{\partial A_3}{\partial z} = -\Delta\beta_{13} + i\frac{\beta_{23}}{2}\frac{\partial^2 A_3}{\partial T^2} + \frac{\beta_{33}}{6}\frac{\partial^3 A_3}{\partial T^3} - \frac{\alpha}{2}A_3 - i\gamma|A_3|^2 A_3 - 2i\gamma A_3 \sum_{n=1, n \neq 3}^4 |A_n|^2$$

$$- i\gamma A_2^2 A_1^* \exp(i\Delta\beta_{2213} z) - 2i\gamma A_1 A_4 A_2^* \exp(i\Delta\beta_{1423} z) - 2i\gamma A_2 A_4 A_3^* \exp(i\Delta\beta_{2433} z) \quad (2.29)$$

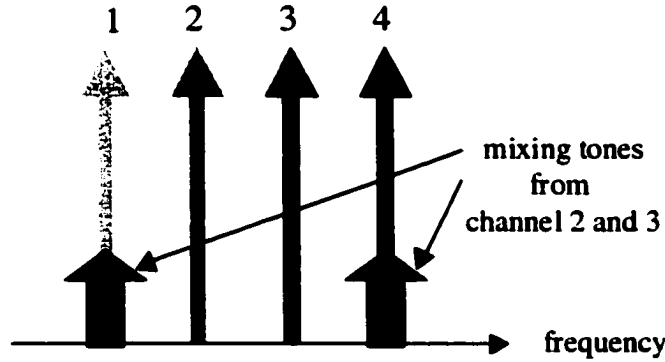
$$\frac{\partial A_4}{\partial z} = -\Delta\beta_{14} + i\frac{\beta_{24}}{2}\frac{\partial^2 A_4}{\partial T^2} + \frac{\beta_{34}}{6}\frac{\partial^3 A_4}{\partial T^3} - \frac{\alpha}{2}A_4 - i\gamma|A_4|^2 A_4 - 2i\gamma A_4 \sum_{n=1}^3 |A_n|^2$$

$$- i\gamma A_3^2 A_2^* \exp(i\Delta\beta_{3324} z) - 2i\gamma A_2 A_3 A_1^* \exp(i\Delta\beta_{2314} z) \quad (2.30)$$

where $\Delta\beta_{pqrs} = \beta^{(p)} + \beta^{(q)} - \beta^{(r)} - \beta^{(s)}$; $\beta^{(x)}$ is the propagation constant, β , for channel x .



(a) Before launching into the fiber



(b) After propagating through the fiber under the strong influence of FWM

Figure 2.7: Effects of FWM and Channel Allocation for 4-channel WDM systems

Diagram (a) in **Figure 2.7** shows the frequency allocation of the four optical channels described by (2.27)-(2.30). As shown in these equations, the nonlinear terms that describe the FWM are formed by the product of either two or three neighboring channels, which is usually referred to as the triplet (the two-channel case is referred to as

the degenerated triplet). Again, the detrimental effect of FWM is spectrum overlapping between the optical channels due to a nonlinearly generated mixing field. The overlapping could cause serious signal distortion. This is illustrated in diagram (b) in **Figure 2.7**. The number of mixing tones due to product terms increases drastically as the number of optical channels increases. Because of the complexity of the coupled nonlinear Schrodinger equations, researchers tend to use equation (2.17) to model the dense WDM system when FWM becomes important.

2.4. Numerical Simulation

The nonlinear Schrodinger equation cannot, in general, be solved analytically (except in some special cases, e.g. soliton); therefore, numerical simulation is required to predict the optical field amplitude A at the output of the optical fiber. The most widely used numerical method for solving the nonlinear Schrodinger equation is the split-step Fourier method [46]. Hardin and Tappert have shown that, over very short distances, the dispersion and the nonlinear effects can be assumed to act separately and independently [46]. As a result, one can divide the entire optical link into small segments and predict the evolution of the optical signal by calculating the dispersion and nonlinear effects separately, segment by segment. Details about this method are given in the following paragraphs.

Formally, (2.17) can be rewritten in an operator form as follows:

$$\frac{\partial A}{\partial z} = (\underline{D} + \underline{N})A \quad (2.31)$$

where

$$\underline{D} = i \frac{\beta_2}{2} \frac{\partial^2}{\partial T^2} + \frac{\beta_3}{6} \frac{\partial^3}{\partial T^3} - \frac{\alpha}{2} \quad (2.32)$$

$$\underline{N} = -i\gamma|A|^2 \quad (2.33)$$

For a small simulation step, Δz , the solution of (2.25) can be approximated as [12, p.51]

$$A(z + \Delta z, T) = \exp(\underline{N}\Delta z) \exp(\underline{D}\Delta z) A(z, T) \quad (2.34)$$

Based on (2.34), the split-step Fourier method uses two steps to update A in each simulation segment. In the first step, the nonlinear step, the method ignores the \underline{D} operator and calculates the intermediate function, $B(T)$, using the following equation:

$$B(T) = F^{-1} \left\{ \exp \left[i \left(\frac{-\beta_2}{2} \omega^2 - \frac{\beta_3}{6} \omega^3 \right) \Delta z \right] \exp \left(-\frac{\alpha}{2} \Delta z \right) F \{ A(z, T) \} \right\} \quad (2.35)$$

where F and F^{-1} denote the Fourier and inverse Fourier transform pairs, respectively. In the second step, the dispersion step, the \underline{D} operator is ignored and $A(z+\Delta z, T)$ is calculated using (2.24) with $B(T)$ replacing $A(z, T)$ on the right side of the equation. This two-step calculation is repeated until the sum of all simulation segments equals the specified fiber length.

Determining a sufficiently small simulation step size is important to ensure accurate simulation results. The simulation step should be chosen such that any further reduction in size will not significantly change the simulation results. The step size can be either constant or adjustable. The use of a constant step size reduces the programming complexity. However, an adjustable step size is preferable because of both possible reduction in computational time and possible reduction in the accumulated truncation error inherent in any real numerical computation.

The step size of each simulation segment is determined by the change in the two sub-steps. In the nonlinear step, the step size is estimated using the nonlinear phase change [47]. In the dispersion step, the step size is estimated by using the overall amplitude change of the signal [47]. The optimal step size is chosen to be the minimum of the two step sizes determined by the above criteria. It has been found that the maximum nonlinear phase change should lie between 0.001 to 0.003 radians [47, 48 and 49]. The maximum nonlinear phase, ϕ_{NL} , is determined by,

$$\phi_{NL, \max} = \gamma P_{peak} \Delta z \quad (2.36)$$

where P_{peak} is the peak power of the optical signal at location z . The maximum amplitude change in the dispersion step should be limited to below 0.5% [47]. For 8-channel WDM systems with 200 GHz channel spacing, Tkach et al. [48] have shown that the criterion for the amplitude change can be met simply by limiting the step size to 100 m. As will be shown in the next subsection, the 100 m limitation is sufficient to guarantee that the amplitude change will be less than 0.5%. This can avoid the need for an explicit calculation of the actual amplitude change in the signal and hence reduce the

computational time in the simulations. In essence, the adjustable step size is determined mainly by (2.36).

Figure 2.8 shows the flow chart for performing the numerical split-step Fourier calculation. The first part of the algorithm determines the maximum step size that meets the requirement for the nonlinear phase change. The algorithm, then, checks whether or not the calculated step size is larger than the maximum allowable value set by the dispersion-step requirement. After the step size is determined, the algorithm would modify the signal according to (2.35) (dispersion step), and then it updates the signal again according to (2.36) (nonlinear step). The above procedures repeat until the signal propagates through the specified fiber length.

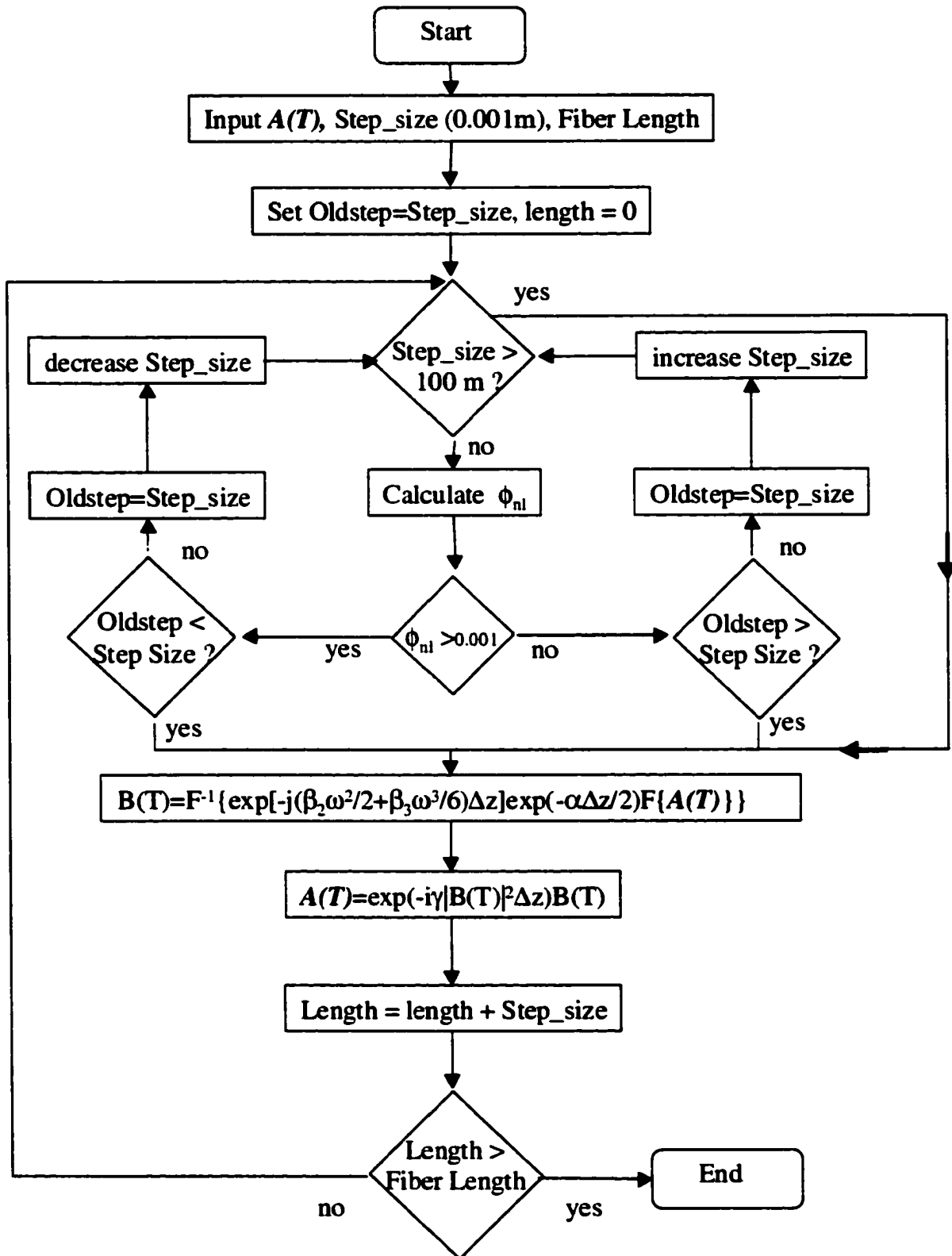


Figure 2.8: Flow Chart for Split-Step Fourier Method Solving the Schrodinger Equation

2.5. Verification of the Simulation Program

Based on the algorithm shown in **Figure 2.8**, a MATLAB simulation program was written to predict the evolution of an optical signal propagating through a fiber. The maximum allowable nonlinear phase change ϕ_N was set at 0.001 rad. The simulation program was tested under four different simulation conditions. These four cases are discussed below.

The first case ignores the nonlinear effects of the fiber and the attenuation. The optical signal is affected solely by chromatic dispersion, and thus equation (2.22) can be used to verify the simulated results. A Gaussian pulse expressed by the equation

$$A(0, T) = \sqrt{P_{in}} \exp\left(-\frac{T^2}{2T_0^2}\right)$$

is used as the optical signal launched into the fiber here; P_{in} is the peak launched power and T_0 is a constant. Derived from (2.22), the optical signal can be expressed at any point z along the fiber as

$$A(z, T) = \sqrt{P_{in}} \left(\frac{T_0^2}{T_0^2 - i\beta_2 z}\right)^{1/2} \exp\left(-\frac{T^2}{2(T_0^2 - i\beta_2 z)}\right)$$

In this set of simulations, the dispersion parameter, D , was set equal to 100 ps/nm/km at 1550.9 nm (which is the wavelength of the laser available in TRLabs). This value is much larger than those for SSMF and NZDSF, which are about 17 ps/nm/km and 4.2 ps/nm/km respectively at 1550 nm. The large D parameter causes the pulse shape of the propagating signal to change more rapidly than in actual fiber, which provide a stricter test of the accuracy of the simulation routine. The corresponding β_2 was set to $-1.2769 \times 10^{-25} \text{ s}^2/\text{m}$. T_0 was set to 100 ps, which is close to the pulse width of an OC-192 OOK pulse. The launched power, P_{in} , was set to 1 W. In this set of simulations, the value of the launched power is not important because nonlinear fiber effects are ignored. The simulated results for different fiber distances are plotted in **Figure 2.9** along with the analytical solutions (solid line). It is clear that the shapes of the simulated pulses match exactly with the analytical solutions at all simulated distances.

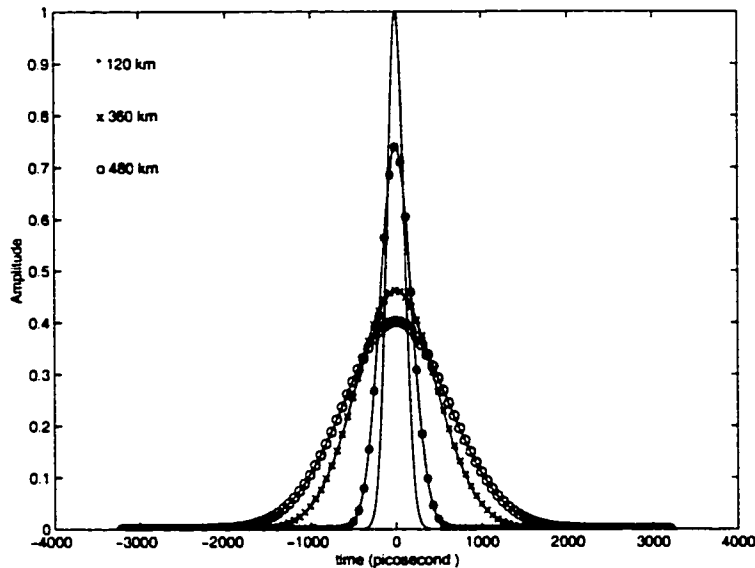


Figure 2.9: Comparison of Analytical and Simulated Results for Gaussian Pulse Propagation Including Only the Chromatic Dispersion Effect

The second case assumes that the dispersion effect is absent but that the nonlinear effects and the fiber attenuation terms are present. The same Gaussian pulse was used in this set of simulations. The peak power of the signal was set equal to 50 dBm (100 W) in order to observe a strong SPM effect. Typically, the average launched power per channel in a commercial fiber system is less than 5 dBm. The peak power is about 3 dB higher than the average power, which is about 8 dB. The exceptionally high power used in this set of simulations causes a large nonlinear phase change as the signal propagates through the fiber (responsible for SPM). This pessimistic test ensures that the simulation routine will function properly under more typical conditions. The attenuation factor, α , was set to 0.22 dB/km (which is a typical value for cabled optical fibers); the nonlinear refractive index, n_2 , was equal to $2.2 \times 10^{-22} \text{ m}^2/\text{W}$; the effective core area, A_{eff} , was set to $80 \text{ } \mu\text{m}^2$. These parameters are close to those for commercial fibers. The wavelength of the laser was 1550.9 nm. The corresponding nonlinear parameter, γ , was 1.0486 /mW. Without chromatic dispersion, SPM changes only the instantaneous phase of the signal. The optical field and its phase change at any location z are governed by the following equations [12]:

$$A(z, T) = A(0, T) \exp\left(\frac{-\alpha z}{2}\right) \exp(i\phi_{NL})$$

$$\phi_{NL}(z, T) = |U(0, T)|^2 (z_{eff} / L_{NL})$$

where $U(0, T) = A(0, T)/P_{in}^{1/2}$; $z_{eff} = [1 - \exp(-\alpha z)] / \alpha$; and $L_{NL} = 1/(\gamma P_{in})$. **Figure 2.10** shows the optical spectra of the two optical signals after propagating through different lengths of fiber. Solid lines on the figure represent the analytical solutions. Again, the simulated results exactly match the analytical solutions.

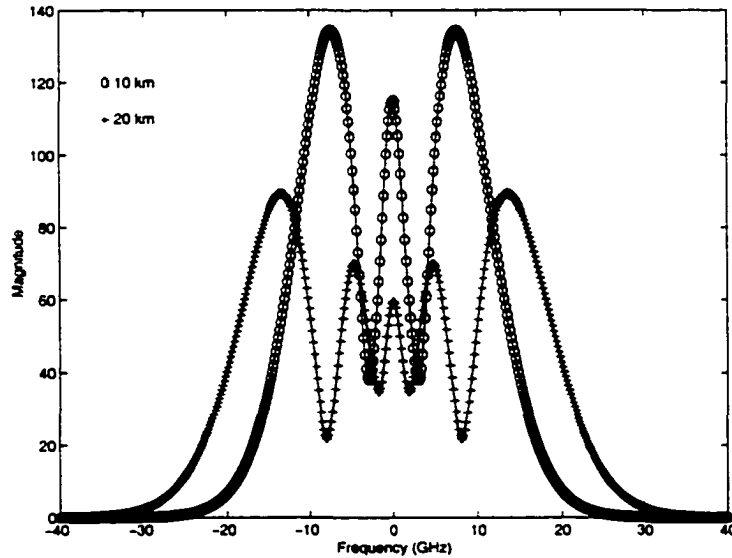


Figure 2.10: Comparison of Analytical and Simulated Results for Gaussian Pulse Propagation including only the nonlinear effects

The first two cases show that the simulation program accurately predicts the evolution of the signal when the dispersion and nonlinear effects are acting separately. The third test uses a soliton pulse to verify the simulation program. A soliton pulse propagates through an optical fiber (subject to both chromatic dispersion and nonlinear effects) without any amplitude shape change. This provides a very good way to verify the accuracy of the program. Under specific conditions (including initial pulse shape, launched power and fiber parameters), the NLSE can be solved analytically using the inversely scattering method [12] to describe the signal pulse shape at any location, z ,

when both chromatic dispersion and nonlinear effects are acting simultaneously. One of the solutions is the soliton as described below.

A soliton pulse in optical fiber is actually a hyperbolic secant pulse, which can be expressed as [12],

$$A(0, T) = \sqrt{P_0} \operatorname{sech}\left(\frac{T}{T_0}\right).$$

To solve this NLSE, both α and β_3 are ignored. The solution requires that the launched power $P_0 = -\beta_2 / T_0^2 \gamma$. The evolution of the soliton can be described by [12, p. 145]

$$A(z, T) = \sqrt{P_0} \operatorname{sech}\left(\frac{T}{T_0}\right) \exp\left(\frac{i\beta_2 z}{2T_0^2}\right)$$

at any location z . Since power cannot be negative, β_2 should remain negative and D should remain positive. Within the 1550 nm communication window, D is indeed positive for most optical fibers and soliton transmission is possible.

Figure 2.11 compares the simulated results and analytical results. In this simulation, D is set to 60 ps/(nm.km) and all other parameters are the same as mentioned above. P_0 is thus equal to 8.5733 dBm (7.2 mW). The transmission distance is set to 1000 km, which is longer than the length of most of terrestrial systems. **Figure 2.11** shows that indeed the pulse shape of the soliton remains the same and the phase advances linearly with distance exactly, according to the equation.

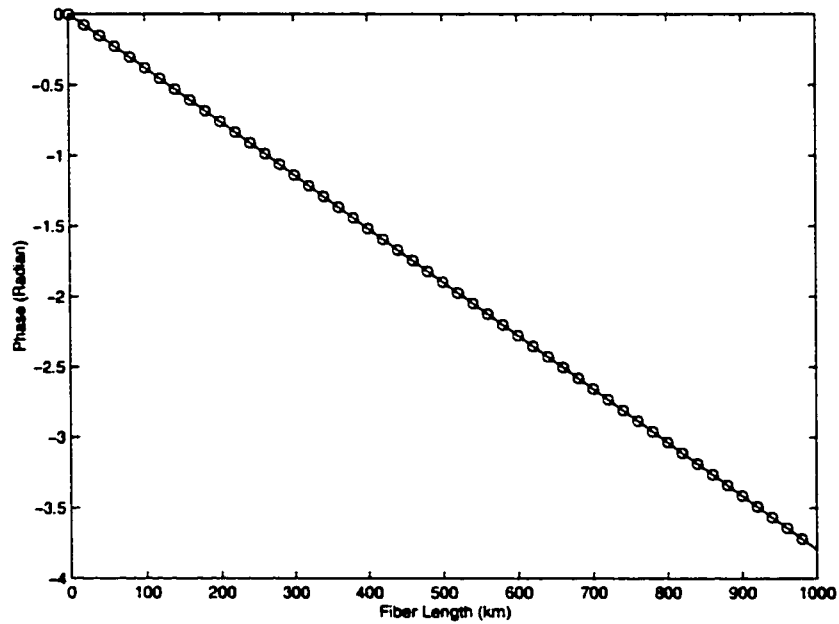
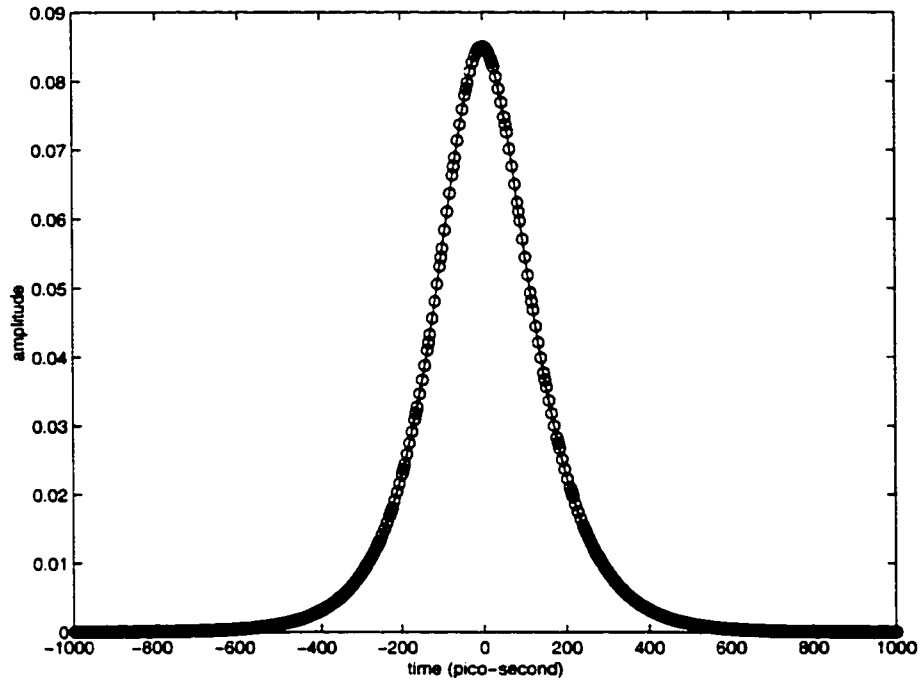


Figure 2.11: Comparison of Analytical and Simulated Results for Soliton Transmission Including Both Chromatic Dispersion and Nonlinear Effects

All verifications have so far been for single-channel systems. To complete the series, the last test examines the simulation program by using FWM. Equations (2.27)-(2.30) in the previous section describe the interaction among four optical channels as signals propagate through the fiber. Approximate analytical solutions can be obtained for the case where channels 2 and 3 act as strong steady-state (continuous waves without any modulation) pump signals that pump both channels 1 and 4 through FWM. To obtain an analytical expression to describe the process, it is assumed that the power transfer from channels 2 and 3 to channels 1 and 4 is small (undepleted pumping) and that the fiber attenuation is zero. Under these assumptions, the solutions for channels 1 and 4 can be written as,

$$A_1 = \frac{\Theta_2}{\Theta_3 - \Theta_1} [\exp(i\Theta_3 z) - \exp(i\Theta_1 z)]$$

$$A_4 = \frac{R_2}{R_3 - R_1} [\exp(iR_3 z) - \exp(iR_1 z)]$$

where $\Theta_1 = -2\gamma(P_2 + P_3)$; $\Theta_2 = -\gamma P_2 \sqrt{P_3}$; $\Theta_3 = \Delta\beta_{231} - 3\gamma P_3$; $R_1 = \Theta_1$; $R_2 = -\gamma P_3 \sqrt{P_2}$; $R_3 = \Delta\beta_{324} - 3\gamma P_2$; and P_2 and P_3 are the power for channels 2 and 3. Since steady-state signals are assumed for channels 2 and 3, the generated signals at channels 1 and 4 would also be steady-state, as described by the above equations. Consequently, the dispersion terms in the nonlinear Schrodinger equation can be neglected.

In this set of simulations, both P_2 and P_3 are set to 50 mW (much larger than the power used for signal propagation in fiber communication systems) to observe strong FWM. The channel spacing is set to 100 GHz. The center wavelength is set at 1550.9 nm (midway between channels 2 and 3). All other parameters are the same as before. **Figure 2.12** shows the power ratio between the generated signals and the original signals obtained both from simulations and from the analytical expressions. Again, the simulated results match well with the analytical solutions. It is expected that the simulated results would deviate from the analytical solution for longer distances because other mixing terms in the equations become increasingly important.

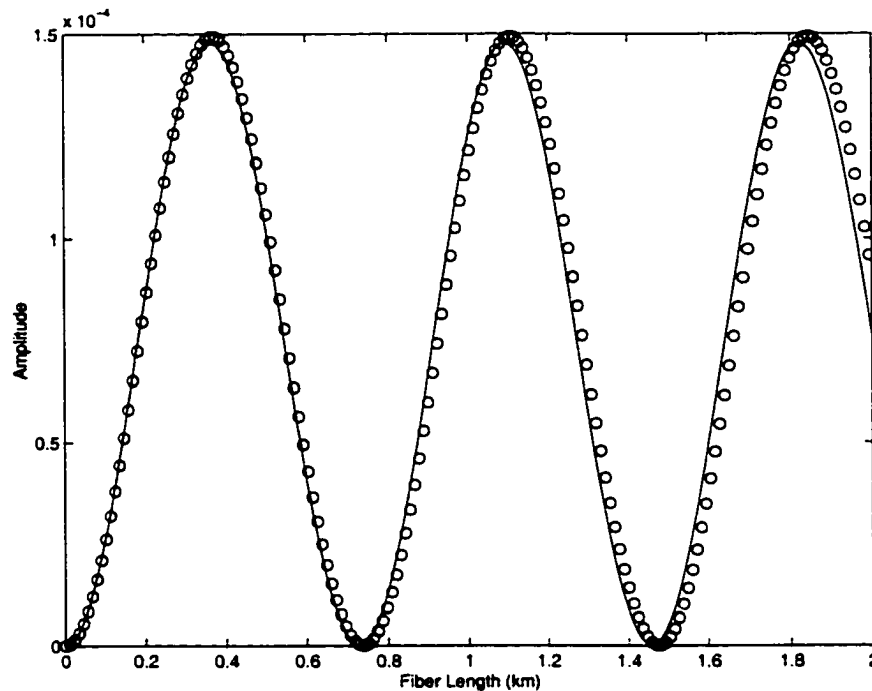


Figure 2.12: Comparison of Analytical and Simulated Results for Four-Wave-Mixing (solid line-analytical, bubble - simulated)

The above verification experiments show that the simulation program accurately predicts pulse propagation governed by the nonlinear Schrodinger equation.

2.6. Calculation of the Q Factor

The final part of the fiber-optic system simulation is to evaluate the quality of the optical signal at the receiving end.

After optical detection, the received signal is first amplified to the required voltage before entering a decision circuit. This is illustrated in **Figure 2.13**. The decision circuit collects one sample of every incoming bit to determine whether the bits are '1' or '0'. The decision is made by comparing the amplitude of the samples with a reference value (a threshold value). Those bit signals that have value less than the reference value are judged to be stamped as '0's, those bit signal that have a higher value than the reference value are taken to be '1's. As will be explained later, for fiber-optic systems, the reference value should be set closer to the '0' value. The sampling time of the decision

circuit is important for correctly judging bit values. The optimal sampling slot should be at the center region of every bit to reduce the intersymbol interference from the neighboring bits and to have maximum separation between '1's and '0's.

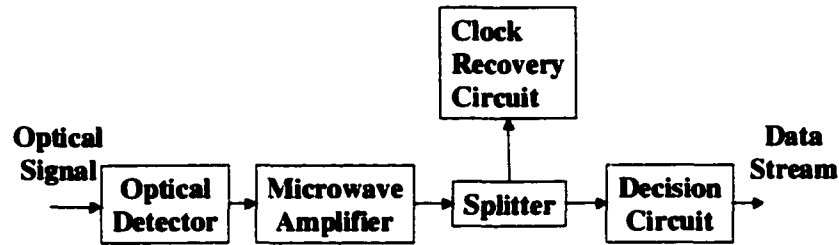


Figure 2.13: Receiver for an Optical-Fiber System

The separation between '1's and '0's is important because of the random signal distortion. Due to various sources of system noises, the amplitudes of the '1' bits (or '0' bits) in a bit sequence are slightly different. Sometimes, the amplitude of certain '1' bits can drop below the threshold value, and errors will occur. A similar situation can also happen for '0's. If the separation between '1's and '0's is maximized, the chance for the '1' bits to drop below the threshold value is minimized.

If the distribution of the signal noise is Gaussian, the statistics of the noise can be completely described by its mean value and standard deviation (or variance). If the mean and the standard deviation are known, then it is possible to compute the rate at which errors occur for a signal, and hence the bit-error ratio (BER). **Figure 2.14** graphically illustrates the noise distribution of '1's in a received optical signal through its eye diagram. An eye diagram is constructed by superimposing few-bit long sequences in a bit stream on top of each other. As shown in the figure, the portion of the noise that is under the decision threshold causes errors for '1's. The BER for the '1' bits can be calculated by integrating the Gaussian probability density function (pdf) from negative infinity up to the decision threshold [53, p. 40]. The Gaussian pdf, $p(x)$, is expressed as,

$$p(x) = \frac{1}{\sqrt{2\pi}} e^{-(x-m_x)/2\sigma^2} \quad (2.37)$$

where m_x and σ are the mean and standard deviation, respectively. The BER can be computed by,

$$\begin{aligned}
 BER_1 &= \frac{1}{\sqrt{2\pi}\sigma_1} \int_{-\infty}^{I_{df}} e^{-(u-m_1)^2/2\sigma_1^2} du \\
 &= \frac{1}{2} \operatorname{erfc} \left(\frac{m_1 - I_{df}}{\sqrt{2}\sigma_1} \right)
 \end{aligned}
 \tag{2.38}$$

where m_1 and σ_1 are the mean and standard deviation for '1' bits, respectively; I_{df} is the decision threshold, and erfc is the complementary error function, defined as [23]

$$\operatorname{erfc} = \frac{2}{\sqrt{\pi}} \int_x^{\infty} \exp(-y^2) dy
 \tag{2.39}$$

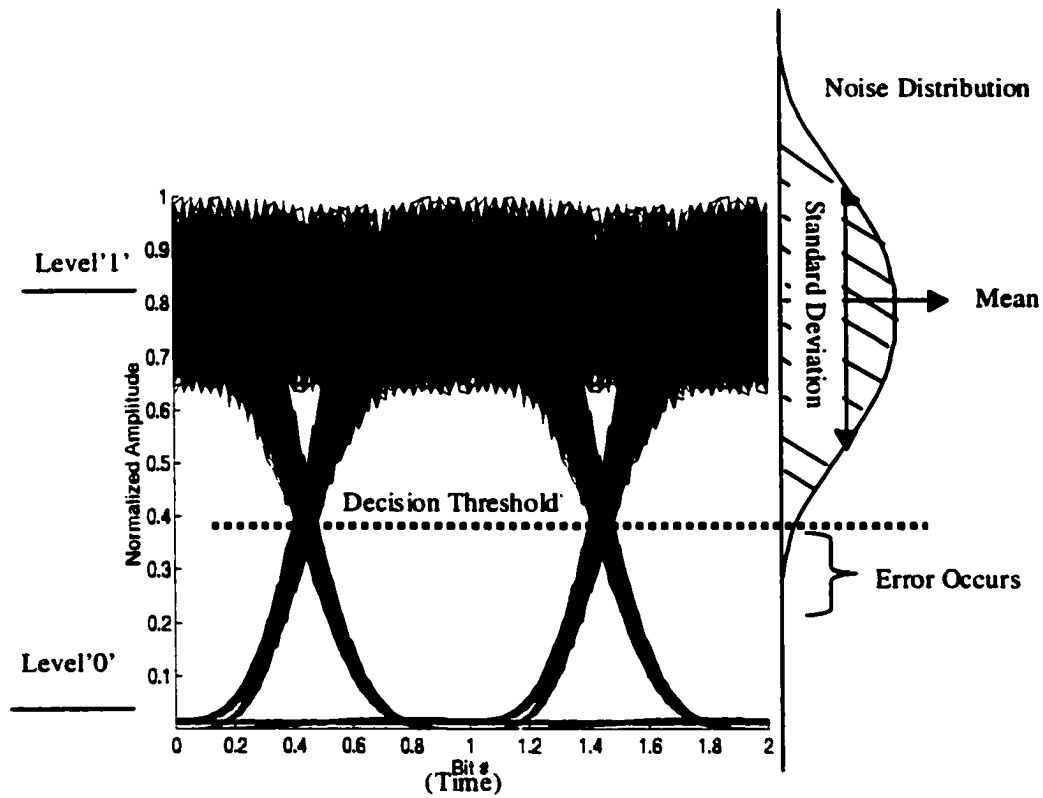


Figure 2.14: Noise Distribution of '1's of a Received Optical Signal

The BER for the '0' bits is calculated using a similar equation,

$$\begin{aligned}
 BER_0 &= \frac{1}{\sqrt{2\pi}\sigma_0} \int_{I_{df}}^{\infty} e^{-(u-m_0)^2/2\sigma_0^2} du \\
 &= \frac{1}{2} \operatorname{erfc} \left(\frac{I_{df} - m_0}{\sqrt{2}\sigma_0} \right)
 \end{aligned}
 \tag{2.40}$$

where m_0 and σ_0 are the mean and standard deviation for '0' bits, respectively. The optimal threshold level for the decision circuit is located where the calculation of BERs for '1's and '0's yield identical result or equivalently where pdf's for '1' bits and '0' bits intersect [23, p. 172]. Mathematically, the optimal threshold value, $I_{df,opt}$, can be derived as follow,

$$\frac{m_1 - I_{df}}{\sigma_1} = \frac{I_{df} - m_0}{\sigma_0} = Q \quad (2.41)$$

$$I_{df} = \frac{\sigma_0 m_1 + \sigma_1 m_0}{\sigma_1 + \sigma_0} \quad (2.42)$$

The BER provides a very good measure of received signal quality or system performance in simulations. In experiments, the BER can be measured directly using a bit-error-rate tester (BERT). However, there is a limitation on how low one can measure the BER experimentally. Usually, in a laboratory setting, the lowest BER that can be measured is in the order of 10^{-14} . To accurately measure lower BER, a very long time is required to accumulate enough statistics, which is impractical. Therefore, another method is required to measure the system performance that does not require the measurement of the lowest possible BER. This is the reason why many researchers switched from using BER as a performance measure to another parameter called the 'Q' factor shown in (2.41), obtaining by substituting (2.42) to (2.41),

$$Q = \frac{m_1 - m_0}{\sigma_1 + \sigma_0} \quad (2.43)$$

Deriving from (2.41), the lowest BER of a signal can be related to Q as [23, p. 172]

$$BER_{\min} = \frac{1}{2} \operatorname{erfc} \left(\frac{Q}{\sqrt{2}} \right) \quad (2.44)$$

Table 2.1 shows examples of BER values corresponding to various possible Q values. The higher the Q values, the lower the BERs.

In experiments, Q can be calculated from knowledge of the means and standard deviations of the '1's and '0's; it does not require direct measurement or knowledge of a low BER. The means and standard deviations are calculated by fitting curves to the

measured BER points collected on both '1' and '0' sides, as shown in **Figure 2.15**. As shown in the figure, two series ('0's and '1's) of BER measurements are first made. Under the assumption that the noise distribution is Gaussian, the means and standard deviations are computed by best fitting two curves into the two series of measured BERs using (2.40) and (2.38). The performance of a fiber system can simply be specified by this calculated Q value, or the Q value can be used to estimate a low BER using (2.44). For simulations, the estimation of Q value is more complicated than for experiments as explained below.

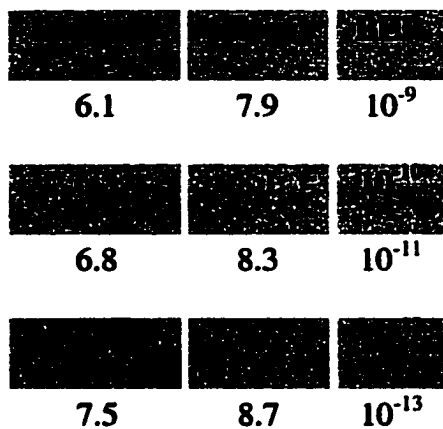


Table 2.1: BERs for Certain Q Factor Values

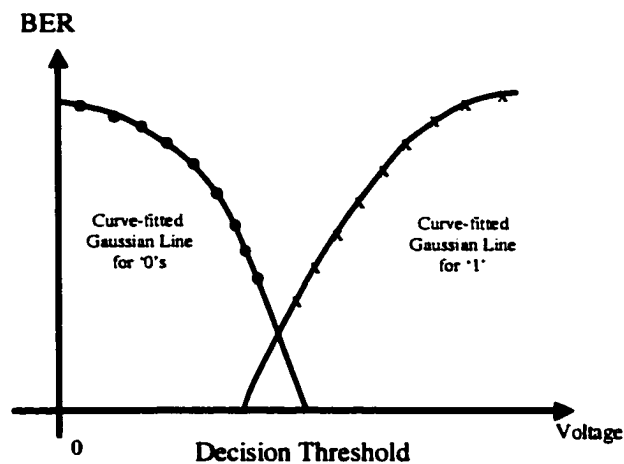


Figure 2.15: BER versus Decision Threshold Curves

In our simulations, the original method of estimating the four parameters [52] for Q calculation was performed by first identifying the '1's and '0's of the bit sequence. Then, the optimal sampling time for '1s' and '0s' was found. The mean of the '1's was found by averaging the amplitude of all '1's pulses in the bit sequence, and vice versa for the '0's. Similarly, the standard deviations of '1's and '0's were calculated. An obvious discrepancy of this method is that the amplitude of the '1's and '0's can be varied simply due to the chromatic dispersion, and not due to any noise. As a result, this original method usually underestimates the actual performance of a system.

A modified approach was therefore developed [52], which takes in account of the so-called patterning effect. With the aid of dispersion-compensating fibers, the pulse distortion due to chromatic dispersion is largely corrected at each inline EDFA. Because of this, it is reasonable to state that the pulse spreading due to the chromatic dispersion would only affect one neighboring bit. In other words, the amplitude of each bit in the bit sequence should be affected by only one left and one right neighboring bit. Therefore, the problem of dispersion-affected amplitude fluctuation can be solved by categorizing each bit into one of eight 3-bit patterns (all possible combinations of a 3-bit binary word). Instead of calculating for all '1's or '0's, the mean and standard deviation of the center bit of each individual pattern is calculated. Four of the center bits of the 3-bit patterns have '1' values and four have '0' values. The final means and standard deviations of the '1's and '0's are calculated by first plotting a BER curve versus the threshold voltage as shown in **Figure 2.15**. At each threshold voltage, the BER of individual bit pattern is calculated from its mean and standard deviation. The total BER of the '1's or '0's at the particular threshold voltage is calculated by averaging the BERs with proper weighting. The weighting is determined by the appearance of the particular bit pattern. For instance, if the number of occurrences for the patterns '010' '011' '110' and '110' of the '1s' are 10, 11, 12 and 13 respectively (with a total of 46 occurrences), the corresponding weightings are 10/46, 11/46, 12/46 and 13/46. Two sets of points (one for the '1's and one for the '0's) are then generated as shown in **Figure 2.15**. The final means and standard deviations are then estimated by fitting an analytical BER curve through the two sets of points.

3. Theoretical and Numerical Comparison of the NRZ, Duobinary and OSSB Formats

3.1. Introduction

This chapter compares the three candidate transmission formats using both simulations and theoretical analysis. The investigation is focused on the system performance under two conditions: (1) under strong influence of the fiber nonlinear effect and (2) under narrow-channel spacing. The fiber nonlinear effect is basically proportional to signal power and inversely proportional to channel spacing. Thus, the two system conditions are inter-related.

As mentioned in Chapter 1, the major advantage of both the duobinary and OSSB formats is their potential to further reduce the channel spacing in dense WDM systems and hence increase their spectral efficiency. For instance, a state-of-the-art OC-192 (10 Gbits/s) commercial system with 50 GHz channel spacing has a spectral efficiency of 20%. A proposed commercialized OC-768 (40 Gbits/s) system with 100 GHz channel spacing has a spectral efficiency of 40%. Both the bandwidth of the optical filter and the stability of the laser signal are limiting factors for OC-192. Another limiting factor could be the channel cross talk, but this has yet to be determined. Thus, one main focus of this chapter is to examine the fundamental channel spacing limit for both the duobinary and OSSB formats.

As mentioned in Chapter 2, the major nonlinear effects in fiber include SPM, XPM and FWM. A typical 32-channel WDM system is affected by all three effects simultaneously. In order to separate the impact of each individual nonlinear effect, simplified simulations were employed. These simplified systems are designed to clearly isolate each individual effect. Hence, a comparison of individual nonlinear effects will be performed. The results and analysis from these simplified simulations are then used to understand and explain the full-scale system simulation results.

Section 3.2 deals with the numerical modeling of the different transmission formats and an optimization required for the duobinary format. Also, fundamental

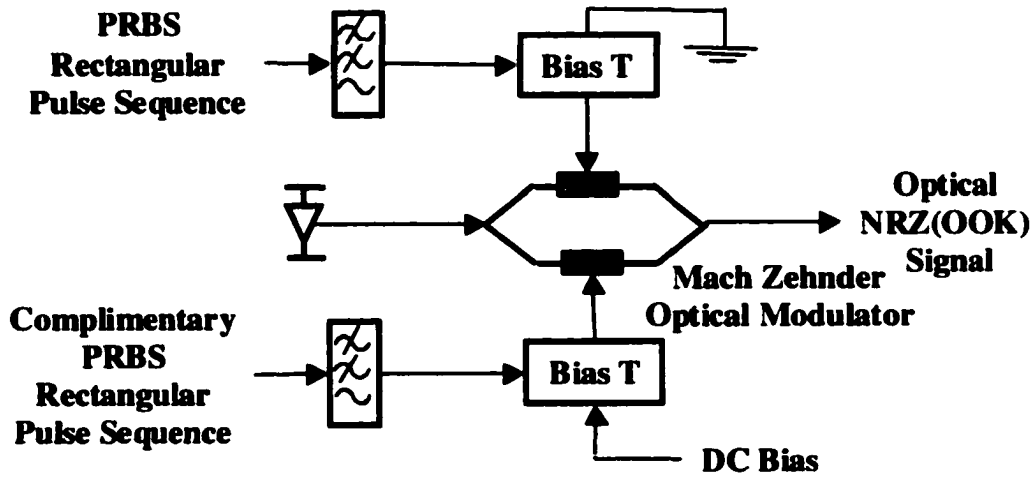
limitations of the duobinary signal due to initial eye closure will also be discussed. Section 3.3 discusses the impact of chromatic dispersion, against which duobinary signaling clearly has advantages under certain conditions. Section 3.4 examines the linear cross talk caused by both same-wavelength interference (from different fibers) and neighboring channels (different wavelength channels in same fiber). Section 3.5 begins the discussion on the first fiber nonlinear effect, SPM.

Section 3.6 uses simplified 2-channel simulations to examine the impact from XPM. Previously, researchers believed that duobinary signaling had advantages over the other formats because of its narrow spectrum. However, the impact of the power ratio between the carrier-tone and the signal spectrum to the XPM penalty has not yet been mentioned, which will be considered in this section. Section 3.7 uses 3-channel simulations to investigate FWM. To the best of the author's knowledge, no journal has discussed the impact of FWM on duobinary and OSSB signals and, therefore, it is still uncertain which of the alternative formats is more advantageous. This section tries to answer this question. Sections 3.8 and section 3.9 discuss full-scale 32-channel systems for short-haul and terrestrial distances, respectively. Section 3.10 summarizes the findings of this chapter.

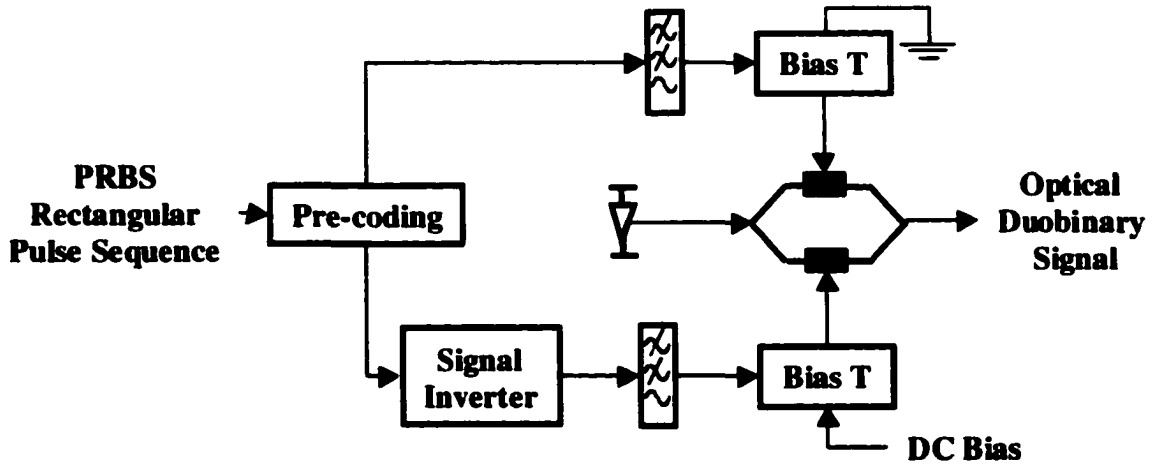
3.2. Modeling of Optical Signals

The section describes the generation of the optical signals modulated by different transmission formats. It should be noted that although the optical signal generated by the transmitter is amplitude-modulated, the detected electrical signal at the receiver side of the optical system is equal to the power of the optical signal due to the square-law detection mentioned earlier.

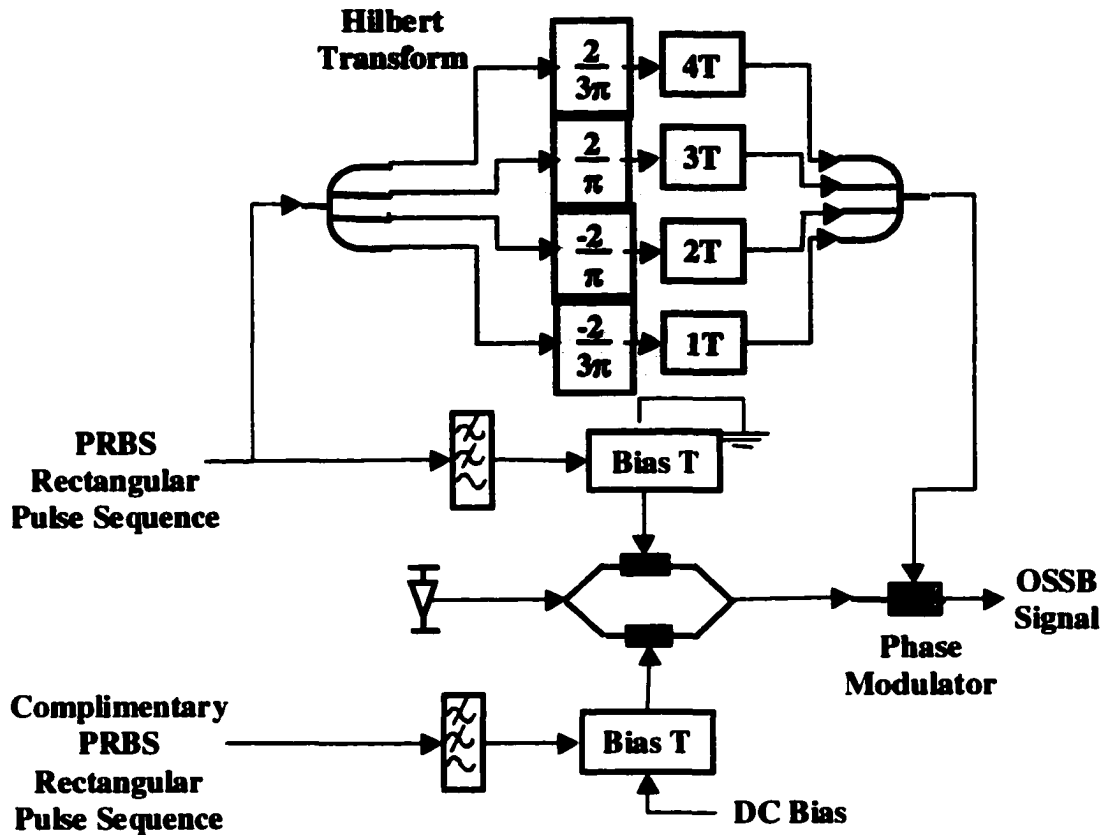
3.2.1 Transmitter Modeling for Different Formats



(a) Transmitter Schematic for OOK Signaling



(b) Transmitter Schematic for Optical Duobinary Signaling



(c) Transmitter Schematic for OSSB Signaling

Figure 3.1: Transmitter Schematics for the Three Transmission Formats

Except for the transmitter, the fiber-optic systems for all three transmission formats are essentially the same. **Figure 3.1** shows the schematics of the transmitter for the three different formats. With the OOK format, the electrical signal that drives the Mach-Zehnder optical modulator is generated in three steps. First, a subroutine generates a pseudorandom bit sequence (PRBS) of impulses. The PRBS is then convolved with a rectangular pulse to form a rectangular pulse sequence. The pulse sequence is low-pass filtered to simulate the actual pulse sequence that drives the optical modulator. The entire process can be described by (3.1).

$$a(t) = \sum_{n=x}^y b_n \text{rect}(t - nT) \otimes \text{LPF}(t) \quad (3.1)$$

where b_n is either 1 or 0, determined by the PRBS; $\text{rect}(t)$ is the rectangular pulse; and LPF is the impulse response of the low-pass pulse-shape filter (Note that convolution in

the time domain is equivalent to multiplication in the frequency domain). A third-order Butterworth filter with 7.5 GHz 3dB bandwidth is used to model the pulse shape filter (for a 10 Gb/s system). The bias T shown in **Figure 3.1** is used to add a DC voltage to the driving signal in order to properly set the operating point of the optical modulator. The optical OOK signal output from the modulator is modeled by (3.2).

$$A_{OOK}(t) = \cos\left(\frac{\pi(V_a - V_b)}{2V_\pi} - \frac{\pi}{4}\right) \quad (3.2)$$

V_a and V_b are the voltages applied to the two arms of the Mach-Zehnder modulator, which have no DC component and swing from $-V_\pi/4$ to $V_\pi/4$. V_π is the switching voltage of the modulator. The ' $\pi/4$ ' term in (3.2) is from the DC bias. It is assumed that the modulator operates in a push-and-pull mode, where V_b is the exact complement of V_a and thus no chirping occurs [8, pp. 83-85]. V_a is actually $a(t)$ from (3.1) with the amplitude adjusted to match the swing mentioned above.

The modeling of duobinary signals is very similar to that of the OOK format. The major difference is the additional encoding and the low-pass filtering. The encoding circuit is basically an XOR logic gate [8,9]. Such a gate is necessary in order to avoid having to modify the receiver. Note that the duobinary signal belongs to a family of partial-response signals [53]. Note that two bits of information are required to determine the value of the current bit. The encoding circuit avoids this extra complexity at the receiver (more details can be found in [53]).

In general, the encoding circuit can be placed at either the transmitter or the receiver (decoder). However, it is always better to encode the signal when the signal-to-noise-ratio is at its highest (i.e. at the transmitter) because if an error occurs before the coding circuit, two errors instead of one would actually appear, due to the partial-response nature of the signal. The PRBS has exactly the same statistics before and after the coding [8]; therefore in the simulation, the encoding circuit was not implemented.

The low-pass filter for the duobinary signal serves two purposes. It is used as a delay-and-add circuit and is used to filter out the high-frequency component of the encoded signal. When first proposed, the duobinary signal was generated by delaying-

and-adding the tributaries [8]. Then later, it was found that even though this 3-level signal can greatly suppress the high frequency components, certain residual high-frequency components remain. Further investigation shows that by filtering out the residual components, the signal becomes more immune to chromatic dispersion [9]. Thus, the current trend is to use a Bessel filter to perform the two processes mentioned above concurrently. More details about the optimization of the Bessel filter will be given below.

The conversion from electrical duobinary to optical duobinary signals is described by (3.3). It should be noted that the operating point of the Mach-Zehnder changes from $-\pi/4$ for OOK format to $-\pi/2$, and that V_a and V_b swings from $-V_\pi/2$ to $V_\pi/2$.

$$A_{Duo}(t) = \cos\left(\frac{\pi(V_a - V_b)}{2V_\pi} - \frac{\pi}{2}\right) \quad (3.3)$$

The OSSB transmitter has one additional phase modulator cascaded with the Mach-Zehnder modulator. The resulting optical signal is described by (3.4).

$$A_{OSSB}(t) = \cos\left(\frac{\pi(V_a - V_b)}{2V_\pi} - \frac{\pi}{4}\right) \exp\left(j\frac{\pi V_c}{V_\pi}\right) \quad (3.4)$$

The cosine term in (3.4) describes the amplitude modulation, which is almost exactly the same as that of the OOK format, with two exceptions. The low-pass filter for converting the rectangular pulses into realistic pulses has a 3dB bandwidth of 6.5 GHz instead of 7.5 GHz, and the electrical signal swings between $-1.1V_\pi/4$ to $1.1V_\pi/4$. The smaller bandwidth is to take into account the fact that the actual implementation of the OSSB format requires the use of a microwave splitter that has low-pass filtering characteristics. The slightly larger modulation depth helps to suppress the high-frequency components of the remaining sideband, which has the added benefit of a slightly larger signal eye opening. The second factor in (3.4) is from the phase modulation. V_c is the approximate Hilbert transform of V_a . A four-tap delay-and-add circuit is used to generate the approximate Hilbert transform, which can be modeled by a transfer function in the frequency domain as shown in (3.5)

$$Hilbert(\omega) = \sum_{n=1}^4 a_n \exp(-jnT\omega) \quad (3.5)$$

where $a = [-2/3\pi, -2/\pi, 2/\pi, 2/3\pi]$; T is the unit delay, which was optimized by Sieben to be equal to 37.5 ps [54]. This scheme yields the best flatness in the first few GHz of signal spectrum for an OC-192 system. The four-tap circuit was implemented by Sieben and will be used in our experiments (more details can be found in Chapter 4). Equation (3.5), in fact, describes a truncated Fourier series that represents the Hilbert transform, with the four most significant coefficients included. The major difference between this OSSB signal and the one mentioned in Sieben's thesis is that in Sieben's case, V_a swings only from $-V_\pi/20$ to $V_\pi/20$ (40% of the maximum swing). The small modulation depth causes the signal to suffer from relatively heavy initial eye penalty. The reason for Sieben's small modulation depth is to ensure that the phase characteristics of the optical signal are efficiently transferred into the electrical domain after the square-law detection at the receiver. This is crucial when performing the electrical chromatic dispersion compensation (for details see [54]). In current and proposed fiber systems, chromatic dispersion is almost always compensated in the optical domain before square-law detection. Thus the signal phase preservation is less important. As will be shown in a later section, greater modulation depth results in improved performance.

3.2.2 Optimization of the Duobinary Filter

A Bessel filter is used for converting an OOK signal into a duobinary signal because its amplitude response closely resembles the delay-and-add circuit and its phase response is linear. The delay-and-add circuit has a transfer function as follows,

$$F_{delay}(\omega) = 1 - \exp(-jT\omega) \quad (3.6)$$

T in the equation is the bit period. Equation (3.6) implies that the delay-and-add circuit has periodic amplitude response, where the period is equal to $2\pi/T$ and the phase response is linear. **Figure 3.2** compares the amplitude of the delay-and-add circuit (for an OC-192 system) with that of the fifth-order Bessel filter, which has 2.47 GHz 3dB bandwidth for generating the electrical duobinary signal. The two curves on the figure have almost identical amplitude responses for frequencies up to 3.5 GHz. For higher

frequencies, the amplitude response of the Bessel filter continues to decrease, contrary to the periodic nature of the delay-and-add circuit.

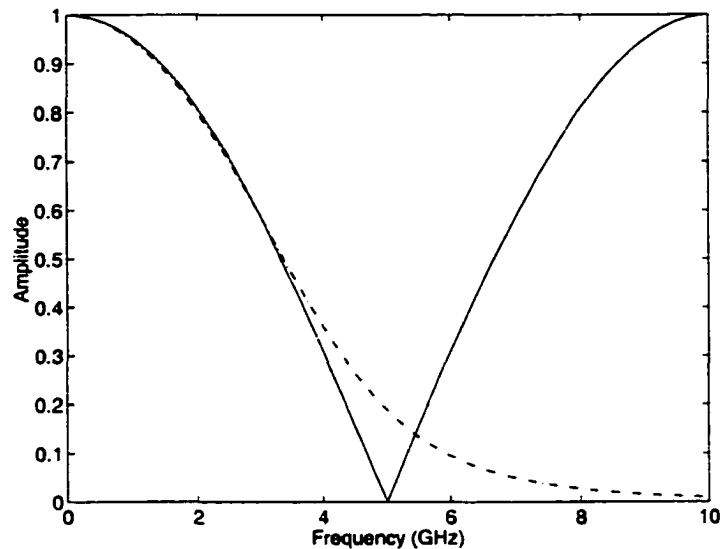
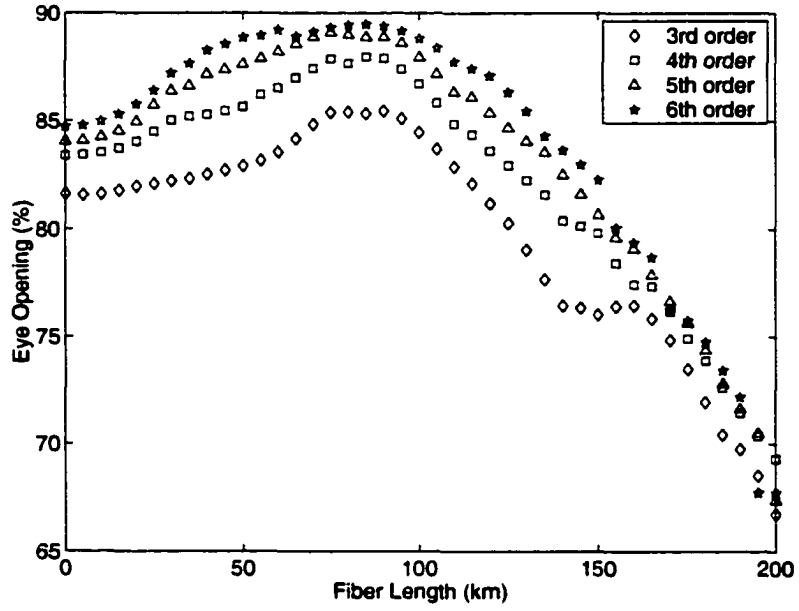


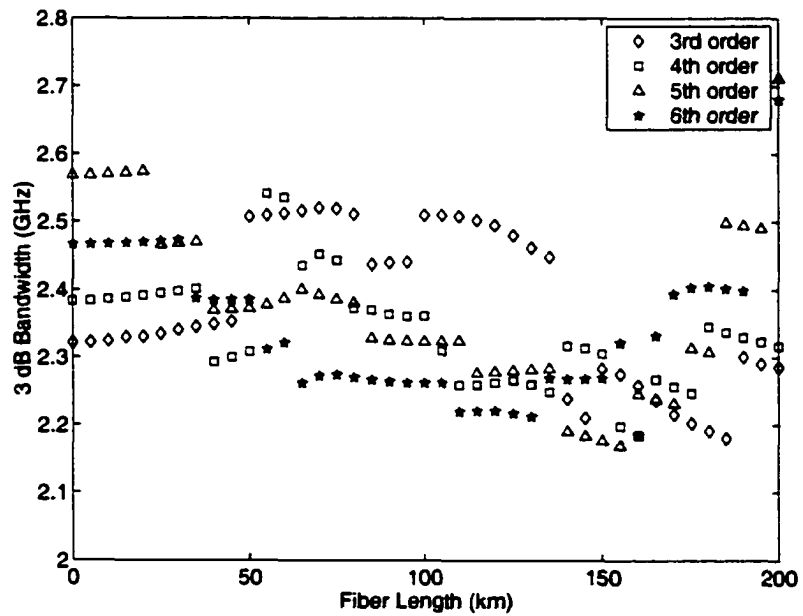
Figure 3.2: Comparison between the Amplitude Response of the Delay-and-Add Circuit and Bessel Filter (solid line-delay-and-add circuit, dashed line-Bessel filter)

For the optical duobinary signal, amplitude distortion occurs during conversion from the electrical to the optical domain, and this distortion needs to be taken into account. The distortion occurs because of the cosine response of the Mach-Zehnder modulator, which introduces a clipping effect at the top of the pulses. The above discussion already explained the reason for using the Bessel filter in the duobinary conversion, but the order of the filter still needs to be determined. Also, the 3dB bandwidth of the filter needs to be optimized to maximize the eye opening.

Figure 3.3 (a) shows the maximum eye opening as a function of the fiber length (without chromatic dispersion compensation) for the received duobinary signals generated using different orders of Bessel filters. A single-mode fiber with the dispersion parameter, D , equal to 17 ps/nm/km at 1550 nm was used for the simulations. At each simulated fiber length, the 3dB bandwidth of the Bessel filter was adjusted to obtain the maximum eye openings for the received signals. The chosen 3dB bandwidth is shown in **Figure 3.3 (b)**. No filter was used to model the receiver response after the square-law detector.



(a) Eye Opening versus Fiber Length



(b) 3 dB Bandwidth versus Fiber Length

Figure 3.3: Maximum Eye Opening at Different Distances of Received Duobinary Signals with Different Bessel Filter Order and Their Corresponding 3dB Bandwidth.

Figure 3.3 (a) shows that the fifth and sixth-order Bessel filters have almost identical eye opening profiles. The absolute maximum eye opening of the duobinary signal is located at around 80 km. Interestingly, chromatic dispersion actually helps to open the eye slightly. As well, the figure shows that the best 3dB bandwidths for different filter orders range from 2.2 to 2.6 GHz. The major difference between filters of fifth and sixth order is the attenuation slope at high frequencies. The sixth-order filter has a steeper slope, which leads to better suppression of high-frequency components, and hence it has slightly better tolerance to chromatic dispersion than a fifth-order filter.

Figure 3.4 (a) compares the maximum eye opening of the received duobinary signal generated by the sixth-order Bessel filter in two different modulation-depth cases. The '10%' curve represents the case where $(V_a - V_b)$ in (3.3) swings between -0.1 to 0.1 of V_π ; the '100%' case has $(V_a - V_b)$ swings between -1 to 1 of V_π . These two cases show how the eye opening is affected by the clipping effect of the Mach-Zehnder modulator. **Figure 3.4 (a)** shows that the maximum eye openings of the two curves differs by about 5%. However, **Figure 3.5** shows that if a third-order Butterworth filter with 8 GHz 3dB bandwidth is used to model the receiver's electrical response, the eye opening difference is reduced to merely 1%. For the rest of the chapter, this filter will be used to model the electrical filtering of the receiver unless otherwise mentioned.

Figure 3.4 (b) shows that the optimized 3dB bandwidth of the filter is quite different in the '10%' and '100%' cases. This shows that the clipping effect does indeed greatly affect the optimization of the Bessel filter. The '100%' case should be used in the actual system because in the actual modulator, the extinction ratio is finite and is usually less than 30 dB. The extinction ratio is defined as the ratio of the maximum output DC power of the modulator to the minimum output power [8, p. 90]. For small modulation depths, the finite extinction ratio would cause more noise to appear for the zero bits than for the one bits because the zero-level is less distinguishable.

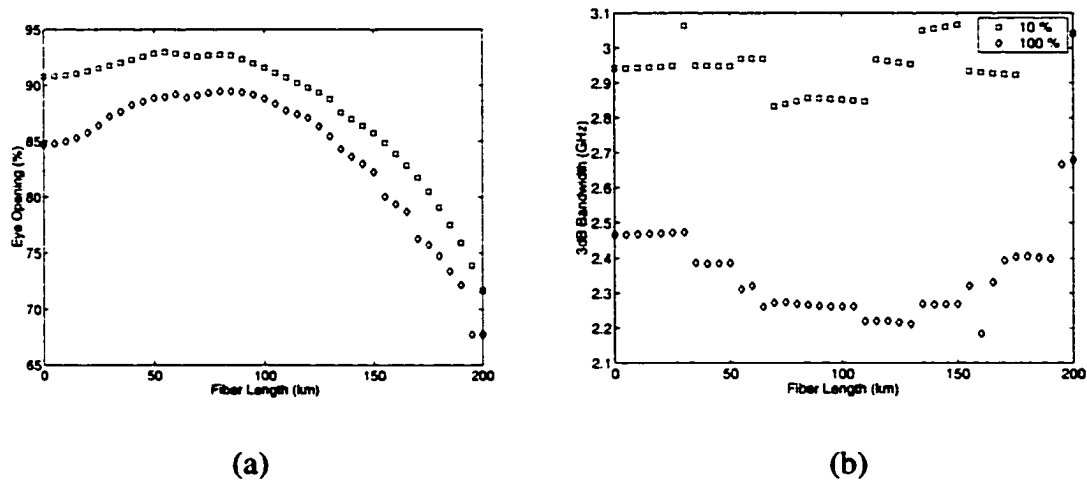


Figure 3.4: Comparison of the Maximum Eye Opening for Two Different Modulation-depth Cases and the Corresponding 3dB Bandwidth (without electrical filtering)

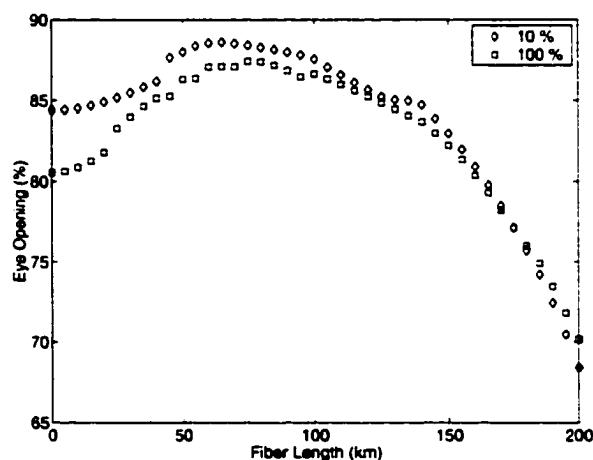


Figure 3.5: Comparison of the Maximum Eye Opening for Two Different Modulation-depth Cases (with electrical filtering)

Based on the above discussion, a sixth-order Bessel filter with 2.24 GHz 3dB bandwidth will be used in subsequent simulations. Even though this 3 dB bandwidth is not optimized for the back-to-back (0 km of fiber) eye opening, even this eye opening is only 0.5% less than the optimized value. Also, this sixth-order Bessel filter has a response that is close to the actual filter used for the actual experiment (shown in Chapter

4). The narrower bandwidth of the filter has the additional advantage of reducing the XPM penalty. More details will be given in section 3.6.

3.3. Chromatic Dispersion and the Eye Closure Penalty

Before commencing the comparison between different formats, it is beneficial review the mechanism of chromatic dispersion.

For any existing fiber system, chromatic dispersion mainly comes from the β_2 parameter, as mentioned in Chapter 2. Mathematically, chromatic dispersion changes the phase of the different frequency components of a signal. The phase change is proportional to the propagation distance and to the square of the frequency [recall equation (2.8) and (2.9)]. For a periodic signal, the signal spectrum consists of discrete frequency components. According to Fourier theory, the amplitudes of the discrete frequency components equal the coefficients of the corresponding Fourier series. An aperiodic signal can be viewed as a periodic signal with an infinite number of Fourier series terms. The exponential Fourier series of a real periodic signal can be expressed as

$$A_{\text{Fourier.exp}} = a_0 + \sum_{n=1}^m a_n e^{jn\omega_0 t} + \sum_{n=1}^m a_n^* e^{-jn\omega_0 t} \quad (3.7)$$

The ‘*’ denotes the unary complex conjugate operator. The first term on the right side of (3.7) is the carrier tone of the signal. The second and third terms form the upper and lower sidebands of the signal spectrum, respectively. The equivalent trigonometric Fourier series can be expressed as

$$\begin{aligned} A_{\text{Fourier.trig}} &= a_0 + \sum_{n=1}^m b_n \cos(n\omega_0 t + c_n) \\ b_n &= 2\sqrt{(a_{nr}^2 + a_{ni}^2)} \\ c_n &= \tan^{-1}(a_{ni}/a_{nr}) \end{aligned} \quad (3.8)$$

where a_{nr} and a_{ni} are the real and imaginary parts of a_n , respectively. Eq. (3.8) shows that a real periodic signal is the sum of a series of cosine functions with possibly different relative time delays c_n . The angular frequency of each cosine function is a multiple of fundamental angular frequency, $\omega_b = 2\pi f_0$.

Under the influence of chromatic dispersion, a real periodic signal contains both real and imaginary parts, as follows

$$\begin{aligned}
 A_{\text{Fourier,CD}} &= a_0 + \sum_{n=1}^m \cos\left(\beta_2 n^2 \alpha_0^2 z / 2\right) b_n \cos(n\omega_0 t + c_n) - j \sum_{n=1}^m \sin\left(\beta_2 n^2 \alpha_0^2 z / 2\right) b_n \cos(n\omega_0 t + c_n) \\
 &= a_0 \\
 &\quad + b_n \sum_{n=1}^m \left[\frac{\cos\left(\beta_2 n^2 \alpha_0^2 z / 2 + n\omega_0 t + c_n\right) + \cos\left(\beta_2 n^2 \alpha_0^2 z / 2 - n\omega_0 t - c_n\right)}{2} \right] \\
 &\quad - j b_n \sum_{n=1}^m \left[\frac{\sin\left(\beta_2 n^2 \alpha_0^2 z / 2 + n\omega_0 t + c_n\right) + \sin\left(\beta_2 n^2 \alpha_0^2 z / 2 - n\omega_0 t - c_n\right)}{2} \right]
 \end{aligned} \tag{3.9}$$

where z is the fiber length. Eq. (3.9) indicates that two processes happen simultaneously. The second term on the right hand side of the equation shows that the chromatic dispersion term changes the relative time delay between the cosine terms of the Fourier series. Each of the cosine terms splits into two and these two parts move in opposite directions in time. The two split cosine functions imply greater separation in time as the frequency of the function increases. The third term in the equation shows that the chromatic dispersion also generates additional imaginary pairs for each Fourier cosine term. These imaginary pairs also change the phase in opposite directions in time. The pulse spreading due to these processes is illustrated in **Figure 3.6**. In the figure, pulse amplitude is plotted against time for size different propagation distances. The label on top of each graph states the propagation distance. A SSMF was used in this example.

The above discussion shows that the wider the signal bandwidth, the greater the degree of pulse spreading due to increased phase shift, which results in increased relative time-delay change. Similarly, the additional imaginary terms in (3.9) would be subject to greater phase shifting with increasing signal bandwidth. As a result, one would expect duobinary signal to preserve their shapes better simply because the signal spectrum is smaller.

For the OSSB format, the situation becomes more complicated because it is not a real signal to start with. The additional phase modulation from the Hilbert transform

alters the dispersion process. The analysis of the dispersion impact on an OSSB format is most conveniently done in the frequency domain. Using the Taylor series expansion and equation (2.22), the dispersion-distorted OSSB signal, $A_{OSSB,CD}$, can be written as

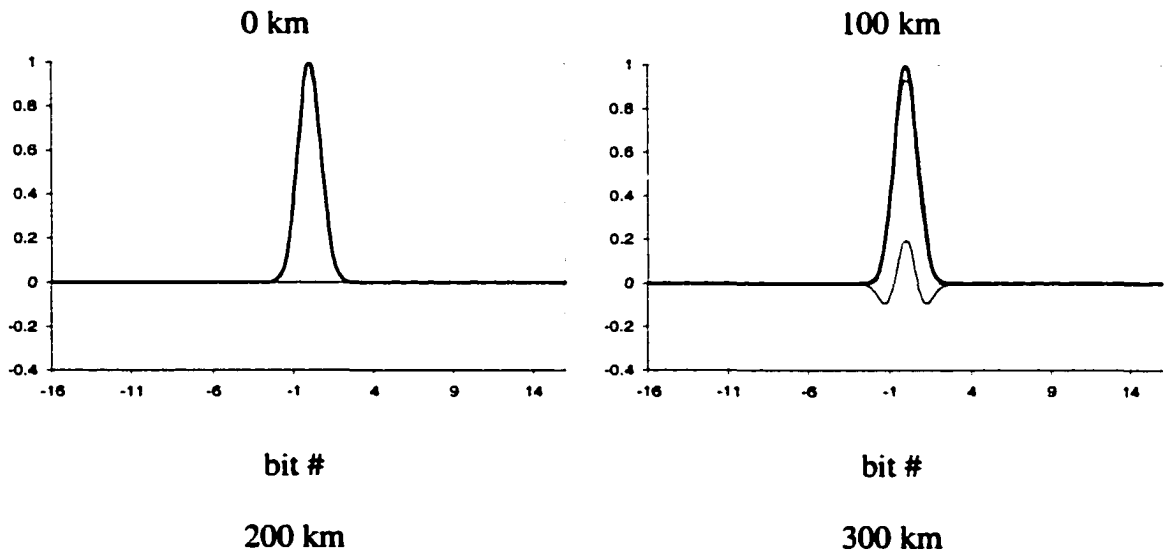
$$A_{OSSB,CD}(\omega) = A_{OSSB} \left(1 + jX - \frac{X^2}{2} - \frac{jX^3}{6} + \dots \right) \quad (3.10)$$

$$\text{where } X = \frac{\beta_2 \omega^2 z}{2}$$

In the time domain we have,

$$A_{OSSB,CD}(t) = A_{OSSB}(t) \left[1 - iY \frac{\partial^2}{\partial t^2} - \frac{Y^2}{2} \frac{\partial^4}{\partial t^4} + \frac{Y^3}{6} \frac{\partial^6}{\partial t^6} + \dots \right] \quad (3.11)$$

$$\text{where } Y = \frac{\beta_2 z}{2}$$



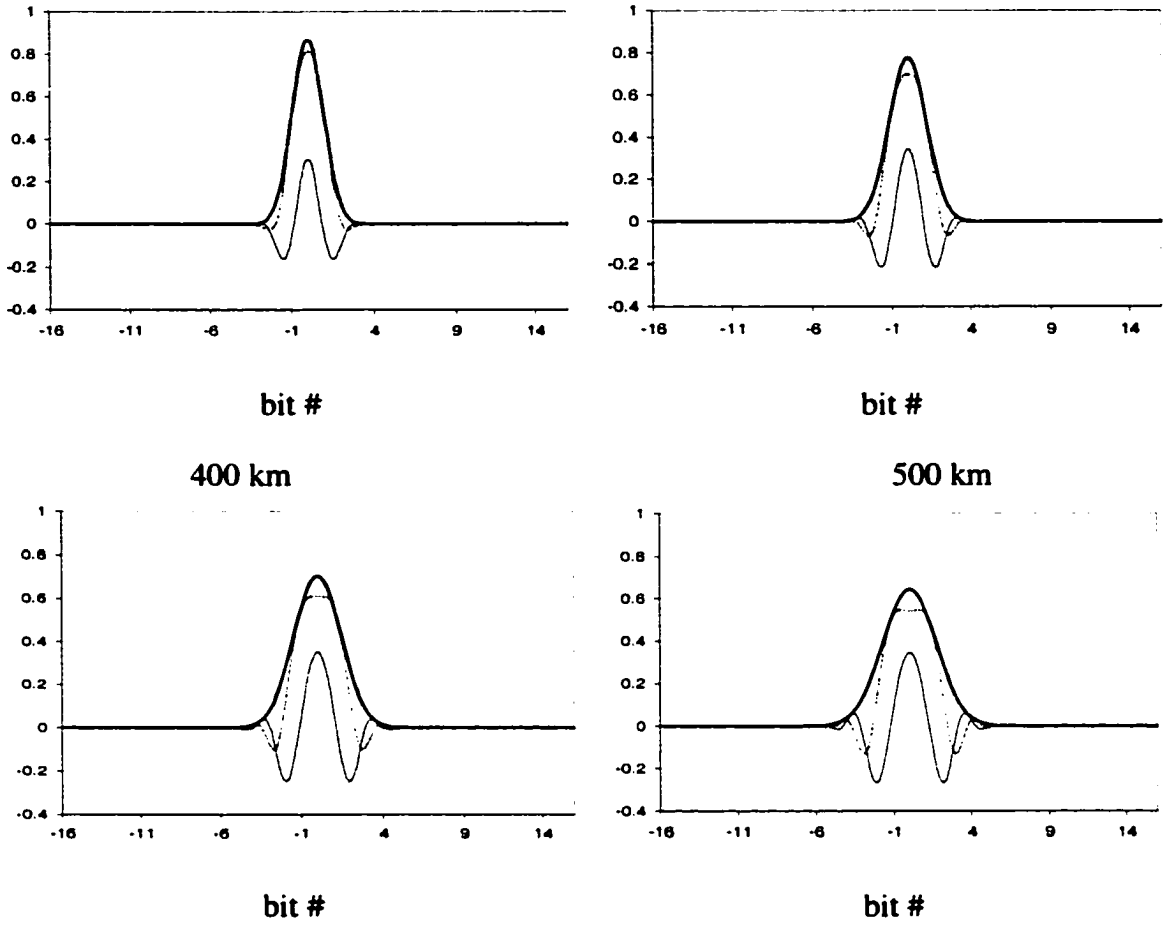


Figure 3.6: Real and Imaginary Parts of a Spreading Gaussian Pulse after Increasing Propagation Distances (real part- light dash, imaginary part- thin solid, absolute amplitude- thick solid)

Eq. (3.11) shows that the distortion from the chromatic dispersion is composed of derivatives of different orders of the signal. The difference in the dispersion impact between the OOK and OSSB formats can be understood by examining the second derivative of the signal. For OSSB, the second derivatives can be expanded as,

$$\frac{\partial^2 A_{OSSB}(t)}{\partial t^2} = \exp(jPh) \left[\frac{\partial^2 Amp}{\partial t^2} + 2j \frac{\partial Amp}{\partial t} \frac{\partial Ph}{\partial t} - Amp \left(\frac{\partial Ph}{\partial t} \right)^2 + jAmp \frac{\partial^2 Ph}{\partial t^2} \right] \quad (3.12)$$

where Amp and Ph are the amplitude (first term) and phase (second term) terms in (3.4), respectively. As shown in (3.12), the second derivative of the OSSB signal contains

four terms. The first term is the second derivative of the OOK signal multiplied by the Hilbert transform phase term. The additional three terms in the equation cause the dispersion impact on the OSSB format to be significantly different from that of the OOK format. It is easy to show that the higher-order derivatives of the OSSB would be even more different from the OOK signal. Whether this difference is beneficial or detrimental can be determined from simulations.

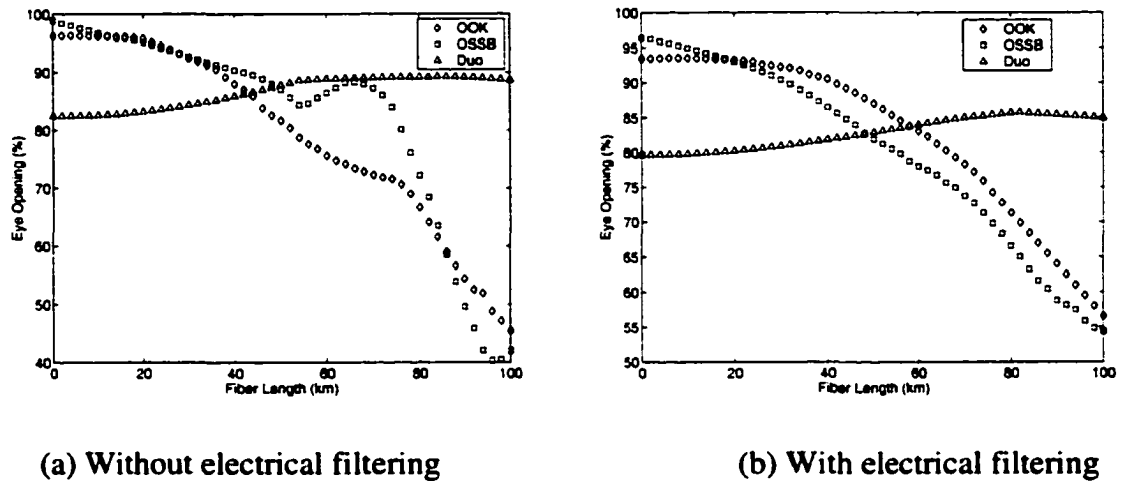


Figure 3.7: Comparison of Eye Opening as a Function of Fiber Length under the Influence of only Chromatic Dispersion

Figure 3.7 compares the eye opening of the three different formats with different fiber lengths (without dispersion compensation). The dispersion parameter, D , is the same as before (17 ps/nm/km). The OSSB format has a slightly larger eye opening when the signal is initially launched into the fiber due to the slightly larger modulation depth; whereas the duobinary signal has the least initial eye opening because of the intentional removal of the high-frequency components, as mentioned previously. This is a fundamental limitation of duobinary signaling.

As the dispersion increases with the fiber length, the eye opening decreases most rapidly for the OSSB signal. This indicates that the additional Hilbert transform terms in (3.12) cause more dispersion distortion. As noted earlier, the duobinary signal is

a lot more resistant to the effects of chromatic dispersion. The duobinary signal can maintain its eye opening for more than 100 km of transmission; whereas the eye openings of both the OOK and OSSB signals drop below 60% for the same transmission distance.

In an actual fiber system, the chromatic dispersion is at least partially compensated by the dispersion compensation module (DCM). A lot of the DCMs in current commercial systems can compensate for the dispersion, but not the dispersion slope [55]. A DCM is usually designed to compensate for the center channel if split-band compensation is not used. As a result, the edge channels would be either overcompensated or undercompensated, depending on the relative wavelength. For instance, if a typical 32-channel OC-192 terrestrial system with 50 GHz channel spacing propagates through 450 km (5 spans of 90 km) of standard single-mode fiber with the center channel fully compensated, then the edge channels would have a residual dispersion of 172.8 ps/nm, assuming the dispersion slope is 0.06 ps²/nm (undercompensated and overcompensated for shorter and longer wavelengths, respectively). Note that 172.8 ps/nm of dispersion is equivalent to the dispersion accumulated in 10.2 km of standard single-mode fiber shown in **Figure 3.7**, which would have little impact on OOK and duobinary signals but causes a slight eye penalty to the OSSB signal.

The above discussion shows that for uncompensated systems, the duobinary format has a clear advantage over the other two formats. For systems with DCM, the advantage of the duobinary format is greatly diminished. The smaller initial eye opening gives the duobinary format a clear disadvantage for systems with dispersion compensation.

3.4. Linear Cross Talk

3.4.1 Cross Talk in an Optical Cross Connect

Two kinds of linear cross talk occur in fiber-optic systems [23, pp. 319-323]. First, cross talk can occur at the optical cross-connect. The function of an optical cross-

connect is to switch an input optical channel from one incoming fiber to any of several possible outgoing fibers that exit the cross-connect, as shown in **Figure 3.8** [56]. If the cross-connect has wavelength-switching capability, the input optical channel can also be switched from one wavelength to another one. As shown in **Figure 3.8**, the WDM channels of each incoming fiber are first de-multiplexed. The channels with the same wavelength from different incoming fibers are then combined together inside a switch fabric. The switch fabric then re-distributes these same-wavelength channels to different outgoing fibers through wavelength multiplexers. Cross talk occurs during the combining and re-distributing processes. Each of these same-wavelength channels would contain a portion of signal power from all other channels.

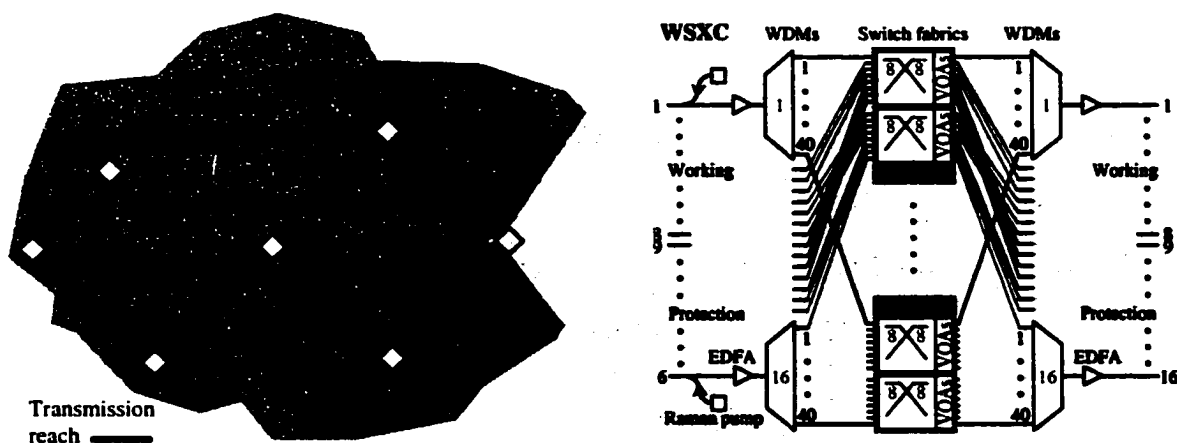


Figure 3.8: Illustration of an Optical Cross Connect

Typical optical cross talk for an optical cross-connect is in the range of 35-45 dB [56]. The cross talk value is defined as the ratio of the optical power of the subject channel to that of all other channels. **Figure 3.9** compares the distorted eyes of the three transmission formats caused by only one same-wavelength interfering channel. To more clearly see the effect, an exaggerated cross talk of 13 dB is used. The same-wavelength channel that causes the cross talk is assumed to have the same PN sequence but with different relative time-delay and laser phase (as explained in the next paragraph). A back-to-back system configuration is assumed, which means the signals are not affected by chromatic dispersion and nonlinear effects. It is very clear from the figure that both the duobinary and OSSB signal eyes are much more distorted than those of the OOK

formats. The reason for the more severe distortion is that significant phase shifting occurs in both the OSSB and duobinary formats.

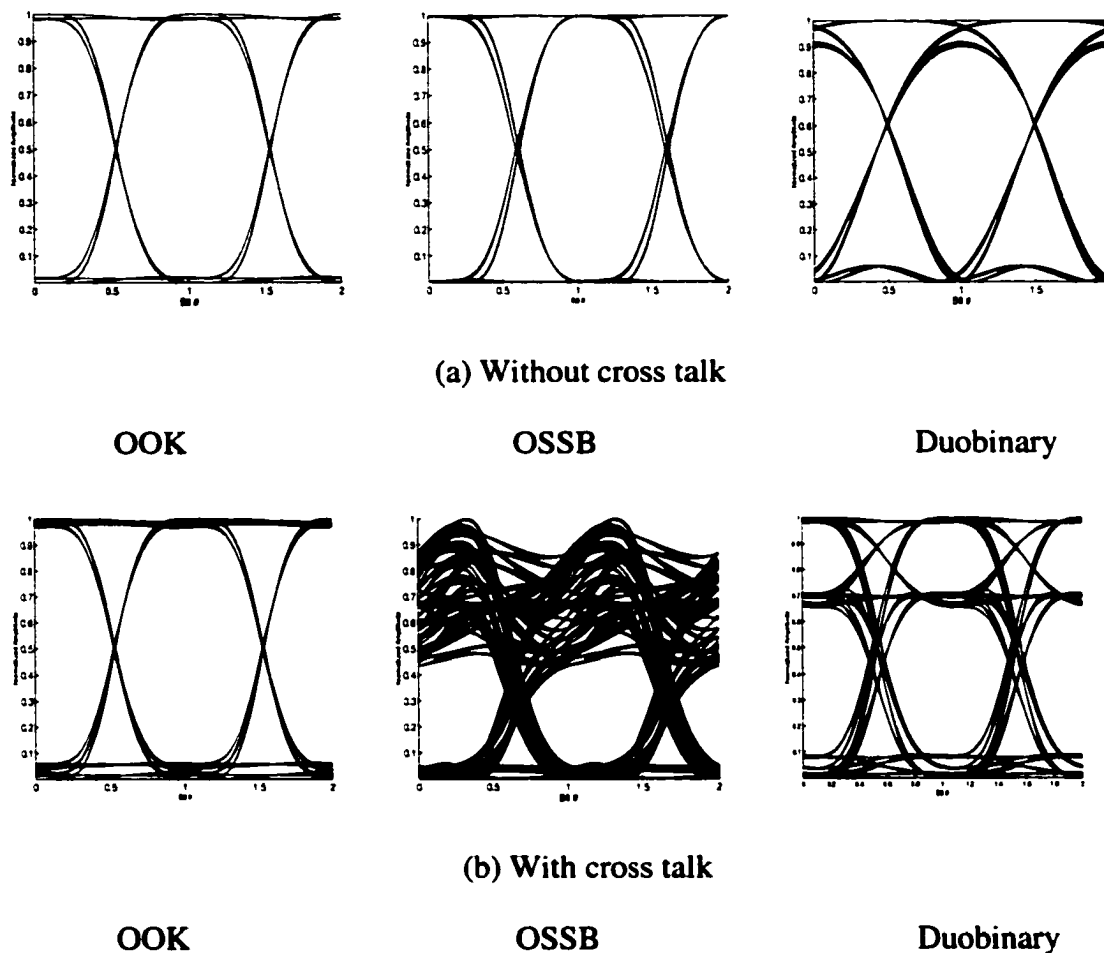


Figure 3.9: Comparison of the Eye Opening of the Three Formats With and Without Same-Wavelength Cross Talk (first case).

Before considering the differences in distortion between the three formats, we will first discuss the modeling of the phase of the optical signal. The output of a continuous-wave (CW) laser used as the optical carrier that is input to the Mach-Zehnder modulator can be described as

$$A_{laser}(t) = K \cos(\omega_c t + r(t)) \quad (3.13)$$

where K is a constant, and ω_c is the angular frequency of the laser. $r(t)$ is the laser phase which is distorted by random phase change (mainly due to the laser relaxation process).

Assuming that the magnitude of the laser phase, $r(t)$, is constant in time (ranging anywhere from 0 to 2π), then the normalized low-pass equivalent (see Chapter 2) of the laser output can be written as

$$A_{laser,lowpass}(t) = \exp(jr) \quad (3.14)$$

For simplicity, equations (3.2) to (3.4) assumed that the laser phase is zero. For multi-channel systems, full modeling of the optical signals requires multiplication of (3.2) to (3.4) with the carrier (3.14). The laser phase is not very important for single-channel systems because there is no second channel to be disturbed by. A major effect of the laser phase for single channels is the generation of phase-to-amplitude relative-intensity noise (RIN), which is usually not the dominating noise source [57].

For OOK signals, the maximum cross talk occurs when the relative laser phase between two channels is either totally-in-phase (0 radians) or totally-out-of-phase (π radians). In the totally-in-phase case, the maximum distortion occurs when the 'zero' bits of the subject channel overlap with the 'one' bits of the interfering channel. When this happens, the bottom level of the eye rises and reduces the eye opening. In the case of the totally out-of-phase, the maximum distortion occurs when the 'one' bits of the subject channel overlap with 'one' bits of the interfering channel. When this occurs, the top level of the signal eye is reduced.

Unlike for OOK signals, the cross talk distortion for OSSB signals can approach these two worst-case scenarios quite a bit more often despite the relative laser phase. This is due to the phase modulation (Hilbert transform) of the OSSB signal required for sideband cancellation. **Figure 3.10** illustrates how the phase of the OSSB signal changes with time. The phase varies within a one π range. Since the relative time delay of the bit sequence of the two channels varies randomly, the in-phase and out-of-phase cases mentioned above have a high probability of occurring independent of the laser phase.

A similar phase shift also occurs with a duobinary signal. Due to the additional 180° out-of-phase signal level, the duobinary signal has a higher chance than the OOK signal of approaching the two worst cross-talk cases mentioned above. Nevertheless, unlike the continuous phase change of the OSSB signal, the duobinary signal changes

phase in a discrete fashion. It is necessary to perform simulations in order to determine which of the two formats suffers the most from cross talk. **Figure 3.11** shows the eye opening penalty as a function of the optical cross talk for the three formats. Each point in the figure represents an average over 100 simulations. For each simulation, the relative time-delay and laser phase for the subject and other same-wavelength channels are varied randomly assuming a uniform distribution. A low-pass filter is used at the receiver. The figure clearly shows that the OOK format is less vulnerable to cross talk than the other two formats. The duobinary signal suffers from the initial eye closure penalty, but the rate of eye opening degradation is slightly less than for OSSB. From these simulation results, OOK signaling suffers the least cross talk penalty, while duobinary signaling suffers the most.

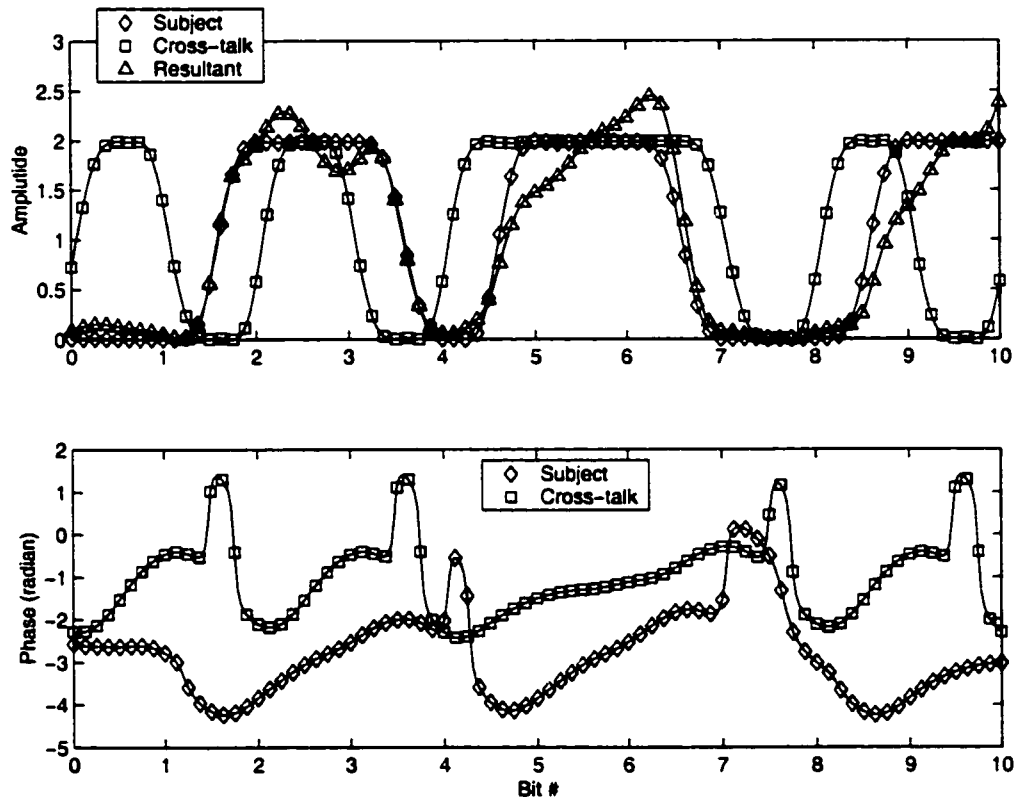


Figure 3.10: Illustration of the Amplitude and Phase Profiles of the OSSB Signals With and Without Cross talk.

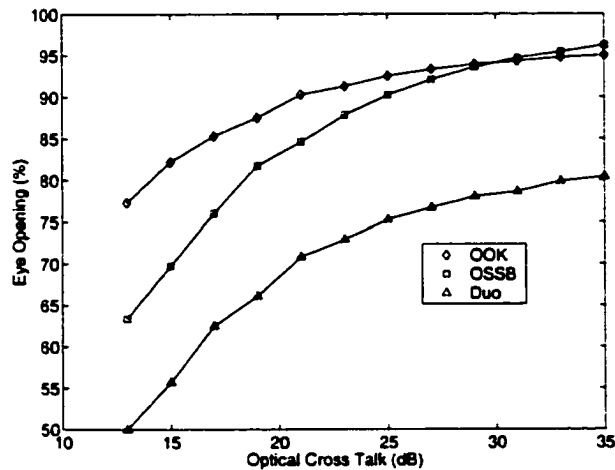


Figure 3.11: Eye Opening Degradation as a Function of Optical Cross Talk.

3.4.2 Cross Talk due to Close Channel Spacing and Optical Demultiplexing Filter

The second type of cross talk arising in an all-optical fiber system happens when the optical channels are placed very close to each other in frequency, which causes the signal spectra to overlap. For narrow channel spacing, the bandwidth and the shape of the optical filter used to isolate each channel become important. Typically, a third-order Butterworth filter is used to model the optical filter. In actual systems, both Fabry-Perot and fiber Bragg-grating types of filters are used for optical filtering. The bandwidth of the fiber Bragg grating can be made narrower than the Fabry-Perot type (0.1 nm full-width half-maximum FWHM). However, the Bragg grating filter suffers from greater amplitude distortion within the passband, and as well as nonlinear phase distortion at the passband edges [58].

For simulation purposes, four types of optical filters, namely, third, fourth and fifth-order Butterworth and rectangular filters, were examined. **Figure 3.12** shows the single-channel simulation results for the three modulation formats. The back-to-back setting is used, and electrical filtering at the receiver is present. In general, the figure shows that the duobinary format can better withstand narrower optical filtering. However, due to the initial eye closure penalty, the duobinary format would not have any significant benefit over an OOK format if the filter bandwidth is greater than 10 GHz and a Butterworth filter is used. The eye closure penalty for both the OOK and OSSB

formats is sensitive to the filter order. As the filter order increases from the third order, the eye openings for these two formats are very similar for filter bandwidths greater than 15 GHz. For narrower bandwidths, the OSSB format suffers from increased eye closure penalty. This is reasonable because the narrow optical filter not only distorts the amplitude response of the OSSB formats, it also disturbs the amplitude and phase relationship of the OSSB formats which creates even more distortion.

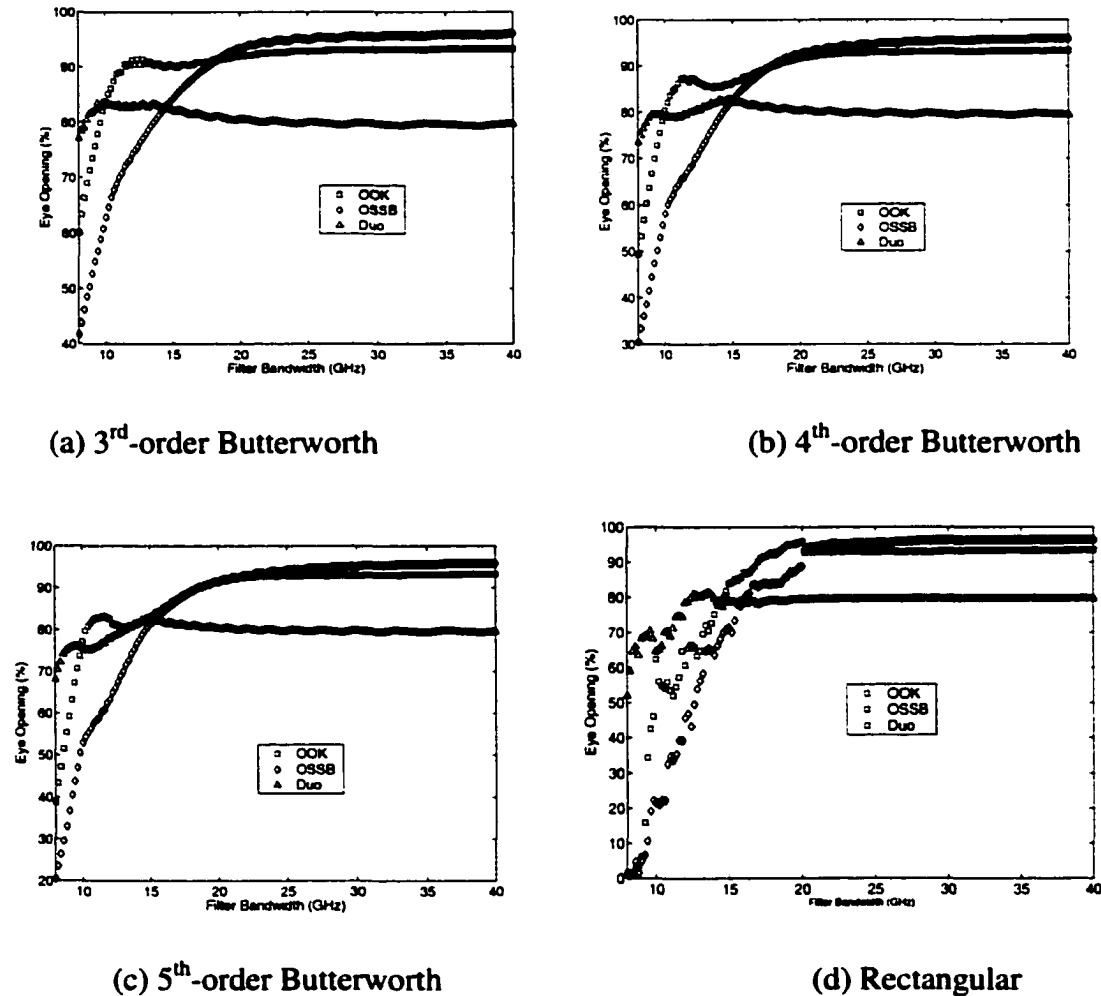


Figure 3.12: Eye Degradation due to Optical Filtering Effect

Figure 3.13 shows the 3-channel simulation results. The x -axis denotes the channel spacing between channels. The eye opening shown on the diagrams is for the center channel. Again, the back-to-back setting is used, and an electrical filter is present at the receiver. Each data point on the diagrams is the average over 50 runs. For each run, both the relative time-delay and laser phase of the three channels were randomly

changed. Four different optical filters were examined. The bandwidth of the optical filter for each channel spacing value was optimized to within 1 GHz.

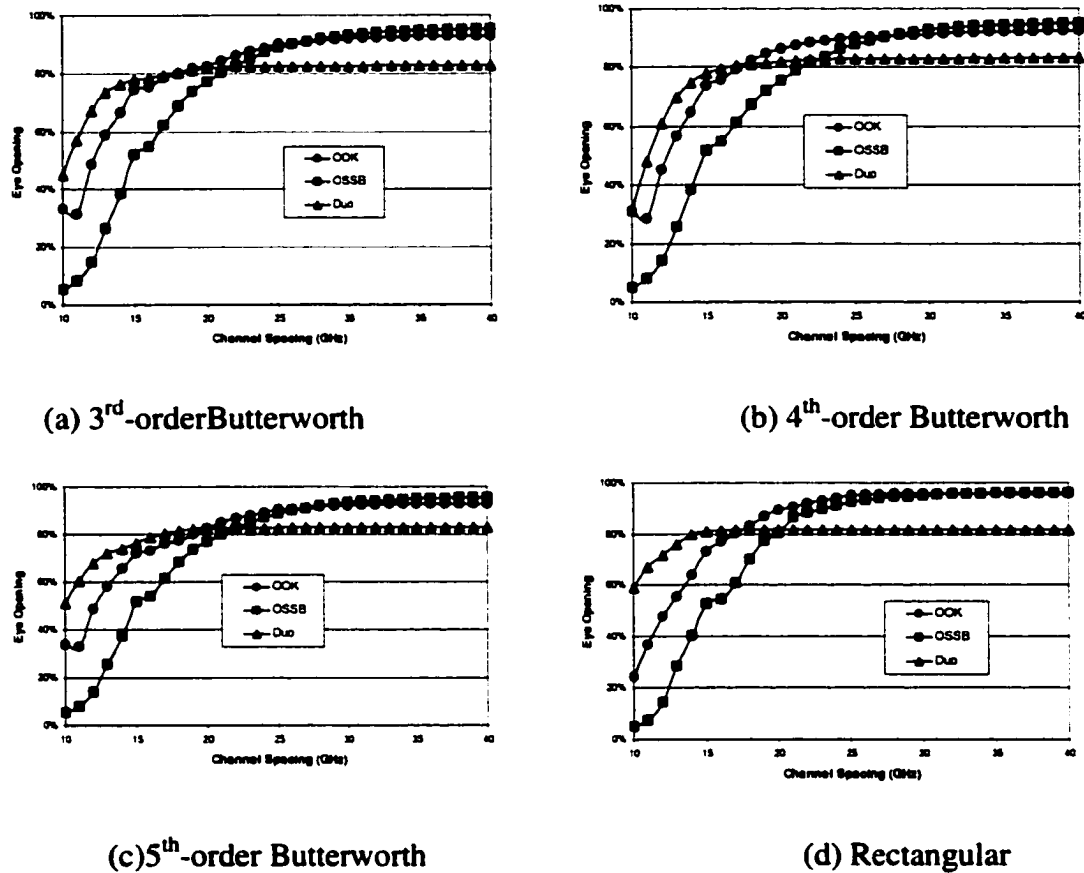


Figure 3.13: Eye Degradation due to 3-Channel Cross Talk using different Optical Filters

Judging from the **Figure 3.13**, the OSSB format suffers the most from cross talk. The eye opening starts to deviate between the OOK and OSSB formats as the channel spacing reduces below 25 GHz. It should be noted that the center frequency of the optical filters is at the carrier frequency of each signal. Slight changes to the center frequency of the optical filter were made in an attempt to produce improvements in the OSSB format due to its single-sidedness. However, the eye closure becomes worse for all shifts of the center frequency. This is due to the fact that shifting the center frequency of the optical filter generates more distortion to the OSSB signal spectrum (because of the optical filter shape), which, as mentioned, then disturbs the amplitude and phase relationship. Moreover, as expected, the duobinary format can better withstand closer

channel spacing. However, as shown in the figure, with the third-order Butterworth filter, the duobinary format only performs marginally better than the OOK format. As the filter bandwidth reduces to less than 15 GHz, both formats follow the same eye degradation trend with a 1.5 GHz margin between them. As the filter order increases (i.e. the filter shape becomes more and more rectangular), the duobinary format has better performance. This is a result of the narrower signal bandwidth of the duobinary signal, which suffers from less distortion from the optical filtering effect shown in **Figure 3.12**.

The above discussion indicates that the OSSB format does not have the narrow channel-spacing benefit as predicted by single-sidedness. Furthermore, the benefit of using the duobinary format for narrow channel-spacing applications largely depends on the type of optical filter available. The main disadvantage of the duobinary signal is still its smaller initial eye closure.

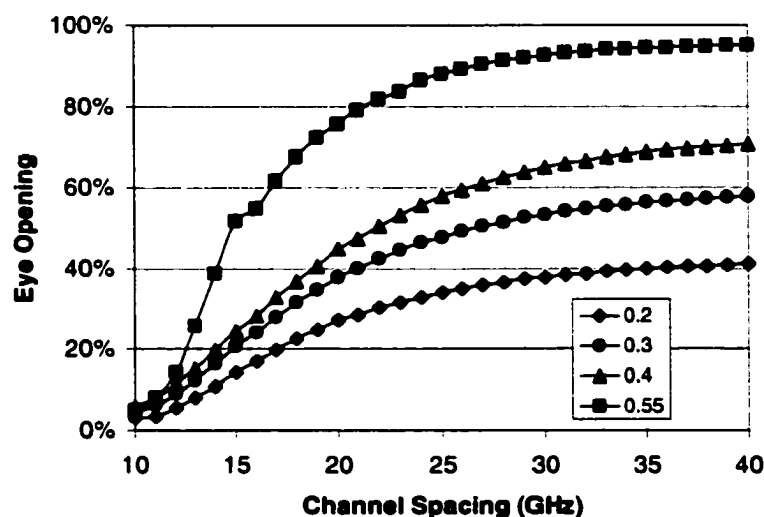


Figure 3.14: Eye Degradation Due to 3-Channel Cross Talk for OSSB Signaling with Different Modulation Depths

Figure 3.14 shows the cross talk eye closure penalty for the OSSB format with four different modulation depths. The legend gives the amplitude swing of the electrical signal in terms of the amplitude V_{π} that drives the OSSB transmitter. It should be noted that the '0.55' modulation depth was used for the immediately preceding simulations. **Figure 3.14** indicates that reducing in the modulation depths does not help to improve the

eye opening because of the increased initial eye closure penalty. Thus, for the remaining simulations reported in this chapter, the '0.55' OSSB signal will be used.

3.5. Self-Phase Modulation

Four cases were examined to explore the effects of SPM on the three different transmission formats. As mentioned in Chapter 1, the focus of this research is on single-span and terrestrial systems. Both standard fiber and NZDSF are commonly used in these fiber systems. Hence, the four different cases include two different transmission distances considered with two types of fibers. Since SPM is not the result of neighboring WDM channels, only single-channel simulations will be examined.

A typical single-channel system ranges in length from a few kilometers (city-wide) to more than 200 km. A long single-span system is useful when it is not possible to use a ground route from point A to point B, in which case the fiber needs to use a sea route without regeneration in between. The typical fiber attenuation for commercial fibers is between 0.2 to 0.25 dB/km depending on the cabling and the type of fiber. For simulation purposes, 0.2 dB/km is used throughout this chapter. This attenuation value is similar to that of the fiber available in the laboratory for the experiments shown in Chapter 4. For the simulations, 160 km of fiber length was used. This guarantees that the nonlinear fiber effects are negligibly small at the far end of the fiber link. As for the terrestrial system, five spans of 90 km of fiber are used for the simulations. At the end of each span, an optical chromatic dispersion compensator was inserted to compensate for 90% of the chromatic dispersion accumulated in the previous span. Also, a chromatic dispersion compensator was inserted before the transmission link to compensate for 50% of the residual dispersion generated by the 10% under-compensation. At the end of the transmission link, a DCM is placed and optimized to yield the maximum eye opening. The dispersion compensator is adjusted (within 20 ps/nm resolution) until the eye opening was maximized. The reason for this dispersion compensation will be explained in subsequent sections. The fiber parameters of the two types of fiber are listed in **Table 3.1**. The wavelength of the signal was set at 1500 nm and this value will be used for most of the remaining simulations of this chapter unless otherwise stated.

	<i>Attenuation</i> (dB/km)	<i>Dis. @1.5μm</i> (ps/nm/km)	<i>Dis. Slope</i> (ps/nm ² /km)	<i>Nonlinear Refractive Index</i> (m ² /Watt)	<i>Effective Core</i> Area (μ m ²)
SSMF	0.2	17	60	2.3x10 ⁻²⁰	85
NZDSF	0.2	4.2	83	2.3x10 ⁻²⁰	72

Table 3.1: Typical Fiber Characteristics.

Figure 3.15 and **Figure 3.16** show the simulation results for the two different fibers with a single-span configuration. **Figure 3.17** and **Figure 3.18** show the 5-span results. The bars and squares on the figures represent the eye opening and residual dispersion (in ps/nm), respectively. The residual dispersion shown on the figure is the dispersion remaining after the optical signal propagates through the dispersion compensator. The most important result shown by **Figure 3.15** and **Figure 3.16** is the eye degradation of the OSSB format as the launched power increases. For both the OOK and duobinary formats, the eye opening slightly increases as the launched power increases. As shown in **Figure 3.15**, as the launched power increases from 2 dBm to 8 dBm, the eye opening of the OSSB format decreases by about 1%; in contrast, the duobinary formats has its eye opening increased by 1.5% and the OOK format has its eye opening only very slightly increase (less than 0.2%).

The differences become more pronounced with the terrestrial system, as shown in **Figure 3.17** and **Figure 3.18**. Moreover, the value of the residual dispersion changes differently with the various modulations formats as the launched power increases. Observing from **Figure 3.15** to **Figure 3.18**, both the OOK and OSSB formats have increased residual dispersion as the launched power increases to achieve maximum eye opening. In contrast, the duobinary format has less residual dispersion as the launched power increases. Recalling **Figure 3.7**, with a purely linear system (without the nonlinear fiber effect), the duobinary format requires about 1500 ps/nm more residual dispersion than the other two formats to achieve the maximum eye opening. As the SPM effect becomes more important, the marginal difference in residual dispersion decreases for the three formats. As shown in **Figure 3.15** to **Figure 3.18**, the difference in residual dispersion to achieve maximum eye opening for the different formats reduces to about

600 ps/nm for a single span and about 150ps/nm to 300 ps/nm for five spans of fiber. As the launched power increases, the difference decreases, indicating that the SPM effect is responsible for observed change in distortion.

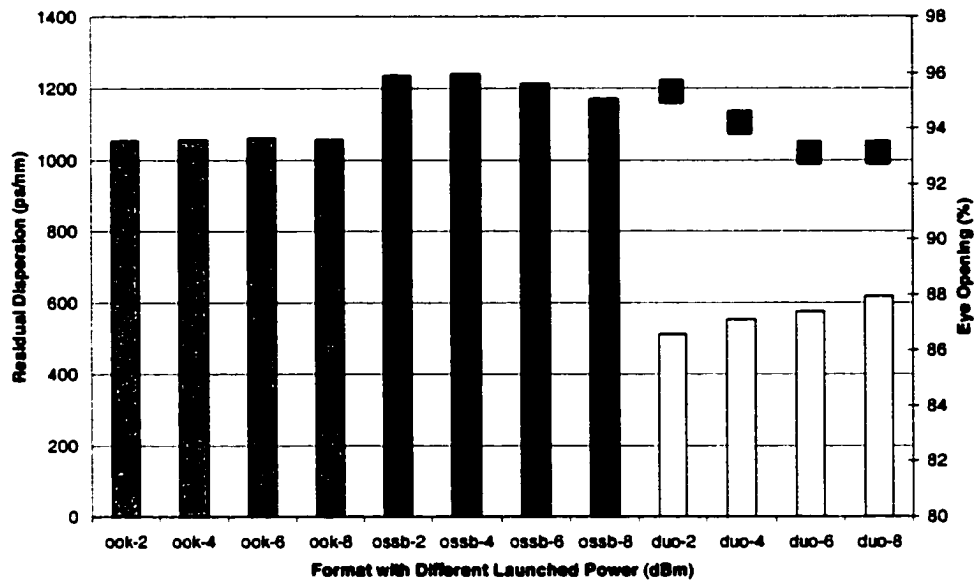


Figure 3.15: Eye Opening and the Corresponding Residual Dispersion under the Influence of SPM (SSMF, 160 km) [Square – dispersion; Bar – Eye Opening]

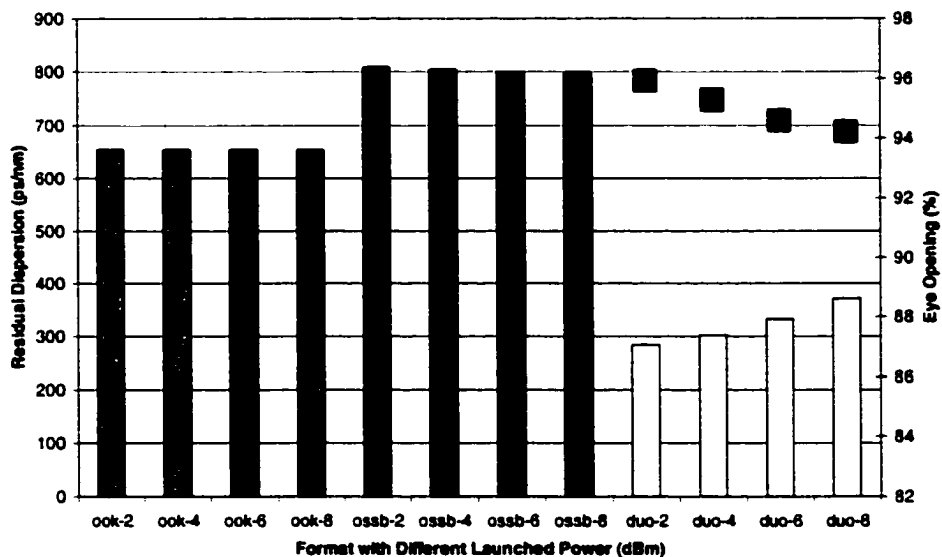


Figure 3.16: Eye Opening and the Corresponding Residual Dispersion under the Influence of SPM (NZDSF, 160 km) [Square – dispersion; Bar – Eye Opening]

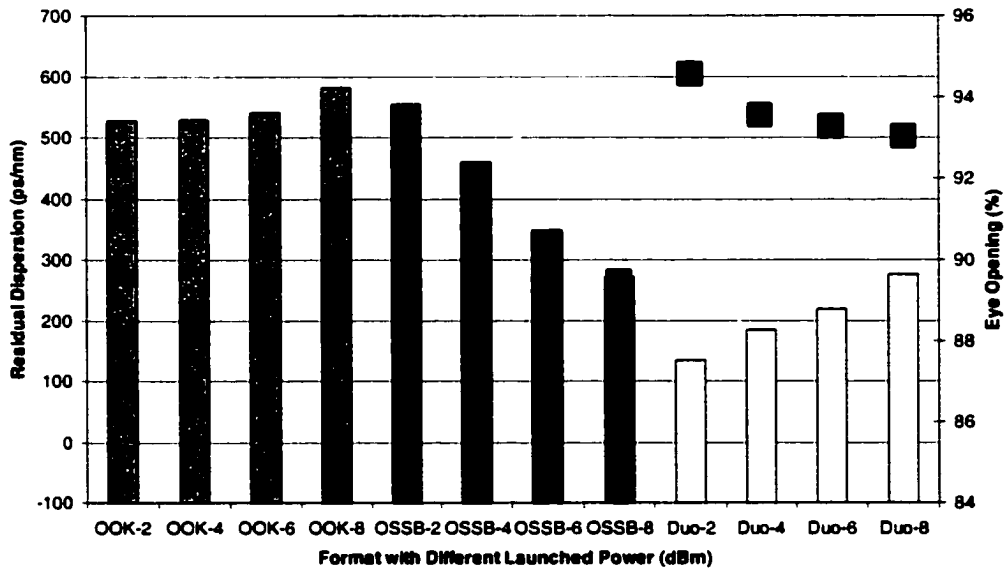


Figure 3.17: Eye Opening and the Corresponding Residual Dispersion under the Influence of SPM (SSMF, 5x90 km) [Square – dispersion; Bar – Eye Opening]

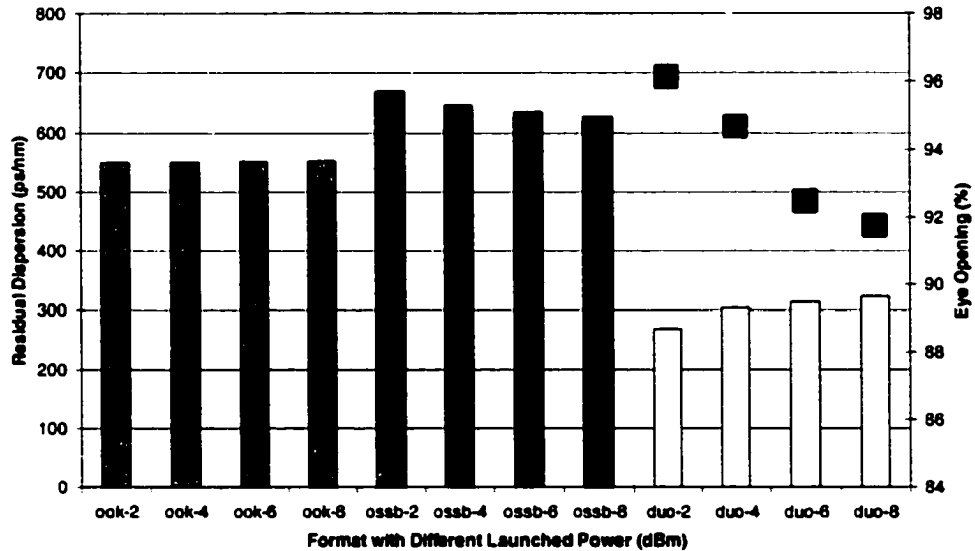


Figure 3.18: Eye Opening and the Corresponding Residual Dispersion under the Influence of SPM (NZDSF, 5x90 km) [Square – dispersion; Bar – Eye Opening]

The phenomena mentioned above can be understood using an approximate analysis. The approximate method separates the SPM distortion from the signal itself.

With this separation, the physical origin of the differences in the SPM distortion for the three formats can be more easily understood.

Recalling from Chapter 2, the NLSE describing the pulse evolution in the optical link satisfies the following equation:

$$\frac{\partial A}{\partial z} - \frac{i}{2} \beta_2 \frac{\partial^2 A}{\partial T^2} + \frac{\alpha}{2} A = -i\gamma |A|^2 A$$

The term accounting for the dispersion slope is omitted in the above equation. The nonlinear disturbance comes from the power term on the right-hand side (RHS) of the equation. The split-step Fourier method can accurately keep track of the change of the optical signal, but it cannot separate out the SPM distortion. If the SPM distortion is small, it can be assumed that the evolution of A along the optical link is caused mainly by chromatic dispersion. As a result, the RHS term can be treated as a separate source that has the same initial conditions (at the launch end of the fiber) as A , but is then only affected by chromatic dispersion and fiber attenuation along the fiber. With this approximation, the solution of the NLSE for short lengths of fiber (assuming chromatic dispersion has negligible effect) can be written as

$$\begin{aligned} \tilde{A}(\omega, \Delta z) &= e^{-\alpha/2} [\tilde{A}(\omega, 0) e^{-i\beta_2 \omega^2 z/2} + R\tilde{K}] \\ \text{where } R &= \frac{-i\gamma}{i\beta_2 \omega^2 / 2 - \alpha} \left(e^{-\alpha} - e^{-i\beta_2 \omega^2 z/2} \right) \end{aligned} \quad (3.15)$$

The ' \tilde{A} ' represents the signal in the Fourier domain; \tilde{K} is the Fourier transform of the $|A|^2 A$ term. In (3.15), the first term describes the linear evolution of the optical signal caused only by the fiber attenuation and the chromatic dispersion. The second term describes the SPM distortion. Thus, the SPM distortion is separated out from the signal. Equation (3.15) only applies to short lengths of fiber where the chromatic dispersion is small.

An iterative approach is required to calculate the accumulated SPM distortion for the entire fiber link. This approach is outlined in **Figure 3.19** in a simple single-span fiber configuration. The entire fiber length is separated into small segments. The SPM distortion for each segment is calculated using (3.15). The ' d 's in the figure are the $R\tilde{K}$

terms in (3.15) multiplied by the fiber attenuation and chromatic dispersion for the remaining fiber length. The total SPM distortion is computed by simply summing up all the d terms. Note that the \tilde{K} term for each segment is constantly modified by the fiber attenuation and chromatic dispersion.

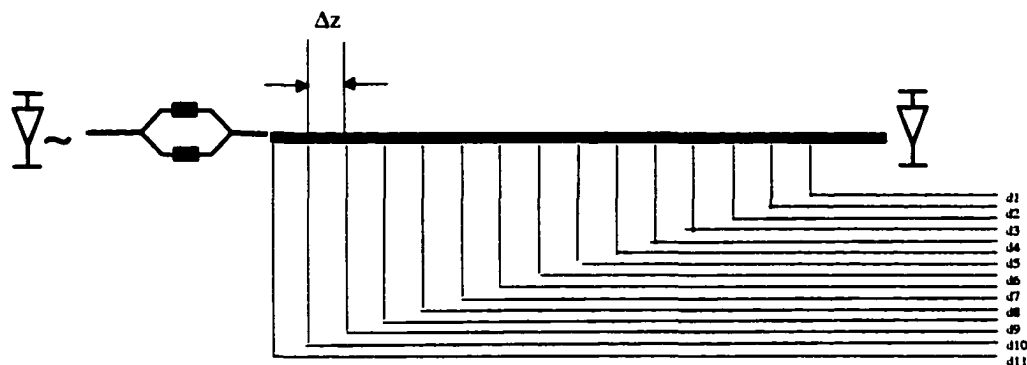


Figure 3.19: Illustration of the Iterative Approximation Method for Evaluating the SPM Distortion

Figure 3.20 compares the eye diagrams obtained from the split-step Fourier method and as well as the approximated method for the three formats. A single span of 160 km of single-mode fiber is used. The average launched power was set to 8 dBm. Each fiber segment was set to 500m. No optical and electrical filters were placed in the systems. An optical chromatic dispersion compensator, set to full compensation was placed at the end of the fiber. The first row of eye diagrams was the original eye diagrams before launching into the fiber. **Figure 3.20** shows that the approximate method provides a fairly good estimate of the SPM distortion even for 8 dBm of launched power, which is above any practical launched power for dense WDM systems.

The difference in SPM distortion for the OSSB formats can be understood by analyzing the individual term that forms the SPM distortion. **Figure 3.21** shows how the SPM contribution evolves as a function of propagation distance. Twenty curves representing twenty equal-length fiber segments are superimposed on each diagram. In order to clearly show how the distortion evolves, individual SPM contributions from only every fourth segment are shown (2 km apart). The curve with the highest amplitude is

for the first fiber segment. The SPM distortion of each subsequent fiber segment has gradually less amplitude because of fiber attenuation. It is quite clear from **Figure 3.20** that the evolution of the SPM distortion for OSSB formats is much more asymmetric as compared to both the OOK and duobinary formats. The rising and falling edges of the OSSB signal pulses degrade in different fashion, which causes the signal eye to look asymmetric, as shown in **Figure 3.20**. Consequently, the eye opening is smaller.

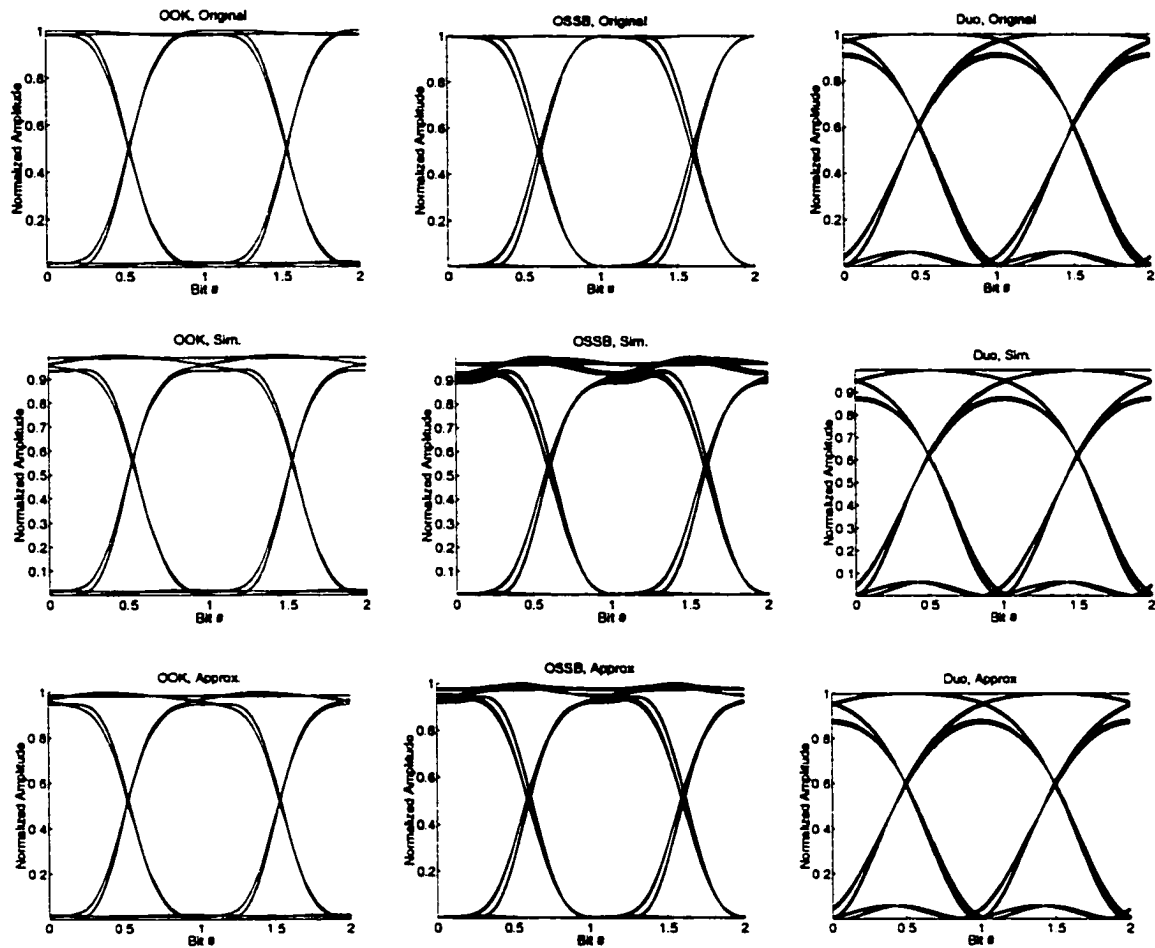


Figure 3.20: Comparison of the simulated and approximated eyes of the Three Formats under the Influence of Chromatic Dispersion and SPM

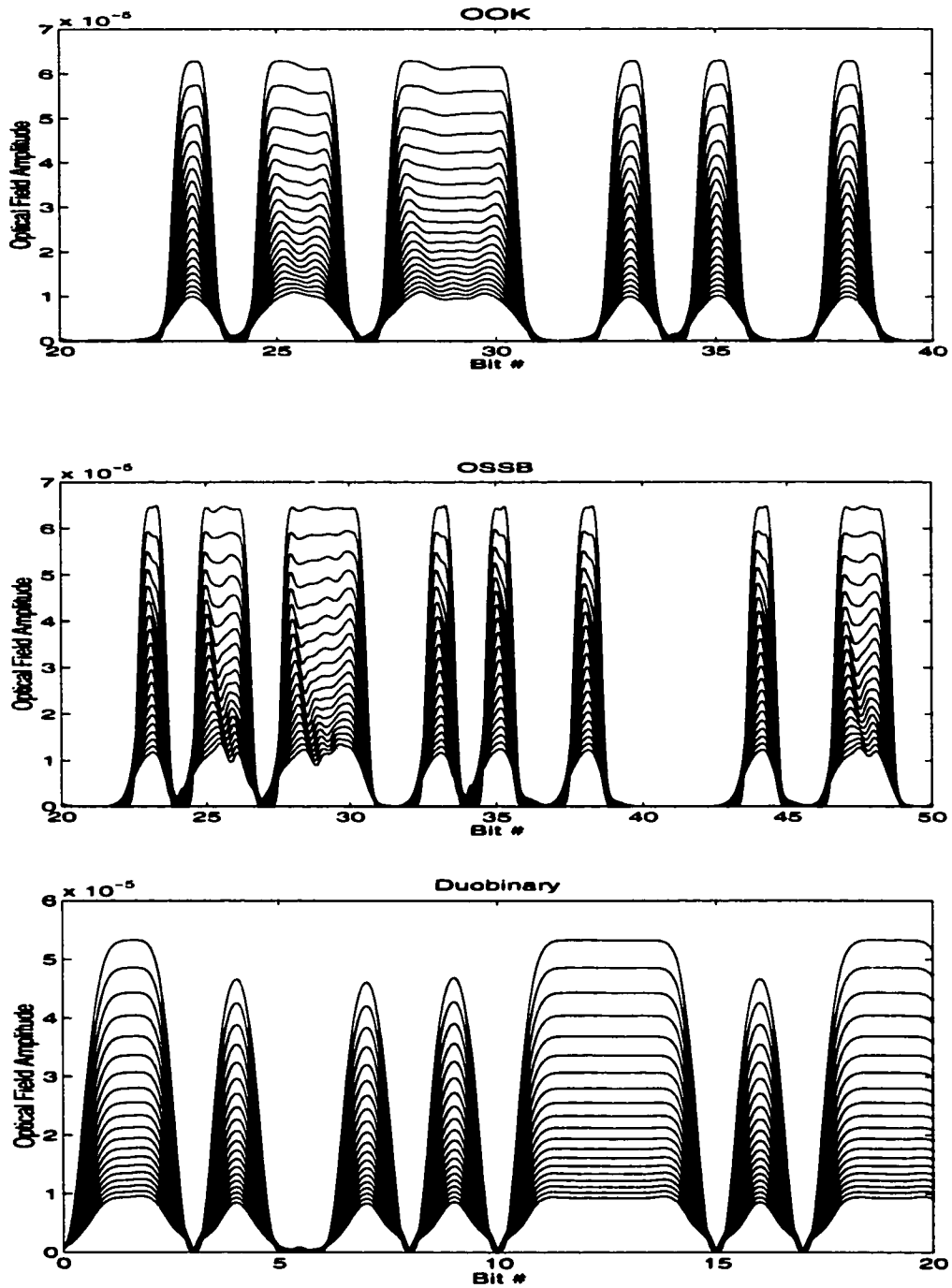


Figure 3.21: Evolution of the SPM Distortion for the Three Formats

The reason for asymmetric SPM distortion evolution in OSSB is due to the Hilbert transform term. As mentioned in Section 3.3, the distortion evolution due solely to the chromatic dispersion is very different for OSSB signals as illustrated by the three extra terms in (3.11). Equation (3.15) shows that the SPM distortion is directly

proportion to the $|A|^2 A$ term in each fiber segment. Note that the $|A|^2 A$ term has asymmetric dispersion evolution along the fiber link. As for the OOK and duobinary formats, the SPM distortions closely resemble the signals themselves, as shown in **Figure 3.21**. Because of this, the SPM distortion could possibly help to improve the signal eye opening slightly. According to **Figure 3.15** to **Figure 3.18**, the SPM distortion can indeed improve the eye opening, but this requires proper adjustment to the residual dispersion.

For both single-span and terrestrial systems, neither the OOK nor duobinary formats are affected significantly by the SPM effect for all simulated power levels. With the OSSB format, the distortion is minimal for single spans, but becomes slightly more significant for terrestrial systems at high power levels. In conclusion, SPM is not a significant distortion for any of the three candidate transmission formats at the OC-192 transmission rate.

3.6. Cross-Phase Modulation

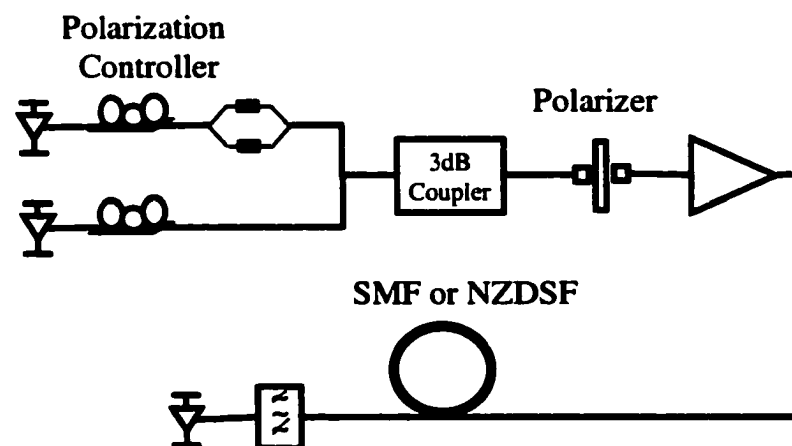


Figure 3.22: Two-Channel XPM System Setup

For WDM systems, SPM, XPM and FWM are present. To investigate the effect of XPM alone on the three different formats, it is necessary to suppress the other two fiber nonlinear effects. This can be achieved by using a simple two-channel system as shown, in **Figure 3.22** [59].

This system consists of a continuous-wave (CW, i.e. constant amplitude) channel and a modulated channel that are separated in the wavelength. The XPM strength is evaluated by launching these two channels into a fiber and measuring the standard deviation of the CW channel after a square-law detector. Without any nonlinear fiber effects, the CW channel would not have any variation in amplitude. By examining the NLSE, the SPM does not affect the CW channel at all except for a constant phase change (but this phase offset would be removed after square-law detection). The amplitude variation in this system comes mostly from the XPM effect. FWM is still present in this system, but the mixing of the two channels would only form a component that is located outside the bandwidth of the two channels. Hence, the only effect of the FWM would be to slightly change the amplitude of the two channels, which in most cases is negligible. The standard deviation can be estimated using an approximated analytical expression given by Hui [60]. This derivation ignores the effect of chromatic dispersion on the nonlinear term of the coupled NLSE. Also, Hui makes a few other assumptions in the derivation; the reason for making these assumptions is not clear. In fact, a simpler derivation can also arrive at the same result, as we show below.

The coupled NLSE for the CW channel, A_{cw} , is shown here for reference

$$\frac{\partial A_{cw}}{\partial z} + \Delta\beta_{1cw} \frac{\partial A_{cw}}{\partial T} - i \frac{\beta_2}{2} \frac{\partial^2 A_{cw}}{\partial T^2} + \frac{\alpha}{2} A_{cw} = -i\gamma |A_{cw}|^2 A_{cw} - 2i\gamma |A_{mod}(T, z)|^2 A_{cw} \quad (3.16)$$

where A_{mod} denotes the optical field of the modulated channel and the dispersion slope term is ignored. For simplicity, the parameters of A_{cw} are not shown. Three assumptions are made. First, the SPM term can be ignored because the sole contribution of the SPM term to the noise spectrum is the DC component. Second, the pulse shape of A_{mod} is not altered by chromatic dispersion when the XPM nonlinear effect is important. Taking into account the difference in propagation speed of the two channels (the $\Delta\beta_{1cw} \frac{\partial A_{cw}}{\partial T}$ term in the equation), the modulated channel can be approximated as $A_{mod}(T, z) \approx A_{mod}(T - z/v_g, 0) \exp(-\alpha z/2)$. Here, v_g is the group velocity difference between the two channels, which is equal to $1/\Delta\beta_{1cw}$. For small channel spacing, $\Delta\beta_{1cw}$ can be written as $\beta_2 \Delta\omega$. The third assumption requires that the A_{cw} in the second term of the RHS be treated as an independent function with the same initial condition, but which

is then modified only by the fiber attenuation throughout the entire signal propagation.

Thus, on the RHS, $A_{cw} \approx A_{cw,initial} e^{-\alpha z/2}$. The coupled NLSE can then be modified as

$$\frac{\partial A_{cw}}{\partial z} - i \frac{\beta_2}{2} \frac{\partial^2 A_{cw}}{\partial T^2} + \frac{\alpha}{2} A_{cw} = -2i\gamma |A_{mod}(T - z/\Delta v_g, 0)|^2 A_{cw,initial} e^{-3\alpha z/2} \quad (3.17)$$

The $\Delta\beta_{1,cw} \frac{\partial A_{cw}}{\partial T}$ term is absorbed according to the assumption for A_{mod} . This modified form of the coupled NLSE has an analytical expression as follows,

$$A_{cw}(\omega, z) = 2\pi \sqrt{P_{cw,initial}} \delta(\omega) e^{-\alpha z/2} + K \tilde{C} \quad (3.18)$$

$$K = \frac{-i2\gamma \sqrt{P_{cw}} e^{-\alpha z/2}}{i\beta_2(\omega^2/2 - \omega\Delta\omega) - \alpha} [e^{(-\alpha - i\Delta\omega\beta_2)\omega z} - e^{-i\omega^2\beta_2 z/2}]$$

where ‘ \sim ’ denotes the Fourier transform and \tilde{C} denotes the Fourier transform of $|A_{mod}(T, 0)|^2 [=P_{mod}(T, 0)]$. The first term in (3.18) represents the linear propagation of the CW channel, while the second term is the XPM distortion. After square-law detection, three terms would be present including the absolute square of the signal, the signal beat with the XPM noise, and the absolute square of the XPM noise. Usually the last term has a much smaller magnitude compared to the other two terms and can be ignored. Thus, the majority of noise comes from the signal-to-XPM beat noise. Following directly from (3.18), the equation describing this noise term [60] is as below:

$$Noise_{xpm} = 2\gamma P_{cw,initial} e^{-\alpha z} P_{mod,initial} \left[\frac{e^{-i\omega^2\beta_2 z/2} - e^{-(\alpha - i\Delta\omega\beta_2)\omega z}}{i[\alpha - i\beta_2(\omega^2/2 - \omega\Delta\omega)]} - \frac{e^{i\omega^2\beta_2 z/2} - e^{-(\alpha - i\Delta\omega\beta_2)\omega z}}{i[\alpha - i\beta_2(-\omega^2/2 - \omega\Delta\omega)]} \right] \quad (3.19)$$

If $e^{-\alpha z}$ is much smaller than 1 and the channel spacing is much larger than the signal bandwidth, then (3.19) can be simplified to

$$Noise_{xpm} \approx \frac{-4\gamma P_{cw,initial} e^{-\alpha z} P_{mod,initial} \sin(\omega^2 \beta_2 z / 2)}{\alpha + i\beta_2 \omega \Delta\omega} \quad (3.20)$$

Observed from (3.20), the carrier power of the modulated channel does not affect the XPM noise penalty because of the sine function in the equation. The noise power is inversely proportional to the fiber attenuation and the channel spacing, but increases with

the nonlinear refractive index, n_2 (γ in the equation). Also, the XPM noise power is proportional to the power spectra of the two channels, not the field spectra. Moreover, the sine function in the equation indicates that as the chromatic dispersion approaches zero (valid for the case involving chromatic dispersion compensation), the XPM noise would approach a minimum. However, it is not equal to zero (the approximation does not model accurately at this point).

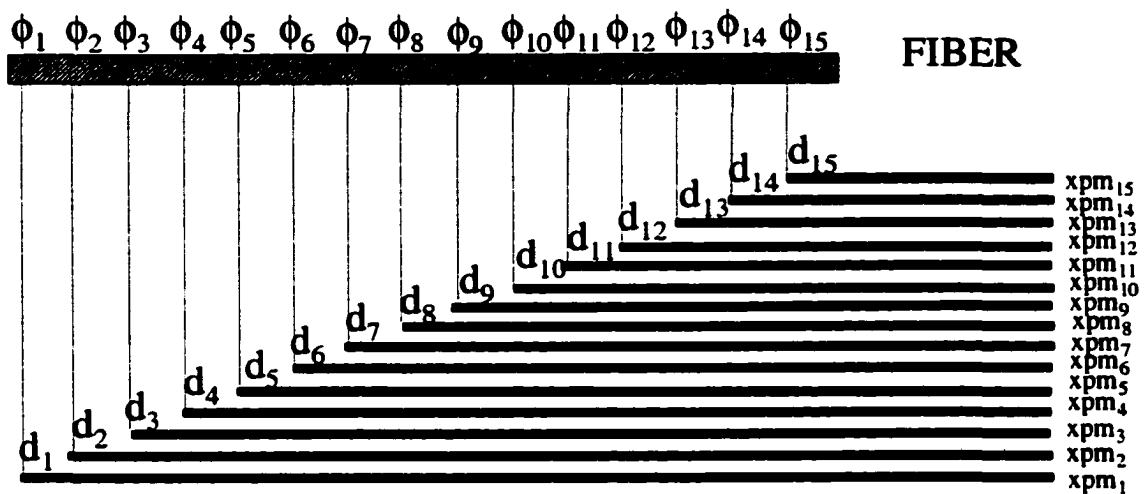


Figure 3.23: Successive Components of XPM Noise Generation

From the split-step Fourier method, one notes that the XPM noise generation involves two processes. First, at any part of the fiber, the power of the modulated channel modulates the phase, ϕ_x , of the CW channel (nonlinear step). The phase change of the CW channel is then converted into amplitude distortion by the chromatic dispersion, d_x , of the remaining fiber length (dispersion step). This is illustrated in **Figure 3.23**. As shown in the figure, the phase-to-amplitude XPM distortion becomes weaker as the signal propagates through the fiber because the length of the remaining fiber length is less and the signal power decreases continuously. To suppress the XPM distortion, a chromatic dispersion compensator is placed at the end of the fiber. However, as shown in **Figure 3.23**, if the compensator could be set to fully reverse the phase-to-amplitude conversion for the ϕ_1 - d_1 pair, the amplitude conversion for ϕ_{15} - d_{15} pair would be even more severe. This explains why, even for full dispersion compensation, the XPM distortion cannot be fully suppressed. Nevertheless, the XPM distortion would be roughly at a minimum for full dispersion compensation simply

because the phase modulation is at a maximum at the beginning of the fiber where signal power is at a maximum. The phase-modulation process alone would not induce XPM noise because the square-law detection is insensitive to phase

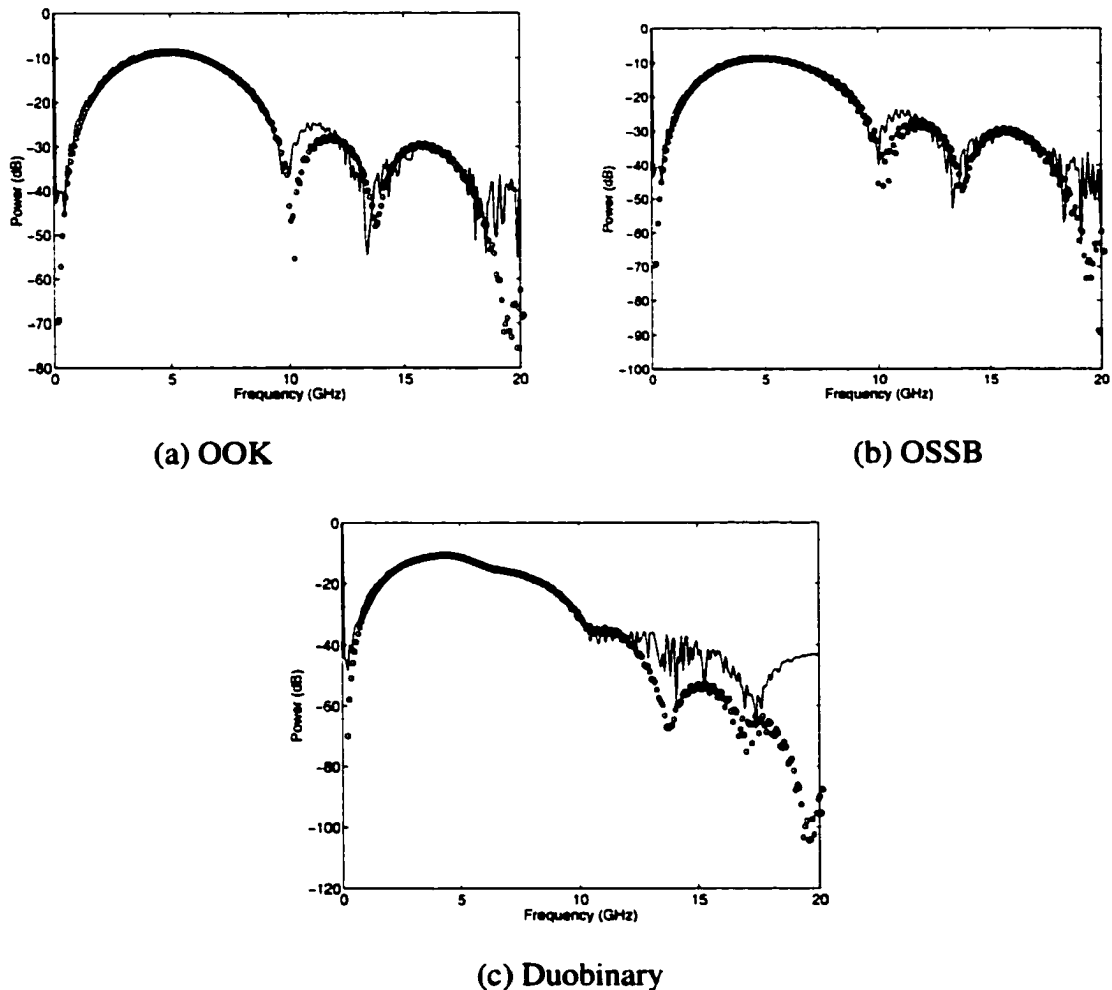


Figure 3.24: Comparison of the Two-channel XPM Simulation Results with the Analytical Approximation for the Three Formats (solid line--Simulation; Bubble-Analytic)

Figure 3.24 compares the two-channel XPM simulation results with the analytical approximation after square-law detection without electrical filtering. In the simulations, 160 km of NZDSF is used, and the average launched power per channel is set at 8 dBm. The figure shows that the analytical equation accurately describes the square-law-detected noise spectra for all three formats.

Figure 3.25 compares the normalized standard deviation versus the residual dispersion between the simulations and analytic approximations. The normalized standard deviation is calculated as the standard deviation divided by the signal power. Different curves on the figure represent different average launched powers per channel. From the bottom curve to the top curve for each diagram in the figure, the average launched power increases from 2dBm to 8 dBm in 2dB steps. **Figure 3.25** shows that the analytic approximation is in good agreement with the simulations, especially when the standard deviation is around its minimum.

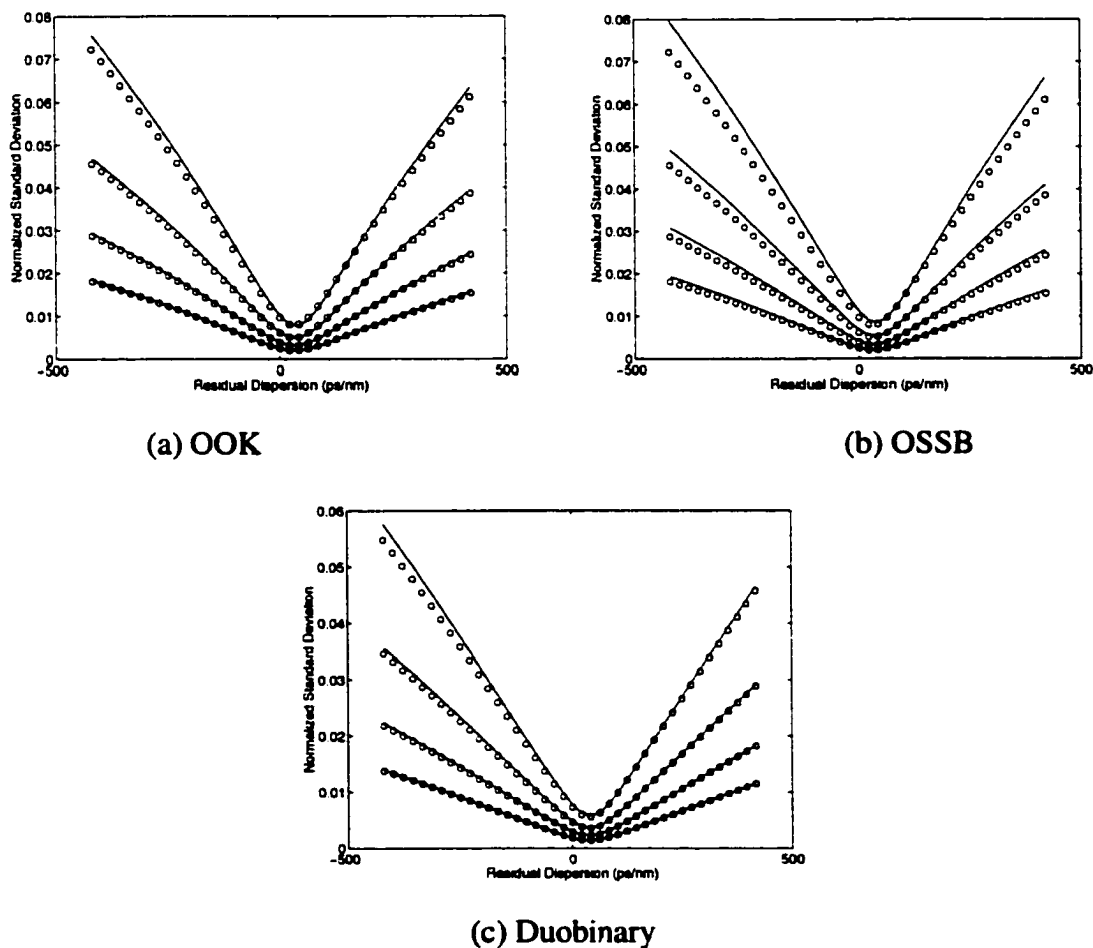


Figure 3.25: Comparison of Normalized Standard Deviation between Simulations and Analytic Approximations (solid line-simulation; bubble-approximation) due to XPM.

Figure 3.26 compares the normalized standard deviation among the three formats with different channel spacings for both types of fiber. As expected, the standard

deviation is approximately the same for both the OOK and OSSB formats, with the OSSB format having a slightly higher value. The duobinary format has less standard deviation, which is directly the result of the larger carrier tone to signal spectrum power ratio. Because of this, with the same average launch power, the duobinary format has larger carrier tone but less AC signal power and thus yields less XPM distortion. The slightly higher deviation value of the OSSB format is due to the slightly larger modulation depth, as mentioned earlier in the early section. The larger modulation depth means that there is less power in the carrier tone, but more power in the signal spectrum for OSSB formats, and, as mentioned before, only the signal spectrum determines the strength of the XPM distortion. Hence, the OSSB format has a slightly higher standard deviation. The NZDSF medium induces higher XPM distortion, which is the result of a smaller effective core area ($72 \mu\text{m}^2$ compare to $85 \mu\text{m}^2$ of SSMF). The γ parameter in (3.19) is inversely proportional to the effective core area, thus the XPM is higher for NZDSF. As will be shown in this section, with NZDSF, the dominant fiber nonlinear effect is FWM, not XPM, for most cases.

Figure 3.27 shows the difference in the frequency spectrum of the absolute-square of the optical signals. It is clear that the duobinary format has a narrower signal spectrum as compared to the other two formats. The larger carrier tone to signal spectrum power ratio is an advantage for resisting XPM distortion, but is a disadvantage for maximizing the eye opening.

A more realistic comparison of the XPM penalty can be achieved by examining a 5-channel WDM system. For a 50 GHz channel spacing or wider, the XPM distortion in the WDM system comes mainly from the neighboring two channels. Thus, the center channel of a 5-channel system should experience most of the XPM effect that occurs in an actual WDM system. Using a CW laser at the center channel to remove the SPM contribution (with the remaining four channels modulated), it is possible to estimate the total XPM distortion from all other channels by calculating the standard deviation after square-law detection. By randomizing the laser phase and relative time-shift of the optical channels, the XPM distortion experienced by the center channel practically behaves like random noise. To suppress the FWM contribution, it is necessary to use a

large walk-off (meaning large local chromatic dispersion) fiber for the simulations, and thus the SSMF is used. **Figure 3.28** shows the results of the 5-channel simulations. A single-span of 160 km of SSMF was used and the channel spacing was set at 50 GHz. Twenty runs were performed for each power level. Again, the figure shows that the duobinary format has less XPM noise compared to the other two formats.

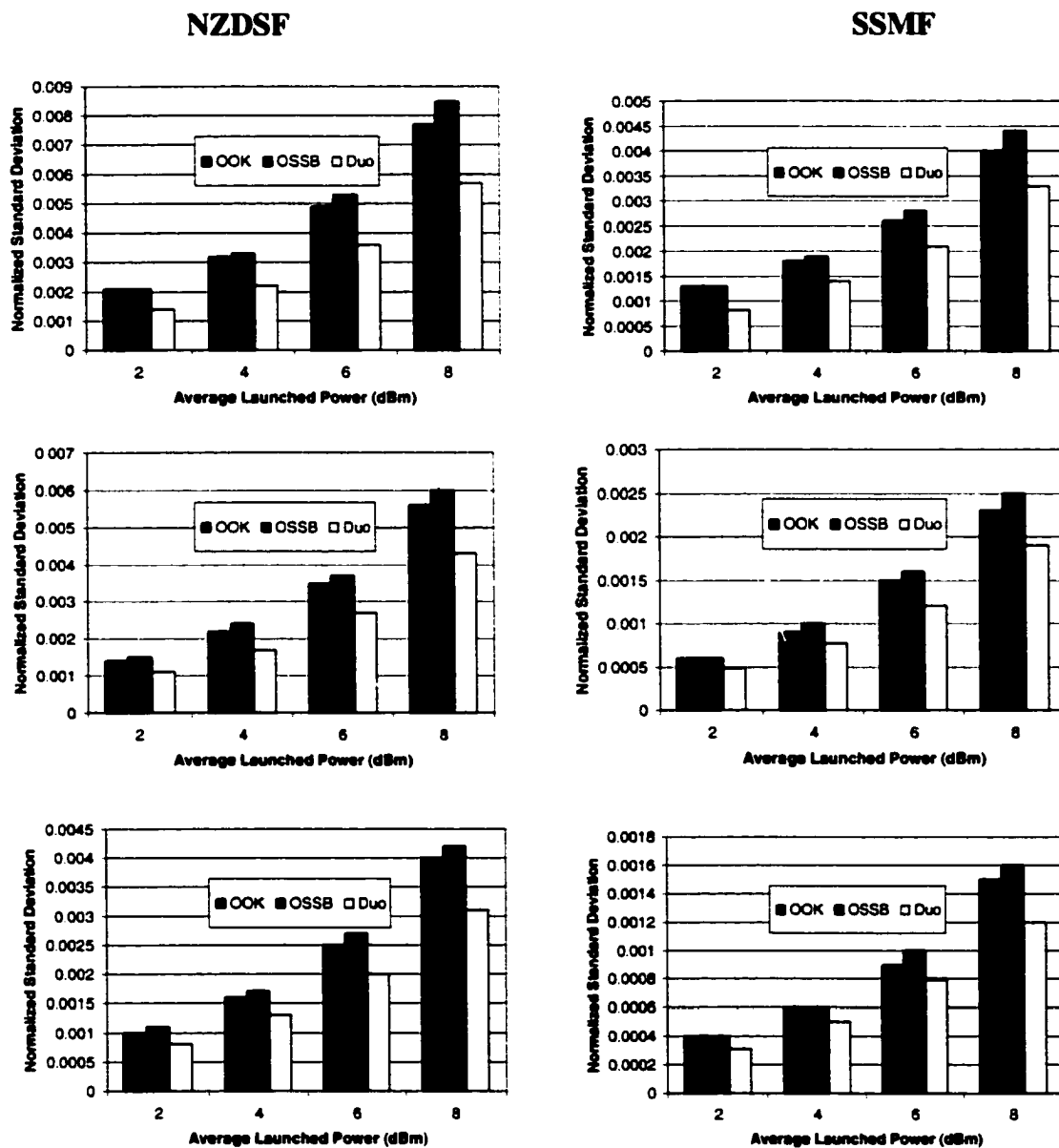


Figure 3.26: Comparison of Normalized Standard Deviation between the Three Formats with Different Channel Spacing Resulting from XPM Effect (channel spacing : top 50 GHz, middle 70 GHz, bottom 90 GHz).

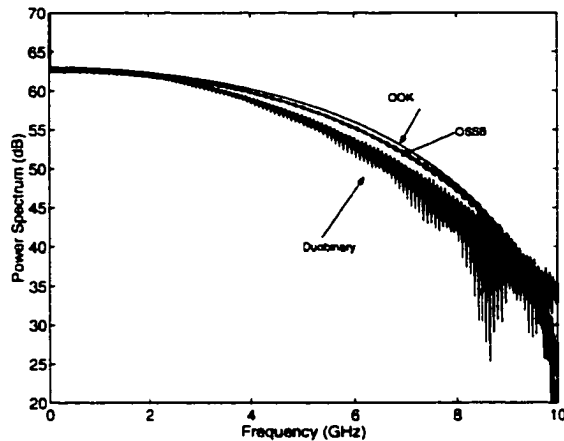


Figure 3.27: Comparison of the Frequency Spectra of the Absolute-Square of the Optical Signals between the Three Formats

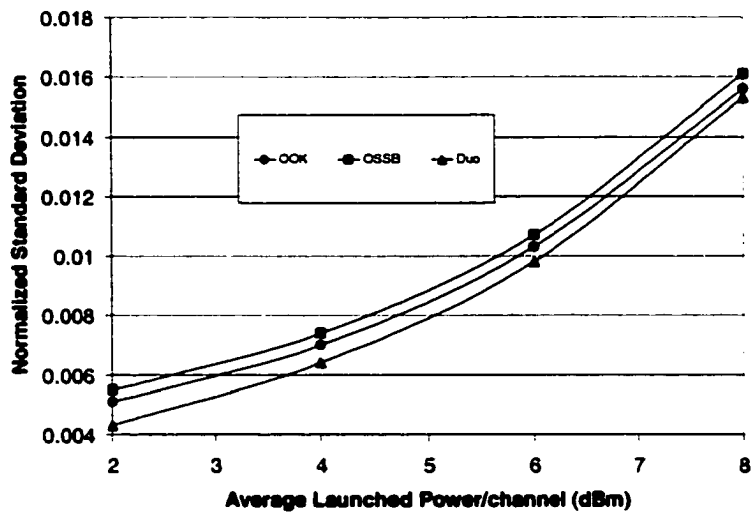


Figure 3.28: Comparison of the Normalized Standard Deviation between the Three Formats in Single-Span 50 GHz Spacing 5-Channel Configuration Resulting from XPM Effect.

Lastly, let's examine a 5-channel system in a terrestrial configuration. For typical functioning fiber systems, the XPM distortion can be considered a small perturbation. The nonlinear XPM distortion mainly occurs at the beginning of each fiber span. With full span-by-span compensation, the relative time-delay between channels is roughly

recovered to the initial launching condition at the beginning of each fiber span. This is not exact because the DCM does not fully compensate the edge channels. Because of this, the nonlinear XPM distortions generated at the beginning of each fiber span are very similar. Therefore, at the end of the entire fiber link, these individual distortion terms would be summed up in a totally constructive manner and would produce the worst case XPM distortion. This is sometimes called the resonance effect [61]. If, however, the span-by-span compensation is slightly under-compensated, the relative time-delay between channels would continuously vary from one span to the next. It is then that the resonance effect would be greatly suppressed. Nevertheless, if the under-compensation is set too high, the XPM distortion would be greatly increased due to the residual dispersion. More investigation is needed to gain a full understanding on this topic. For this research, 10% under-compensation was used.

The under-compensation scheme has one serious setback. At the end of the entire fiber link, the XPM distortion term from each span would accumulate different amounts of residual dispersion (residual from the under-compensation of each span). For instance, with a 5-span terrestrial system with 10% under-compensation, the XPM distortion from the first span would accumulate dispersion equivalent to 50% of single-span dispersion whereas the XPM distortion from the fifth span would only have 10% of the single-span dispersion. Evidently, if a chromatic dispersion compensator is placed at the end of the fiber link, it can never suppress all of the XPM noise terms to a minimum. As shown in **Figure 3.25**, the standard deviation increases quite linearly with residual dispersion, which means the variance of the XPM noise increases quadratically with residual dispersion. Since noise accumulates quadratically, the total XPM noise would greatly increase if any individual XPM noise term has excess residual dispersion. Thus, the minimum XPM noise would be obtained roughly if the dispersion compensator is set to fully compensate for the middle span such that the XPM term for the first and last spans have about the same amount of residual dispersion.

The above discussion is still not complete: The span-by-span under-compensation with the 'mid-span' post-compensation would cause the optical signal to have a certain amount of residual dispersion at the end of the optical link. The amount of residual dispersion is equal to the percentage of under-compensation multiplied by half the

number of spans. This residual dispersion causes the signal eye to be smaller, which affects the system performance. To compensate for this residual dispersion, a pre-compensation scheme is required, where a dispersion compensator is placed before the fiber link to compensate for the amount of dispersion mentioned. This final scheme is sometimes called the '50-50' compensation scheme (50% pre-compensation and 50% post-compensation) [62].

Figure 3.29 shows the 5-span simulation results for the OOK format to verify this hypothesis. Five spans of 90 km of SSMF are used in these simulations and 10% under-compensation is applied. The channel spacing is set at 50 GHz. It should be noted that the standard deviation shown on the diagram is renormalized to the minimum value obtained within the simulated range in order to clearly show the concave shape of the curves for all three launched power levels. The residual dispersion is referenced to the residual dispersion counting from the third span. The figure clearly shows that the minimum XPM noise occurs when the mid-span XPM distortion is fully compensated. **Figure 3.30** compares the XPM noise of the three formats in this 5-span under-compensated terrestrial system configuration. Not surprisingly, the duobinary format has less XPM noise compared to the other two formats.

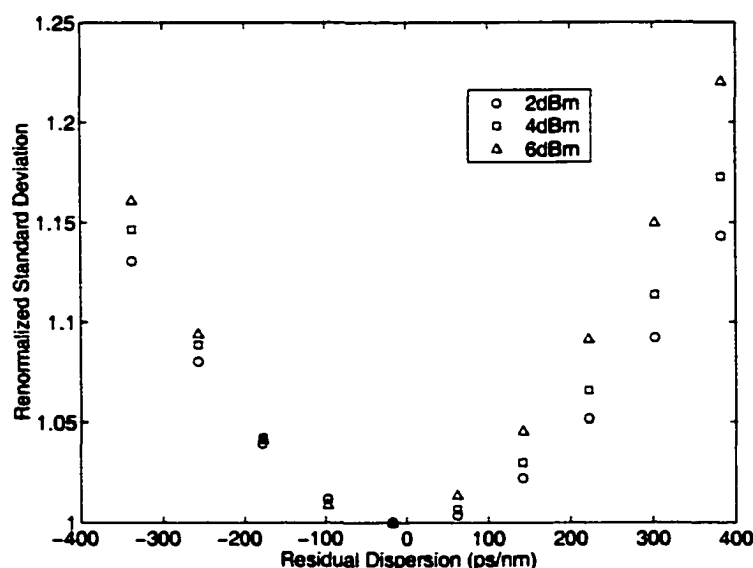


Figure 3.29: Renormalized Standard Deviation versus Residual Dispersion for a 5-Span Configuration

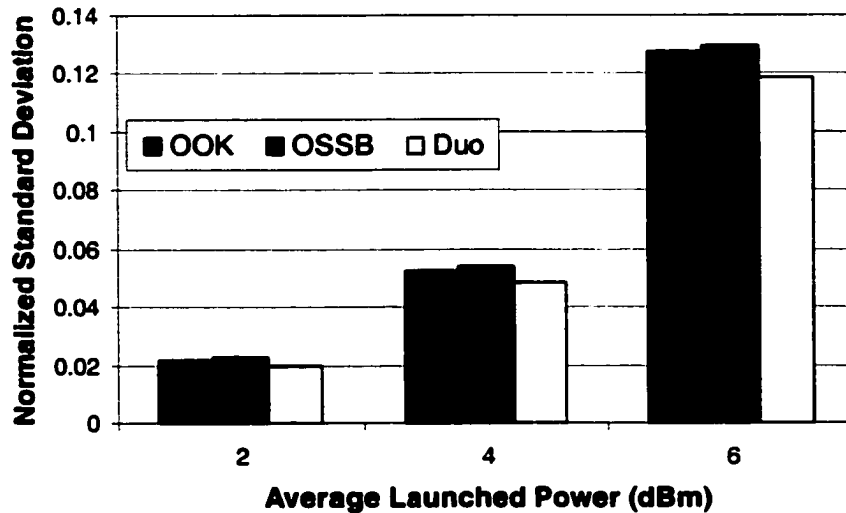


Figure 3.30: Comparison of the XPM noise of the Three Formats in Terrestrial System Configuration

3.7. Four Wave Mixing

As described in Chapter 2, it is necessary to have a triplet (3 channels, or 2 channels in the degenerate case) to induce FWM in an optical system. In a typical dense WDM system, the FWM distortion of any particular channel is induced by many different triplets. For typical systems (using SSMF or NZDSF) with channel spacings of 50 GHz or wider, the FWM distortion comes mainly from the neighboring two channels on each side of a particular channel. Thus, let's look at a simple case of a 3-channel system consisting of two modulated channels and a CW channel as shown in **Figure 3.31**. In this system, both XPM and FWM would co-exist. In order to reduce the effect of XPM, NZDSF is used because it has less chromatic dispersion. This makes FWM generation more efficient because the phase matching is better (more details below). Hence the magnitude of FWM distortion is significantly higher than that of XPM. However, the XPM distortion would always be present, which makes the FWM penalty comparison more difficult.

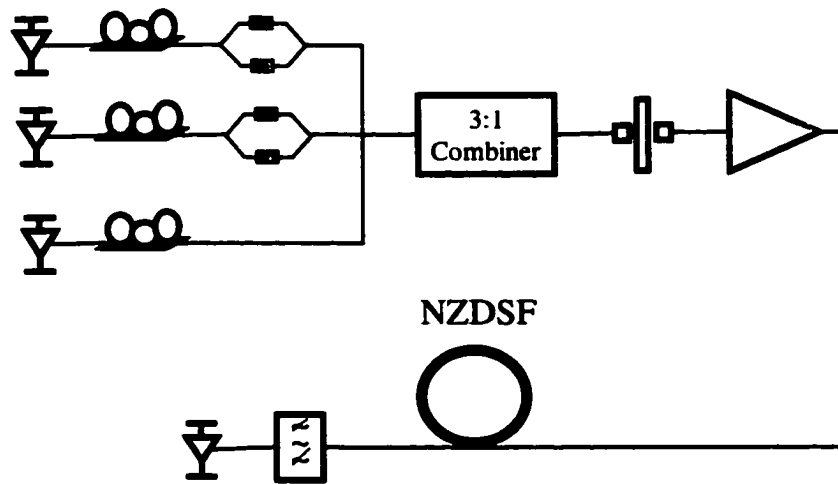


Figure 3.31: Schematic Diagram of the 3-Channel System for Examining the FWM Penalty

With a few assumptions, a simple analytical equation can be derived to reasonably predict the magnitude of FWM distortion in this 3-channel system. The first assumption is that the FWM-induced distortion is still relatively small compared to the signals, and hence the power of the signals is affected mainly by fiber attenuation. Second, similar to XPM, it is assumed that the chromatic dispersion does not significantly affect the signals within the fiber's nonlinear regime. The third assumption is that the 'walk-off' (i.e., difference in propagation speed) between channels is small. This assumption is reasonably acceptable for NZDSF, since the chromatic dispersion parameter, D , for NZDSF is about 4.2 ps/nm/km at 1550 nm. This means, for 20 km of fiber (for which nonlinear effects should occur), two neighboring channels with 50 GHz spacing would have a differential time delay of 33.6 ps (one third of the bit period). The final assumption is that both SPM and XPM can be ignored which will be justified from the comparison between the simulation results and the theoretical analysis shown later. With these assumptions, the coupled NLSE describing the FWM for the CW channel can be simplified into the following

$$\frac{\partial A}{\partial z} + \frac{\alpha}{2} A = -i\eta pqr^* e^{i\Delta\beta z} e^{-3\alpha z/2} \quad (3.21)$$

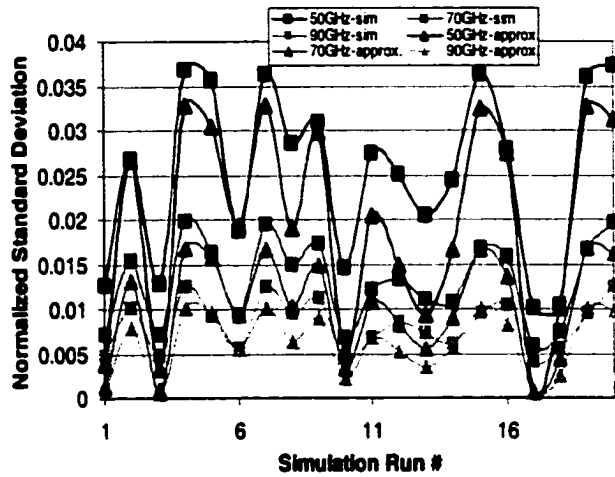
where p, q, r are the optical channels comprising the triplet; $\eta = 1$ if $p=q$ (for the case of a 3-channel system, $p=q$), otherwise $\eta = 2$; $\Delta\beta$ is equal to $\beta^p + \beta^q - \beta^r - \beta^{fwm}$ (β^{fwm} is

the propagation constant of the subject channel and β , β^i and β^j are the propagation constants for the constituent channels). The solution of the equation is,

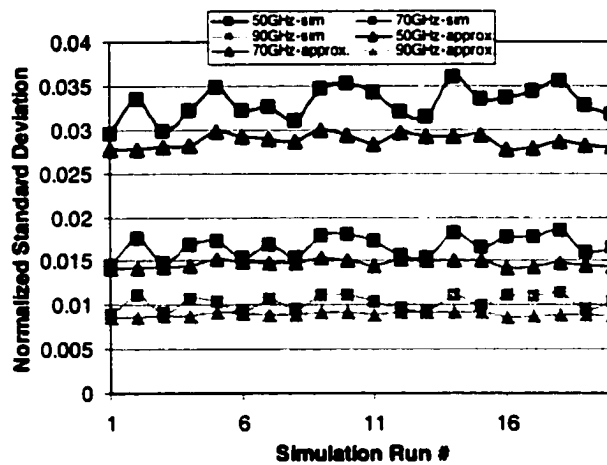
$$A_{fwm}(z, T) = \frac{-i\eta p q r^* (e^{i\Delta\beta z - \alpha z} - 1)e^{-\alpha z/2}}{i\Delta\beta - \alpha} \quad (3.22)$$

Equation (3.22) indicates that the magnitude of the FWM distortion is roughly inversely proportional to $\Delta\beta$ (the difference in propagation speed among channels), and hence the FWM should become stronger as the dispersion parameter D becomes smaller. Since the value of D is smaller for NZDSF than for SSMF, the FWM efficiency is higher for NZDSF than for SSMF. Also, (3.22) shows that the FWM distortion is directly proportional to the magnitude of the triplet.

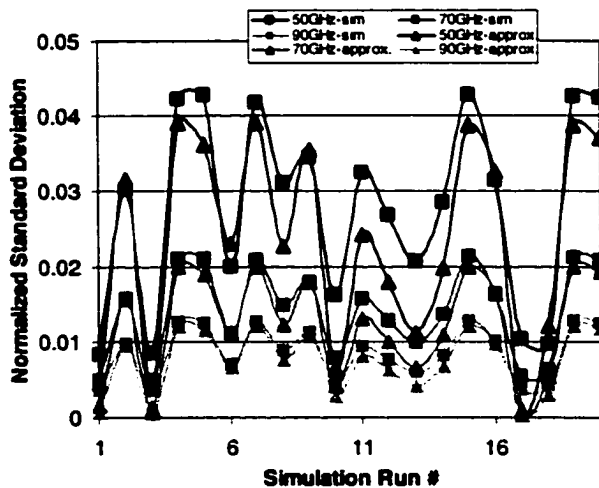
Figure 3.32 and **Figure 3.33** compare the 3-channel simulation results with the approximate analysis. A single-span of 160 km of NZDSF is used. The wavelength of the CW channel is 1550 nm, with the other two channels having longer wavelengths. Twenty simulation runs with random laser phase and relative time-delay were performed for each channel spacing and launch power setting. The normalized standard deviations shown in the figures were calculated after square-law detection and without any electrical filtering. **Figure 3.32** shows that the approximate equation predicts the simulation results reasonably accurately for each individual simulation run. It should be noted that the XPM distortion is always present in the simulations. **Figure 3.33** shows that after averaging over the 20 runs, the approximate equation always predicts the FWM penalty to be slightly less than the values from the simulations. This is likely because XPM is not taken into account.



(a) OOK



(b) OSSB



(c) Duobinary

Figure 3.32: Comparison between Simulations and Approximated Analysis for 3-Channel FWM Systems

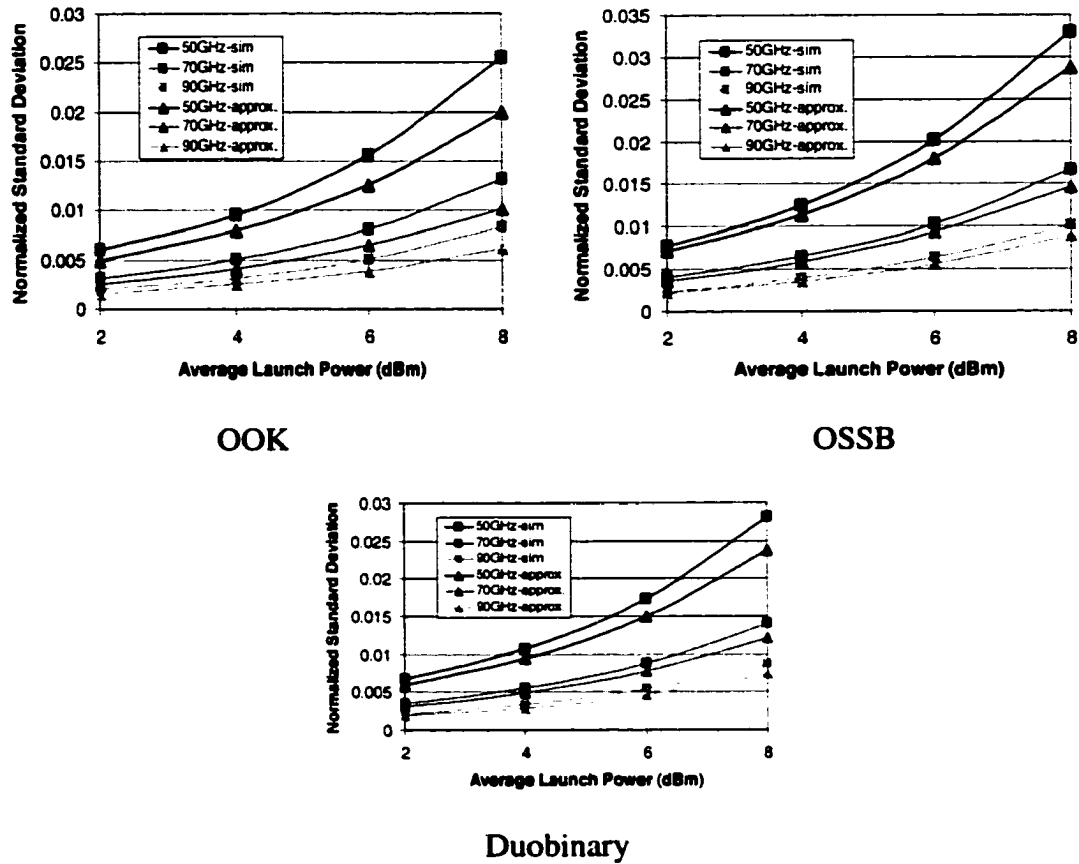


Figure 3.33: Comparison between the Simulations and Approximate Analysis for 3-Channel FWM Systems (each point is average over 20 simulation runs)

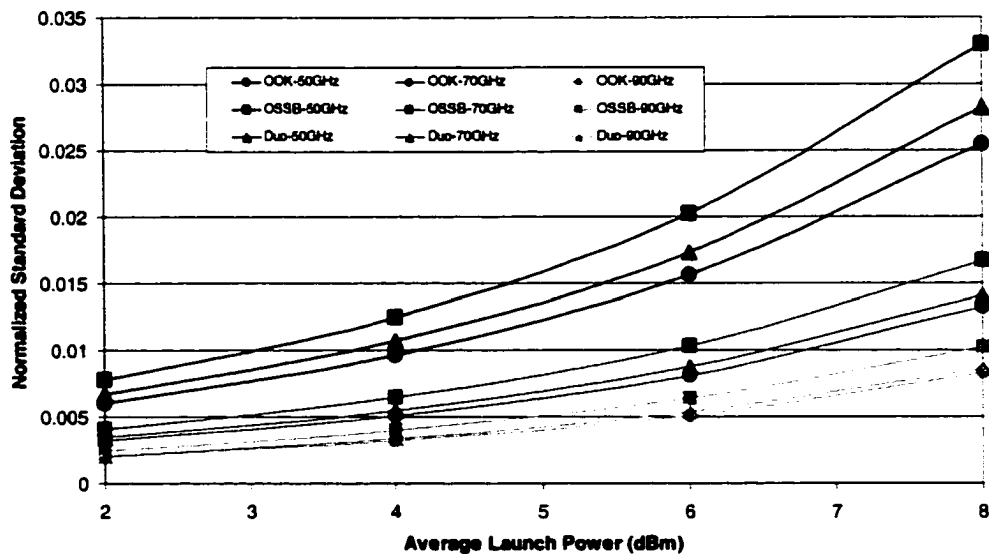


Figure 3.34: Comparison of the FWM Penalty between the Three Formats

Figure 3.34 combines the simulation curves of the three formats from **Figure 3.33** for a better comparison. It is evident from the figure that the OOK format has the least FWM penalty and the OSSB format has the most. As a side note, comparing the standard deviations shown in **Figure 3.34** to those shown in **Figure 3.26**, the standard deviations for the 3-channel system is about four times higher than the 2-channel system for 50 GHz spacing. This large increase in standard deviation is apparently due to the FWM effect. This shows that the dominant nonlinear effect for NZDSF with 50 GHz spacing is FWM. **Figure 3.32** shows that for all simulation runs, the FWM penalty for OSSB does not fluctuate much as compared to both the OOK and duobinary formats. Because of this, the averaged FWM penalty is higher for OSSB than the other two formats. Also from **Figure 3.32**, both the OOK and duobinary formats have very similar trends in the FWM penalty fluctuation, but the duobinary format always has slightly higher penalty than the OOK format. The explanation is given in the following paragraphs.

Equation (3.22) shows that the FWM distortion is approximately proportional to the triplets at the launching end. Thus, the difference in FWM distortion among these three formats could be explained by examining the difference in the triplets. **Figure 3.35** compares the magnitude of the product of the mixed optical triplets, their optical phase and the magnitude after the square-law detection. One distinct difference among the three formats is the optical phase of the signal. The phase (in the time domain) of the OOK format is constant, whereas the phase of the OSSB format varies continuously and the phase of duobinary formats varies discretely. The continuous phase variation of the OSSB format is due to the Hilbert transform, as mentioned before, and the discrete phase variation of duobinary format is due to the three-level signaling. Because of this optical phase difference, the square-law-detected magnitude of the triplets for both OSSB and duobinary formats have wider magnitude swing than the OOK format. Thus, the standard deviation of these two formats is higher than that of the OOK format.

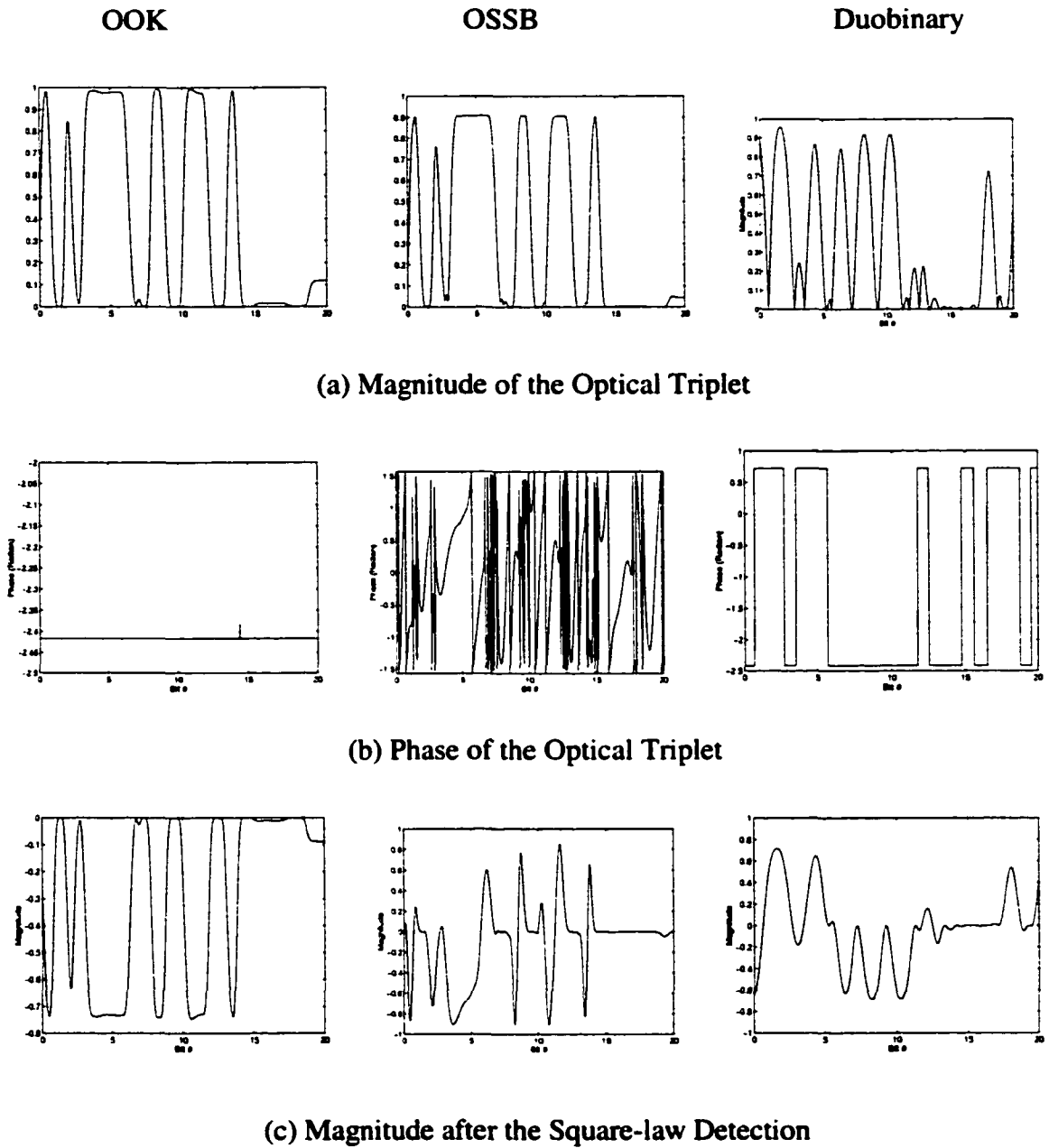


Figure 3.35: Difference in the FWM Triplets between the Three Formats

In addition, (3.22) shows another factor that causes OSSB format to have higher FWM penalty. In essence, the optical FWM distortion described by (3.22) is given by a complex constant multiplied by the triplet, for which (3.22) can be rewritten as

$$A_{fwm}(z, T) = |k|(\cos \theta + j \sin \theta)[\text{real}(\text{triplet}) + j * \text{imag}(\text{triplet})]$$

where both k and θ are constant. After the square-law detection (i.e., absolute square of the above expression), the FWM distortion can be written as

$$FWM = \sqrt{P_{cw}(z)}k \left[2\text{real}(\text{triplet})\cos(\Phi - \theta) - 2\text{imag}(\text{triplet})\sin(\Phi - \theta) \right] \quad (3.23)$$

where $P_{cw}(z)$ is the power of the CW channel at the end of the fiber link and Φ is the phase of the CW laser channel. The absolute square of the optical FWM distortion is usually small and can be ignored. Eq. (3.23) shows that if the triplet is a real signal, the FWM distortion term would become smaller as $(\Phi - \theta)$ increases from 0 to π . This is the case for both the OOK and duobinary formats. As for the OSSB format, due to the Hilbert transform, the OSSB triplet has both real and imaginary parts, and therefore the FWM distortion would not decrease as with the other two formats. Thus, statistically (when the laser phase is randomized), the FWM distortion of the OSSB format would not fluctuate as much as the other two formats. In practice, all three formats would become complex because of the SPM and chromatic dispersion. Nevertheless, the above discussion provides a first-order explanation.

To assess the FWM penalty in a realistic fiber system setting, let's examine a 5-channel system with single and multi-span configurations similar to those used in the previous section. NZDSF is used in the simulations to maximize the FWM distortion. From the discussion above, we know that both OSSB and duobinary have more FWM penalty for single-span configurations because of the signal phase. In a multi-span configuration, the two discrete signal phases (180° apart) could be a benefit for the duobinary format. This is due to partial cancellation of the triplets that are located on each side of the subject channel, as illustrated by a 5-channel system in **Figure 3.36** ($a*b^2$ and $d*c^2$ in the figure).

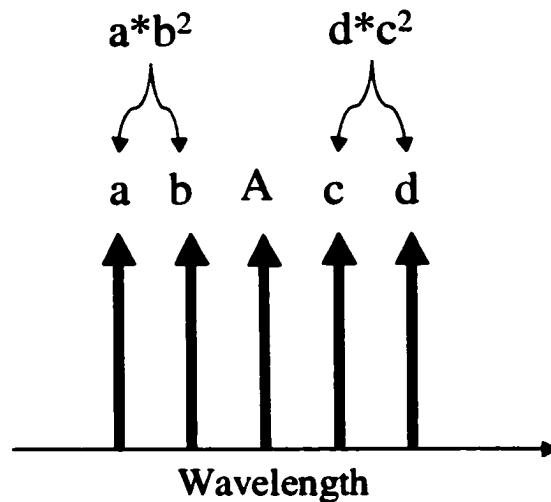
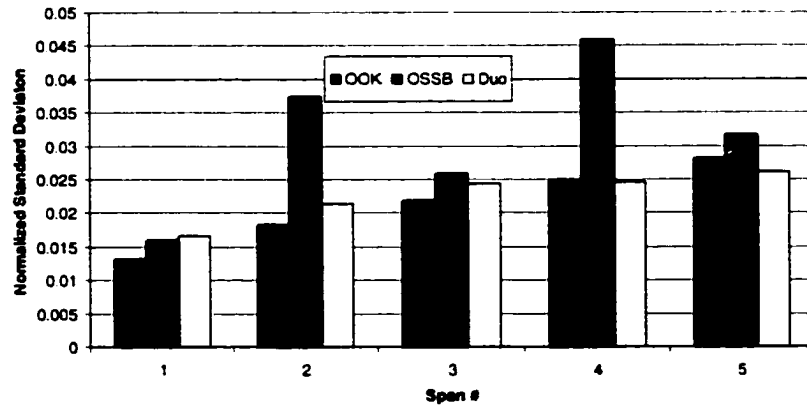
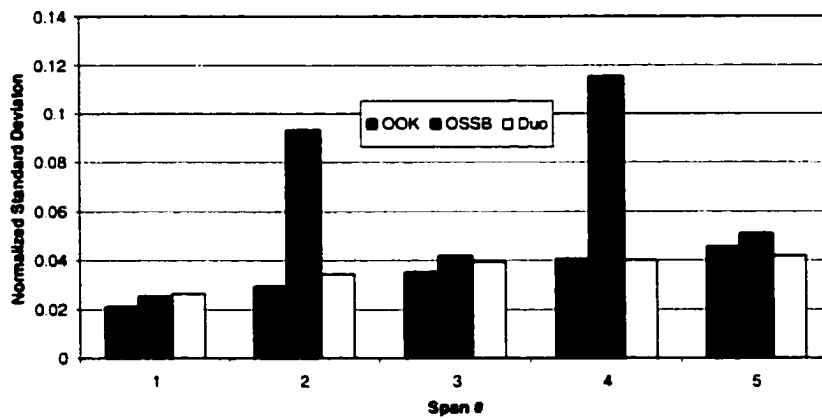


Figure 3.36: Illustration of the Two Degenerate FWM Triplets Mainly Responsible for the FWM Distortion in a 5-Channel WDM System using NZDSF

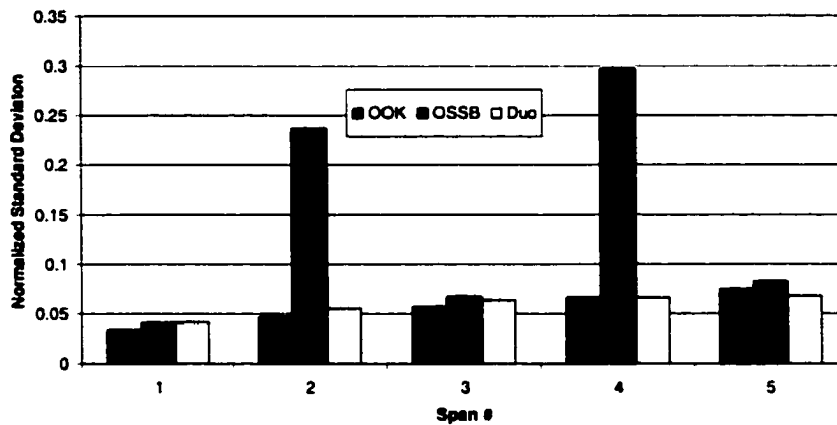
For this 5-channel example, the FWM distortion appearing in the center channel is generated most strongly at the beginning of each span where the optical power is at a maximum. Each of these FWM distortion terms would largely consist of the sum of the two triplets at each side of the center channel (assuming the distortion is still a small perturbation to the system). At the end of the fiber link, the total FWM distortion of the center channel would be mainly the sum of all these triplets from each span and from the channels at each side of the center channel. For the OOK format, whether the triplets are added up constructively or destructively largely depends on the relative phases of the mixing channels. Assuming the laser phases of the optical channels are constant with time, two triplets can cancel each other out if the resultant phase (sum of the laser phase from the mixing channels) of the two triplets is 180° out of phase. For the duobinary format, the 3-level signaling provides an additional 180° phase factor for cancellation. Thus the duobinary format should have a better chance of the triplets canceling each other out and hence the FWM distortion should be reduced. As for the OSSB format, the signal phase changes continuously with time, and it is not quite easy to predict the outcome of the summing of the FWM triplets. Simulations are therefore required to examine the FWM penalty.



(a) 2 dBm



(b) 4 dBm



(c) 6 dBm

Figure 3.37: Comparison of the 5-Channel FWM Induced Standard Deviation for Different Numbers of Spans (the power under each diagram denotes the average launch power per channel)

Figure 3.37 shows the 5-channel WDM simulation results. As expected, the standard deviation of the duobinary format increases at a slower rate than the other two formats. As the span number progresses to five, it is clear that the duobinary format has the least FWM noise at all launched power levels. On the other hand, the OSSB format has a larger FWM distortion than the other two formats. In addition, the OSSB format has a large fluctuation in standard deviation from one span to the next. The most probable cause is due to the continuous phase change of the signal due to the Hilbert transform. This phase change causes the summing of the FWM triplets to be very different from one span to the next one. This large degree of fluctuation does not actually occur for the OSSB format in an actual system, as explained in the next paragraph.

The discussion above assumes perfectly spaced channels, where the FWM distortion signals completely overlap the subject channel. In an actual system, however, the optical sources of the WDM channels can never perfectly stay at the nominal specified wavelength, and thus there is a minor fluctuation in the channel spacing from one pair of optical channels to the next pair. This turns out to be a benefit for the OSSB format, which suppresses the large fluctuation in FWM distortion. **Figure 3.38** illustrates how the FWM distortion differs at the center CW channel of a 5-channel system. The FWM distortion from the two triplets is slightly off from the carrier tune and causes the DC components of the distortion to be away from the CW channel carrier. The consequence of this is the sinusoidal modulation of the FWM distortion is illustrated in **Figure 3.39**, which compares two cases of the square-detected CW channel under the influence of the FWM triplets. It is evident that with a slight channel spacing difference, the shape of the FWM distortion is modulated by a low-frequency sinusoidal wave. In this particular example, the two channels on the long wavelength side of the CW channel are 3.9 MHz and 117 MHz away from the exact 50 GHz spacing, respectively. The channels on the short wavelength side have the exact channel spacing.

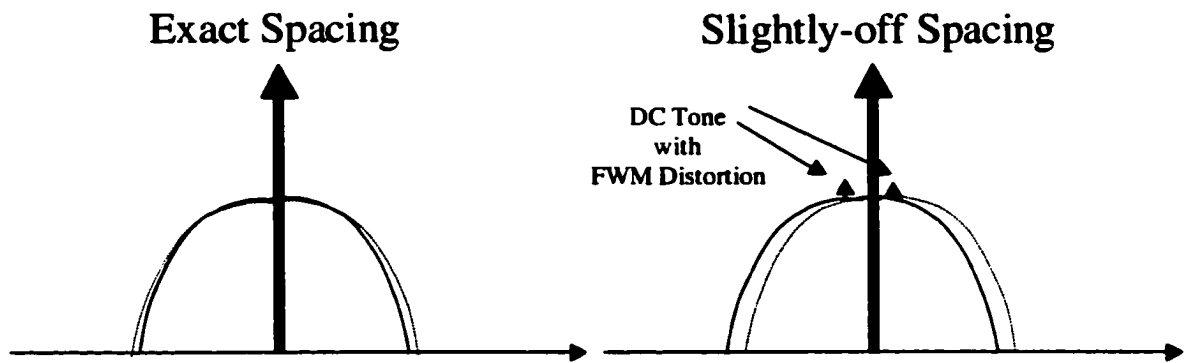


Figure 3.38: Illustration of the Sinusoidal-Modulation when the Channel Spacing is Not Exact for the 5-channel System.

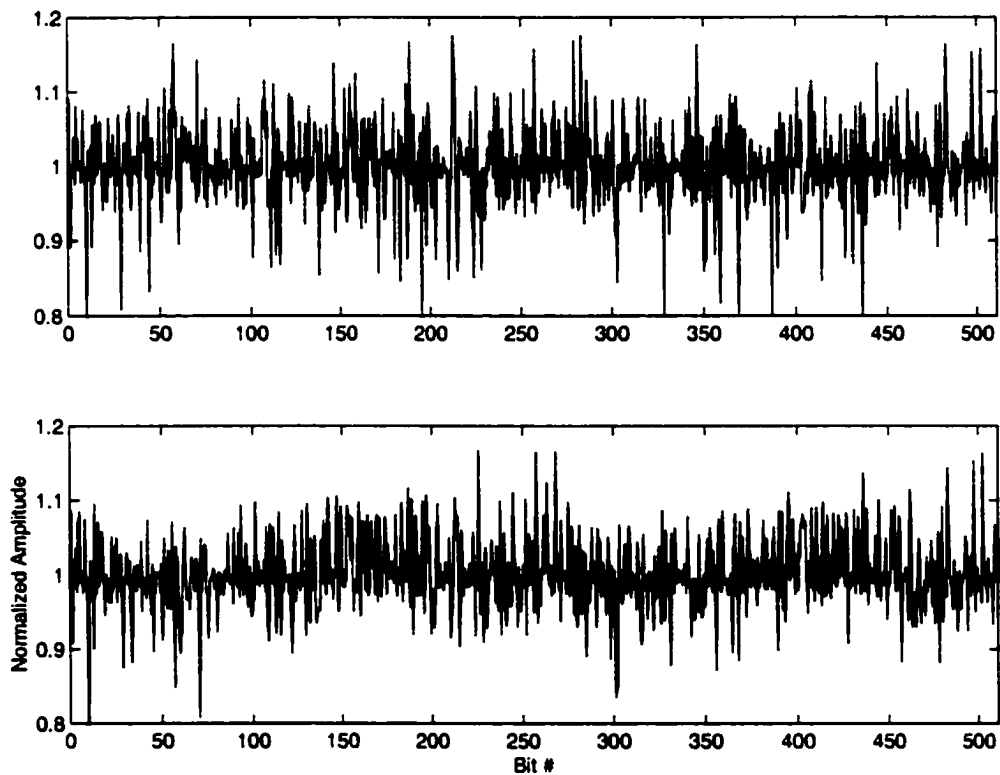
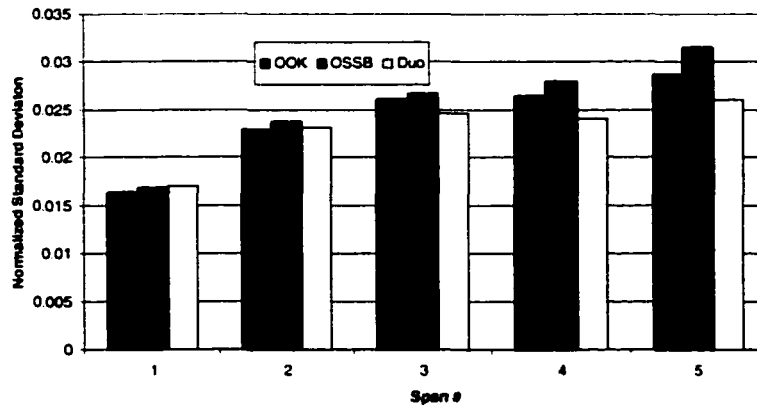
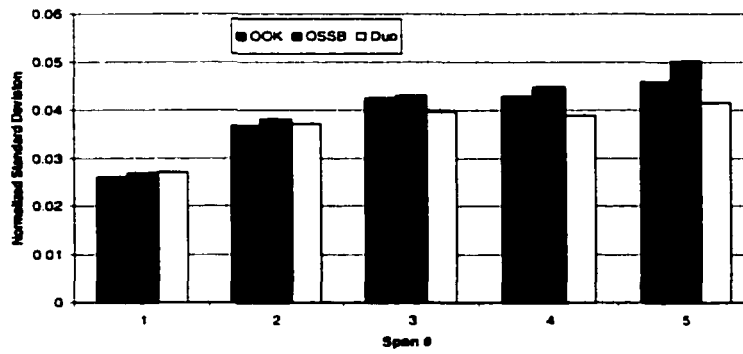


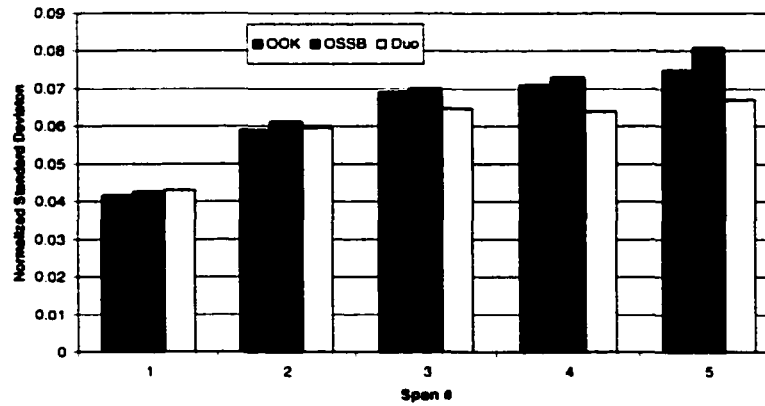
Figure 3.39: Comparison of the Square-detected CW Channel under the Influence of the FWM Triplets for Exact and Slightly-off Channel Spacing (top-exact spacing, bottom-slightly-off spacing)



(a) 2 dBm



(b) 4 dBm



(c) 6 dBm

Figure 3.40: Comparison of 5-Channel FWM Penalty for Different Numbers of Spans with Detuned Carrier Frequencies (power under each diagram denotes the average launch power per channel)

Figure 3.40 compares the FWM distortion with different launched power and numbers of spans for the three formats under the slightly-off channel spacing condition. It is evident from the figure that the sinusoidal modulation removes the large fluctuation in the OSSB FWM distortion. However, the OSSB format still has a slightly higher distortion than the other two formats. Moreover, the standard deviations for all three formats are almost the same as for the single-span configuration. The sinusoidal modulation increases the standard deviation of the OOK format.

In conclusion, for a single-span configuration the OOK format has slightly less FWM distortion. For multi-span configurations, the duobinary format has the least distortion due to the averaging effect. The OSSB format almost always has the highest FWM penalty due to the phase modulation from the Hilbert transform.

3.8. Full-Scale Short-haul Simulations

The previous sections discuss the various factors individually that affect the performance of the three different transmission formats. Yet full-scale simulations with all factors acting together are required in order to fully compare the system performance of these three transmission formats. This section focuses on the single-span configuration using two types of fibers. For 50 GHz channel spacing, the dominating nonlinear effects for SSMF and NZDSF are XPM and FWM, respectively. Moreover, in order to examine the performance of the three formats in an ultra-dense WDM system, 25 GHz-spaced systems are also simulated in addition to a state-of-the-art 50 GHz spaced system. Thirty-two optical channels are used in the simulations, which should be sufficient to truly reflect the penalty of various impairments mentioned in the previous sections that occur in systems with more channels. In order to clearly observe the penalty due to various nonlinear effects, the ASE noise is not included. The EDFAs used in the simulations are assumed to have an ideal response, which means that they introduce no amplitude distortion.

Figure 3.41 shows the schematic diagram of the single-span simulations. In order to accumulate sufficient statistics, 20 simulation runs are performed for each average launch power setting. For each run, the laser phase and relative time delay of each channel in the WDM system are randomly varied. A third-order Butterworth filter is

used for the optical filtering to isolate an individual channel before the square-law detection. Bandwidths of 25 GHz and 50 GHz are used for 25 GHz and 50 GHz-spaced systems respectively. After the detection, a third-order Butterworth filter with 8 GHz 3dB bandwidth is used to simulate the low-pass filtering due to the chain of signal amplification before reaching the BERT. To simulate the actual lasers, the wavelengths of the lasers were slightly off from the nominal wavelength spacing. For both 25 GHz and 50 GHz-spaced systems, the center wavelength of the entire WDM system is 1553 nm.

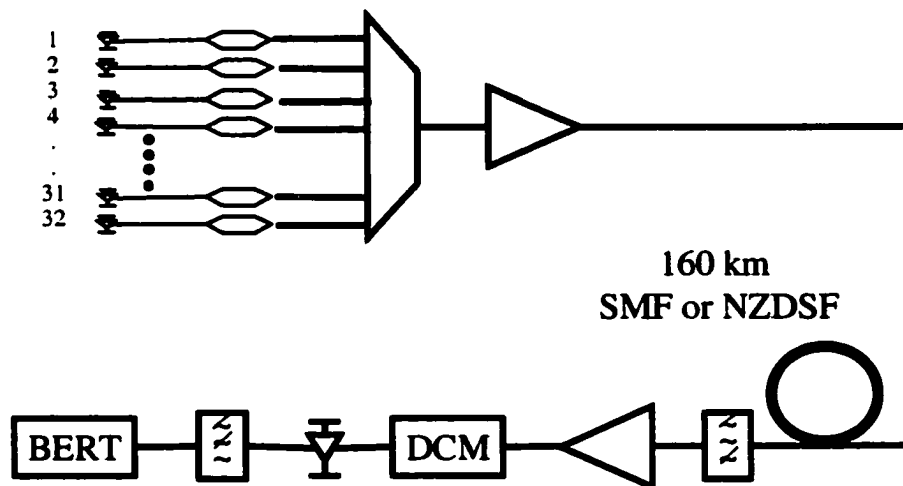


Figure 3.41: Schematic Diagram of the Single-span 32-Channel Simulations

Figure 3.42 depicts the averaged value of the ones and zeros of the 3-bit pattern (the center bit of the 3-bit pattern) mentioned in Chapter 2 for calculating the Q values. SSMF is used in this set of simulations. The values of the four ones in the 3-bit pattern are the four curves on top of each diagram; similarly the four zeros are the four curves at the bottom of each diagram (the curves are very close to each other and appear to be less than four). The DCM is optimized until the Q values are maximized. The carrier frequencies of the channels increase as the channel number increases. As expected, the duobinary format has lower amplitudes for the ones due to the low-pass filtering. The OSSB format has slightly higher values for the ones due to the slightly larger modulation depth.

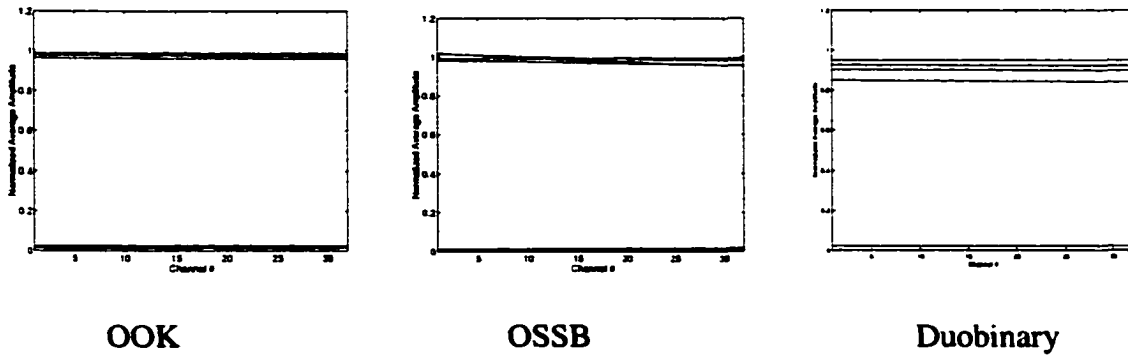


Figure 3.42: Comparison of the Average Amplitude of the '1's and '0's in 3-bit Patterns (1 span, 50 GHz spacing, SSMF, 6 dBm average launched power)

Figure 3.43 shows the average standard deviation (averaged over 20 simulation runs) of each of the 3-bit pattern, for all 32 channels, with a 6 dBm average launched power per channel. As expected, the duobinary format has less XPM penalty and the standard deviations of the ones are less than for the other two formats. The standard deviations of the OSSB and OOK formats are very close to each other. The standard deviations of the zeros are much smaller than the ones; thus, the Q value is mainly determined by the standard deviation and the average value of the '1's. Also, it should be noted that the standard deviation is less for the edge channels because the edge channels have fewer neighboring channels on one side and hence the XPM distortion is less.

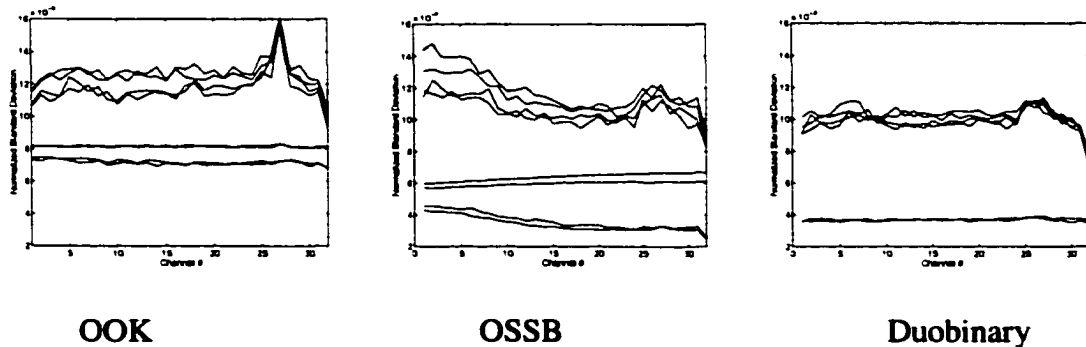


Figure 3.43: Comparison of the Normalized Standard Deviation of the '1's and '0's in 3-bit Patterns (1 span, 50 GHz spacing, SSMF, 6 dBm average launched power)

Figure 3.44 shows the average Q value for all channels. Table 3.2 shows the average Q values and the standard deviation over the 32 channels. The left value inside each box in the table is the average value and the right value is the standard deviation.

The OSSB format has a higher Q value than the other two formats because of the higher value of the ones (and thus a larger eye opening). The smaller noise variance of the duobinary signals does not compensate for the smaller eye opening and the Q values are still lower than the other two formats. Moreover, the rising trend of the Q value with increasing channel number of the OSSB format is likely due to the residual chromatic dispersion since the DCM does not compensate for the dispersion slope. The OSSB format is more sensitive to the residual chromatic dispersion than the other two formats, as mentioned.

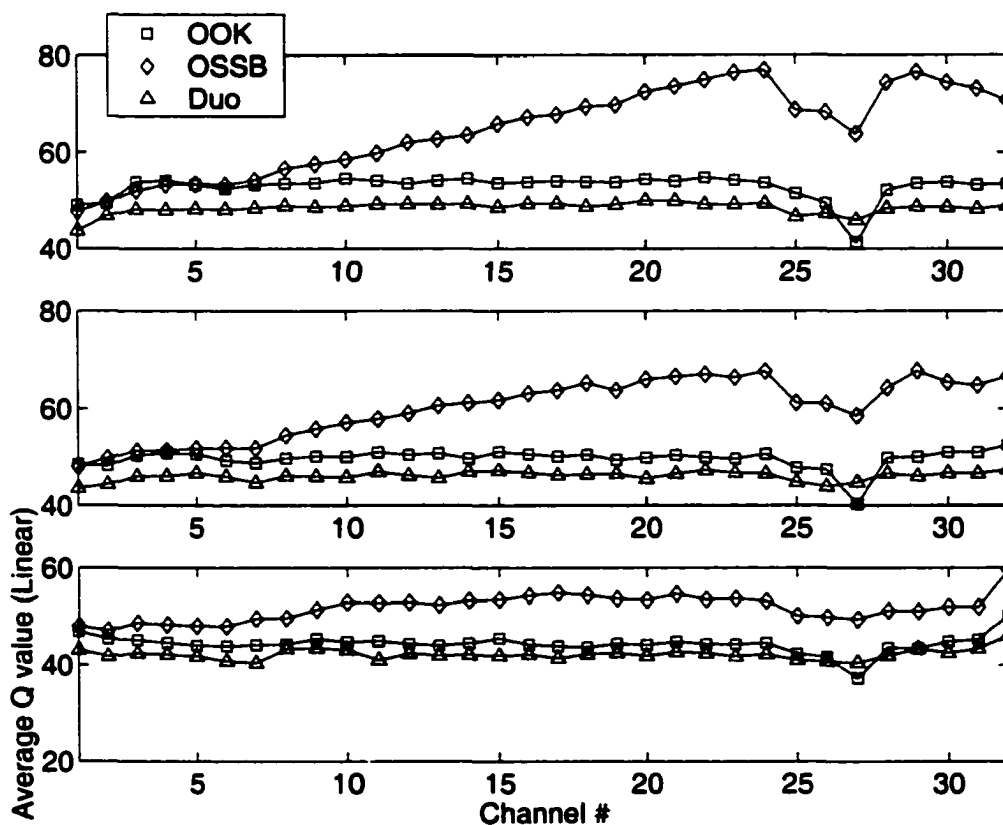


Figure 3.44: Comparison of Q value at Different Average Launched Power Level (1 Span, 50 GHz spacing, SSMF) [top 2dBm, middle 4 dBm, bottom 6 dBm]

Figure 3.45 shows the standard deviation of the Q values across the channels calculated from 20 simulation runs. This figure shows that the value of the standard deviation is just over 2.0 for all three formats and over all power levels. It also shows that 20 simulations are sufficient to accumulate a statically significant amount of data.

Launch Power	OOK	OSSB	Duobinary
2	52.8 \pm 2.52	68.7 \pm 7.40	48.4 \pm 1.22
4	49.7 \pm 1.96	62.0 \pm 4.10	46.2 \pm 1.00
6	44.3 \pm 1.87	51.8 \pm 2.63	42.2 \pm 1.10

Table 3.2: Average Q over 32 Channels (1 span, SSMF, 50 GHz spacing)

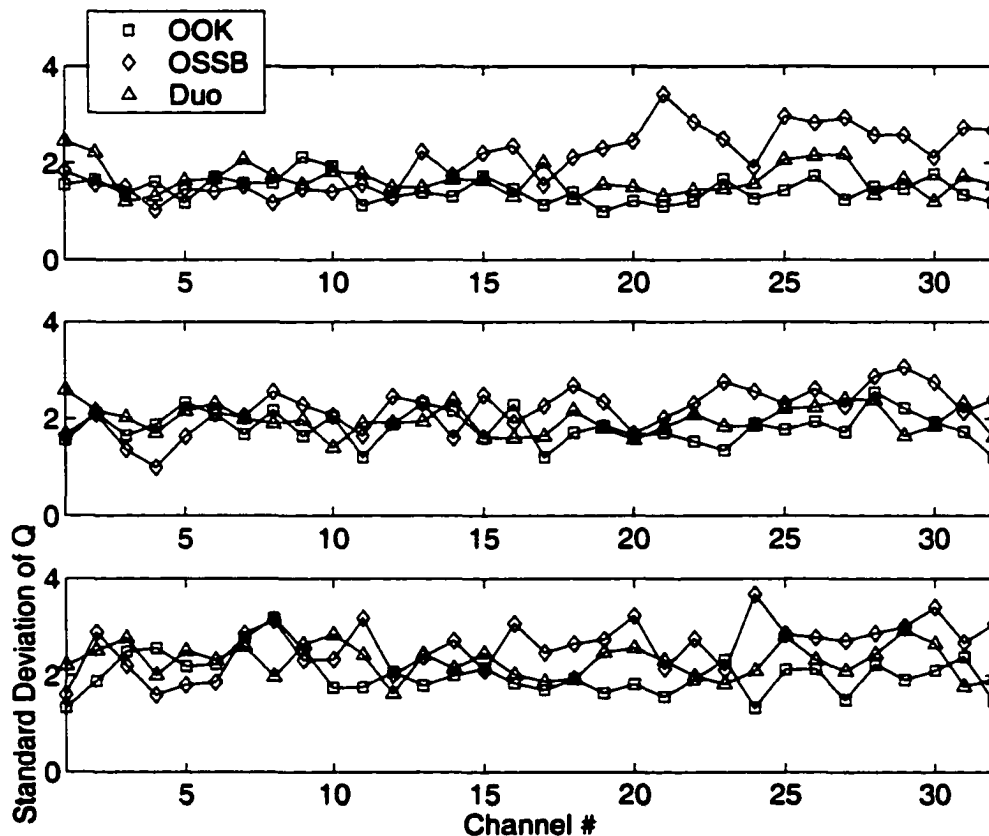


Figure 3.45: Comparison of the Standard Deviation of Q at Three Different Average Launched Power Levels (1 Span, 50 GHz spacing, SSMF) [top 2 dBm, middle 4 dBm, bottom 6 dBm]

For the NZDSF, Figure 3.46 shows the standard deviation of the ones and zeros of the 3-bit patterns with a 6 dBm average launched power per channel. The values are almost identical for all three formats, which agrees with the discussion in the previous section. As shown, the dominating distortion is from FWM. As suggested by the 5-channel simulations, the FWM penalty from all three formats is about the same for the

single-span configuration. Hence, the standard deviations of all formats are about the same.

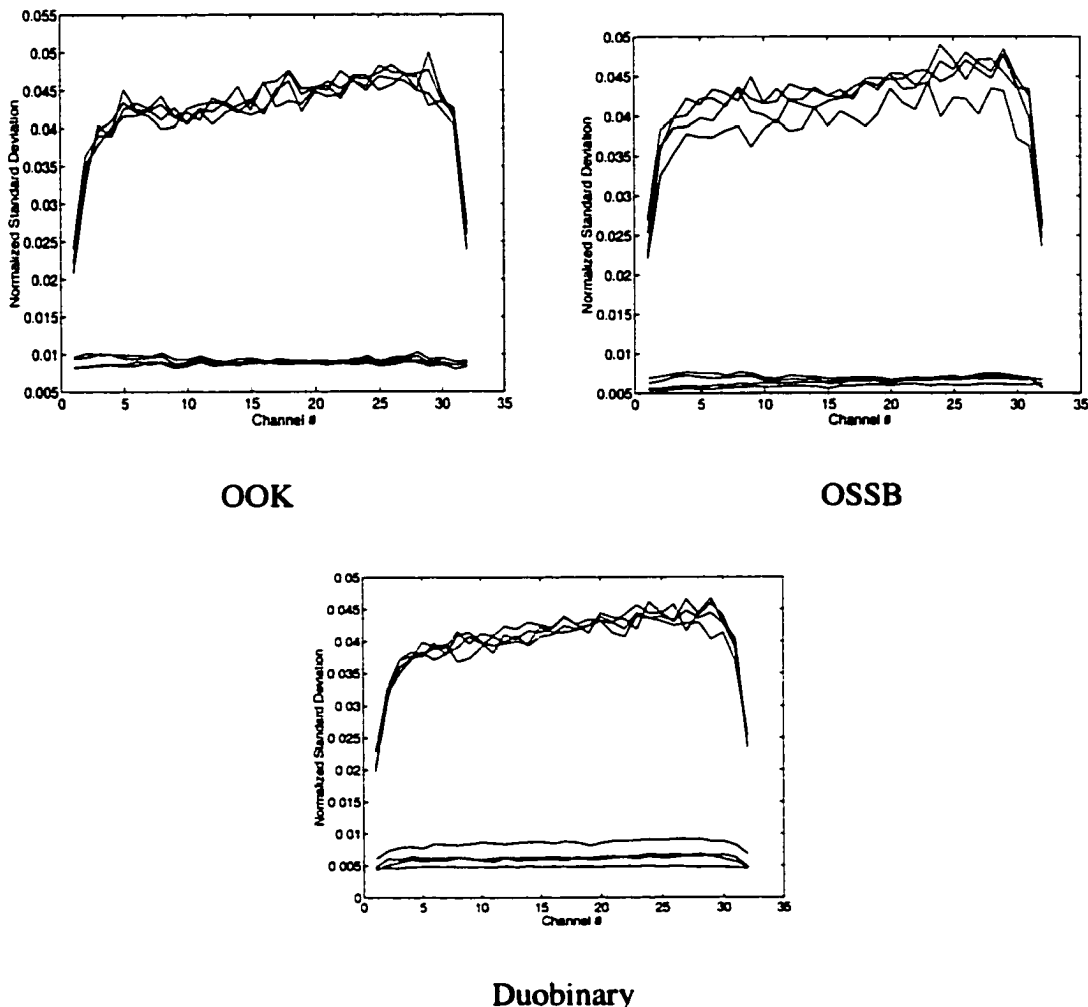


Figure 3.46: Comparison of the Normalized Standard Deviation of the ‘1’s and ‘0’s in 3-bit Patterns (1 span, 50 GHz spacing, NZDSF, 6dBm average launched power)

Figure 3.47 shows the average Q values of all 32 channels. Table 3.3 displays the average Q values over 32 channels. The nonlinear noise is significantly higher than those results with SSMF because of the stronger FWM effect. Because of this effect, the ratio of the average values to the standard deviation of the ‘1’s becomes closer for all three formats. Hence the separation of the Q values becomes smaller for the three formats. Nevertheless, Table 3.3 shows that the OSSB format still has a slight benefit over the other two formats because of the larger eye opening.

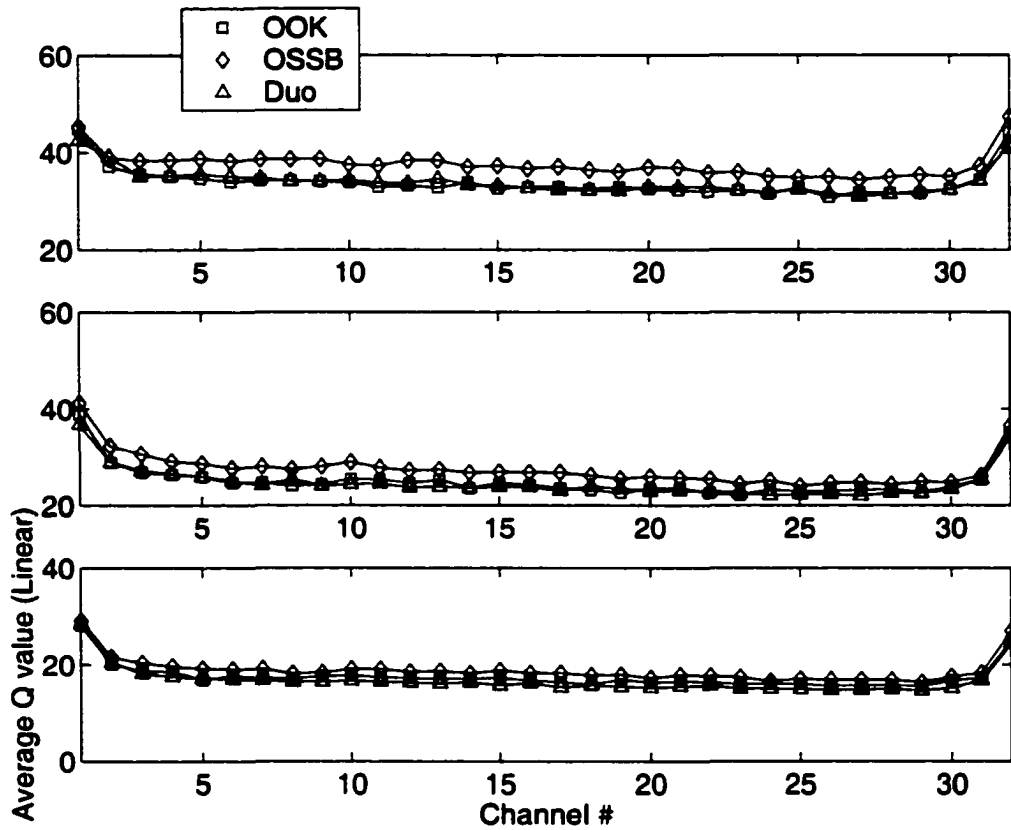


Figure 3.47: Comparison of the Q Values at Different Average Launched Power Levels (1 Span, 50 GHz spacing, NZDSF) [top 0 dBm, middle 2 dBm, bottom 4 dBm]

Launch Power	OOK	OSSB	Duobinary
2	33.8 3.04	37.5 2.65	33.9 2.63
4	25.0 3.43	27.5 3.50	24.7 3.18
6	17.5 2.56	18.8 2.62	16.7 2.79

Table 3.3: Average Q over 32 Channels (1 span, NZDSF, 50 GHz spacing)

Figure 3.48 depicts the normalized standard deviation of the ones and zeros for a 25 GHz-spaced system using SSMF with a 2 dBm average launched power per channel. As expected, the OSSB format has the highest noise level because this format is most vulnerable to channel cross talk. Moreover, the channels at the two edges of the WDM spectrum have less noise since they receive less cross talk because no channel is present on one side.

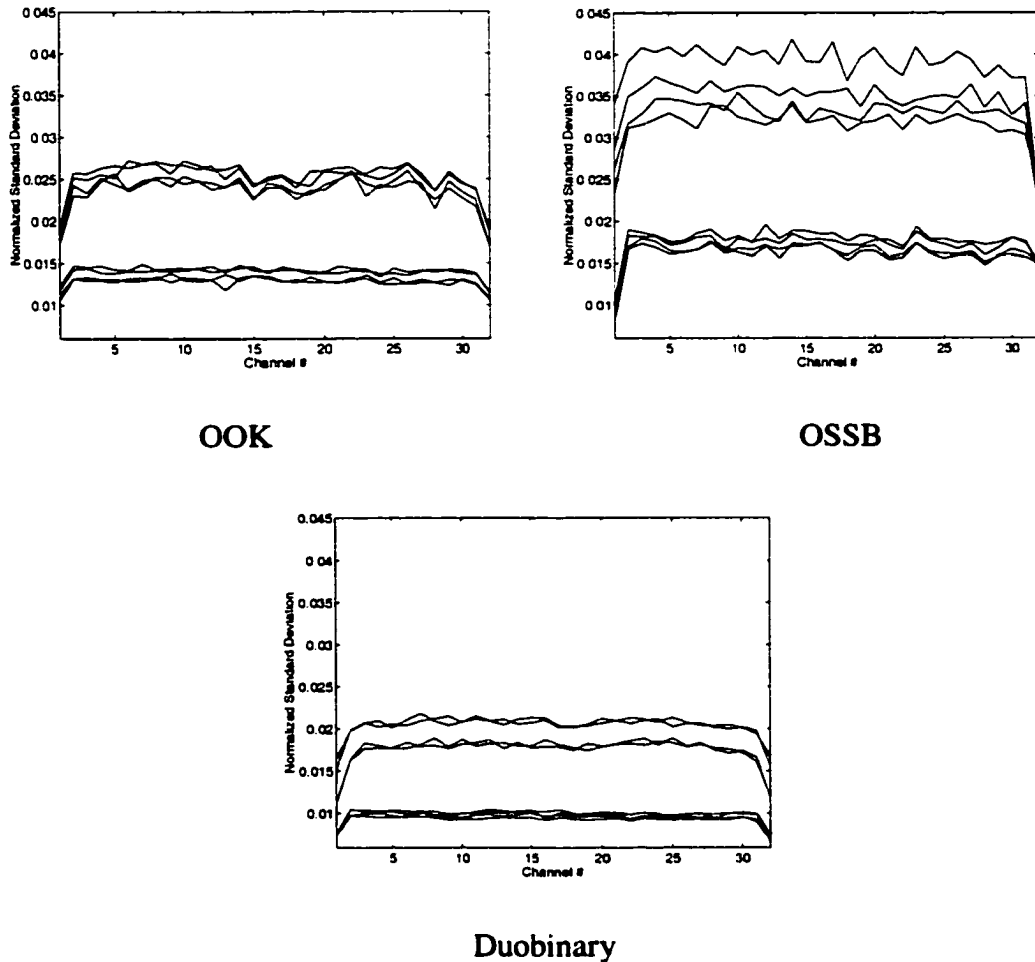


Figure 3.48: Comparison of the Normalized Standard Deviation of the ‘1’s and ‘0’s in 3-bit Patterns (1 span, 25 GHz spacing, SSMF, 6 dBm average launched power)

Figure 3.49 shows the average Q values for three different launched power levels. As shown in the figure, at a low launched power level (2 dBm), the cross talk is the dominating noise source and the OSSB format suffers the most. As the launched power increases to 6 dBm, the nonlinear effects become more significant and the Q-value difference becomes lower for all three formats. As shown in **Table 3.4**, the average Q values over the 32 channels becomes closer for all three formats. The smaller eye opening of the duobinary format is compensated for by the better cross talk performance at the low launched power level. At a high launched power level, the duobinary format has a slight benefit because the XPM penalty is less. It should be noted that for this channel spacing, the FWM is also an important noise source.

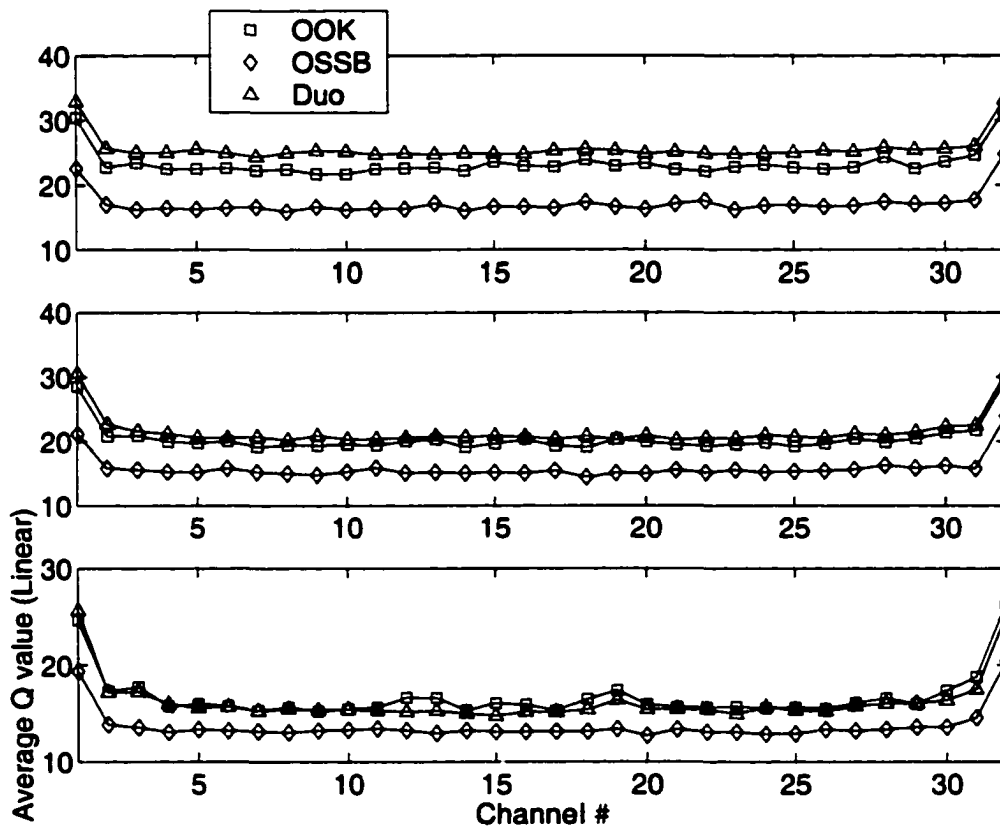
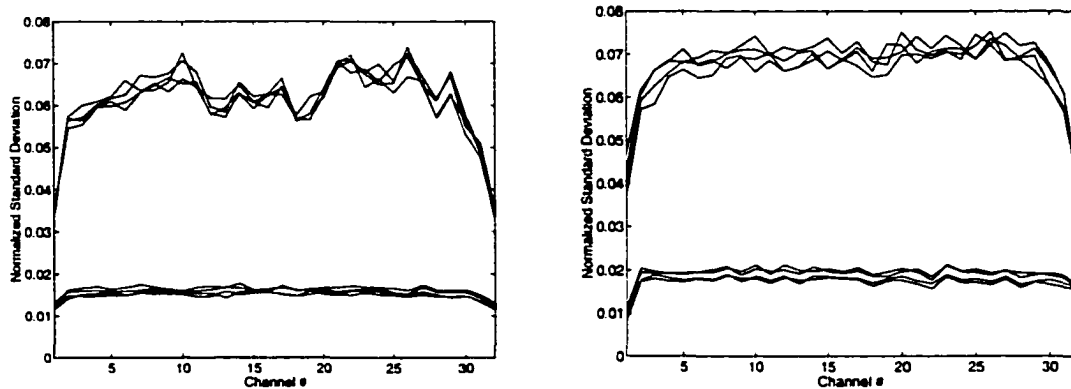


Figure 3.49: Comparison of Q values at Different Average Launched Power Levels (1 Span, 25 GHz spacing, SSMF) [top 2dBm, middle 4 dBm, bottom 6 dBm]

Launch Power	OOK	OSSB	Duobinary
2	23.3\2.07	17.1\1.77	25.6\1.94
4	20.5\2.30	15.8\1.82	21.5\2.42
6	16.7\2.42	13.7\1.64	16.3\2.44

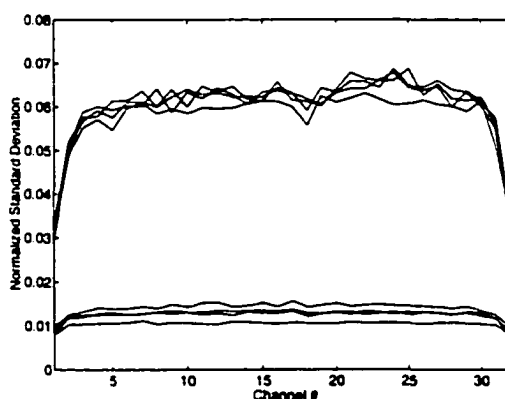
Table 3.4: Average Q over 32 Channels (1 span, SSMF, 25 GHz spacing)

Figure 3.50 compares the normalized standard deviation of the ones and zeros for the 32-channel 25 GHz-spaced system using NZDSF at 2 dBm average launch power per channel. For this system configuration, the dominating noise source is the FWM. The FWM distortion is so strong that the Q value drops to less than 12 at 2 dBm launched power, as shown later. Because of this, the standard deviations are very similar for all three formats. The OSSB format has a slightly higher noise penalty because it still suffers more from cross talk.



OOK

OSSB



Duobinary

Figure 3.50: Comparison of the Normalized Standard Deviation of the ‘1’s and ‘0’s in 3-bit Patterns (1 span, 25 GHz spacing, NZDSF, 6 dBm average launched power)

Figure 3.51 and Table 3.5 shows the average Q_s of the 32 channels and the average Q over 32 channels, respectively, at two launched power levels. The Q value of OSSB format is less than the other two formats at low power levels. At high power levels, all three formats have about the same Q values.

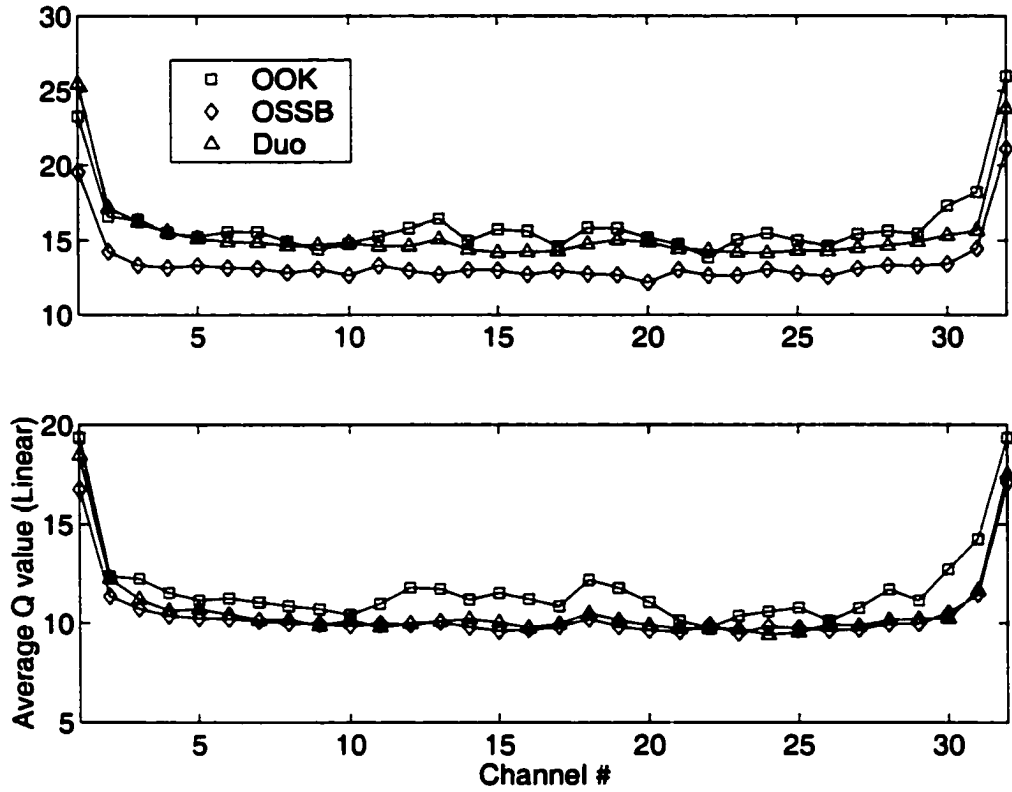


Figure 3.51: Comparison of the Q Value at Different Average Launched Power Levels (1 Span, 25 GHz spacing, NZDSF) [top 0 dBm, bottom 2 dBm]

Launch Power	OOK	OSSB	Duobinary
0	16.1/2.38	13.5/1.85	15.4/2.46
2	11.8/2.13	10.5/1.72	10.7/1.97

Table 3.5: Average Q Over 32 Channels (1 span, NZDSF, 25 GHz spacing)

3.9. Full-Scale Terrestrial System Simulations

The simulations for full-scale terrestrial systems use the same system configuration as mentioned in section 3.6. Five spans of 90 km of fiber are used. The span-by-span dispersion compensation is 10% under-compensated. The 50-50 pre- and post-compensation is employed. To simulate the actual DCM, the dispersion slope of the compensator is set to zero. The optical and electrical filters are the same as those used in the previous section.

Figure 3.52 compares the average Q values of the 32 channels for a 5-span WDM system using SSMF and 50 GHz channel spacing. Differing from the single-span system, the edge channels have less Q value than the center channels. This is simply due to more residual dispersion at both sides of the WDM spectrum because the dispersion compensator does not compensate for the dispersion slope, as mentioned. At a launched power of 0 dBm, the OSSB format has a better Q value. This is because the nonlinear effect is not significant (evident from the high Q value), and the eye opening of the OSSB format is larger. Similar to the single-span configuration, as the launched power increases, the gap between different formats reduces because the nonlinear effects increase. The duobinary format suffers less XPM penalty and the Q-value difference becomes lower. The average Q values over 32 channels are summarized in **Table 3.6**.

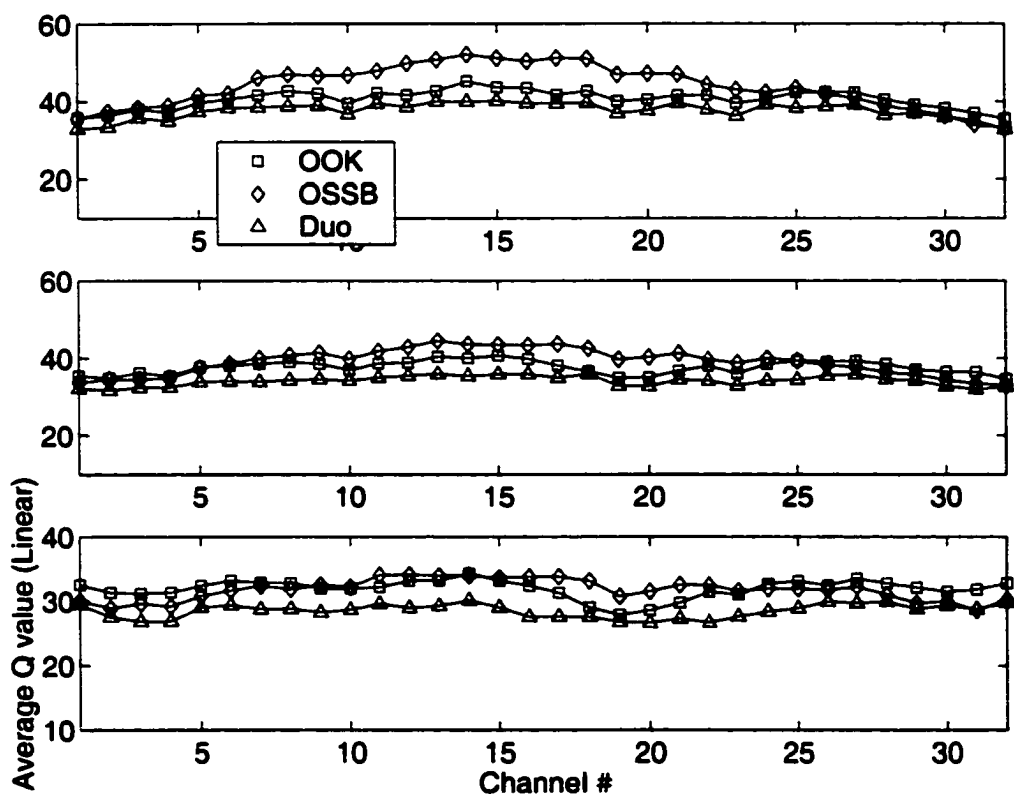


Figure 3.52: Comparison of Q Values at Different Average Launched Power Levels (5 Span, 50 GHz spacing, SSMF) [top 0 dBm, middle 2 dBm, bottom 4 dBm]

Launch Power	OOK	OSSB	Duobinary
0	40.52.37	43.85.46	37.62.06
2	37.61.74	39.03.37	34.11.28
4	31.91.43	31.71.60	28.51.07

Table 3.6: Average Q over 32 Channels (5 span, SSMF, 50 GHz spacing)

Figure 3.53 compares the Q values for the system using NZDSF and 50 GHz spacing. Since the chromatic dispersion of the NZDSF is only about 25% of that for SSMF, the residual dispersion that the edge channels suffer is much less than that of the SSMF system. Thus, the Q values for the edge channels are not very different from those of the center channels. The Q-value ripple across the 32 channels is possibly due to the FWM effect, which causes the signal power to vary among channels. Compared to the single-span configuration, the Q-value curves of the three formats for the terrestrial configuration are even closer to each other. As mentioned, the FWM penalty of the duobinary format is relatively less for a multi-span system because of the averaging effect. The smaller eye opening of the duobinary format is compensated for by the smaller FWM effect. On the other hand, the OSSB format has a slightly higher FWM penalty than the OOK format. The larger eye opening of the OSSB format is offset by the slightly higher FWM distortion. Thus, the Q-value curves of the three formats are very close to each other. The average Q values over 32 channels are summarized in **Table 3.7**.

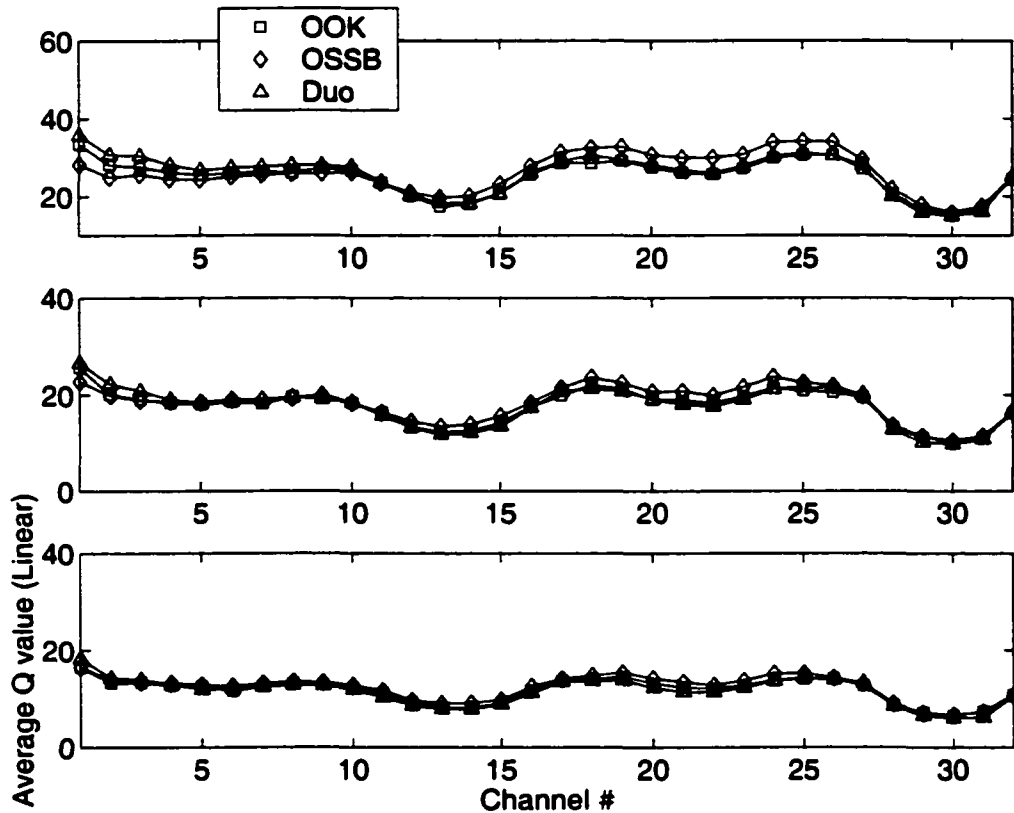


Figure 3.53: Comparison of Q value at Different Average Launched Power Levels (5 Span, 50 GHz spacing, NZDSF) [top 0 dBm, middle 2 dBm, bottom 4 dBm]

Launch Power	OOK	OSSB	Duobinary
0	25.2/4.48	26.2/4.96	25.9/5.03
2	17.7/3.57	18.4/3.62	17.7/3.96
4	11.7/2.42	12.3/2.56	11.5/2.72

Table 3.7: Average Q over 32 Channels (5 spans, NZDSF, 50 GHz spacing)

Figure 3.54 compares the Q values for systems with SSMF and 25-GHz channel spacing. As with the single-span configuration, the channel cross-talk is the dominating noise source for low launched power, and thus the duobinary format performs better. As the launched power increases, both cross talk and nonlinear effects become equally important. The duobinary format has only a slight advantage over the other two formats and this advantage is offset by its smaller eye opening. Because of this, the Q-value

curves for the three formats are close to each other at a high launched power. The average Q values over 32 channels are summarized in **Table 3.8**.

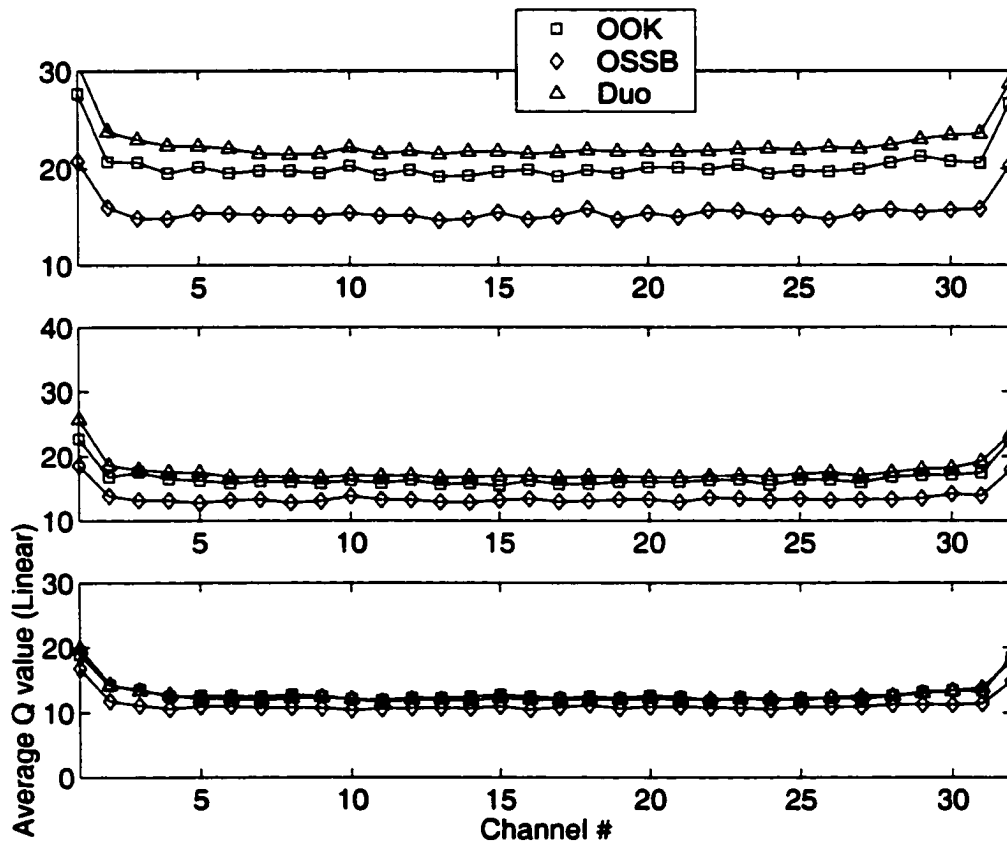


Figure 3.54: Comparison of Q Values at Different Average Launched Power Levels (5 Span, 25 GHz spacing, SSMF) [top 0 dBm, middle 2 dBm, bottom 4 dBm]

Launch Power	OOK	OSSB	Duobinary
0	20.4/1.82	15.6/1.33	22.6/2.02
2	16.6/1.62	13.6/1.24	17.7/1.91
4	12.9/1.56	11.2/1.26	12.8/1.68

Table 3.8: Average Q over 32 Channels (5 span, SSMF, 25 GHz spacing)

Lastly, **Figure 3.55** compares the Q values for systems with NZDSF and 25-GHz channel spacing. As in the 50 GHz-spaced system, the FWM effect is the dominating noise source. The duobinary format has a slight advantage over the other two formats, but this is again offset by the smaller eye opening. The net result, as shown in the

figure, is that the Q-value curves of the three formats are very close to each other. The average Q values over 32 channels are summarized in **Table 3.9**.

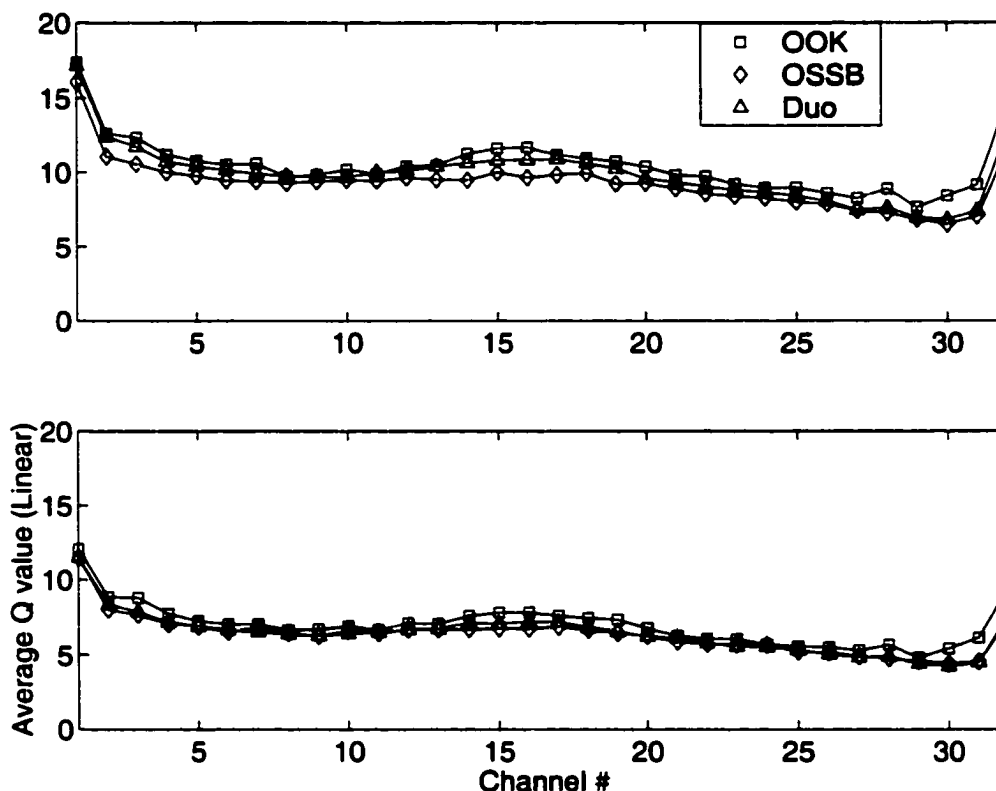


Figure 3.55: Comparison of the Q Values at Different Average Launched Power Levels (5 Span, 25 GHz spacing, NZDSF) [top 0 dBm, middle 2 dBm]

Launch Power	OOK	OSSB	Duobinary
0	10.5\1.86	9.3\1.67	9.9\1.95
2	7.0\1.40	6.4\1.29	6.4\1.37

Table 3.9: Average Q over 32 Channels (5 span, NZDSF, 25 GHz spacing)

3.10. OC-768 line-rate Simulations

The next generation of the fiber optic system will have a transmission rate of at least 40 Gbits/s. This is referred to as the OC-768 system. A state-of-the-art OC-192 system has channel spacing of 50 GHz [24]. With this channel spacing, the spectral efficiency is 20%. The proposed OC-768 system can have a spectral efficiency of 40%,

which translates into 100 GHz channel spacing. The obvious advantage of the OC-768 is the increase in spectral efficiency, which translates into higher data capacity. Another benefit of the OC-768 system is the reduction in nonlinear effect. With its higher spectral efficiency, the OC-768 system actually has wider channel spacing, which reduces both XPM and FWM distortion. The major disadvantage of this new system is the requirement of higher signal power and the tighter requirement for dispersion compensation.

The signal spectrum of the OC-768 signal is four times larger than that of the OC-192 system. This means the ASE noise within the signal spectrum is four times that of the OC-192 system. Thus, to maintain the same signal-to-noise ratio, the ASE noise needs to be suppressed to 25% of that of the OC-192 system or to increase the signal power by four times. Moreover, due to the much wider spectrum, pulse spreading increases much faster with dispersion in the OC-768 system as compared to in an OC-192 system. The challenge is not simply to accurately compensate for the dispersion, but to fabricate a device that can compensate for both dispersion and dispersion slope. As mentioned above, most of current DCMs do not compensate for the dispersion slope, which is still acceptable for the OC-192 system as shown by the simulations in the previous two sections. The DCMs for OC-768 systems, on the other hand, must be able to compensate for the dispersion slope to ensure that the residual dispersion of the edge channels in the WDM system is reduced to an acceptable level. This section assumes that the DCM can perfectly compensate for the dispersion slope and on that basis the performance of the three transmission formats in this proposed system is investigated.

Both single-span and 5-span terrestrial systems are simulated. Sixteen channels with 100 GHz spacing were used. The center wavelength of the WDM system was fixed at 1553 nm. As mentioned, the DCM was assumed to be able to compensate for the dispersion slope. Both optical and electrical filters were again assumed to be of the Butterworth type. The optical and electrical filters were taken to have 3dB bandwidths of 100 GHz and 32 GHz (80% of the transmission rate), respectively. Again, ASE noise was not included in the simulation.

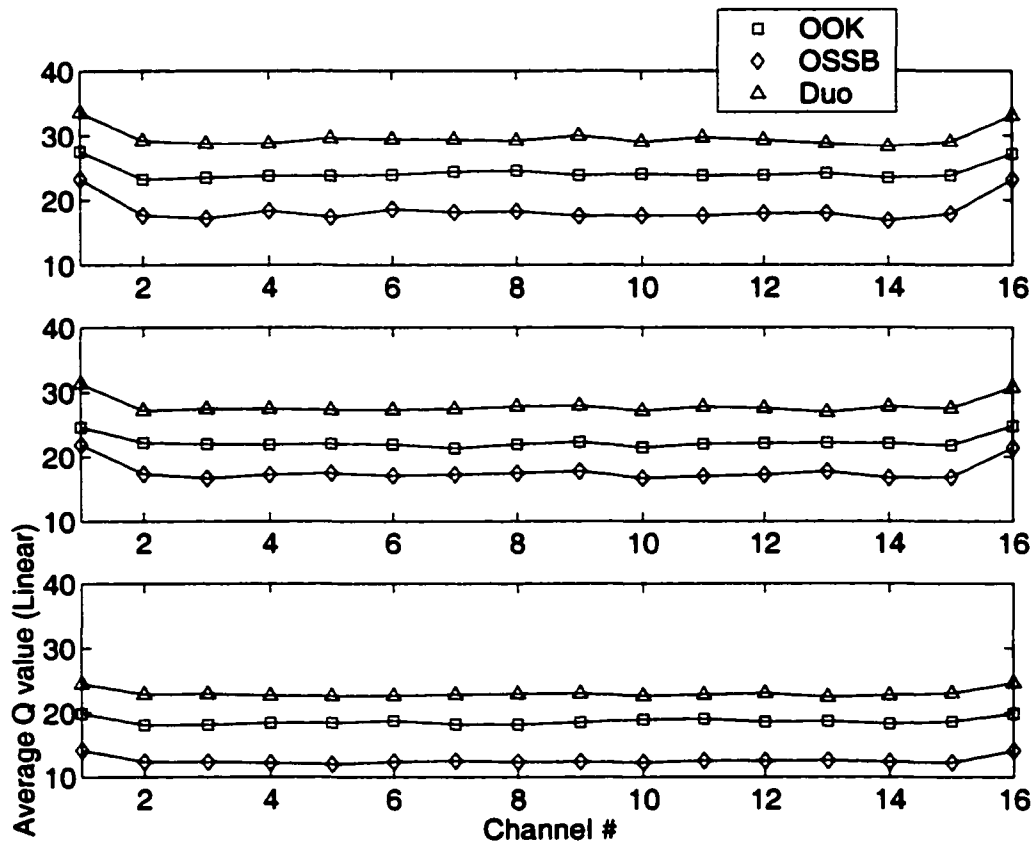


Figure 3.56: Comparison of Q Values at Different Average Launched Power Levels (1 Span, 100 GHz spacing, SSMF) [top 2 dBm, middle 4 dBm, bottom 6 dBm]

Launch Power	OOK	OSSB	Duobinary
2	24.3\1.19	18.5\1.85	29.7\1.44
4	22.3\0.94	17.7\1.52	27.9\1.22
6	18.7\0.53	15.8\0.95	23.0\0.63

Table 3.10: Average Q over 32 Channels (1 span, SSMF, 100 GHz spacing)

Figure 3.56 compares the average Q values of the single-span 16-channel systems with SSMF. It should be noted that the simulations do not include the ASE noise. Thus, the calculated Q values are only due to the nonlinear effects of the fiber. With 40% spectral efficiency, cross talk becomes one of the main distortion sources. As shown in the figure, the duobinary format performs better than the other two formats, which indicates that the cross talk distortion is much stronger than the nonlinear effects. Also, compared to the 25 GHz-spaced OC-192 system (i.e. same spectral efficiency), the Q

values are higher, which clearly indicates that the nonlinear effects are weaker because both systems would have the same amount of cross-talk distortion. The average Qs over 16 channels are summarized in **Table 3.10**.

Figure 3.57 compares the average Q values of the single-span 16-channel systems with NZDSF. At low launched power, the Q values are about the same as those shown in **Figure 3.56**. This shows that cross talk is still the main source of distortion. The FWM effect is not as strong as in a single-span OC-192 system using the same type of fiber due to the double channel spacing. This demonstrates the resistance to nonlinear effects of the OC-768 system. At high launched power (6 dBm), the duobinary format is still slightly better than the OOK format, and both are clearly superior to the OSSB format. This shows that the FWM distortion is still not very significant. The average Qs over 16 channels are summarized in **Table 3.11**.

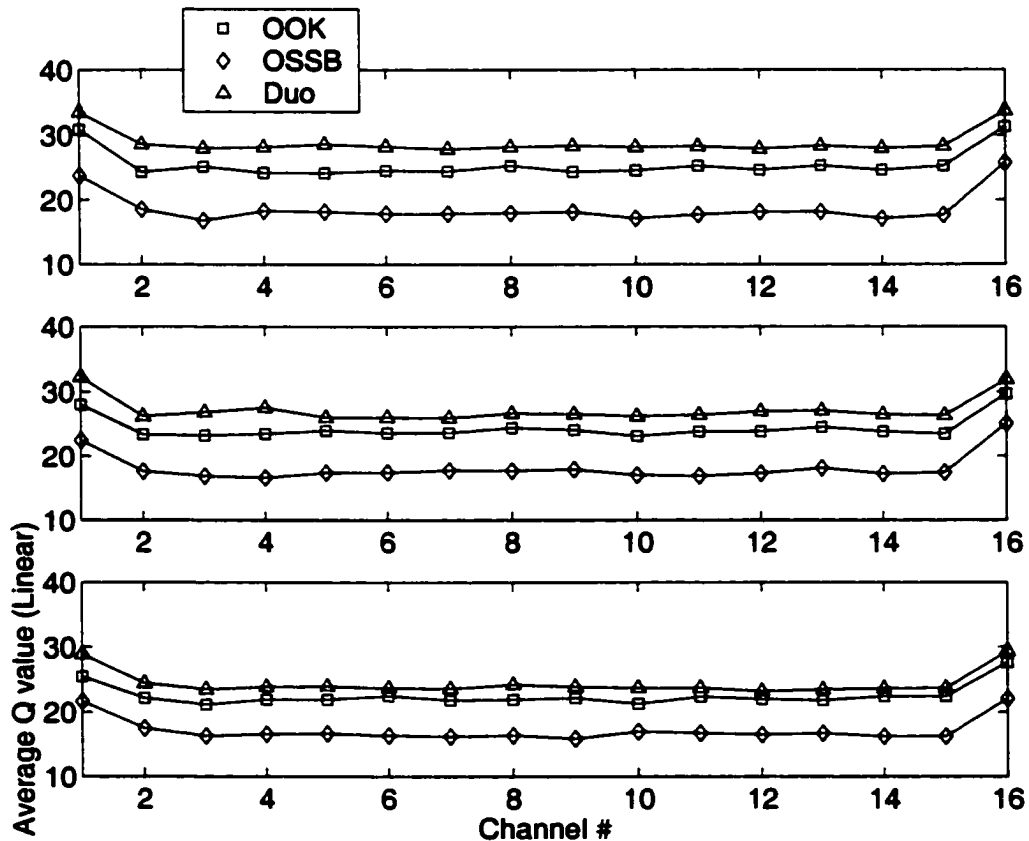


Figure 3.57: Comparison of Q Values at Different Average Launched Power Levels (1 Span, 100 GHz spacing, NZDSF) [top 2dBm, middle 4dBm, bottom 6dBm]

Launch Power	OOK	OSSB	Duobinary
2	25.5/2.14	18.7/2.35	28.9/1.81
4	24.3/1.76	18.2/2.19	27.2/1.74
6	22.6/1.61	17.2/1.81	24.4/1.81

Table 3.11: Average Q over 32 Channels (1 span, NZDSF, 100 GHz spacing)

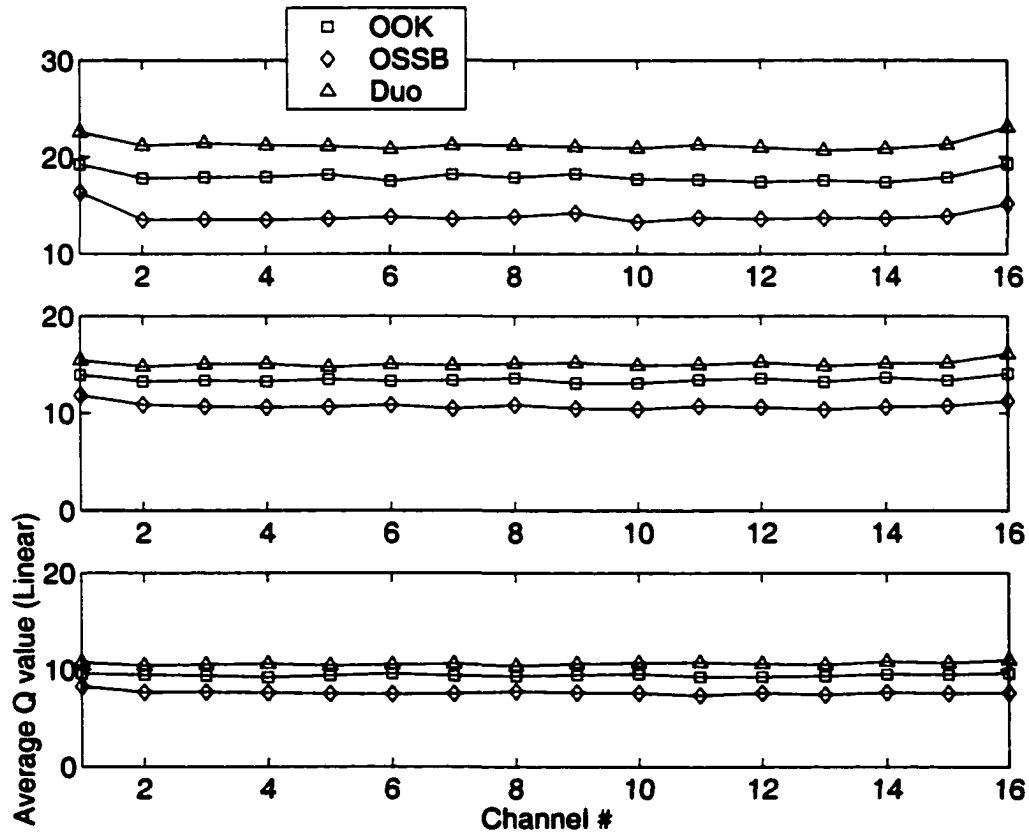


Figure 3.58: Comparison of Q Values at Different Average Launched Power Levels (5 Span, 100 GHz spacing, SSMF) [top 2 dBm, middle 4 dBm, bottom 6 dBm]

Figure 3.58 compares the average Q values of the 5-span, 16-channel systems with SSMF. At low launched power, even after 5 spans of fiber transmission, the duobinary format still performs better than the other two formats. This indicates that cross talk is still more significant than the nonlinear effects of the fiber. Only when the

launched power increases to 6 dBm do the three formats have about the same Q values. The average Q values over 16 channels are summarized in **Table 3.12**.

Launch Power	OOK	OSSB	Duobinary
2	18.0 \pm 0.55	13.9 \pm 0.75	21.3 \pm 0.62
4	13.4 \pm 0.26	10.7 \pm 0.35	15.1 \pm 0.31
6	9.4 \pm 0.12	7.61 \pm 0.19	10.6 \pm 0.15

Table 3.12: Average Q Over 32 Channels (5 span, SSMF, 100 GHz spacing)

Figure 3.59 compares the average Q values of the 5-span 16-channel systems with NZDSF. The duobinary format clearly performs better when the launched power is below 4 dBm. The average Q values over 16 channels are given in **Table 3.13**.

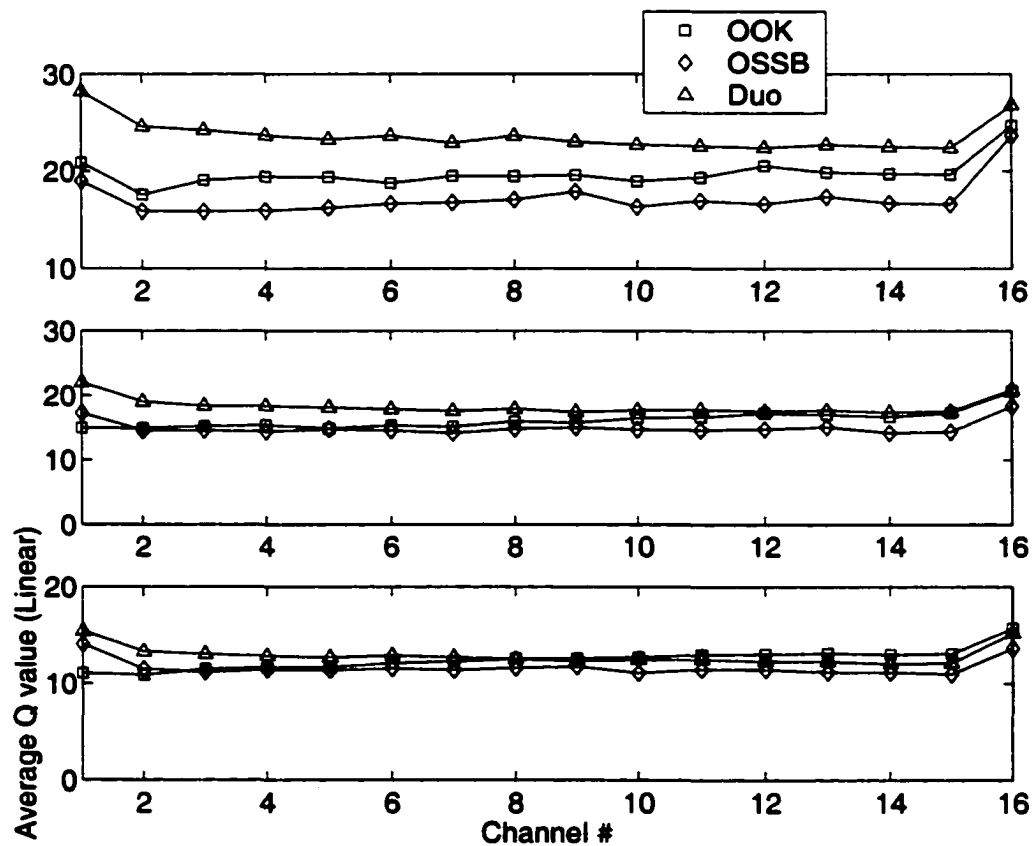


Figure 3.59: Comparison of Q Values at Different Average Launched Power Levels (5 Span, 100 GHz spacing, NZDSF) [top 2 dBm, middle 4 dBm, bottom 6 dBm]

The simulations in this section show that with 100 GHz channel spacing, the main distortion source for the OC-768 system for both single and multi-span terrestrial systems is channel cross talk. Because of this, the duobinary format performs better than the other two formats due to its narrower signal spectrum. On the other hand, the OSSB format does not perform better than the OOK format. This indicates that the residual power left in the cancelled signal sideband still causes significant cross talk distortion when the neighboring channels are very close to each other.

Launch Power	OOK	OSSB	Duobinary
2	19.8\1.46	17.2\1.84	23.7\1.59
4	16.2\1.42	15.0\1.10	18.3\1.27
6	12.5\1.10	11.7\0.85	12.9\0.96

Table 3.13: Average Q over 32 Channels (5 span, NZDSF, 100 GHz spacing)

3.11. Summary

For systems without dispersion compensation, the duobinary format has a clear advantage over the other two formats because of its narrow frequency spectrum. However, for commercial systems, dispersion compensation is usually available (for OC-192 or higher transmission rate systems). The impact of the residual dispersion is insignificant for OC-192 systems with 32 channels and 50 GHz spacing. The duobinary format, on the other hand, could have benefits for higher transmission rate systems and systems with more channels. However, this largely depends on advances in dispersion compensation devices. Regarding cross talk, both the duobinary and OSSB formats have a clear disadvantage because of the phase modulation inherent in these formats. The duobinary format does show a benefit over the other two formats for ultra-dense systems (< 18 GHz spacing for OC-192) because of its narrower spectrum.

As for fiber nonlinear effects, the three formats have very similar performance. The OSSB has a slightly higher distortion under the influence of the SPM effect because of the phase modulation from the Hilbert transform. However, this distortion is minimal and does not significantly affect system performance. As for the XPM effect, the duobinary performs better because it has more carrier power in its ‘absolute-square’

spectrum than the other two formats with the same average launched power. The FWM comparison is slightly more complicated. For single-channel systems, both the OSSB and duobinary formats perform worse, again because of the signal phase modulation. For multi-channel systems, the discrete phase modulation gives the duobinary format better performance. Overall, the distortion caused by the FWM is similar for all three formats.

Regarding a full-scale system, the duobinary format has a disadvantage because of the initial eye penalty caused by the low-pass filtering during the duobinary conversion. For OC-192 systems with 50 GHz or larger channel spacing, the duobinary format performs slightly worse than the other two formats simply because of the slight advantage from the nonlinear effect is offset by the smaller eye opening. For OC-192 systems with narrower 25 GHz channel spacing, the duobinary format shows its superiority. Its narrower spectrum reduces the channel cross talk and the performance is better. However, if the nonlinear effects are equally important in the ultra-narrow-spacing systems, the duobinary format has performance comparable to the other two formats. For OC-768 systems with 40% spectral efficiency, channel cross talk and ASE noise become the main factors that determine the system performance. With only the channel cross talk, the duobinary format clearly shows better performance than the other two formats. Nevertheless, if the ASE noise is sufficiently strong, then both the duobinary and OSSB formats could perform better.

Recent published journals have shown that the OSSB format could reduce the ASE noise simply because it has approximately one sideband [63,64], in which the amount of ASE noise present in the signal bandwidth would be reduced by roughly half. As a result, the signal-to-noise ratio could be increased by 3 dB. Similarly, the narrower spectrum of the duobinary format could also increase the signal-to-noise ratio. Nevertheless, whether or not these two alternative formats actually have an ASE-noise advantage is mainly determined by the frequency response of available optical filters. For OC-192 systems, it is very difficult to fabricate optical filters that are narrow enough to take the advantage of the ASE noise-reduction. For future higher transmission-rate systems with wider signal bandwidths, it could be possible to make optical filters that take the advantage of this situation; this will be largely determined by the development of various technologies for filter fabrication.

4. Experimental Comparison of the Three Transmission Formats

4.1. Introduction

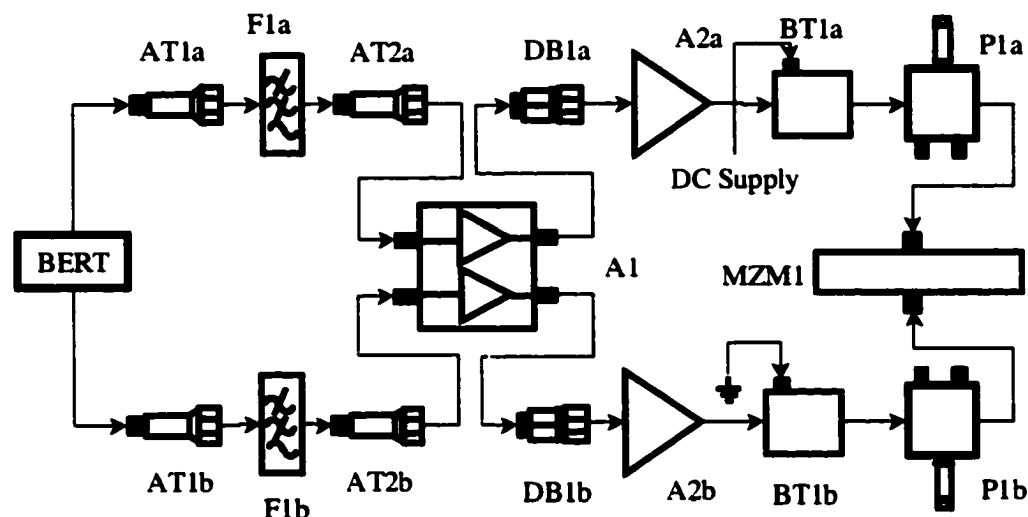
In the previous chapter, we presented a theoretical comparison of the three transmission formats. This chapter focuses on the experimental comparison of actual systems. Various issues regarding the hardware implementation will be discussed in section 4.2. Previous experiments for the duobinary system mentioned in the literature are limited in PRBS length to less than or equal to $2^{15}-1$ bits [34, 66, 67]. Our duobinary implementation functions with a commonly used $2^{31}-1$ PRBS bit sequence that should provide more realistic results. Also, in the previous implementation of the OSSB system [54], the characteristic tones in the frequency spectrum at the transmission rate were not observable, but they are clearly visible in the simulations. There was no explanation given for this discrepancy. Section 4.2 will also investigate whether or not these tones are actually present. Section 4.3 compares the cross talk penalty of the three formats. Section 4.4 and section 4.5 compare the XPM and FWM penalty using a method similar to those strategies used in the previous chapter. The performance comparison of the full-scale single-span and multi-span terrestrial systems will be presented in sections 4.6 and 4.7. To the best of my knowledge, the narrowest channel spacing for OC-192 WDM systems reported in the literature is 25 GHz, which implies a spectral efficiency of 40% [68, 69]. As will be shown in these two sections, we further reduce the channel spacing to 20 GHz for our WDM experiments, thereby demonstrating an improved spectral efficiency of 50%. Section 4.8 will summarize the findings of this chapter.

4.2. Transmitter Setup

4.2.1 Duobinary Signal

Figure 4.1 shows the schematic diagram of the duobinary transmitter test-bed. The Bessel filter was custom-made by Lorch Inc. (Salisbury, Massachusetts, United State). After several design iterations, this filter was optimized to give the best eye opening. The major difficulty in realizing the Bessel filter was to obtain the correct cut-off characteristics at high frequencies (> 5 GHz). The initial idea was to best match the

frequency response of the filter used in the simulations. However, it was not possible for the manufacturer to perfectly match the magnitude response shape. The phase response of the Bessel filter, on the other hand, is linear, which can be quite easily matched. Thus it was necessary to model the frequency response of the available filter to optimize the eye opening of the actual experimental duobinary signal.



AT1a, AT1b	RRA 10 dB Attenuator
AT2a, AT2b	ARRA 20 dB Attenuator
F1a, F1b	Lorch custom-made Bessel Filter
DB1a, DB1b	Picosecond Lab 5500A DC Block
A1	Veritech VM10CMD-320 Dual-arm Amplifier
A2a, A2b	SHF 107cp 20 GHz Amplifier
BT1a, BT1b	Picosecond Lab 5530A Bias T
P1a, P1b	ARRA Phaser
MZM1	Sumitomo 20 GHz Dual-arm Intensity Modulator

Figure 4.1: Schematic Diagram of the Duobinary Transmitter

The measured frequency response of the actual filter that was used for converting the OOK signal to a duobinary signal is shown in **Figure 4.2**. As shown in **Figure 4.2 (a)**, the 3 dB bandwidth of the filter is 2.8 GHz. Also shown in **Figure 4.2 (b)**, the phase response of the filter is quite linear within the measured bandwidth. A major problem for this type of reflective filter is the reflection from both the input and output sides. This reflection interferes with both the incoming and outgoing signals of the filter and causes serious distortion. To solve this problem, attenuators are required at both the input and output sides of the filter. Thus, in **Figure 4.1**, 10 dB and 20 dB attenuators are placed at

the input (AT1a, AT1b) and output (AT2a, AT2b), respectively. The attenuators were optimized experimentally to balance two conflicting factors, namely, the SNR and the strength of the reflection. If the attenuation is great enough, the reflection can be mostly eliminated, but then the SNR would likely drop to an unacceptable level.

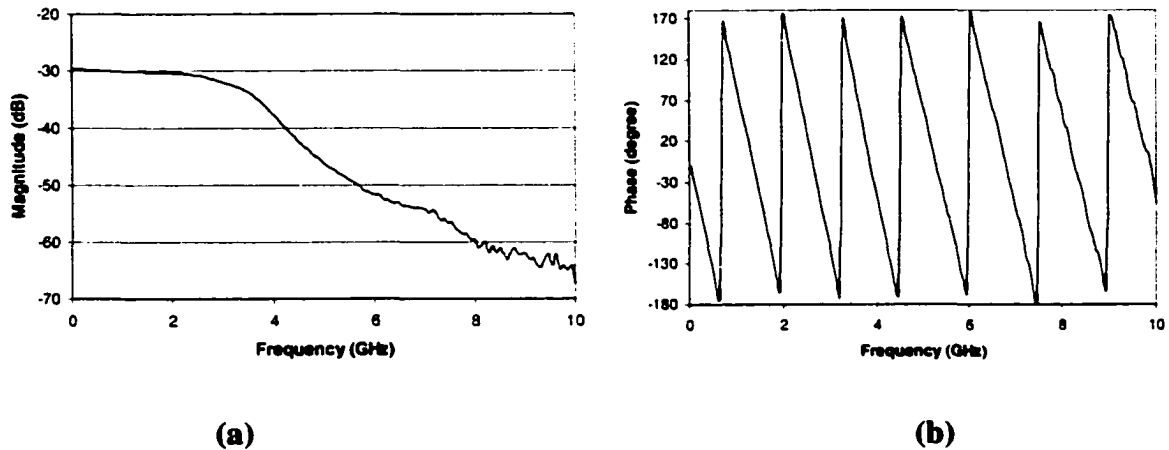


Figure 4.2: Frequency Response of the Bessel Filter for the Duobinary Conversion

A dual-arm modulator is especially necessary for the duobinary transmitter due to the doubled voltage swing requirement. As mentioned in Chapter 3, the duobinary signal has three signal levels, with two levels having the same magnitude but opposite phase. Thus, the signal that drives the modulator is required to swing over a maximum range of two switching voltages, V_{π} (as compared to only one switching voltage for both OSSB and OOK formats). The typical swing voltage of a single-arm modulator has a switching voltage of 9 volts as compared to the 4.5 volts in a dual-arm modulator (because two signals are fed to the dual-arm modulator). It is extremely difficult to amplify a duobinary signal to that high an amplitude [70], thus the dual-arm modulator is needed. The dual-arm modulator is operated using the conventional push-and-pull mode (i.e. the signals driving the two arms of the modulator are complements of each other). The two PRBSs that are output from the BERT are complements of each other. To maintain the complementary relation of these two PRBSs, the amplifiers used in the two separate paths from the BERT to the two arms of the modulator are of the same model.

The dual-arm amplifier shown in **Figure 4.1** is ideal for maintaining the complementary relationship. However, only one such amplifier (A1) was available for

the experiment. The second set of amplifiers (A2a, A2b) was necessary to boost the electrical signal to reach the required voltage swing because of the heavy attenuation incurred during the duobinary conversion. The phasers shown in the figure (P1a, P1b) adjust the relative time delay between the two signals that drive the modulator to ensure that the modulator operates in push-and-pull mode. The electrical signal at the output of one of the phasers is shown in **Figure 4.3**. This duobinary eye has a smaller eye opening than predicted from the simulation due to imperfections when realizing the designed Bessel filter. One important quality for a duobinary signal is that, in the corresponding eye diagram, the lower eye should be as close as possible to being the mirror image of the upper eye. This is crucial because of the square-law detector, which literally flips the lower eye up to overlap with the upper eye. If the upper and lower eyes have very different shapes then, the resultant eye opening after square-law detection would be greatly reduced. As shown in the figure, the measured eyes were quite symmetric. The eye openings and frequency spectra of the three transmission formats will be compared later.



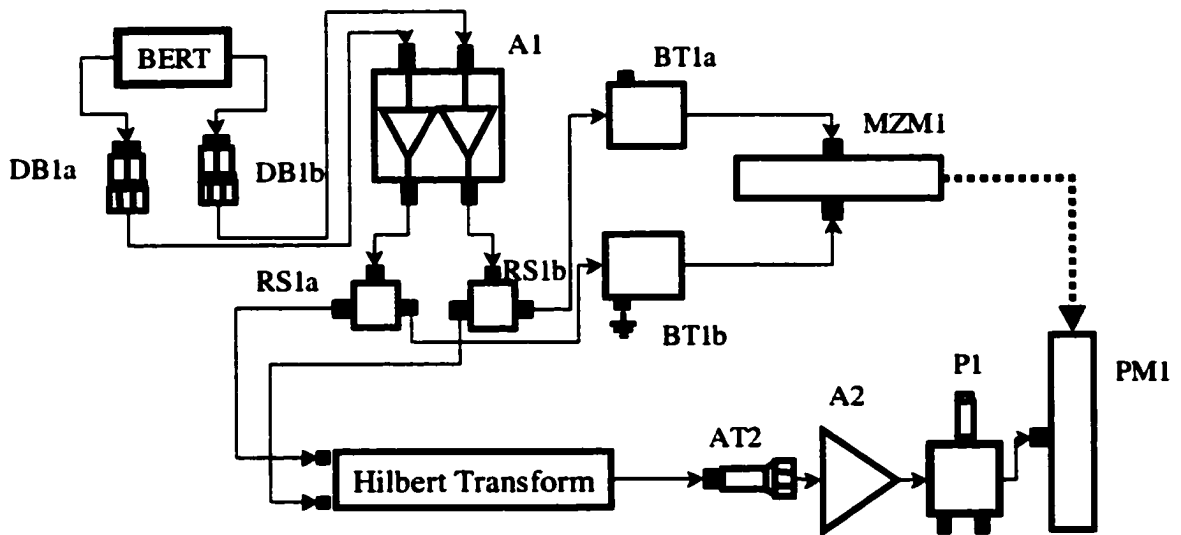
Figure 4.3: Experimental Three-Level Duobinary Eyes

4.2.2 OOK and OSSB Signals

Figure 4.4 and **Figure 4.5** show the schematic diagrams of the experimental OOK and OSSB transmitters, respectively. The schematic diagram of the Hilbert transform circuit is shown in **Figure 4.6**. Basically the difference between the OOK and OSSB transmitters is the additional Hilbert transform circuit and the optical phase

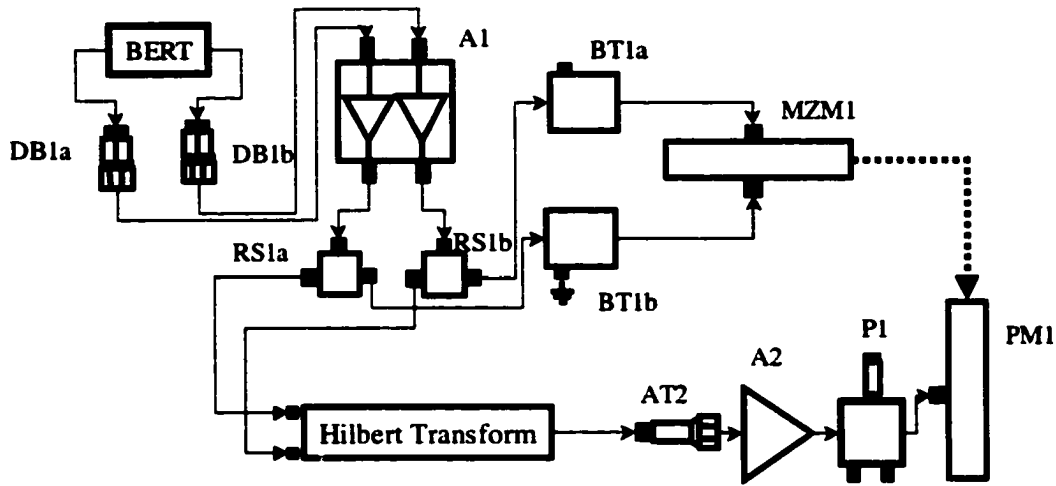
modulator (PM1 in **Figure 4.4** and **Figure 4.5**). **Figure 4.4** actually shows a typical OOK transmitter except for the pair of resistive splitters. The resistive filters are actually not necessary. The purpose of the splitters was to simplify the switching between the OOK and OSSB formats. As will be presented in later sections, the time required to measure the Q factors for all channels in a full-scale system usually took more than 10 hours. To better compare the OOK and OSSB formats, it would be desirable to have the same lab environment when performing the measurements for both systems. With the resistive splitters, the switching from OSSB signals to OOK signals can be done simply by turning off the Hilbert transform. Thus, it becomes practical to alternately measure the BERs (and hence the Q factors) of OSSB and OOK system from one channel to the next. The experimental setup was thus slightly different from the simulations, which did not include the splitters in the OOK transmitter.

The most difficult part of implementing the Hilbert transform in the OSSB transmitter is matching the time-delay among the four signal paths shown in **Figure 4.6**. This was done by carefully adjusting the time-delay of the line stretchers, which have a similar function to the phasers. The time-delay of the line stretcher is set by simply changing its physical length. Because of this, it is necessary to use flexible, semi-rigid cables for the connections to accommodate length adjustments. The amplitude ratio between the four signal paths of the Hilbert-transform circuit is as mentioned in the Chapter 3. The output signal from the experimental Hilbert transform circuit is shown in **Figure 4.7**. Both the information signal and its complement are used as the input signals. The ideal Hilbert transform of a Gaussian pulse centered at $t=0$ would asymptotically approach zero as time goes to either positive or negative infinities. Moving from the negative infinity toward zero in time, the amplitude of the ideal Hilbert transform would approach negative infinity. At $t=0$, the amplitude would switch from negative infinity to positive infinity and gradually decrease. As time increases, the amplitude would then approach zero toward positive infinity. In reality, it is not possible to switch from negative infinity to positive infinity instantaneously. **Figure 4.7** shows that the output of the Hilbert transform circuit indeed has the amplitude profile close to that of the Ideal Hilbert transform. At the center of each pulse, the output signal switches from the negative extremum to the positive extremum with finite switching time.



AT1a, AT1b	ARRA 10 dB Attenuator
AT2	ARRA 6 dB Attenuator
A1	Veritech VM10CMD-320 Dual-arm Amplifier
A2	SHF 107 20 GHz Amplifier
BT1a, BT1b	Picosecond Lab 5530A Bias T
DB1a, DB1b	Picosecond Lab 5500A DC Block
MZM1	Sumitomo 20 GHz Dual-arm Modulator
P1	ARRA Phaser
PM1	Uniphase APE PM-1.5-8-1-1-C Phase Modulator
RS1a, RS1b	Picosecond Lab 5330A Resistive Splitter
WC1	Merrimac 4:1 Custom-made Wilkinson Power Combiner

Figure 4.4: Schematic Diagram of the OOK Transmitter



- | | |
|------------------|---|
| AT1a,AT1b | ARRA 10 dB Attenuator |
| AT2 | ARRA 6 dB Attenuator |
| A1 | Veritech VM10CMD-320 Dual-arm Amplifier |
| A2 | SHF 107 20GHz Amplifier |
| BT1a,BT1b | Picosecond Lab 5530A Bias T |
| DB1a,DB1b | Picosecond Lab 5500A DC Block |
| MZM1 | Sumitomo 20GHz Dual-arm Modulator |
| P1 | ARRA Phaser |
| PM1 | Uniphase APE PM-1.5-8-1-1-C Phase Modulator |
| RS1a,RS1b | Picosecond Lab 5330A Resistive Splitter |
| WC1 | Merrimac 4:1 Custom-made Wilkinson Power Combiner |

Figure 4.5: Schematic Diagram of the OSSB Transmitter

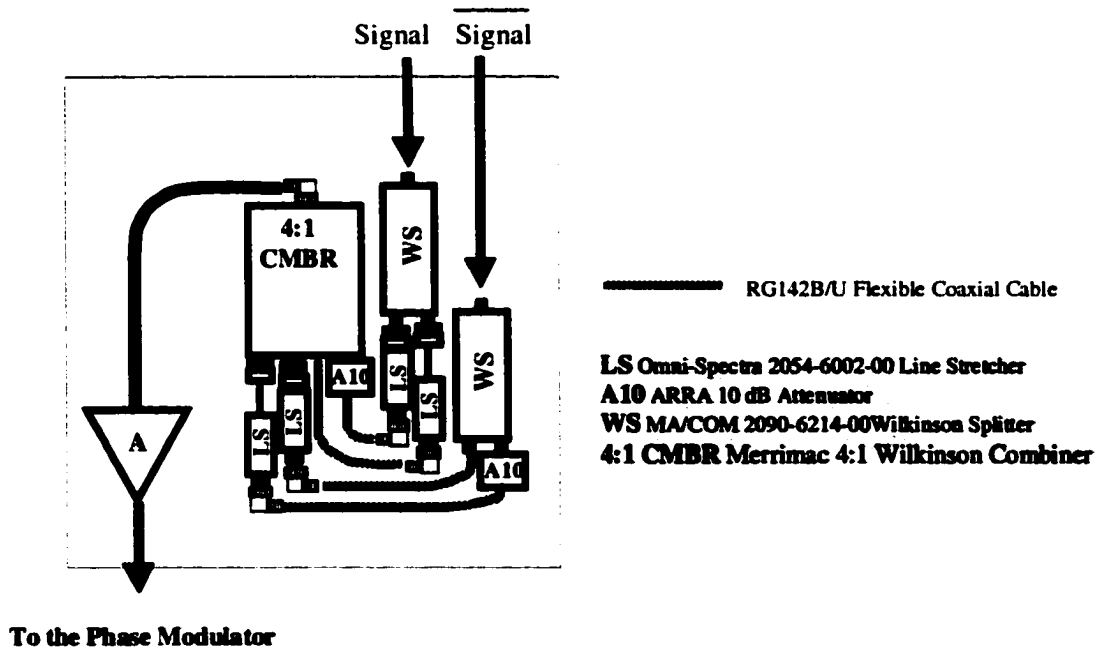


Figure 4.6: Schematic Diagram of the Hilbert Transform Circuit



Figure 4.7: Measured Output of the Hilbert Transform Circuit

The crucial step in implementing the OSSB transmitter is matching the time-delay of the signals driving the intensity and phase modulators. The difficulty stems from the unknown time-delay of the optical path from the intensity-modulator to the phase modulator. Fortunately, different lengths of semi-rigid coaxial cables were available in the laboratory. Thus, time-delay matching could be performed by trial-and-error, in which different lengths of coaxial cable were inserted between the phaser and the phase modulator to coarsely match the time delay. The fine adjustment was then done using the phaser. The time-delay matching was performed while the frequency spectrum of the signal was being monitored.

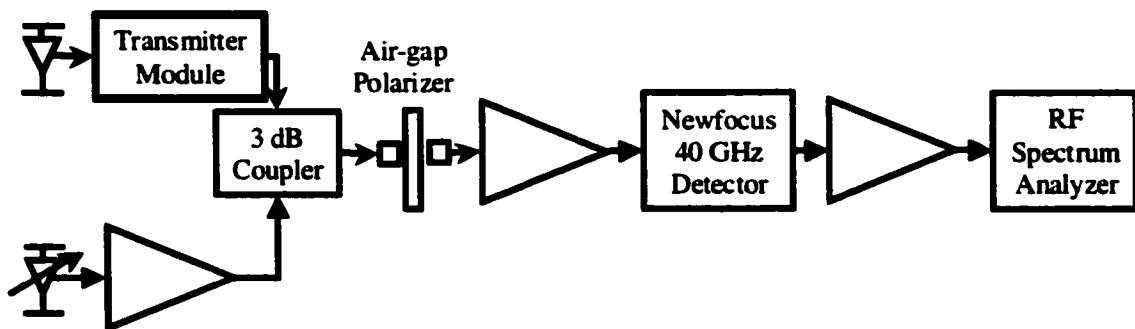


Figure 4.8: Schematic Diagram for the Heterodyne Method for Measuring the Optical Spectrum of the Signal

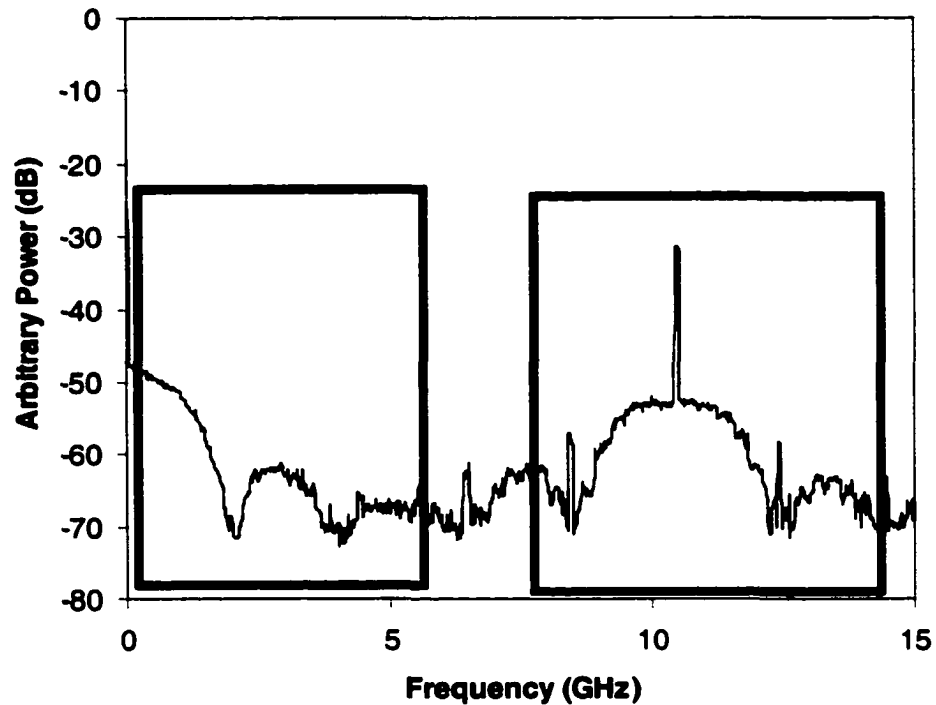


Figure 4.9: Composite Spectrum obtained from the Heterodyne Method (on the left-optical spectrum, on the right box- square-law-detected spectrum)

A heterodyne method was used to display the optical spectrum of the signal. The corresponding setup is shown in **Figure 4.8**. As shown in the figure, the heterodyne method combines a tunable CW laser signal with the optical signal to be displayed. The resulting product signal then goes through the square-law detector. The air-gap polarizer, shown in the figure, was used to keep the polarization of the two signals close to each other for better mixing. An RF spectrum analyzer after the square-law detector was used to display the frequency spectrum of the detected signal shown in **Figure 4.9**. Note that the spectrum contains both the square-law-detected signal spectrum and the optical signal spectrum. The separation of the two spectra equals the frequency spacing between the optical signal and the CW laser. An OC-48 OOK signal is displayed in the example shown in **Figure 4.9**. Because of this, the two spectra do not overlap with each other. In practice, the frequency separation of these two spectra is limited by the available bandwidth of the electrical amplifier after the square-law detector, which is 20 GHz at that moment. Because of this, for an OC-192 signal, the two spectra are partially overlapped. To clearly observe the optical spectrum, it is necessary to adjust the power

ratio between the optical signal and the CW laser to greatly suppress the square-law-detected spectrum. This is the reason for including the extra optical amplifier before the 3 dB coupler in the CW-laser path.

4.2.3 Signal Spectra and Eye Diagrams

Figure 4.10 compares the optical signal spectra of the three transmission formats. As expected, the duobinary signal spectrum is narrower than the other two formats. Also, there is no carrier tone in the duobinary spectrum because of the three-level signaling. Another important observation is the presence of tones at the transmission rate on both sidebands of the OSSB signal. The earlier implementation [54] does not show such tones, which are clearly present in the simulations. **Figure 4.10** confirms that these tones do in fact exist, in agreement with the simulations. The absence of the tones in the previous measurement is possibly due to the resolution limitations that obscured detail in the optical signal spectrum. The observed amount of sideband cancellation of the OSSB signal is close to that expected from simulations. Moreover, **Figure 4.10** also shows that the OOK signal has two tones at the transmission rate. This is due to the cosine function response of the intensity modulator, which generates harmonics of the signals at these tones.

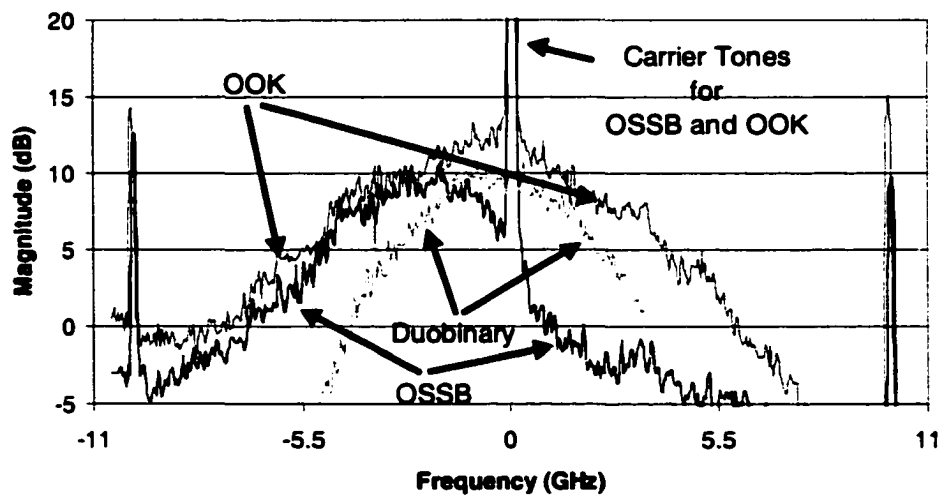


Figure 4.10: Frequency Spectra of the Three Transmission Formats

Figure 4.11 shows the back-to-back (i.e. folded) eye opening of the duobinary and OOK signals. The OSSB and OOK formats have the exact same back-to-back eye opening because the phase modulation is removed by the square-law detection, as mentioned in the Chapter 3. As shown in the figure, the duobinary eye is smaller than the OOK eye, as expected. The initial eye penalty of the duobinary signal appears to be more serious than that predicted by the simulations. A more quantitative measurement will be given in the next section. It should be noted that the eye diagrams are actually up-side-down due to an inverting amplifier in the amplification chain at the receiver. Thus, the '0' level actually lies at the top of the diagrams. The schematic diagram of the receiver is shown in **Figure 4.12**.

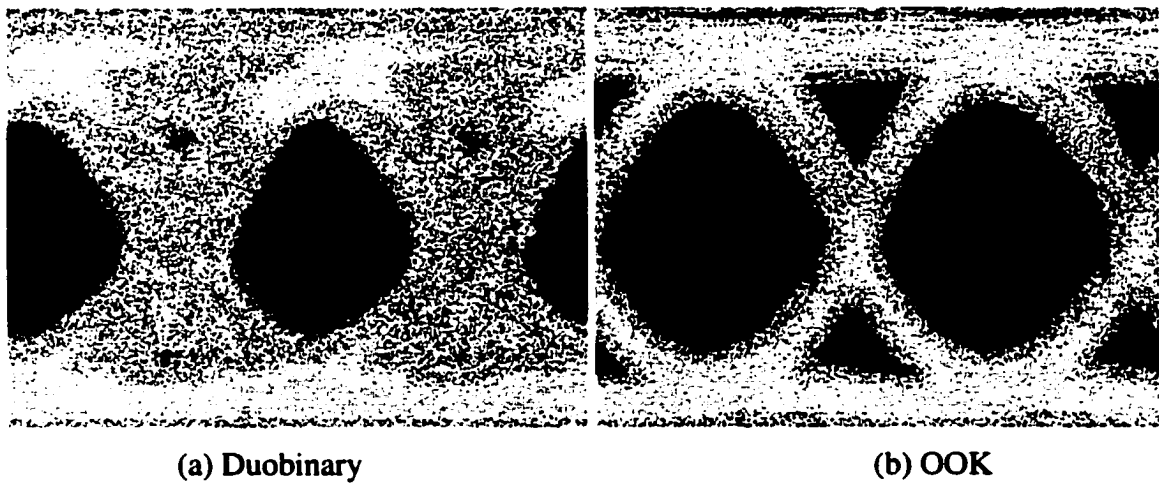


Figure 4.11: Comparison of the Back-to-Back Eye Diagrams of the Duobinary and OOK Signals.

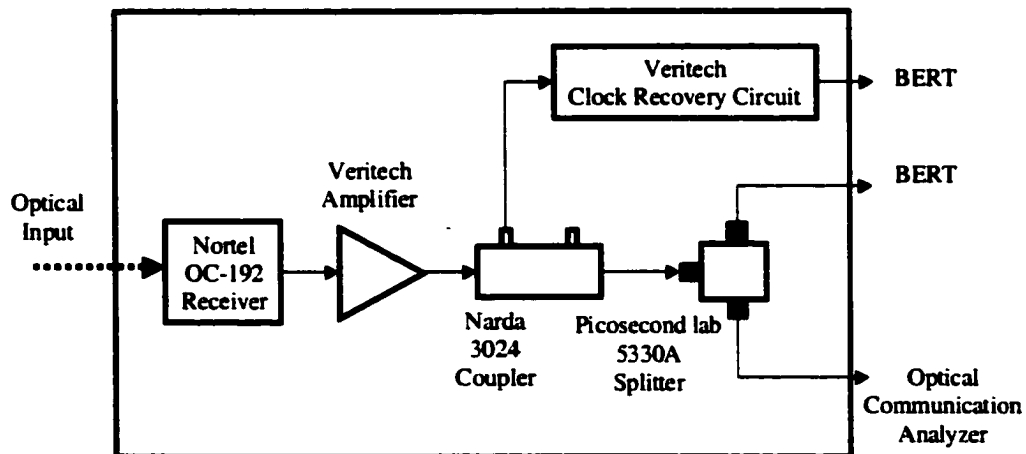


Figure 4.12: Schematic Diagram of the Optical Receiver

Figure 4.13 shows how the eye of the duobinary signal evolves as it propagates through different lengths of SMF. As predicted by the simulations, the duobinary eye becomes slightly bigger as the signal propagates through the fiber. The eye shape changes from an oval to a diamond shape after 80 to 100 km of SMF where the maximum eye opening occurs, as predicted by the simulations.

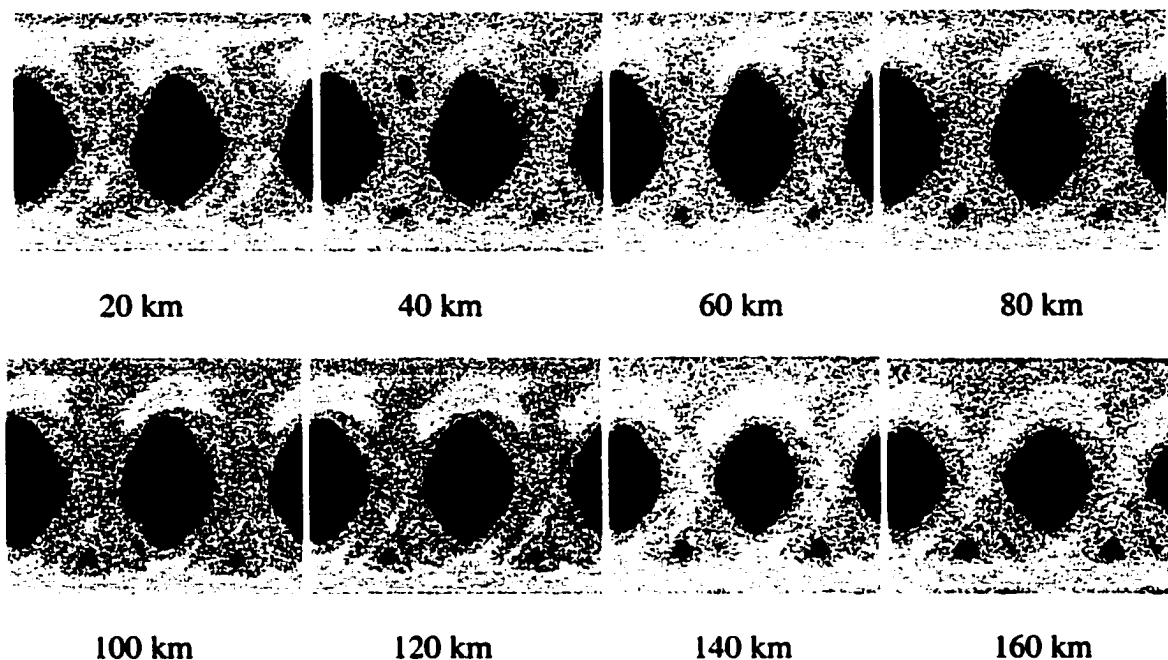


Figure 4.13: Evolution of the Square-law-detected Duobinary Eye with Different Lengths of SMF

4.3. Channel Cross Talk

Figure 4.14 shows the experimental apparatus used to measure the channel cross talk. Three input channels are present in the set-up. The wavelength of the center channel is fixed while the other two channels can be slightly wavelength-tuned. The major disadvantage of this experimental setup is the use of only one transmitter. As a result, a single modulator modulates all three channels, and thus the resulting signals are correlated. The consequence of the channel correlation is smaller cross-talk penalty. The reason is that the bit patterns are identical for all channels. Hence, the '1' and '0' bits are almost perfectly lined up in time. Because of this, the '0' bits are only distorted by the '0' bits of neighboring channels, instead of both '1' and '0' bits in the real situations.

Therefore, the distortion is less for the '0' bits. Unfortunately, there were only enough components to build one set-up, OSSB or duobinary, at one time.

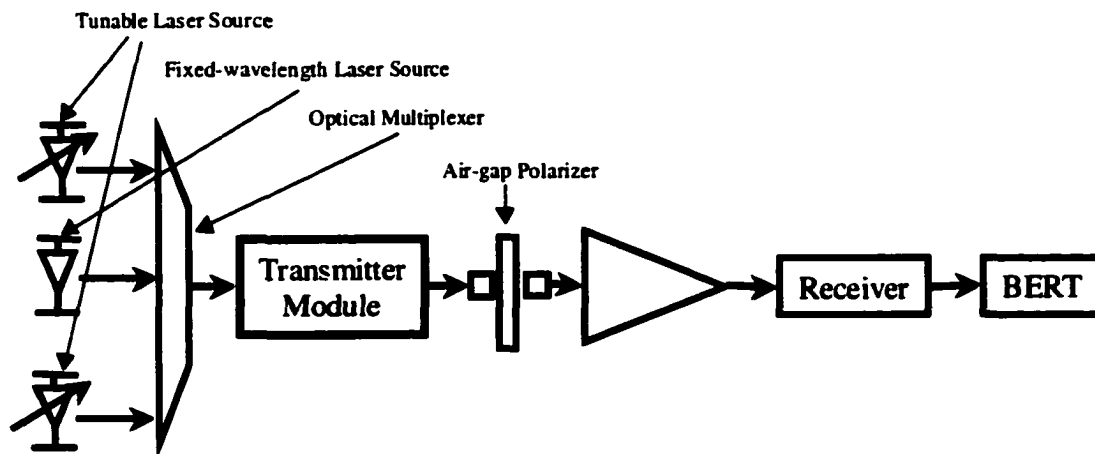


Figure 4.14: Schematic Diagram for the Cross Talk Measurement Set-up

A Q measurement can be used to determine quantitatively the performance difference between the three formats [52, 56]. Q is obtained by first measuring the BER versus the threshold voltage of the BERT. The Q is then determined by fitting the means and standard deviations to the '1' and '0' curves, as described in Chapter 2. The threshold voltage is the reference voltage of the BERT for determining whether the bit under examination is a one or a zero. Thus if the threshold voltage is set too low, there will be many errors due to the misidentification of ones, and similarly a lot of misidentification on zeros if the voltage is set too high.

Figure 4.15 shows a typical BER versus threshold voltage curve. For a typical OOK format, the lowest BER should be located closer to the '0' level. In this example, the left-hand side is the '0' level and the right-hand side is the one level. Usually, the '1's of the signal have more noise due to the signal-to-spontaneous beat noise [23]. Thus the BER drops more slowly from the one-level side moving toward the center as compared to moving from the zero-level side toward the center. Consequently, the optimal threshold voltage should be set closer to the zero side. The Q factor is calculated by fitting the '1' and '0' curves to determine the mean and standard deviation.

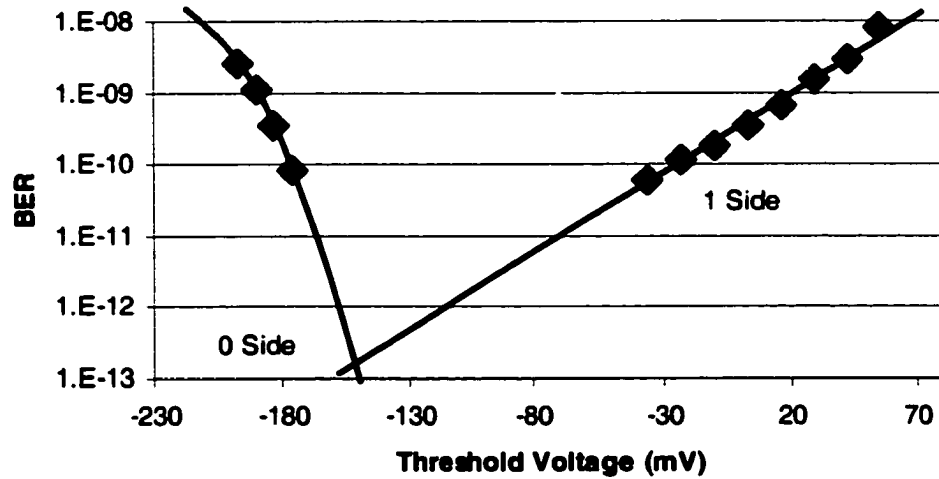


Figure 4.15: Example of the BER versus Threshold Voltage Curve

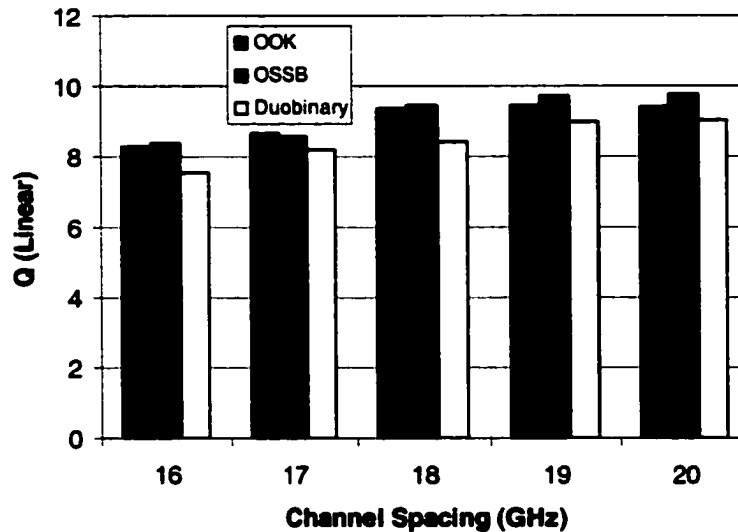


Figure 4.16: Q versus Channel Spacing from Experimental Results

Figure 4.16 shows the measurement results for the cross talk experiments. As shown in the figure, the duobinary format clearly performs worse than the other two formats. As mentioned previously, the actual eye opening of the duobinary signal is less than that predicted by simulation. As a result, the advantage of the narrower spectrum of the duobinary format is greatly offset by the smaller eye opening. Hence, the Q values are worse for the duobinary format. As for the OOK and OSSB formats, the Q values are essentially the same for both formats. According to the simulations, the OSSB format

should perform worse than OOK because of the extra phase modulation. The discrepancy between the simulated and experimental results is possibly due to the correlation between the three channels use in the experiment. Further simulations showed that (see new paragraphs), because of the correlation, the eye opening of both OSSB and OOK increases.

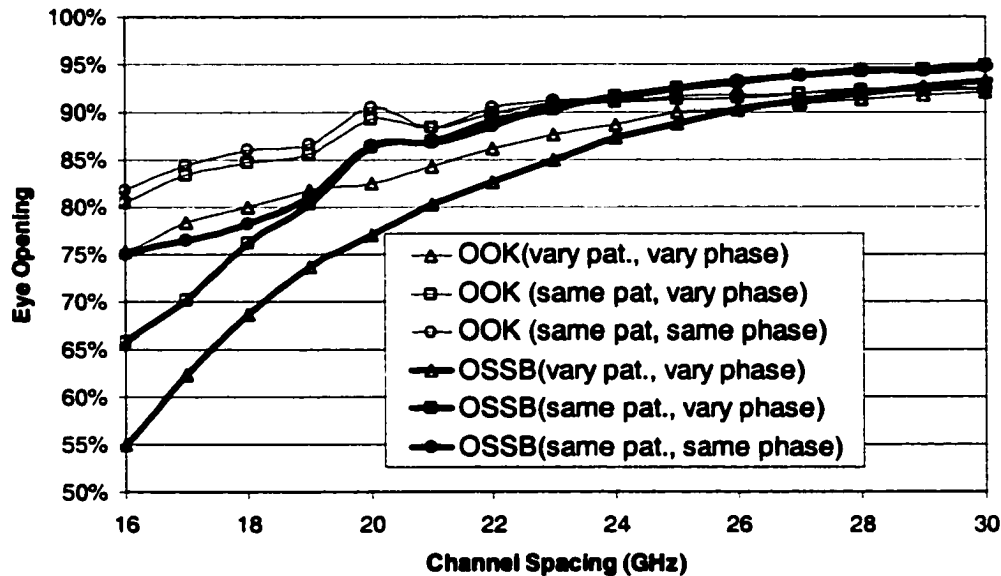


Figure 4.17: Simulated Eye Opening of OOK and OSSB Formats with Different Channel Spacing under Three Different Conditions

Figure 4.17 compares the simulated eye opening of the two formats under three different conditions: (1) varying both the relative time delay and laser phase among the three channels; (2) fixing the relative time delay, but varying the laser phase; and (3) fixing both the relative time delay and laser phase. Condition (2) is close to the actual experimental condition, whereas condition (1) is similar to a real commercial system. Figure 4.17 shows that for both conditions (2) and (3), the eye openings for both formats are larger compared to those of condition (1). As the channel spacing increases, the difference between the two formats gets narrower. With a channel spacing of 16 GHz, the eye opening difference between the two formats under condition (3) is about 5% compared to 20% for the difference obtained under condition (1). We can therefore deduce from these simulation results, it is very likely that the bit-pattern correlation among the three closely-spaced channels caused the measured Q-value difference

between the OOK and OSSB formats to be very small. Moreover, it should be noted that the calculated Q values are lower than expected. This is possibly due to the bit-pattern correlation of the three channels, which causes the noise distortion for both '1' and '0' bits to be non-Gaussian. As a result, the curve-fitting algorithm under-estimated the Q values.

4.4. XPM Measurement

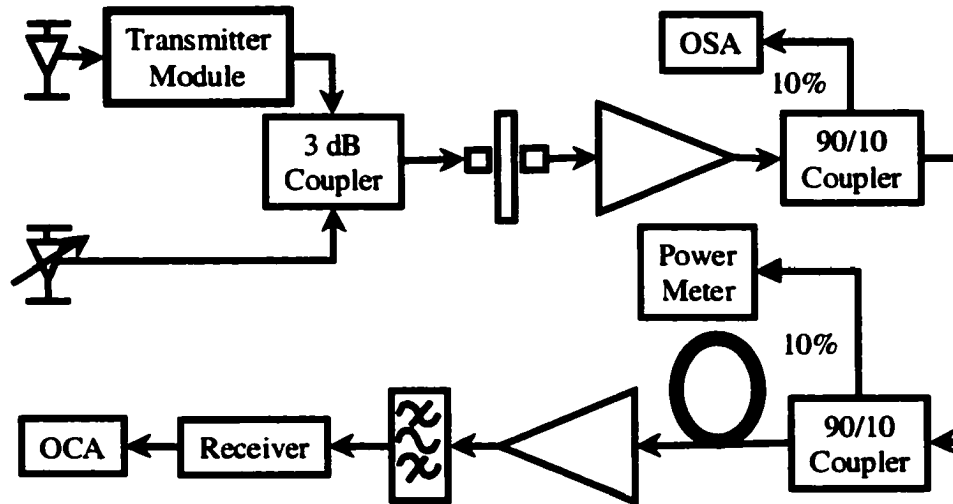


Figure 4.18: Experimental Setup for the 2-Channel XPM Measurement

Figure 4.18 shows the schematic diagram that was used to measure the XPM penalty. Two channels (with one modulated signal and one CW laser) were used, which is the same as the set-up used in the simulations presented in Chapter 3. The evaluation of the XPM penalty is done by measuring the standard deviation of the CW channel after the square-law detector. An optical spectrum analyzer (OSA) was used to monitor the power of the two channels to ensure that they had the same optical level. The power meter alone is not sufficient because the polarization of the two channels can change slightly over time (and hence change the power ratio of the two channels), but the total power would remain the same. No dispersion-compensating fiber was placed in the system. With dispersion compensation, the XPM penalty would simply be too small to be measured. Thus the system was left uncompensated. The difficulty in the XPM measurement is the removal of the ASE noise, which is inevitably present in this kind of experiment. The ASE noise is roughly removed by using the built-in averaging function

of the optical communication analyzer (OCA). A 1000-measurement averaging window was used. The simplifying assumption is that the ASE noise has a distribution close to Gaussian (but not exactly Gaussian [72]) and should have a mean of zero. Thus averaging should effectively remove the ASE noise.

Figure 4.19 and **Figure 4.20** show the XPM measurement for both SMF and NZDSF. The curves labeled '50GHz' and '100GHz' denotes the channel spacing between the two channels set in the experiments. The normalized standard deviations were calculated by dividing the measured standard deviations from the average values of the measured signals. For both types of fiber, the measurements show that the XPM penalty of the three formats is almost identical. For NZDSF, the XPM penalty is slightly less for the duobinary format. However, for SMF, the duobinary format has no advantage over the other two formats. The simulation results presented in Chapter 3 indicate that the duobinary format has slightly less penalty due to the higher ratio of carrier-tone power to signal power. The slight discrepancy between the experimental and simulation results can be attributed to an averaging effect, as explained below.

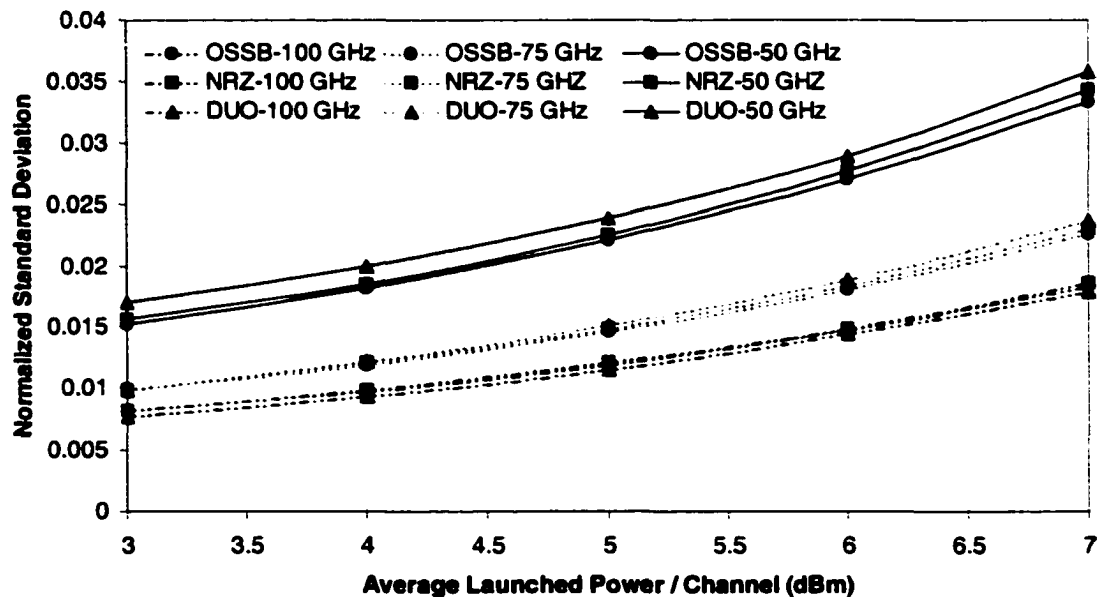


Figure 4.19: Normalized Standard Deviation versus Launched Power for Three Different Channel Spacings (SMF)

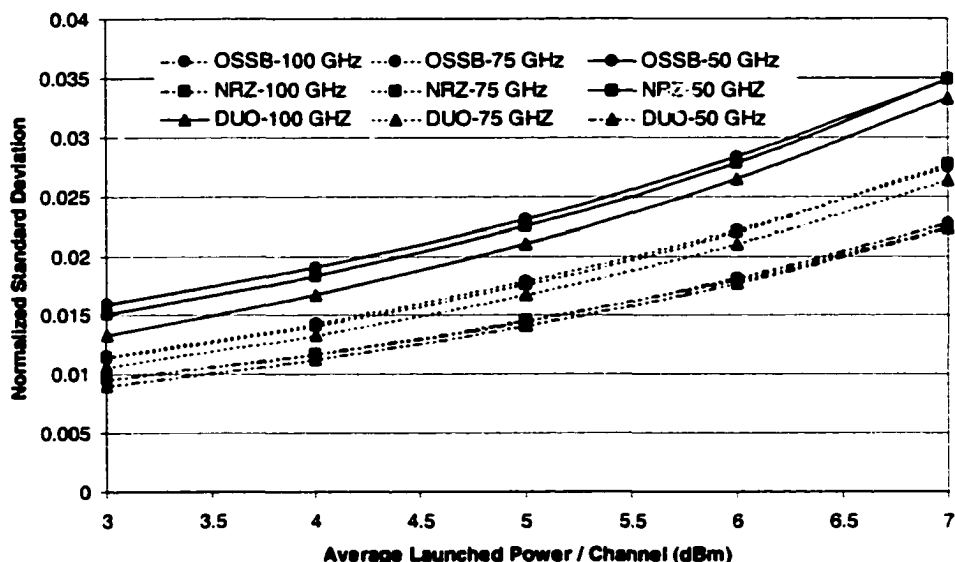
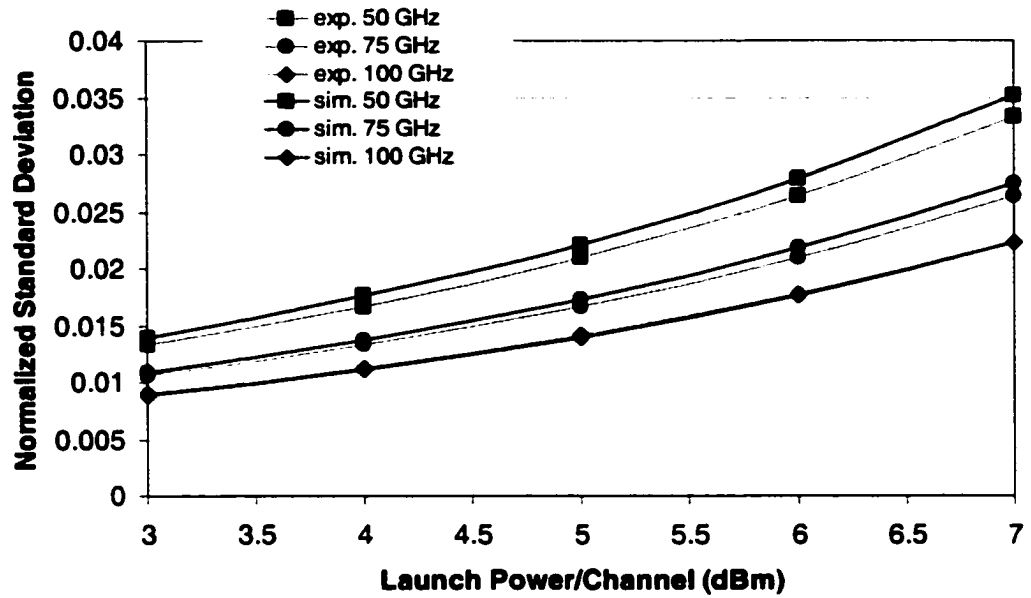
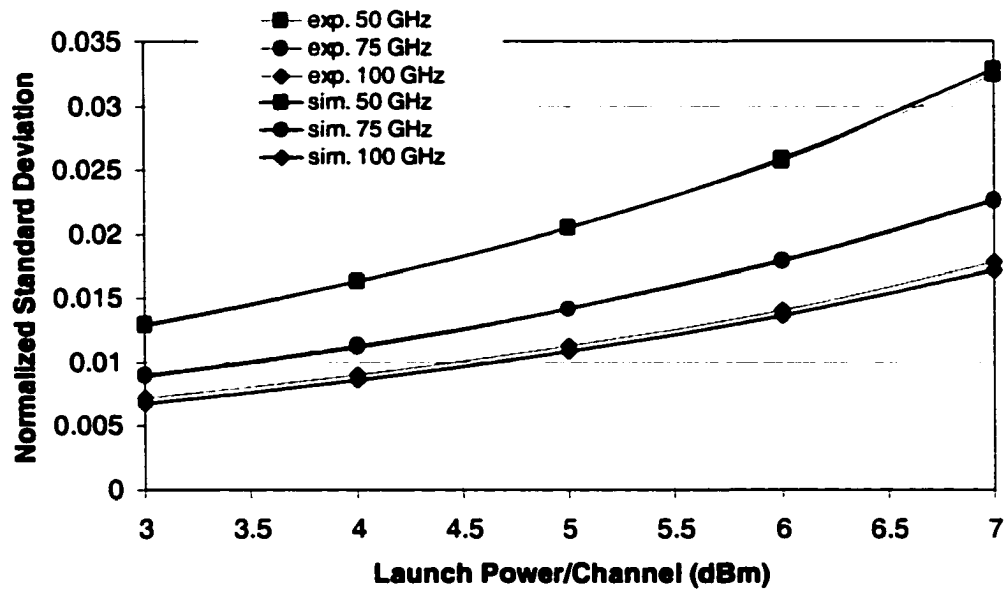


Figure 4.20: Normalized Standard Deviation versus the Launched Power for three Different Channel Spacings (NZDSF)

Figure 4.21 compares the normalized standard deviation between the experimental and simulated results for the duobinary format for the same three channel spacings. The figure shows that the experimental results are in good agreement with the simulated results, with the experimental results being slightly less than the simulation results. The difference can be understood from Figure 4.22. Figure 4.22 shows examples of time traces of the XPM-distorted CW signal after the square-law detector for both the OOK and duobinary formats. As shown in the figure, the simulation agrees well with the experiments except that the amplitude swing of the experimental results is less than that of the simulation results. This is possibly due to the averaging, which does not totally remove the ASE-noise and which causes the signal to have less amplitude swing. The time trace of the duobinary format is quite different from that of the OOK format. Note that the amplitude overshoot at the peaks of the traces is less for the duobinary signal. As a result, the duobinary signal time trace is less affected by the averaging effect, and its standard deviation measurements are closer to the simulation results than was the case for the OOK format.



(a) NZDSF



(b) SMF

Figure 4.21: Experimental and Simulation XPM Distortion for Duobinary Format

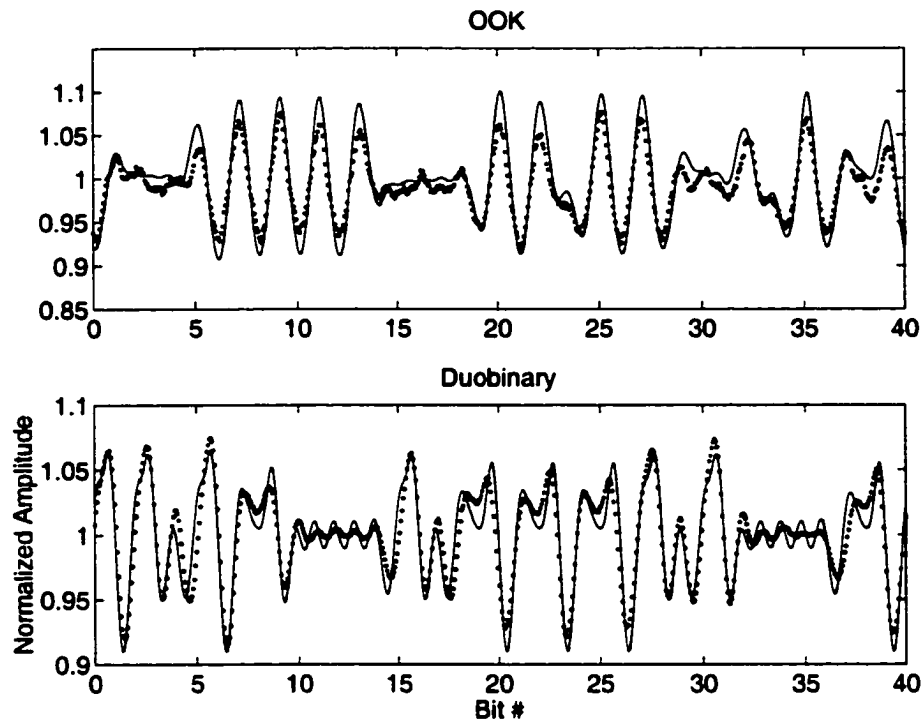


Figure 4.22: Experimental and Simulated XPM Distortion Results (solid - simulation, dots- experiment)

The measurements agree fairly well with the simulations. The XPM penalties for all three formats are similar, with duobinary format having slightly less penalty.

4.5. FWM Measurement

Figure 4.23 shows the experimental set-up for measuring the FWM penalty. Different from the set-up used in the simulations (see Chapter 3), the set-up has only two channels, instead of three channels, and both channels are modulated. This arrangement allows the direct measurement of the optical power ratio between the original signal and the FWM-generated distortion signal. Due to the FWM effect, two additional optical signals are expected to be generated on either side of the two-channel spectrum. The 3-channel set-up used in the simulations (see Chapter 3) would also require the cancellation of the ASE noise, similar to the XPM experiments; whereas the two-channel experiment shown in **Figure 4.23** does not require the noise cancellation. Also, in the 3-channel experiment, the strength of the FWM is affected by the laser phase of the CW channel relative to that of the other two channels. Since the laser phase of the lasers is unknown,

this 3-channel experiment would have more uncertainty in the measurement. Thus, the 2-channel experiment is preferred.

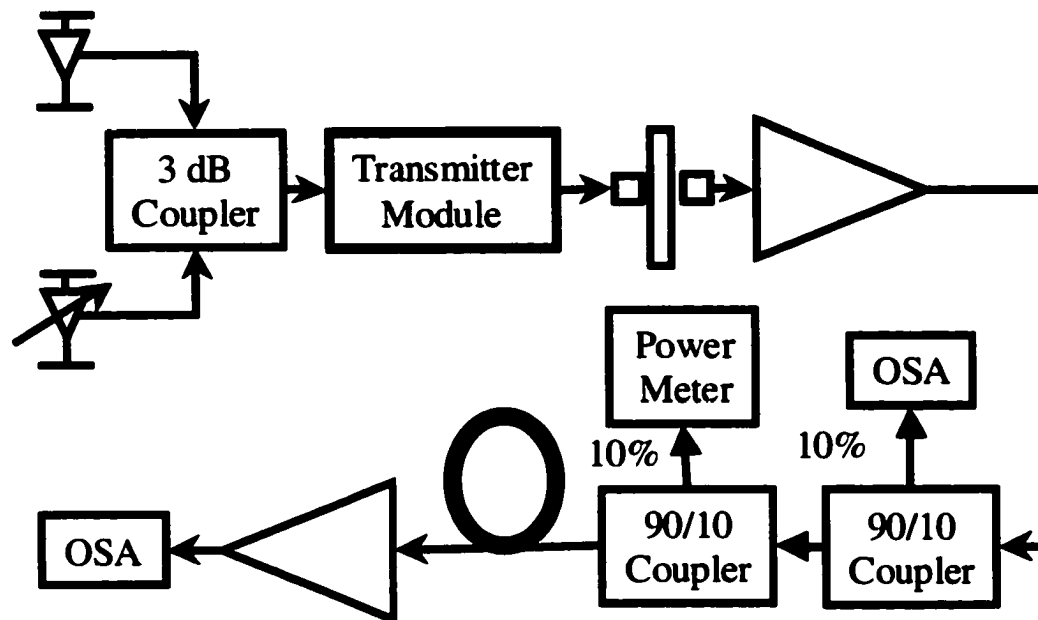


Figure 4.23: Experimental Set-up for the 2-channel FWM Measurement

The optical power of the FWM-generated signal is measured using the OSA. Basically, the OSA slices the specified frequency spectrum to be displayed into smaller wavelength slots and then measures the optical power of each slot. An example of the OSA output display is shown in **Figure 4.24**. In this example, the OSA scans a 17-channel WDM system with 20 GHz channel spacing. The OSA uses a wavelength-tunable optical band-pass filter to scan through a range of wavelengths, slot by slot. The bandwidth of the optical filter is adjustable.

To ensure that the OSA can completely capture the power of an OC-192 signal and the corresponding FWM-generated signal within one wavelength slot, the bandwidth of the bandpass filter needs to be approximately 0.2 nm (25 GHz). **Figure 4.25** shows the measured results of the ratio of the original signal power to the FWM-generated signal power for different channel spacings (between the two original channels). In this experiment, a special type of fiber was used to increase the FWM generation efficiency. The zero-dispersion wavelength of this fiber is close to 1561 nm. The wavelength of the two channels in the experiment was centered at 1553 nm. Thus the FWM was extremely

strong because the 'walk-off' between the two channels was small. 'Walk off' occurs when the propagation speeds of two channels are different which leads to the pulses in one channel move faster than those of the other channel.

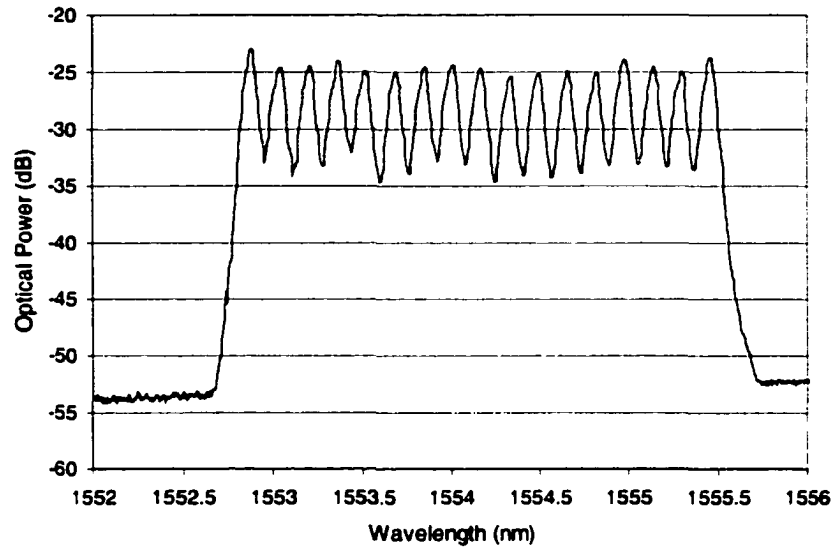


Figure 4.24: Experimental Setup for 2-channel FWM Measurement

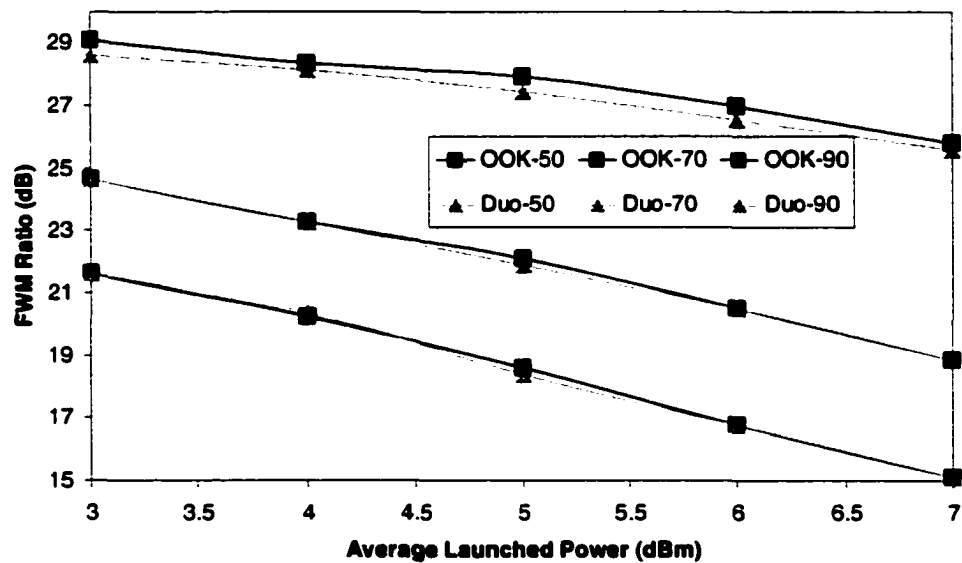


Figure 4.25: FWM Ratio between the Original Signal and the FWM-generated Signal

In **Figure 4.25**, the low ratio values indicate a strong FWM effect because the FWM-generated signal has higher power. Consistent with the simulation results, within the measuring resolution, the FWM strength for both the duobinary and OOK formats is almost the same. The results for OSSB signal are not shown on the figure because the results are essentially identical to those of the OOK format.

4.6. Single-Span System Experiments

The simulation results in Chapter 3 indicate that only for ultra-dense WDM systems does the duobinary format have significant benefits over the other two formats. Thus, for the full-scale system comparison, the remaining experiments focused on an ultra-dense system with 20 GHz channel spacing. To the best of the author's knowledge, this is the highest spectral efficiency ever reported for an OC-192 WDM system. As for OC-384 systems, spectral efficiencies as high as 66.7% and 100% have been reported [34, 66]. Both of these experiments were conducted using the duobinary format. Unfortunately, the PRBS used in these two high spectral-efficiency experiments was limited to a 2^7-1 bit length. For the 50% spectral efficiency, a statistically preferable $2^{31}-1$ bit length was used for all experiments described in the remainder of the chapter.

Figure 4.26 shows the experimental set-up for a full-scale single-span experiment. For the duobinary experiment, 16 lasers were available that could be wavelength-tuned to be 20-GHz apart. Later on, during the OSSB and OOK experiments, an additional laser was available. Thus there were 17 channels present in the experimental results for both OOK and OSSB, but only 16 channels in the duobinary results. As shown in **Figure 4.26**, a distributed Raman amplifier was used in the system, which can help suppress ASE noise. This is especially important for single long-span systems, where ASE noise could be the dominating factor. With the combination of the Raman amplifier and EDFA, the total noise is less than would be generated using only the EDFA [56]. The transmission fiber consists of one piece of SMF followed by one piece of NZDSF. The SMF is placed at the launching end of the system to reduce the fiber's nonlinear effect; SMF is not affected as much because of its larger effective core area. The NZDSF is used to enhance the Raman amplification efficiency, which is greater because of the smaller effective core area. The nonlinear effect is not significant

at later sections of the transmission link because the signal is already attenuated significantly. The DCM was experimentally optimized to give the best performance. Two tunable Bragg-grating optical filters were installed at the end of the transmission link to extract individual channels for detection. Two filters were required to suppress cross talk from the neighboring channels. The center wavelengths of the two filters were slightly detuned to give the best Q value (achieved by better isolation from the neighboring channels).

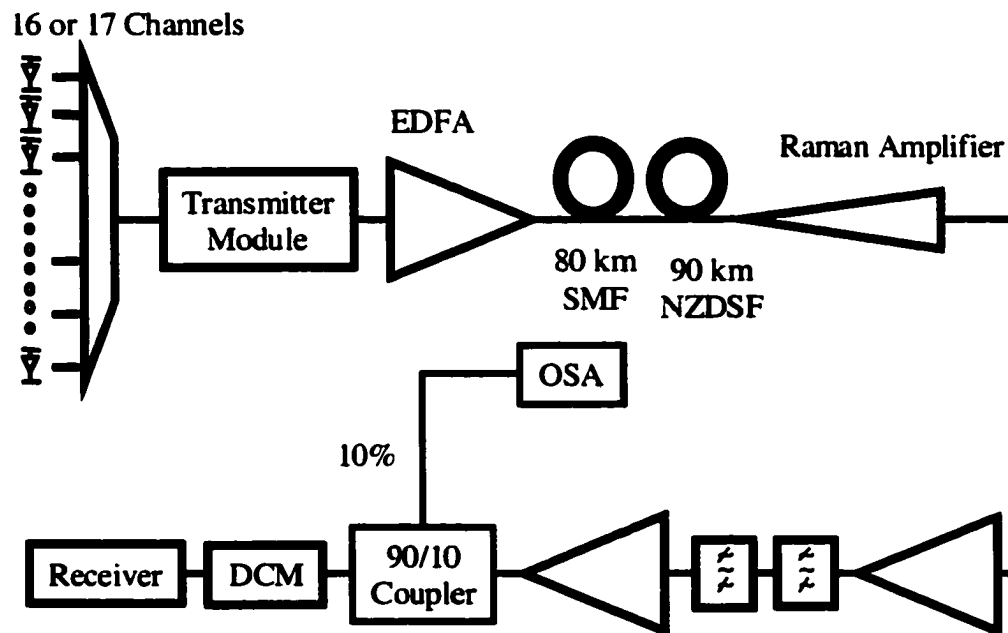


Figure 4.26: Experimental Setup for Full-scale Single-span Experiment

It was found that the optimal DCM for the duobinary format is different from that for the OOK and OSSB formats. The total dispersion of the entire transmission link was 1869 ps/nm. The DCM for duobinary format gave the best performance when it was tuned to compensate for 40 km of SMF (i.e. -640 ps/nm); by contrast, -1655 ps/nm of DCM (almost full compensation) was required to give the best performance for both the OSSB and OOK formats. It should be noted that the individual DCMs are preset in the factory to roughly compensate for one particular length of fiber. Thus, it was not possible to very finely adjust the dispersion of the DCM. It was only possible to cascade different combination of DCMs, for which the resolution could only be close to the value that is equivalent to compensating 10 km of SMF (about -170 ps/nm). The reason for the

difference in the DCM values for different formats was possibly due to the fact that the duobinary signal has the maximum eye opening when the residual dispersion is equivalent to about 80 km of SMF (as shown in an earlier section). After dispersion compensation of -640 ps/nm, the residual dispersion experienced by the duobinary signal was about 1229 ps/nm, equivalent to about 72 km of SMF. Moreover, it should be noted that due to the limited components available, a single modulator modulated all channels. The consequence of this is that the channel signals were correlated. Consequently, the channels experienced strong systematic nonlinear effects as explained below.

Figure 4.27 shows the measured FWM power versus the total launched power for the duobinary experiment. Due to the narrow channel spacing, it was necessary to turn off three channels around the center region (1553 nm) to clearly observe the spectrum generated by the FWM. The measurements show that even with SMF, noticeable FWM was generated when the total launched power was higher than 14 dBm. This total level is equivalent to 2.86 dBm per channel (only 13 channels were present during this measurement). To suppress the FWM, the launched power per channel was limited to below 2 dBm. To determine the contribution to FWM generation due to the Raman amplification, the Raman amplifier was turned off; however no change was observed. The amplifier thus appeared to have negligible impact on FWM.

Figure 4.28 shows the eye diagrams of channels 1, 8 and 16 (the wavelength increases with channel number) after 170 km of fiber propagation. It is evident that the eye opening of both channels 1 and 16 are asymmetric whereas channel 8 has a symmetric eye opening. For channel 1, the XPM distortion was generated only by the channels that traveled more slowly than itself. Because of this, the leading edge of the each pulse received strong XPM phase change, as illustrated in Fig. 3. This phase change would then turn into amplitude noise after mutual interaction with the chromatic dispersion. Similarly, channel 16 was distorted by channels that traveled faster, and as a result it received stronger phase change at the trailing edge of each pulse. Hence, channel 1 had less eye opening on the left side and channel 16 has less eye opening on the right side. As for channel 8, almost half of the channels traveled faster and half of the channels traveled slower. Thus, channel 8 had a symmetric eye. In practical commercial systems, the channel signals are not correlated, and hence the ones in the bit sequence of

the various channels would not start at the same time slot, and such strong XPM (and FWM) effects would not occur.

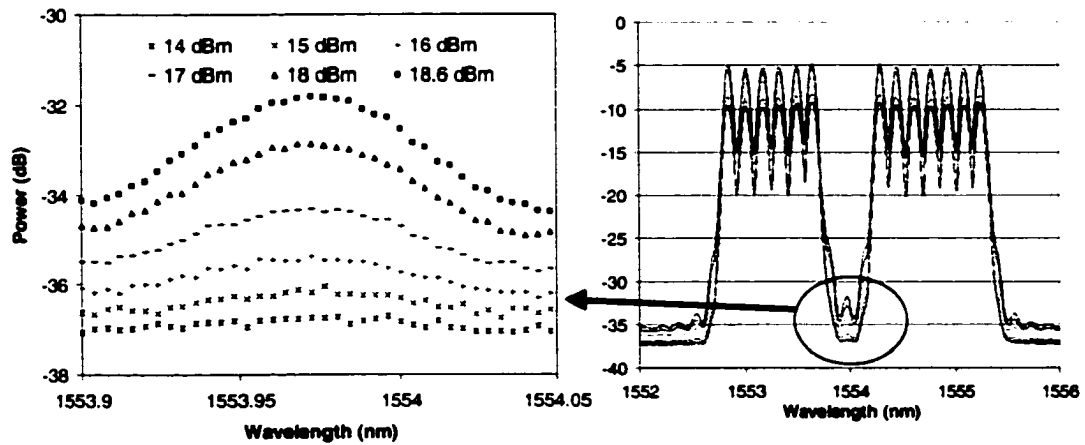


Figure 4.27: FWM-generated Distortion as a Function of the Launched Power for Duobinary Signaling

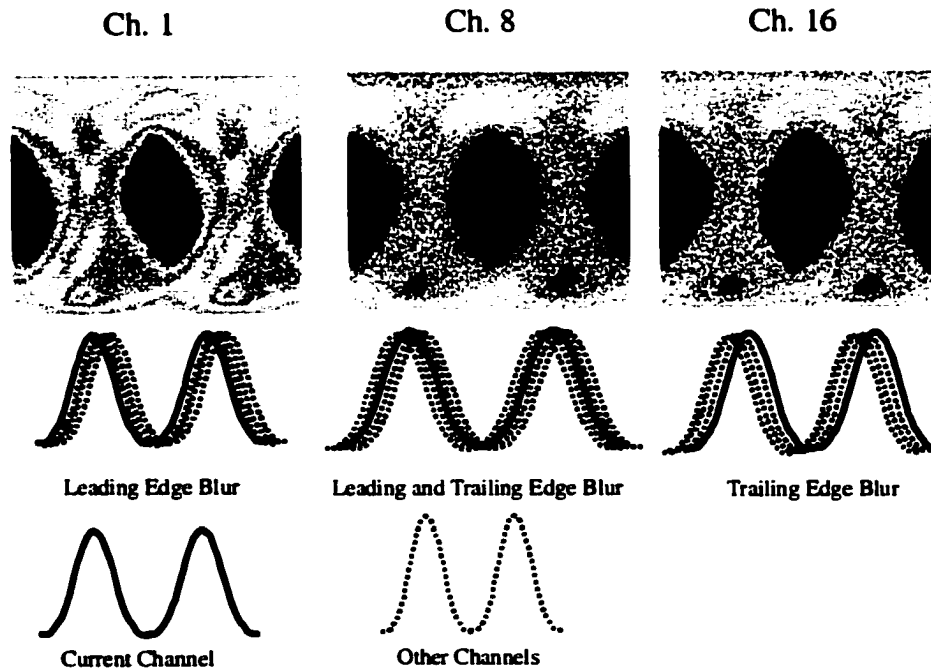


Figure 4.28: Eye diagram after 170 km of Propagation for the Duobinary Format

Figure 4.29 plots the measured Q values of the three formats. The duobinary format has Q values of about 0.5 dB less than the other two formats. In a 20 GHz ultra-

dense WDM system, the duobinary format still does not show the full expected benefits over the other two formats. One major reason is likely that the initial eye penalty for the duobinary format is more severe than was predicted by the simulations because of the imperfect implementation.

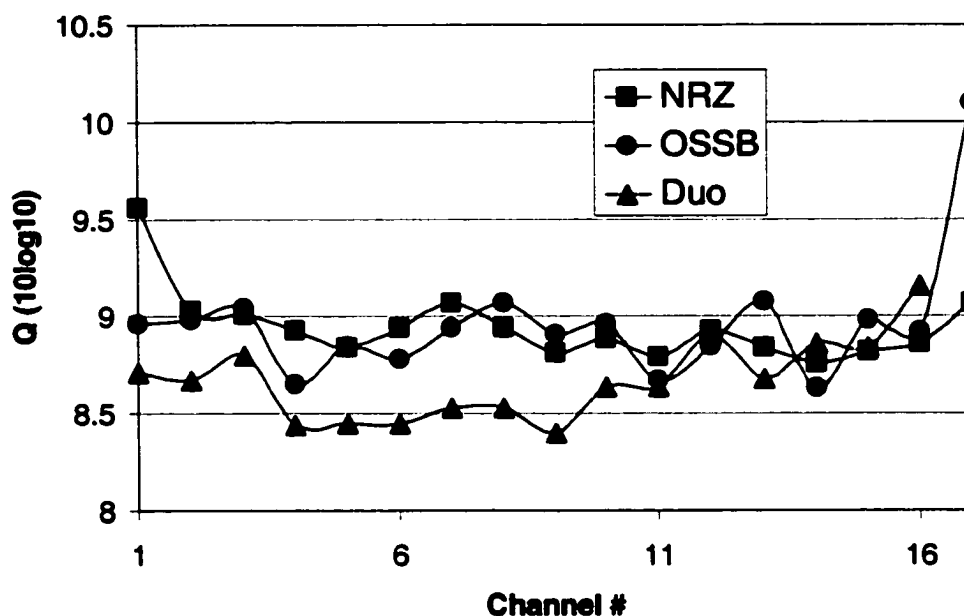


Figure 4.29: Q Comparison of the Three Formats in Single-span Configuration

4.7. Multi-Span Terrestrial System Experiments

The multi-span experiment was carried out using a re-circulating loop. For a simple set-up, the re-circulating loop could be configured to simulate one fiber span per one re-circulation. By re-circulating the WDM signal multiple times inside the loop, the set-up could simulate multi-span propagation. The advantage of using the re-circulating-loop is the reduction in the number of system components. For a more complex set-up, each loop could be configured to simulate several spans of fibers. This provided more flexibility when performing experiments. For this research, the simple set-up was used. A brief explanation of the operation of the re-circulating loop is given below.

The operation of the re-circulating loop can be broken down into two periods, namely, the loading period and the circulating period. **Figure 4.30** shows the schematic diagram of the re-circulating loop set-up for multi-span experiments. The acousto-optic

modulator (AOM) in the figure was used as an optical switch. During the loading period, AOM1 before the loop (before the right 3dB coupler) is turned on. Meanwhile AOM2 inside the loop is turned off. This allows the WDM signal to enter the loop through a 3 dB coupler, until the signal propagates around the entire loop. Because AOM2 is off, the optical signal cannot re-circulate, and the over-loaded signal is simply dissipated inside AOM2. The switching operations are executed by an electronic controller.

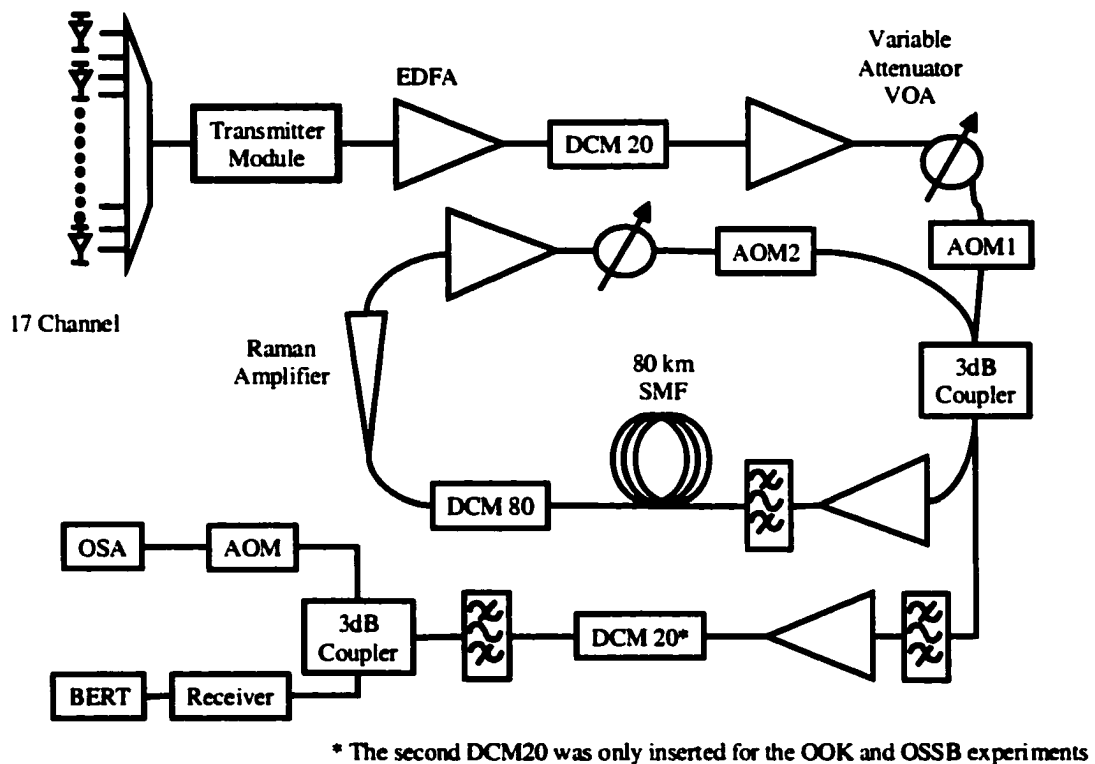


Figure 4.30: Experimental Setup for Multi-span Experiment using SMF

After the loading period, AOM1 is turned off and AOM2 is turned on. Thus, the signal from the transmitter side cannot enter the loop and is simply dissipated in AOM1. The pre-loaded signal inside the loop, on the other hand, continues to re-circulate inside the loop via the 3dB coupler.

The 3dB coupler shown in the figure has two input and two output ports. The two input ports are connected to the two AOMs. One output port is connected to the entrance of the re-circulating loop. The other output is connected to the path linked to the

receiver. Thus, during both the loading and re-circulating periods, there is always an optical signal leaving the 3dB coupler and entering into the optical receiver. For the BER measurement, these two periods are repeated iteratively.

The top diagram of **Figure 4.31** shows the profile of the optical signal leaving the loop. The x-axis in the diagram is time. The y-axis shows the magnitude of the optical power of the composite WDM signal leaving the loop. As shown in the figure, during each iteration, only a fraction of the time period corresponds to one particular loop propagation. Thus, the BERT is required to switch in a gating mode in order to properly sample and count the BER of the signal that travels the specific loop in each iteration. The gating control signal is also depicted **Figure 4.31**. The detailed operation of the re-circulating loop can be found in existing manuals from the manufacturers [73, 74].

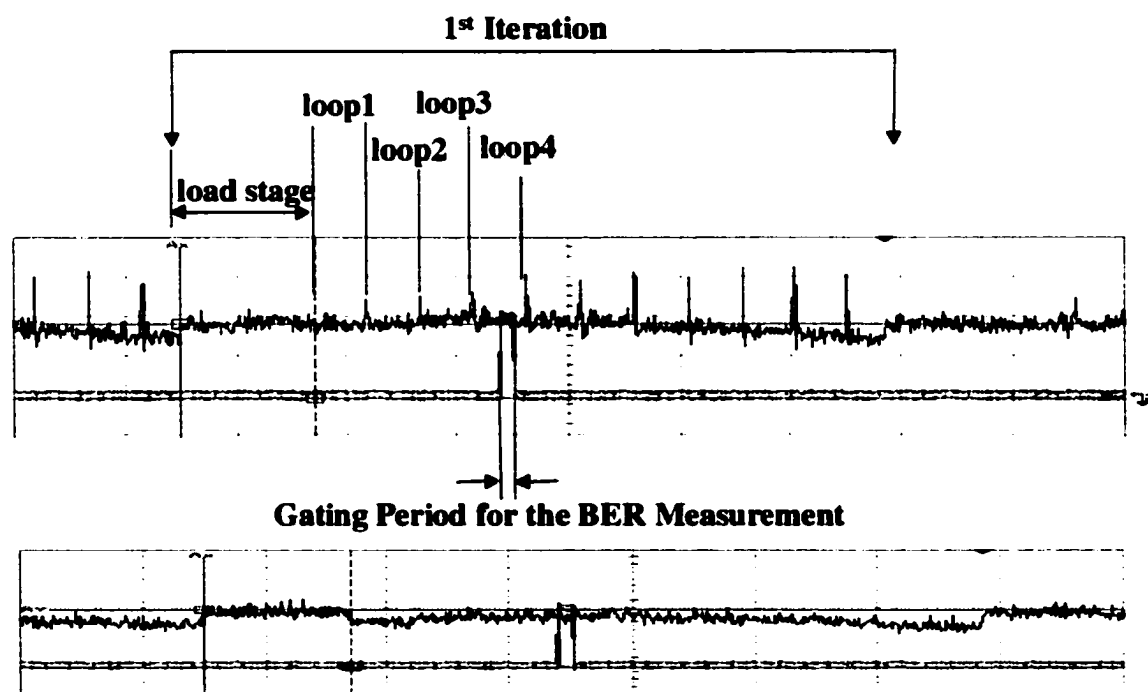


Figure 4.31: Optical Output from the Re-circulating Loop

In **Figure 4.31**, both the top and bottom diagrams show the profile of the signal leaving the loop. The only difference between these two diagrams is that the top diagram has spikes at the beginning of each loop-propagation. This is due to the fact that the polarization of the signal continuously evolves as it propagates along the fiber. As a result, there is a possibility that in one loop the ion population inversion of one

polarization of the Erbium-doped fiber (EDF) is maintained because the propagating signal has its polarization aligned with the other polarization of the EDF. In the next loop, the propagating signal can change its polarization such that its polarization is close to the polarization of the EDF, which has most of the ions in the excited state. Consequently, the signal receives a huge transient amplification and the spike occurs. The transient response would be damped gradually as the EDFA re-establishes equilibrium. The top diagram indeed depicts this phenomenon. The bottom diagram was captured after changing the signal polarization waiting until after the spikes disappeared. To protect the system components, it is better to remove this transient response.

There is one major difference between the simulations and the actual experiments. The DCM was assumed to be a linear device in the simulations, one that does not introduce any nonlinear effects into the signal. In the actual system, the DCM has a much smaller effective core area than either the SMF or NZDSF. Thus, with the same launched power, a stronger nonlinear fiber effect should occur in the DCM. For 50 GHz channel spacing, the nonlinear fiber effect of the DCM is not that important. However, for the case of 20 GHz spacing, the nonlinear effect becomes important and the placement of the DCM becomes crucial. Typically, the DCM is inserted in between the amplifying stages within an EDFA for both 50 GHz or 100 GHz spaced systems [71]. For a 20 GHz system, the intermediate signal power inside the EDFAs is still high enough to generate significant nonlinear effects in the DCM. In addition, the nonlinear effects generated in the DCM could possibly cause more XPM distortion at the far end of the transmission link, as will be explained below.

For the simple case of a two-span WDM system with full span-by-span dispersion compensation, the nonlinear XPM phase distortion generated at the beginning of the first in-line DCM would propagate through the remainder of that DCM, the next fiber span, and the entire second DCM before arriving at the optical detector. Therefore, this phase distortion would have a residual dispersion equal to almost the dispersion in one DCM. As mentioned in Chapter 3, the large residual dispersion would greatly increase the XPM penalty. It can be deduced that for systems with more fiber spans, this kind of XPM distortion would be more severe because the phase change generated at each DCM would have large residual dispersion.

To suppress the nonlinear effects, the DCMs need to be placed before the in-line EDFAs. However, this would reduce the optical SNR as the power of the signal entering the EDFA is less. By placing the Raman amplifier between the DCM and the EDFA, this conflict can be partially solved. However, the pump power of the Raman amplifier must be well controlled to optimize the amplification to ensure that no significant phase change is induced in the DCM.

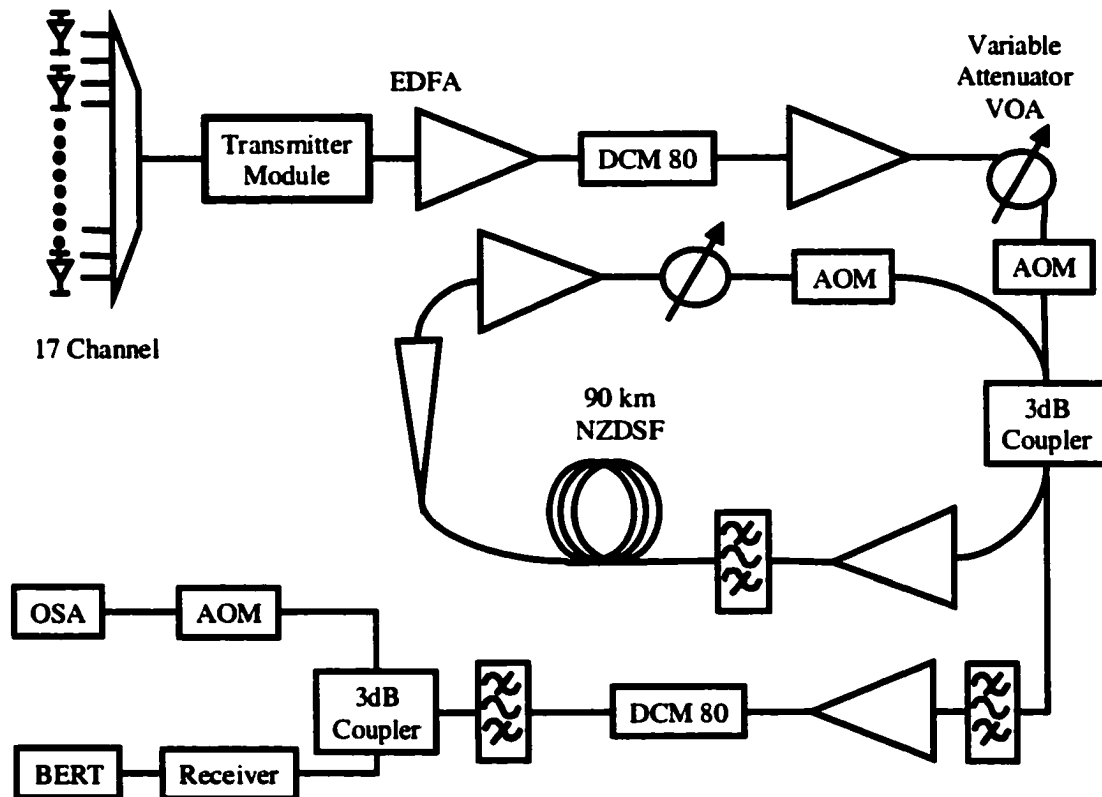


Figure 4.32: Experimental Setup for Multi-span Experiment using NZDSF

Figure 4.30 and Figure 4.32 show the schematic diagrams of the re-circulating experiments using SMF and NZDSF, respectively. The experimental set-ups of these two experiments are slightly different. The system with SMF has both pre- and post-dispersion compensations with the in-line dispersion compensation. The dispersions for the SMF and the inline DCM are 1443.73 ps/nm (80 km) and -1323 ps/nm, respectively. This is equivalent to 9% under-compensation for each fiber span. The dispersions for the pre- and post- compensations are -340 ps/nm and -332 ps/nm, respectively. This system is roughly optimized for 7-loop circulation, which follows the ‘50-50’ compensation

scheme mentioned in Chapter 3. The system with NZDSF (**Figure 4.32**), on the other hand, has no in-line DCM: only pre- and post-dispersion compensations are available. The dispersions of the pre- and post-compensation in the NZDSF system are -1323 ps/nm and -1316 ps/nm. The NZDSF has 424.84 ps/nm of dispersion (90 km). The reason for this arrangement is to allow the Raman amplifier to operate at full strength, which can help to increase the optical SNR. The disadvantage of this scheme is that more residual dispersion is present. However, the NZDSF has only 25% of the dispersion as compared to the SMF. Thus, it is worthwhile to examine whether or not this scheme would give better performance. If the dispersion scheme used for the SMF system is also used for the NZDSF system, we would expect that the resulting performance would not be as good as for the SMF. This reason is that, as shown in Chapter 3, the penalty from the nonlinear fiber effects is less for the SMF because of its large effective core area.

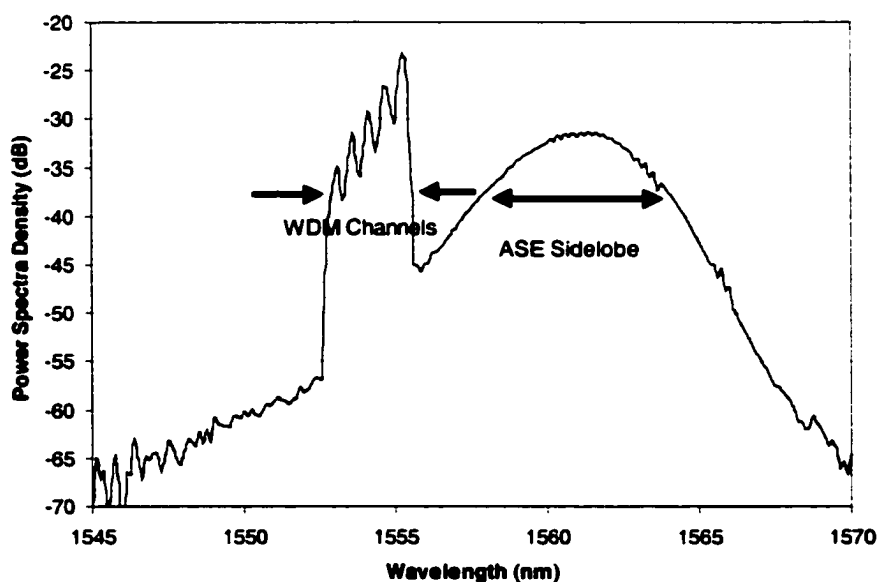


Figure 4.33: Illustration of the Build-up of the ASE-noise Sidelobe

For both systems shown in **Figure 4.30** and **Figure 4.32**, an optical filter was placed inside the loop. The function of the optical filter is to suppress the generation of the out-of-band ASE sidelobe, as shown in **Figure 4.33**. The sidelobe shown in the figure centered at 1560 nm was generated by the ASE noise accumulated after multi-loop propagation when the optical filter was not installed. Since the EDFAs have to amplify both the WDM signal and the out-of-band ASE sidelobe, the optical SNR would drop

faster as the signal propagates. To suppress this ASE sidelobe, an optical filter with 3 nm bandwidth was placed inside the loop. The bandwidth of this filter is just wide enough to allow all 17 WDM channels to pass through; meanwhile the out-of-band ASE noise is filtered away.

Another difference between the simulations and the experiments is the gain tilt of the EDFA. In the simulations, the EDFA is assumed to have an ideal response, which amplifies all channels with the same gain factor. In practice, however, the EDFA does not amplify all channels equally. **Figure 4.34** compares the WDM spectrum after allowing the signal to circulate circulating for different numbers of loops. The figure shows that, at the output of the transmitter, the spectrum is reasonably flat, with a power difference of less than 2 dB among channels. However, after six circulation loops, the power difference between the first and last channels is close to 14 dB. This causes a large fluctuation in Q values among the channels. To solve this problem, a technique called pre-emphasis was used. Basically, this method pre-adjusts the power of the semiconductor lasers, so that the channels that are expected to have suffered greater attenuation are given higher initial power. The goal is to keep the optical SNR of all channels to be about the same upon their arrival at the square-law detector.

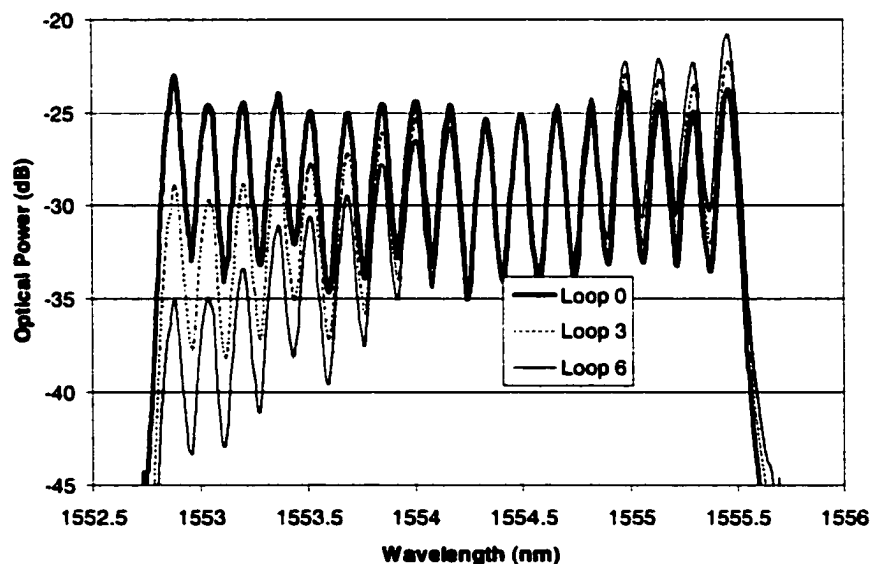


Figure 4.34: Illustration of Gain Tilt Effect

After making these optimizations, the total average signal power launching into each fiber span, for both SMF and NZDSF, was about 11.2 dBm. This is roughly close to -1.1 dBm per channel. For the SMF experiment, the total signal power leaving the Raman amplifier was 0.17 dBm; for the NZDSF experiment, the WDM signal leaving the Raman amplifier had a total power of 6.8 dBm.

Figure 4.35 plots the Q values of the three formats for the multi-span experiment using SMF. The Q values of the OOK and OSSB systems are about the same. The duobinary system, on the other hand, performs worse than the other two systems. For similar Q values, the duobinary signal can only propagate through 4 loops of SMF as compared to 6 loops for both the OOK and OSSB systems. The main cause of the poor performance of the duobinary format is possibly due to the initial eye penalty.

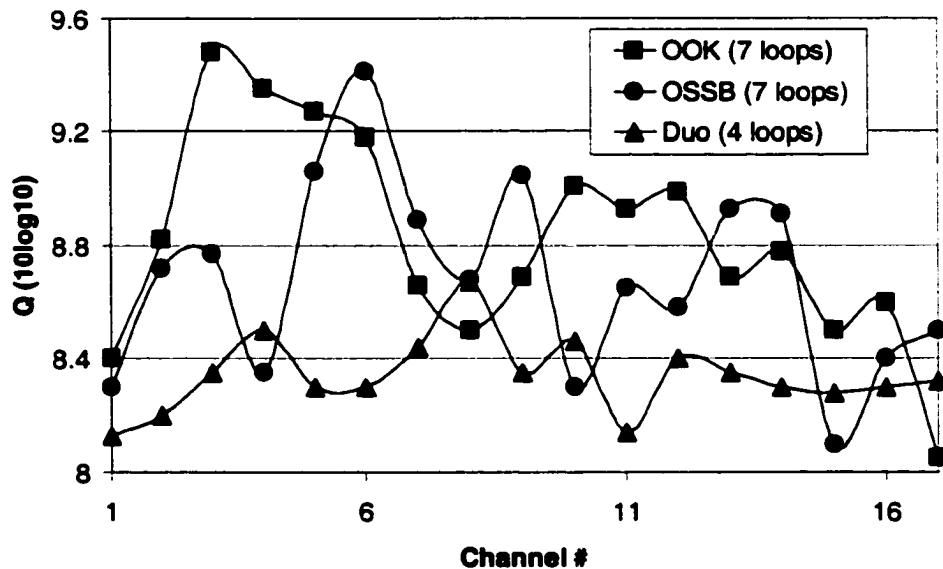


Figure 4.35: Q Values for Multi-span System using SMF

Figure 4.36 shows the Q measurement of the OOK format after circulating for 6 loops of NZDSF. The higher Q values of the last few channels are due to the fact that the pre-emphasis was set higher than required for these channels. In general, it is not easy to adjust the pre-emphasis to completely flatten the Q curve of a WDM system. For a shorter propagation distance (540 km compared to 560 km) and fewer loops (6 loops compared to 7 loops), the Q values for the NZDSF experiments are less than those for the

SMF experiments. The NZDSF simply induces stronger nonlinear fiber effects than SMF and is therefore not suitable for the contemplated ultra-dense WDM system. This agrees with the simulation results.

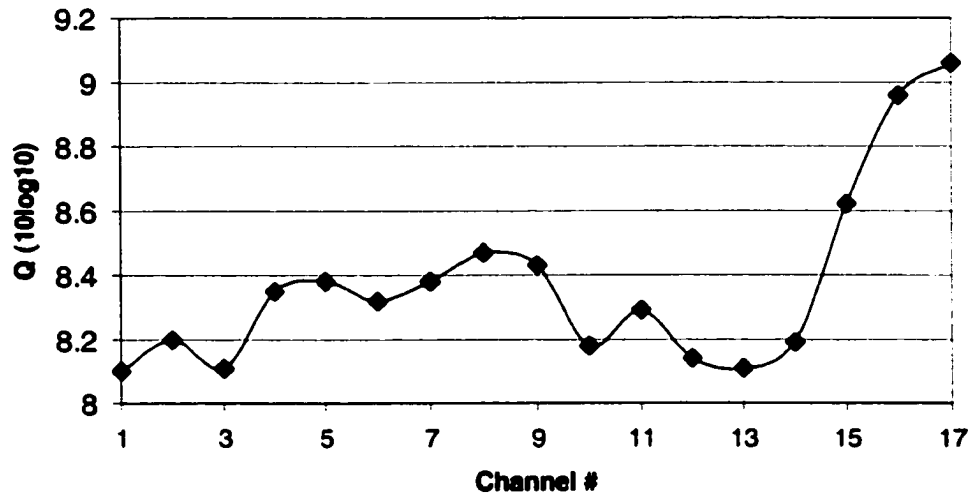


Figure 4.36: Q Measurement for OOK signal after circulating 6-loops with NZDSF

4.8. Summary

The experimental results show that neither the duobinary nor the OSSB formats appear to have any benefits over the OOK format. In fact, the OSSB format has very similar performance compared to the OOK format. The duobinary format clearly performs worse than the other two formats. The back-to-back duobinary signal has a smaller eye opening than predicted from simulations. This smaller eye opening leads to greater inter-symbol interference. As a result, the performance of the duobinary format in both single-span and terrestrial systems is worse than the other two formats.

Finally, due to the unrealistic correlation among channels in our experiments, the measured performance of the three formats was possibly better than what would be measured in an actual commercial system setting with uncorrelated channel signals.

5. Optical Single Sideband Duobinary Transmission

5.1. Introduction

Both OSSB and duobinary signals are capable of reducing the signal spectrum width by approximately one half. This chapter discusses the possibility of combining these two formats together to further reduce the signal bandwidth. Section 5.2 briefly introduces different types of OSSB formats that can be used in a fiber optic system. Section 5.3 discusses compatibility issues related to the OSSB and duobinary formats. Section 5.4 outlines the transmitter modification that is required for combined OSSB-duobinary transmission. Section 5.5 presents the scheme for converting a single-sideband signal into a double-sideband signal, which is a necessary step for the OSSB-duobinary system. Section 5.6 shows the single-channel performance of the OSSB-duobinary system using simulations. The findings of this chapter are summarized in section 5.7.

5.2. Optical Single Sideband Transmission

To the best to our knowledge, three types of single-sideband signals can be used in an optical transmission system. Each of these SSB signals can be implemented in more than one way. Most of the implementations require the generation of the Hilbert transform. In the Fourier domain, the Hilbert transform can be expressed as

$$H(\omega) = \begin{cases} -j & , \omega > 0 \\ 0 & , \omega = 0 \\ j & , \omega < 0 \end{cases} \quad (5.1)$$

Essentially, the Hilbert transform adds a 90° phase shift (negative in the upper sideband and positive in the lower sideband) to the frequency-translated signal spectrum.

5.2.1 Conventional Single-sideband Signal

The conventional SSB signal can be expressed as

$$A_{SSB,convention}(t) = A(t) + jh\{A(t)\} \quad (5.2)$$

where $h\{\}$ denotes the Hilbert transform in the time domain. Substituting (5.1) into (5.2), it can be seen that the lower sideband of the signal, A , is cancelled by its Hilbert transform, while the upper sideband simply has its magnitude doubled. If the positive sign in (5.2) is instead negative, then the upper signal sideband will be cancelled and the resultant signal is referred to as a lower SSB signal [hence we get the upper SSB for (5.2)]. There is no special requirement on the signal A for the SSB conversion. The major problem with conventional single sideband signals is that an additional optical signal processing step is required at the end of the transmission link for proper detection. More details will be mentioned in section 5.3.

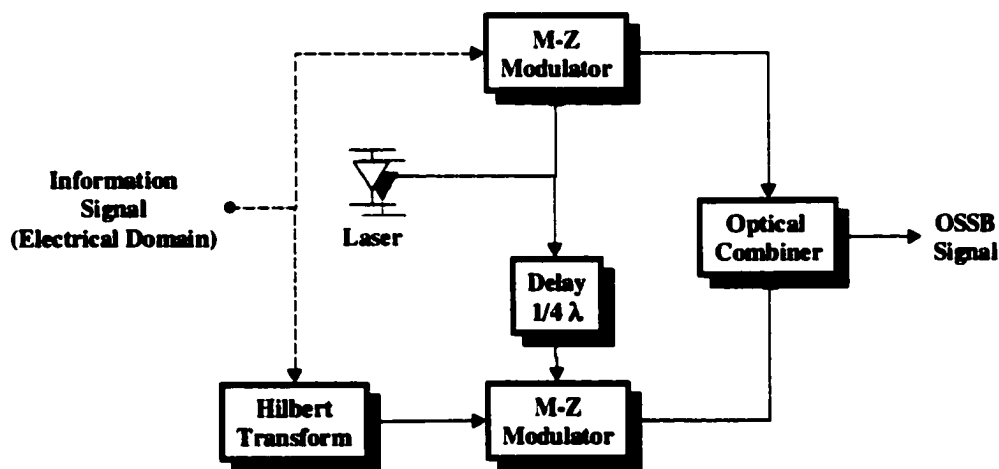


Figure 5.1: Conventional Optical SSB Signal Generator (solid line-electrical path, dotted line-optical path)

There are two ways of implementing a conventional SSB signal. Figure 5.1 shows one of the implementation schemes. It requires two optical modulators. The relative time delay between the two optical paths leading to the two optical modulators is $1/4$ of the carrier wavelength. In practice, the Hilbert transform shown in the figure can only be approximated using a tap-and-delay circuit (i.e. transversal filter) with appropriately set tap weights. The second implementation scheme uses an optical filter to remove one of the two sidebands. Mathematically, the removal of one sideband by

optical filtering is equivalent to the operation described by (5.2). Such an optical filter would be placed immediately after a conventional OOK modulator. The major problem with this implementation scheme is that actual optical filters do not have the required ideal rectangular filter shape. There is always a transition region between the pass-band and the stop-band of a real optical filter. Due to this transition region, a portion of the supposedly eliminated sideband still remains after the filtering and thus the resulting signal is only vestigial-single-sided (VSB).

5.2.2 Compatible Single-sideband Signal

The second type of SSB signals is called a compatible sideband (CSSB) signal. Basically, the single-sidedness of the CSSB signal is achieved through pole-zero cancellation between the optical OOK signal and an additional phase term. The following paragraph briefly describes the pole-zero cancellation method from [75].

If a signal is always positive and band-limited, it can be described by a product-of-sum expression as follows:

$$A_{positive}(t) = K \prod_{n=1}^N (1 - b_n e^{j\omega_n t}) (1 - b_n^* e^{-j\omega_n t}) \quad (5.3)$$

where $|b_n| < 1$, K is a constant, and $*$ denotes the complex conjugate. The above equation is derived from the Fourier series of the signal (more details can be found in [75]). Taking the natural logarithm of (5.3), we obtain

$$\ln [A_{positive}(t)] = \ln(K) + \sum_{n=1}^N \ln(1 - b_n e^{j\omega_n t}) + \sum_{n=1}^N \ln(1 - b_n^* e^{-j\omega_n t}) \quad (5.4)$$

Since $|b_n| < 1$, the $\ln(1 - b_n e^{j\omega_n t})$ terms in the first complex geometric series have all zeros outside the unit circle of the complex plane. Thus this series is analytic (pole-free) within the unit circle. Following Cauchy's integral theorem, a function is upper single-sided if the function is analytical within the unit circle. Similarly, the second expression is lower single-sided because the $(1 - b_n^* e^{-j\omega_n t})$ terms are zero-free outside the unit circle. Taking the Hilbert transform of (5.4), the $\ln(k)$ term vanishes because it represents a zero-frequency tone in the Fourier domain. The second and third terms in (5.4) are multiplied

by $-j$ and j , respectively, because of the single-sidedness of these two terms in frequency domain [see eq. (5.1)]. Thus, the Hilbert transform of (5.4) becomes

$$\begin{aligned} h\{\ln[A_{positive}(t)]\} &= -j \sum_{n=1}^N \ln(1 - b_n e^{j\omega_0 t}) + j \sum_{n=1}^N \ln(1 - b_n^* e^{-j\omega_0 t}) \\ &= -j \ln\left(\prod_{n=1}^N \frac{(1 - b_n e^{j\omega_0 t})}{(1 - b_n^* e^{-j\omega_0 t})}\right) \end{aligned} \quad (5.5)$$

This is the expression for the additional phase term that multiplies with the optical OOK signal when generating the CSSB signal. Mathematically, the compatible single-sideband signal can be expressed as

$$A_{SSB,compatible}(t) = A_{positive}(t) \exp\left(jh\{\ln[A_{positive}(t)]\}\right) \quad (5.6)$$

Substituting (5.3) and (5.5) into (5.6),

$$\begin{aligned} A_{SSB,compatible}(t) &= K \prod_{n=1}^N (1 - b_n e^{j\omega_0 t}) (1 - b_n^* e^{-j\omega_0 t}) \ln\left(\prod_{n=1}^N \frac{(1 - b_n e^{j\omega_0 t})}{(1 - b_n^* e^{-j\omega_0 t})}\right) \\ &= K \prod_{n=1}^N (1 - b_n e^{j\omega_0 t})^2 \end{aligned} \quad (5.7)$$

As mentioned previously, the $(1 - b_n e^{j\omega_0 t})$ terms are zero-free inside the unit circle. The squaring operation in (5.7) merely changes the original zeros from first order into second order, which means the signal is still analytic inside the unit circle and thus the signal is still single-sided. Consequently, the expression in (5.7) contains only one sideband with slightly bigger bandwidth because of the second-order zeros.

The advantage of the CSSB signal is that, except for the modification of the transmitter, no additional modification is required for the rest of the fiber optic system. Since the square-law detector removes any phase information of the detected signal, the additional phase term of the CSSB signal does not affect anything at all. The major disadvantage of the CSSB signal is that the information signal needs to be positive because the generation of the additional phase term requires first obtain the natural logarithm of the signal. Also, the implementation of the CSSB signal requires relatively sophisticated signal processing at the transmitter.

Figure 5.2 shows one way of implementing the CSSB signal in the fiber optic system. The difficulty of this implementation comes from the generation of the natural logarithm of the signal and the approximation of the Hilbert transform. A limiting amplifier could be used to approximate the natural logarithm circuit. As far as I am aware, CSSB transmitter has never been implemented in fiber-optic systems.

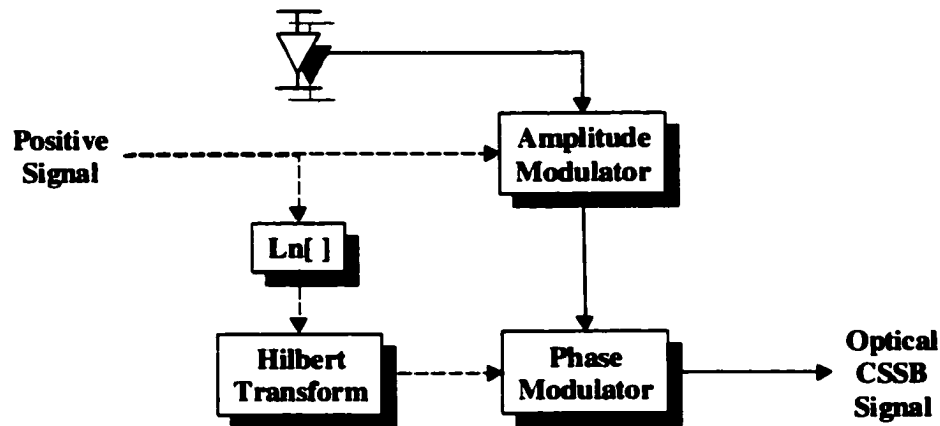


Figure 5.2: CSSB Signal Generator for a Fiber Optic System (solid line-electrical path, dotted line-optical path)

5.2.3 Approximated Single-sideband Signal

The third SSB signal was developed by Sieben at TRLabs [54]. It is a hybrid of the conventional SSB and the CSSB signals. The single-sidedness of Sieben's SSB signal is also achieved by multiplying the optical OOK signal by an additional phase term. The additional phase term is the Hilbert transform of the signal, instead of the Hilbert transform of the natural logarithm of the signal, as in CSSB. Mathematically, Sieben's SSB signal can be expressed as

$$A_{SSB, Sieben}(t) = A_{positive}(t) \exp(h\{A_{positive}(t)\}) \quad (5.8)$$

The single-sidedness of this SSB signal can be shown by viewing $A_{positive}$ as an optical signal consisting of AC components and a normalized DC (to 1) component ($A_{positive} = A_{a.c} + 1$). By expanding the exponential term in (5.8) as a Taylor series about zero gives

$$\exp(h\{A_{positive}(t)\}) = \sum_{n=0}^N j^n h\{A_{positive}(t)\}^n \quad (5.9)$$

Substituting (5.9) into (5.8),

$$A_{SSB,Sieben}(t) = 1 + A_{a.c}(t) + jh\{A_{positive}(t)\} + jA_{a.c}(t)h\{A_{positive}(t)\} + \dots \quad (5.10)$$

The Hilbert transform of $A_{positive}$ is the same as that of $A_{a.c}$ because the DC component is removed during the transformation. Thus, the first three terms in (5.10) form the conventional SSB signal, as in (5.5). Sieben's SSB signal is only an approximated SSB signal because of the presence of the higher-order terms of the Taylor series. The relative magnitude of these higher order terms can be decreased by reducing the modulation index of the optical OOK signal. Equations (5.8) and (5.10) indicate that Sieben's scheme also requires that the optical OOK signal to be a positive signal. In addition, it should be noted that the above analysis does not take into account the cosine transfer function of the intensity modulator, which increases the number of higher order terms in (5.11).

As with the CSSB signal, no extra modification is required at the receiver end for this scheme. However, Sieben's scheme is better than the CSSB scheme in terms of its practicality for implementation. The disadvantage of his scheme is that the signal can only be approximately single-sided. Also, there is a trade off between the eye opening of the received signal and the quality of the single-sidedness of its frequency spectrum. Reducing of the modulation depth improves the single-sidedness but reduces the eye opening. The implementation of Sieben's scheme is similar to the CSSB scheme except that the natural-logarithm operator is removed. Sieben also showed that his scheme could be implemented using either one or two M-Z modulators [54].

5.3. Compatibility Problems of Single-sideband Signals with Duobinary Signals

One of the distinctive characteristics of the duobinary signal is that its frequency spectrum contains no optical carrier (i.e.; it is a suppressed-carrier signal). As discussed in section 5.2, both CSSB and Sieben's SSB signal require the present of the optical

carrier because both types of SSB signal requires the optical OOK signal to be positive. Thus, only the conventional SSB signal is compatible with the duobinary signal. The major problem of combining the conventional SSB signal with the duobinary signal is the extra optical signal processing at the ends of the fiber link. Ignoring both chromatic dispersion and nonlinear fiber effects, square law detection of the conventional optical SSB signal produces the following electrical signal:

$$\begin{aligned}
 S_{REC,SSB,convention}(t) &= |A_{SSB,convention}(t)|^2 \\
 &= |A(t) + jh\{A(t)\}|^2 \\
 &= A^2(t) + h\{A(t)\}^2
 \end{aligned} \tag{5.12}$$

Equation (5.12) shows that, in addition to the usual squared OOK signal, the received electrical signal contains an extra term, which is the square of the Hilbert transform of the optical OOK signal. This additional term is a source of distortion in the received signal.

The implementation of the OSSB-duobinary system involves two parts: (1) converting the duobinary signal from double-sideband into single-sideband at the transmitter, and (2) solving the distortion problem described in (5.12).

5.4. Transmitter Module for a Single-sideband Duobinary Signal

According to the discussion in section 5.2.1, the OSSB-duobinary signal can be generated based on the scheme shown in **Figure 5.1**. **Figure 5.3** shows a complete schematic diagram for the OSSB-duobinary transmitter including the conversion of the electrical OOK signal to the duobinary signal.

Sieben used a 5-tap transversal filter to approximate the Hilbert transform. The tap weights of Sieben's transversal filter are the five most significant coefficients of the Fourier series of the impulse response of the Hilbert transform. This method of generating the Hilbert transform can be improved simply by optimizing the tap weights. The goal of the optimization is to minimize the residual power in the cancelled sideband.

The signal spectrum after the optimization is shown in **Figure 5.4**, which shows reasonable sideband cancellation.

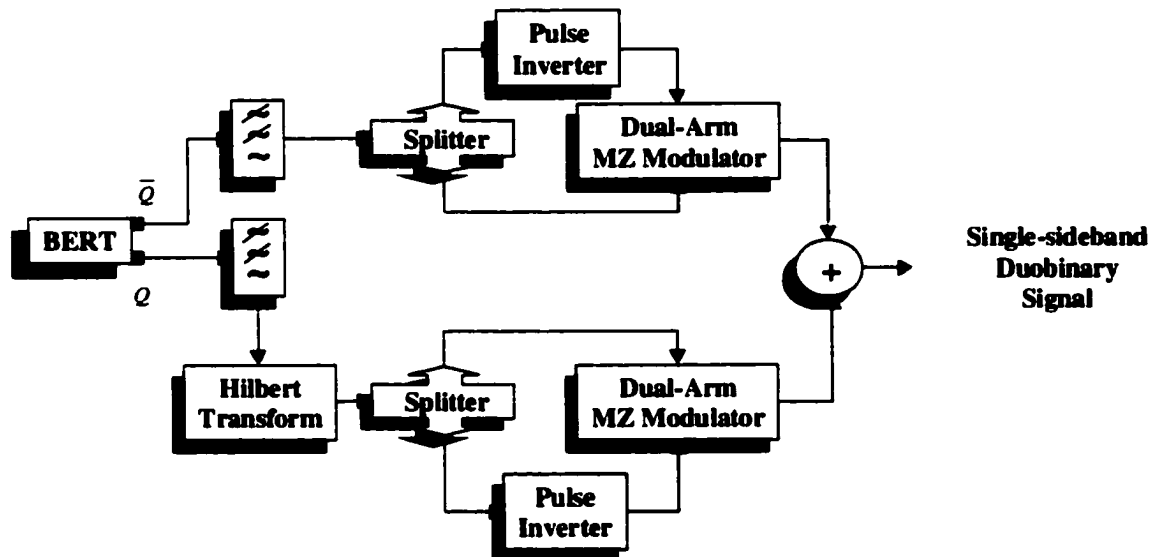


Figure 5.3: Phase Cancellation Method for Generating the OSSB-Duobinary Signal

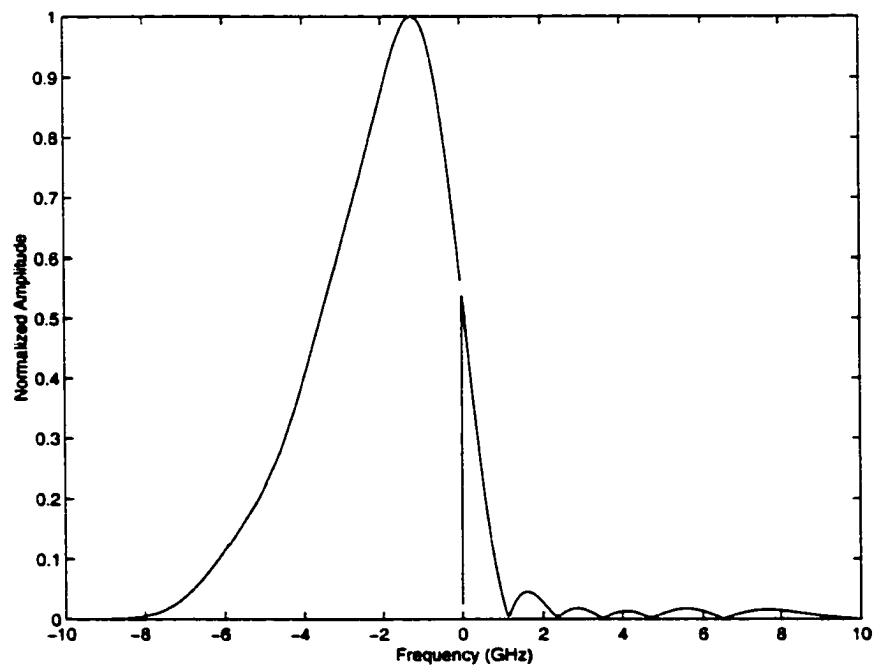


Figure 5.4: Field Spectrum of the Single-sideband Duobinary Signal using an Optimized 5-tap Transversal Filter to Realize the Hilbert Transform

5.5. Single-Sideband to Double-Sideband Conversion

The distortion predicted in (5.12) can be avoided in two different ways. One way of solving the problem is to use coherent detection [53]. A second way is first to convert the OSSB-duobinary signal back to double sideband before square-law detection. The following describes our new conversion scheme.

To simplify the analysis, both chromatic dispersion and nonlinear fiber effects will be ignored. With this assumption, the optical signal, $s_{ssb,duo}$, at the far end of the optical link can be described as follows

$$s_{ssb,duo}(t) = s_{duo}(t) + jh[s_{duo}(t)] \quad (5.13)$$

where s_{duo} denotes the duobinary signal. The double-sided duobinary signal can be retrieved by removing the second term in (5.13). This can be done by adding the conjugate of $s_{ssb,duo}$ to itself

$$s_{ssb,duo}(t) + s_{ssb,duo}^*(t) = s_{duo}(t) + jH[s_{duo}(t)] + s_{duo}(t) - jH[s_{duo}(t)] = 2s_{duo}(t) \quad (5.14)$$

One type of frequency shifter uses the FWM effect to perform the necessary single-sideband to double-sideband conversion. A frequency shifter is used for switching the optical channel from one wavelength slot to another wavelength slot. For instance, some of the current metropolitan networks still use the wavelength allocations in the 1310 nm communication window. In order to connect these metropolitan networks to the continental SONET network, the 1310 nm optical channels need to be shifted to the 1550 nm communication window.

The basic operating principle of this frequency shifter is to combine a high-power continuous-wave pump light signal with the optical signal to be shifted [76]. The spacing between the pump light and the optical signal is set to equal half the frequency spacing between the original wavelength slot and the new wavelength slot. The combined signal then propagates through an optical medium (not necessarily optical fiber) that has very small or no chromatic dispersion to avoid excess signal distortion. The four-wave mixing of the optical medium mixes the high-power light with the optical signal and generates the conjugate of the optical signal located that is frequency-shifted to the new wavelength slot.

This frequency-shifter must be modified to generate a signal conjugate at the same wavelength as the original optical signal. To achieve this, two pump lights are required [76]. The light source frequencies are located at both sides of the frequency of the optical signal. The frequency spacing between the two high-power pump signals should be wide enough so that, after the conversion, the high-power signals can be easily filtered out.

Figure 5.5 shows the schematic diagram of this single-sideband-to-double-sideband converter. A semi-conductor amplifier (SOA) is used as the optical medium for performing the four-wave mixing. The advantage of the SOA over dispersion-shifted fiber is that the chromatic dispersion is very small over a wide range of frequencies (across the entire band from 1530-1560 nm) [77]. The mechanism for this converter is explained below.

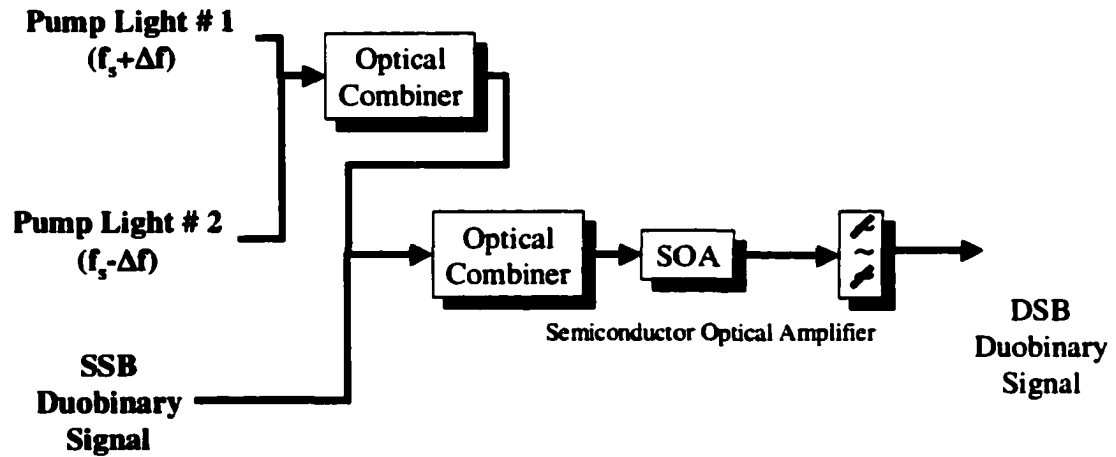


Figure 5.5: Single Sideband-to-Double-Sideband Converter

The combined optical signal, $A(T, z)$, containing the two pump lights and the OSSB-duobinary signal can be written as

$$A(T, 0) = \sqrt{P_{peak}} U(T, 0) \quad (5.15)$$

$$U(T, 0) = 2 \sqrt{\frac{P_0}{P_{peak}}} \cos \omega_{lo} T + \frac{a(T, 0)}{\sqrt{P_{peak}}} \quad (5.16)$$

where P_{peak} is the peak optical power of the combined signal; P_0 is the power of each pump light signal (assuming that both pump signals have the same optical power and the same phase); $a(T,z)$ is the OSSB-duobinary signal; ω_o is the angular frequency equal to half the frequency separation between the two high-power pump lights. The first term in (5.16) describes the two high-power pump lights. When this signal is launched into an optical medium with zero dispersion, the output signal at distance z , $U(T,z)$, has an analytical solution expressed as (derived from the NLSE, see Chapter 2)

$$U(T, z) = U(T, 0) \exp \left[-j\gamma P_{peak} |U(T, 0)|^2 L_{eff} \right] \quad (5.17)$$

$$L_{eff} = \frac{[1 - \exp(-\alpha L)]}{\alpha}$$

where L is the length of the optical medium. The squared magnitude of $U(T,0)$ can be expanded as

$$|U(T,0)|^2 = \frac{4P_0}{P_{peak}} \cos^2 \omega_o T + \cos \omega_o T \left[a(T,0) + a^*(T,0) \right] \sqrt{\frac{4P_0}{P_{peak}}} + \frac{|a(T,0)|^2}{P_{peak}} \quad (5.18)$$

Let $K = -\gamma P_{peak} L_{eff}$, then $U(T,z)$ can be written as

$$U(T, z) = \left[2 \sqrt{\frac{P_0}{P_{peak}}} \cos \omega_o T + \frac{a(T, z)}{\sqrt{P_{peak}}} \right] \exp \left(jK \frac{4P_0}{P_{peak}} \cos^2 \omega_o T \right) \quad (5.19)$$

$$\exp \left\{ jK \cos \omega_o T \left[a(T, z) + a^*(T, z) \right] \sqrt{\frac{4P_0}{P_{peak}}} \right\} \exp \left[jK \frac{|a(T, z)|^2}{P_{peak}} \right]$$

The exponent in the third exponential factor is very small and so the factor can be approximated as 1. The exponent in the second exponential factor is also small and thus the factor can be approximated using Taylor series expansion as

$$\exp \left\{ jK \cos \omega_o T \left[a(T, z) + a^*(T, z) \right] \sqrt{\frac{4P_0}{P_{peak}}} \right\} = 1 + jK \cos \omega_o T \left[a(T, z) + a^*(T, z) \right] \sqrt{\frac{4P_0}{P_{peak}}} \quad (5.20)$$

The first exponential factor in (5.19) can be written as the sum of cosine and sine complex pairs. The cosine and sine terms can be further expanded into power series. The expanded expression for the first exponential factor is as follows:

$$\exp\left(jK \frac{4P_0}{P_{peak}} \cos^2 \omega_o T\right) = \sum_{n=0}^{\infty} (-1)^n \frac{(4KP_0 \cos^2 \omega_o T)^{2n}}{(2n)! P_{peak}^{2n}} + j \sum_{n=0}^{\infty} (-1)^n \frac{(4KP_0 \cos^2 \omega_o T)^{2n+1}}{(2n+1)! P_{peak}^{2n+1}} \quad (5.21)$$

With the above approximations and substitutions,

$$U(T, z) = X + Y \quad (5.22)$$

where

$$X = \frac{a(T, z)}{\sqrt{P_{peak}}} \left[\sum_{n=0}^{\infty} (-1)^n \frac{(4KP_0 \cos^2 \omega_o T)^{2n}}{(2n)! P_{peak}^{2n}} + j \sum_{n=0}^{\infty} (-1)^n \frac{(4KP_0 \cos^2 \omega_o T)^{2n+1}}{(2n+1)! P_{peak}^{2n+1}} \right] \quad (5.23)$$

$$\left\{ 1 + jK \cos \omega_o T [a(T, z) + a^*(T, z)] \sqrt{\frac{4P_0}{P_{peak}}} \right\}$$

$$Y = 2 \sqrt{\frac{P_0}{P_{peak}}} \cos \omega_o T \left[\sum_{n=0}^{\infty} (-1)^n \frac{(4KP_0 \cos^2 \omega_o T)^{2n}}{(2n)! P_{peak}^{2n}} + j \sum_{n=0}^{\infty} (-1)^n \frac{(4KP_0 \cos^2 \omega_o T)^{2n+1}}{(2n+1)! P_{peak}^{2n+1}} \right] \quad (5.24)$$

$$\left\{ 1 + jK \cos \omega_o T [a(T, z) + a^*(T, z)] \sqrt{\frac{4P_0}{P_{peak}}} \right\}$$

Note that (5.22)-(5.24) show that $U(T, z)$ contains a lot of harmonic terms located outside the OSSB-duobinary signal spectrum. These harmonic terms can simply be removed using an optical band-pass filter; therefore the remaining derivation can focus on the terms with spectra overlapped with the OSSB-duobinary signal spectrum (referred to as carrier terms in the following).

The expansion of X in (5.23) produces a complex power series of $\cos \omega_o t$. The $\cos^n \omega_o t$ term can be written as

$$\cos^n \omega_o T = \frac{(e^{j\omega_o T} + e^{-j\omega_o T})^n}{2^n} = \frac{e^{jn\omega_o T}}{2^n} \sum_{N=0}^n c_N e^{jN\omega_o T} \quad (5.25)$$

In this expression, except for the constant term, all other frequency terms are located outside the duobinary signal spectrum and thus can be neglected. Note that the exponent, n , is an odd number, so the $\cos^n \omega_o T$ does not have a constant term. Thus all odd power-order $\cos^n \omega_o T$ terms can be ignored. The second term in the last bracket of (5.23) can thus be ignored. The coefficients of the $\cos^n \omega_o T$ expansion can be calculated using the

binomial expansion. The coefficients of the M^{th} term in the series expansion of (5.25) where (the series begins with the smallest power of $\exp(j\omega_b t)$) is expressed as

$$c_M = \frac{n!}{M!(n-M)!} \quad (5.26)$$

The constant term of (5.25) is located at the middle of the series; therefore $M=n/2$, where n is an even number, for the constant term.

Given the above information, the carrier term of X , $X|_{\text{carrier}}$, can be expressed as

$$X|_{\text{carrier}} = \frac{a(T,0)}{\sqrt{P_{\text{peak}}}} \bullet \left[\sum_{n=0}^{\infty} (-1)^n \frac{(4KP_0)^{2n}}{(2n)! P_{\text{peak}}^{2n}} \frac{(4n)!}{2^{4n} (2n)! (2n)!} + j \sum_{n=0}^{\infty} (-1)^n \frac{(4KP_0)^{2n+1}}{(2n+1)! P_{\text{peak}}^{2n+1}} \frac{(4n+2)!}{2^{4n+2} (2n+1)! (2n+1)!} \right] \quad (5.27)$$

Similarly, the carrier term of Y can be expressed as

$$Y|_{\text{carrier}} = j \frac{4P_0}{P_{\text{peak}}} \left[a(T,0) + a^*(T,0) \right] \bullet \left[\sum_{n=0}^{\infty} (-1)^n \frac{(4KP_0)^{2n}}{(2n)! P_{\text{peak}}^{2n}} \frac{(4n+2)!}{2^{4n+2} (2n+1)! (2n+1)!} + j \sum_{n=0}^{\infty} (-1)^n \frac{(4KP_0)^{2n+1}}{(2n+1)! P_{\text{peak}}^{2n+1}} \frac{(4n+4)!}{2^{4n+4} (2n+2)! (2n+2)!} \right] \quad (5.28)$$

Expression (5.27) contains only the OSSB-duobinary terms while (5.28) contains the sum of both the OSSB-duobinary expression and its complex conjugate. The goal of the SSB-to-DSB conversion is to add the OSSB-duobinary signal with its conjugate with equal magnitude. Therefore, the X terms in (5.27) need to be small relative to the Y terms in (5.28).

The equations derived above were verified by comparing with simulations. The simulations used a perfect SSB duobinary signal for the SSB-to-DSB conversion. The lower sideband of the perfect OSSB-duobinary signal was removed by an ideal rectangular band-pass filter. A 511-bit PRBS with 128 samples per bit was used as the information source. Dispersion-shifted fiber (DSF) was used as the optical medium. It was assumed that the fiber has zero dispersion. The nonlinear refractive index, n_2 , of the DSF was set at $2.3 \cdot 10^{-20}$ m/W. The effective core area was 80 μm^2 . The fiber attenuation was 0.22 dB/km. The length of the fiber was 3 km. The two pump beams were separated

by 200 GHz. The simulated results are compared with the analytical prediction in **Figure 5.6**.

Figure 5.6 shows the magnitude of the carrier terms of X and Y [equations (5.27) and (5.28)] along with the corresponding eye opening of the received DSB-duobinary signal after square law detection. The figure shows that the DSB-duobinary signal has the maximum eye opening when the X term drops to zero. When the difference between the X and Y terms is minimized, the eye opening is also minimized (locally). This shows that the simulations agree with the theoretical prediction.

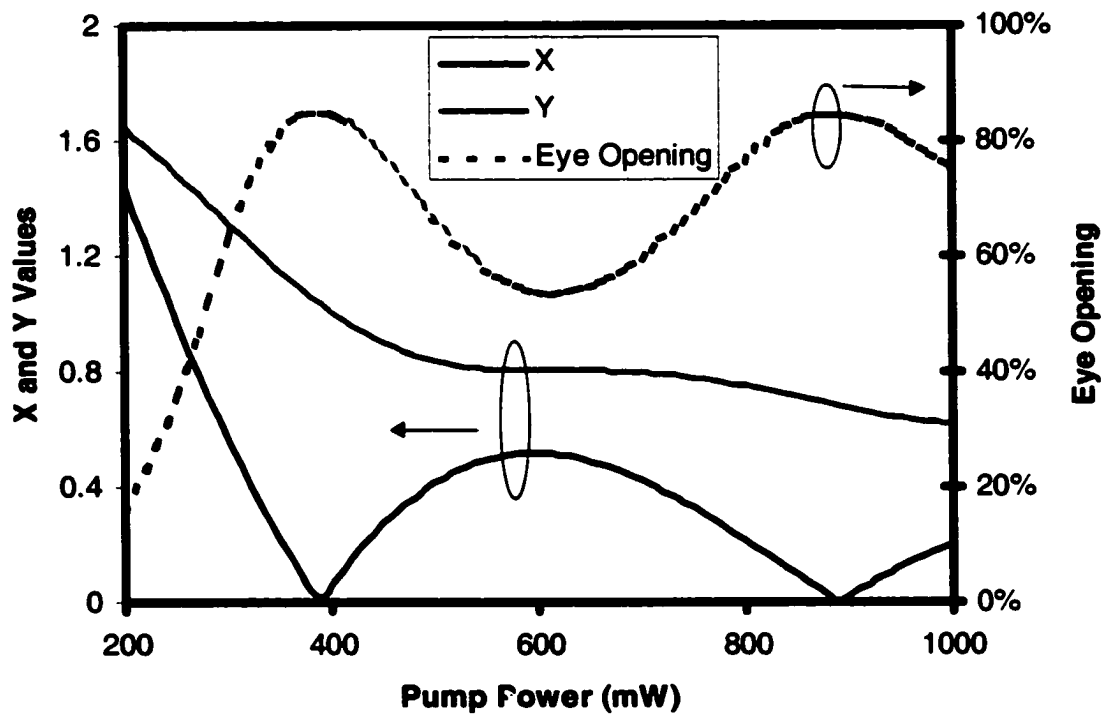


Figure 5.6: Plot of the X and Y Terms from Equation (5.22) and the Resulting Eye Opening of the Simulated SSB-to-DSB Signal

5.6. Single-channel Simulations and Analysis

Single-channel simulations, including fiber propagation effects, were also performed. The optical link consisted of five 80 km-spans of NZDSF fiber. The signal

power was recovered to its launch level at each fiber span input and the chromatic dispersion was fully compensated span-by-span. The ASE noise from the inline EDFAs was ignored. **Figure 5.7** and **Figure 5.8** show the eye openings of the final received DSB signals for both perfect OSSB- and vestigial-sideband- (VSB) duobinary modulations respectively. The perfect OSSB-duobinary signal was generated using an ideal rectangular optical filter to remove one sideband. The VSB-duobinary signal was obtained using the transmitter shown in **Figure 5.3**. **Figure 5.7** and **Figure 5.8** show that the VSB-duobinary signal actually performs better than the ideal OSSB-duobinary signal.

A closer examination of (5.13) shows that as long as both the duobinary signal and its approximated Hilbert transform pair are real signals, no distortion will be added during the SSB-to-DSB conversion. Thus, the VSB signal will not receive significant additional distortion during the conversion process. On the other hand, the figures show that the slightly larger bandwidth (less than 10%) of the VSB signal significantly improves the transmission performance (possibly due to the higher tolerance to the spectrum broadening caused by the self-phase modulation). For a transmission distance of 640 km, the received signal eye opening decreases by 13% for 1 dBm of launched power. At a launched power of 3 dBm, the quality of the signal starts to degenerate rapidly, suggesting that this transmission format is best operated between 1 and 3 dBm of launched power.

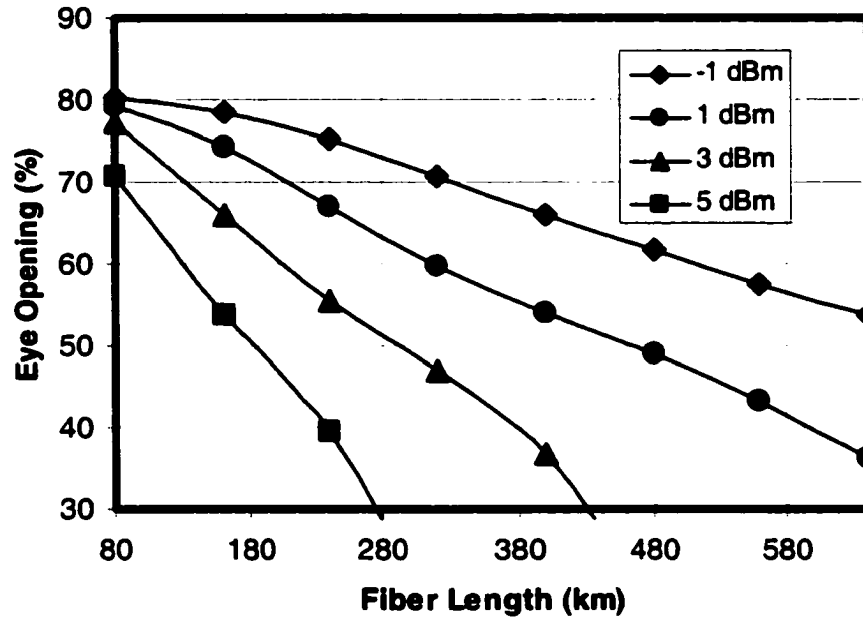


Figure 5.7: Received signal eye opening versus fiber length for Perfect OSSB Duobinary

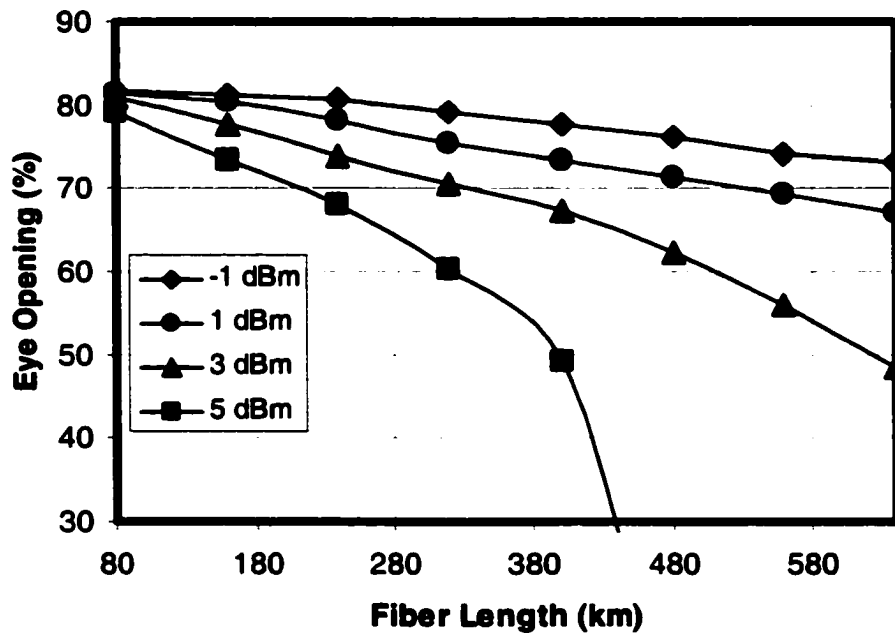


Figure 5.8: Received signal eye opening versus fiber length for VSB Duobinary

5.7. Summary

This chapter described a method for constructing an OSSB duobinary system. The results of the single-channel simulations were presented. The results indicated that the vestigial SSB duobinary signal can actually tolerate nonlinear fiber effects better than the perfect SSB duobinary signal. Also, it was found that for single-channel systems, the eye closure penalty is still acceptable if the average signal power is below 3 dBm. The performance of a multi-channel WDM system depends on the system configuration. Further simulations are required to better explore the potential of specific system configurations.

6. Investigation of Different RZ Formats

6.1. Introduction

This chapter considers a different kind of return-to-zero (RZ) format. In general, the RZ format performs better than the non-return-to-zero (NRZ; in this thesis, also referred to as the OOK) format because of the interaction between the self-phase modulation (SPM) and the chromatic dispersion [78]. Under certain system conditions, the RZ format is also less susceptible to both XPM and FWM. The following paragraphs briefly discuss the difference in various nonlinear fiber distortions between the NRZ and RZ formats.

The difference in the SPM distortion between the two formats is due to the difference in the pulse-to-pulse interaction. The pulses of the NRZ bit sequence have a relatively large overlap among neighboring bits because of the 100% duty cycle. By contrast, in for the RZ format, depending on the duty cycle, the overlap among neighboring pulses can be very small. This small overlap greatly suppresses the effects of the SPM. It is known that for a single Gaussian pulse, the combined effects of SPM and chromatic dispersion would not change the shape of pulse, but will simply change the width of the pulse [83]. Therefore, with proper dispersion control, the amplitude distortion due to the SPM distortion can be greatly reduced for single pulse propagation. As for multi-pulse propagation, the eye-closure penalty can be greatly suppressed for the RZ format if the overlap is small enough to avoid serious nonlinear interaction between neighboring pulses. As for the NRZ format, the pulse-to-pulse interaction simply cannot be avoided and hence the SPM penalty is higher.

As discussed in previous chapters, the XPM distortion is caused by phase modulation from neighboring channels. Due to the smaller duty cycle, the overall phase change for the RZ format within the nonlinear interaction portion of the fiber (at the beginning of each fiber span) can be greatly reduced under certain conditions. This is illustrated by a simple example of a two-channel system with single-pulse propagation in each channel [12]. In this system, a solitary pulse is launched into the fiber for each of the two channels, assuming that the pulse of channel 1 just trails in time the pulse of

channel 2. The transmission link is assumed to be a long span of SMF, and the channel spacing is assumed to be large (100 GHz). With this system setting, the two channels propagate at different speeds along the fiber. Assuming that channel 1 propagates faster than channel 2, the relative time delay between the two channels after 10 km of propagation could reach about 130 ps, which is more than one bit period. Thus, the pulse of channel 1 would overtake the pulse of channel 2 within the first 10 km. During this 10 km of propagation, the dispersion effect is negligible. The phase-to-amplitude conversion of the XPM distortion occurs mainly in the later portion of the fiber.

The chirping experienced by the pulse in channel 2 during this 10 km of propagation is illustrated in **Figure 6.1**. The x-axis is the time axis. Chirp is defined as the time derivative of the phase of the signal. A discussion of the phase change of a particular point in time would be meaningless unless it is in relation with a neighboring point. **Figure 6.1** captures three moments during the first 10 km of propagation: (1) the channel 1 pulse trailing the channel 2 pulse, (2) the channel 1 pulse overlapping with the channel 2 pulse, (3) the channel 1 pulse leading the channel 2 pulse. At moment (1), the leading part of channel 1 pulse overlaps with the channel 2 pulse. As a result, the chirp received by channel 2 is purely positive. At moment (2), the two pulses completely overlap in time with each other, and the chirp is very similar to the one induced by SPM. The leading edge of the channel 2 pulse has positive chirp and negative chirp is induced at the trailing edge. At moment (3), the channel 1 pulse passes through the channel 2 pulse and the induced chirp is purely negative. The overall chirp experienced by the channel 2 pulse after the 10 km of propagation would then be almost zero. Hence, the net XPM distortion experienced by the channel 2 pulse is very small. For the RZ format, the pulses are largely separated, and the process of XPM-induced phase change for each pulse would be very similar to the single-pulse case. As for the NRZ format, the pulses are overlapped to a much greater extent and the chirping would not be suppressed as for the case of the single pulse. Therefore, the RZ format would be less susceptible to the XPM effect as compared to the NRZ format.

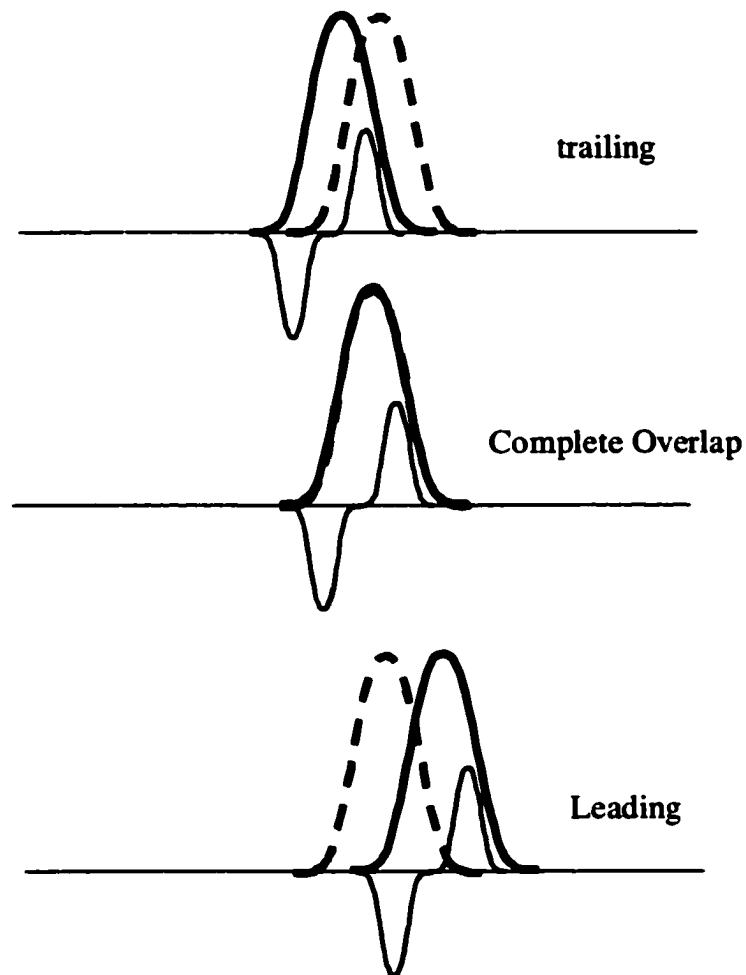


Figure 6.1: Illustration of XPM-induced Chirping of Two-channel Cases (thick solid line - pulse of channel 1, dashed line - pulse of channel 2, light solid line-induced chirp from channel 1) (adapted from Fig. 7.11 [12])

As mentioned in Chapter 3, the FWM distortion is roughly proportional to the product of the time traces of neighboring channels (i.e. triplets of channels interact). Due to the small duty cycle, the amplitude of the triplet can be greatly reduced under certain conditions for the RZ format as illustrated in **Figure 6.2**. The figure shows the time traces of two neighboring RZ channels containing consecutive ones that would induce FWM (a degenerated triplet), where the pulses of one channel lead the pulses of the other channel by half of a bit period in time. It is obvious that the product of these two traces would be small in amplitude. If the RZ channels are replaced by the NRZ channels, the amplitude would be essentially constant throughout the entire time period, and the

product of the two time traces would be much higher. As a result, the FWM distortion is much higher for the NRZ channels than for the RZ channels.

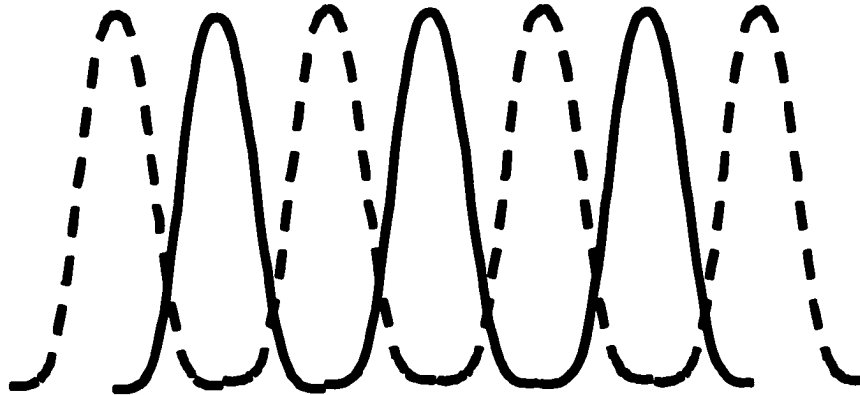


Figure 6.2: Illustration of the Situation where the FWM is Close to a Minimum for the RZ Format

Because of the benefits mentioned above, the RZ signal can safely operate at higher channel powers, which translates into longer fiber spans, or longer transmission distances [79]. The disadvantage of the RZ format is its relatively wider spectrum caused by the low duty cycle.

Miyamoto et al., recently showed that by suppressing the optical carrier, the RZ format can handle even higher channel powers, but no physical explanation is given [79]. In essence, this carrier-suppressing RZ signal is a bi-polar (BP) coded signal. In this chapter we compare two additional carrier-suppressed RZ formats, duobinary RZ (D-RZ) and modified-duobinary RZ (MD-RZ), with the BP-RZ and conventional RZ formats. We will show that the benefits can be attributed to the optical phase shifting between adjacent pulses. Also, by comparing these different formats, we are able to isolate the distortion due solely to the intra-channel four-wave mixing (FWM) [80] caused by the discrete tones of the RZ signals.

6.2. Signal Generation

Figure 6.3 shows the schematic diagrams for generators of the different types of RZ signals. The RZ signal is generated by cascading a second Mach-Zehnder amplitude modulator after a conventional NRZ amplitude modulator. This second modulator is

modulated by a sinusoidal wave with frequency equal to the transmission rate, T , that swings between zero and V_π . The D-RZ signal is generated by cascading the same sinusoidal-wave-driven modulator to a delay-and-add NRZ duobinary modulator [81]. The generator of the MD-RZ signal is almost identical to that of the D-RZ signal, except the delay-and-add circuit in the NRZ duobinary modulator is replaced by a delay-and-subtract circuit [53]. The generator of the BP-RZ signal is similar to the conventional RZ signal with one crucial difference: The frequency of the sinusoidal wave of the second modulator is reduced by half and the sinusoidal wave swings between zero and $2V_\pi$ [79].

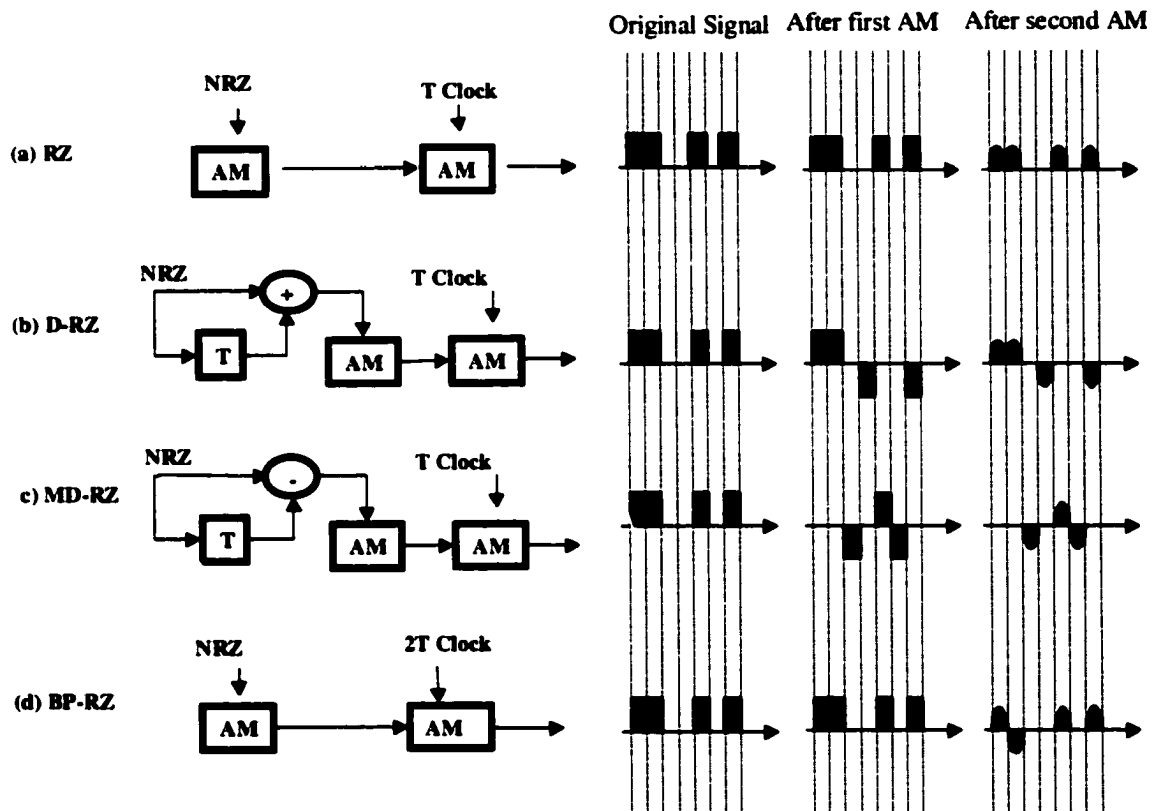


Figure 6.3: Schematic Diagram for Generating Different Types of RZ Signals

Both the D-RZ and MD-RZ formats suppress all of the discrete frequency tones that appear in the conventional RZ signal spectrum: on the other hand, the BP-RZ format only suppresses the optical carrier tone and shifts all other sideband tones toward the carrier frequency, as shown in **Figure 6.4**. All three of these alternative RZ signals have three optical-field levels with two levels having the same magnitude but opposite phase and which are separated by a zero-magnitude level, as shown in **Figure 6.3**. For both

MD-RZ and BP-RZ, the consecutive ones in the bit sequence alternate between the two opposite-phase levels; whereas the D-RZ cannot transit between two opposite-phase levels in one bit-period. Since both D-RZ and MD-RZ signals are partial-response signals, a pre-coding scheme at the transmitter or a decoding scheme at the receiver is almost always required [53].

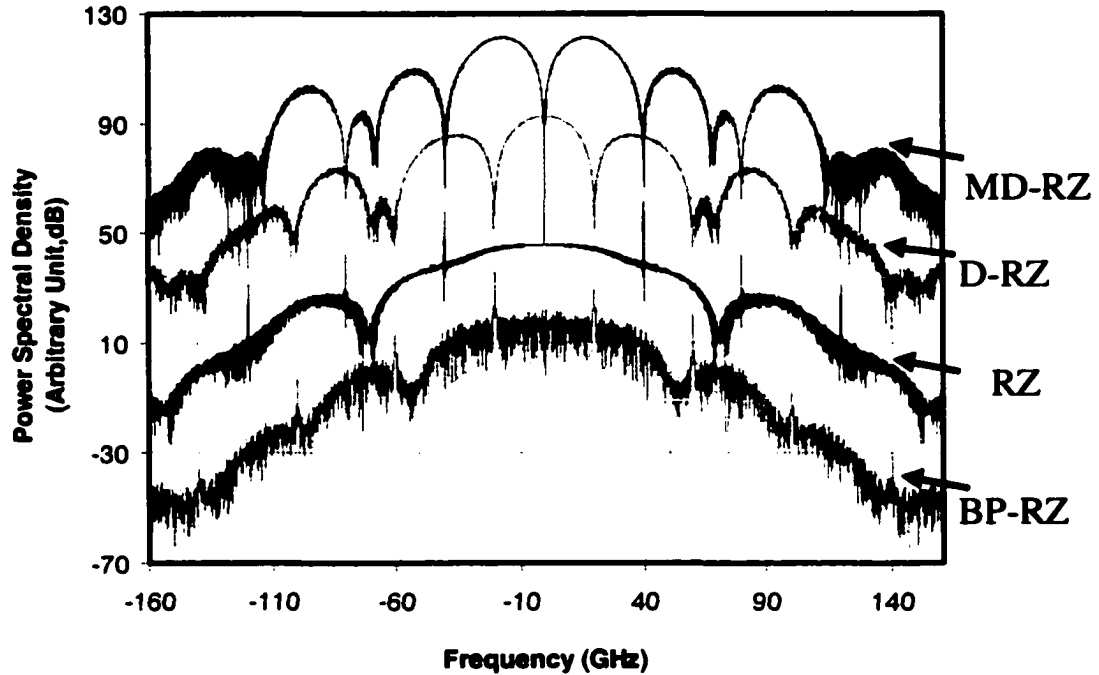


Figure 6.4: Optical Spectra of Four Different RZ Formats

6.3. Performance Comparison

Both single-channel and 8-channel WDM simulations were performed assuming the OC-768 (40 Gbits/s) line rate. The optical link used in the simulations consisted of three spans of dispersion-managed fiber (DMF) consisting of a section of single-mode fiber (SF) followed by a section of reverse-dispersion fiber (RF) (span #1 [75km (SF) 53.2km (RF)], span #2 [74.8km (SF) 42.3km (RF)], span #3 [75.2km (SF) 46.5km (RF)]). A similar dispersion map configuration was also used by Miyamoto et al. [79]. The fiber parameters are listed in **Table 6.1**. The nonlinear refractive index and fiber loss for all fibers was assumed to be the same and equal to $2.3 \times 10^{-20} \text{ m}^2/\text{W}$ and 0.22 dB/km, respectively. For the 8-channel WDM simulations, the first and last channels are located

at 1546.1 nm and 1557.3 nm with 200 GHz channel spacing. The residual dispersion after fiber propagation is -3 ps/nm and 16 ps/nm for first and last channels, respectively. A 2^9-1 pseudorandom bit sequence was used in the simulations. Also, for the 8-channel system, the simulations were repeated 40 times with different time delays between channels and individual carrier laser phase (but with the same pseudorandom information sequence) for each RZ format at different launched powers, in order to accumulate statistically significant results.

The resulting single-channel eye closure penalties and the 8-channel average Q_s are shown in **Figure 6.6**. No ASE noise was added for the single-channel simulations; for the 8-channel WDM simulations, the inline and post-amplifiers are assumed to have a 6 dB noise figure. An 80 GHz (FWHM), 5th order Butterworth filter and a 30 GHz, 3rd order Butterworth filter were used to model the optical and electrical filters at the receiver, respectively.

	Dispersion, D (ps/nm/km)	Dispersion Slope, S (ps/nm ² /km)	Effective Core Area, A_{eff} (μm^2)
SMF	17	0.06	85
RDF	-26.91	-0.083	25

Table 6.1: Fiber Parameters

In the single-channel case, the eye penalties of both BP-RZ and MD-RZ increase more slowly as the average channel power increases. For instance, at the 1 dB eye penalty, both of these formats can operate at a channel power 1 dB or more higher than the conventional RZ. These results are consistent with the results shown in [79]. As for the D-RZ format, the performance is only slightly improved, which indicates that the improvement is not merely due to the suppression of the discrete tones in the signal spectrum. **Figure 6.5** depicts the received signal eyes with 9 dBm average channel power. It is clear that both BP-RZ and MD-RZ have less timing jitter and amplitude distortion. Also, for both the D-RZ and MD-RZ signals, the bottom traces in the eye diagrams have less variance compared with BP-RZ and RZ, which indicates less distortion in the zero bits due to the absence of the “ghost” pulses. Ghost pulses are pulses centered approximately at the center of the zero bits, which are the result of nonlinear distortion [80] (more details in the next section). The full-scale 8-channel simulations also show that BP-RZ and MD-RZ have about 1.5 dB and 2 dB ($20\log Q$)

improvement over conventional RZ, respectively, at the optimum channel power (between 8 and 9 dBm). By contrast, the D-RZ format has about 1 dB improvement in the Q. Moreover, the simulations results show that the MD-RZ format can operate at an average channel power 2 dB higher than the RZ format with a Q of 18.3 dB (maximum for RZ) as compared to 1.3 dB power advantage for the BP-RZ format.

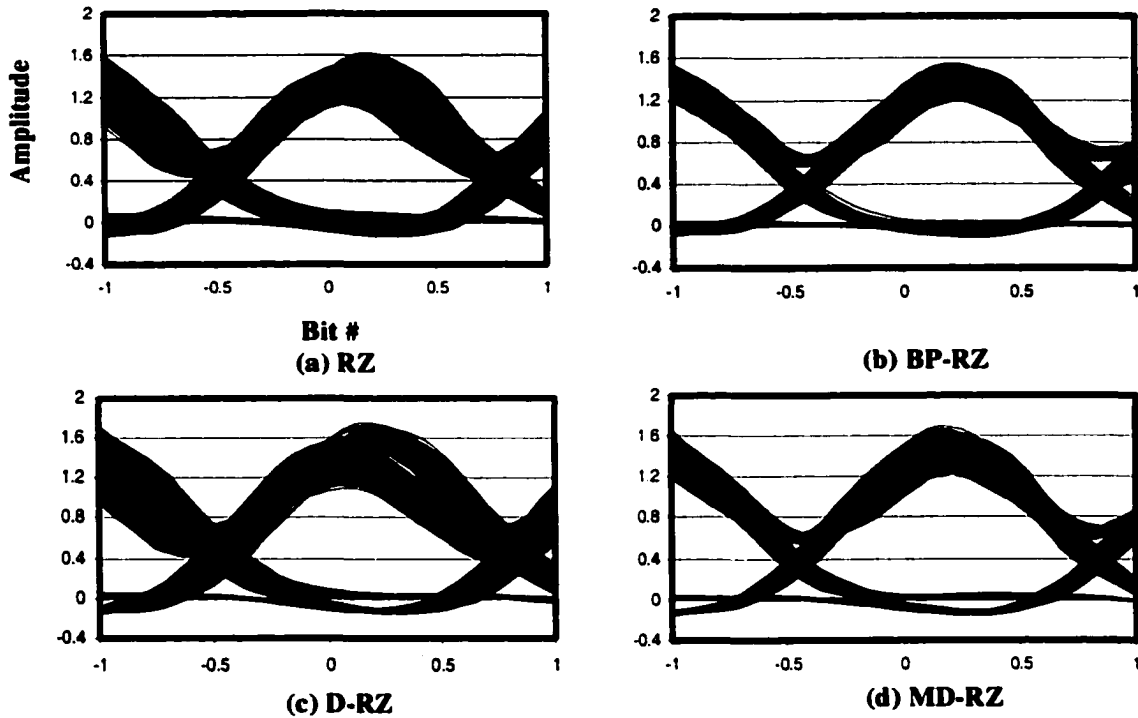


Figure 6.5: Received Signal Eyes with 9 dBm Average Launched Channel Power

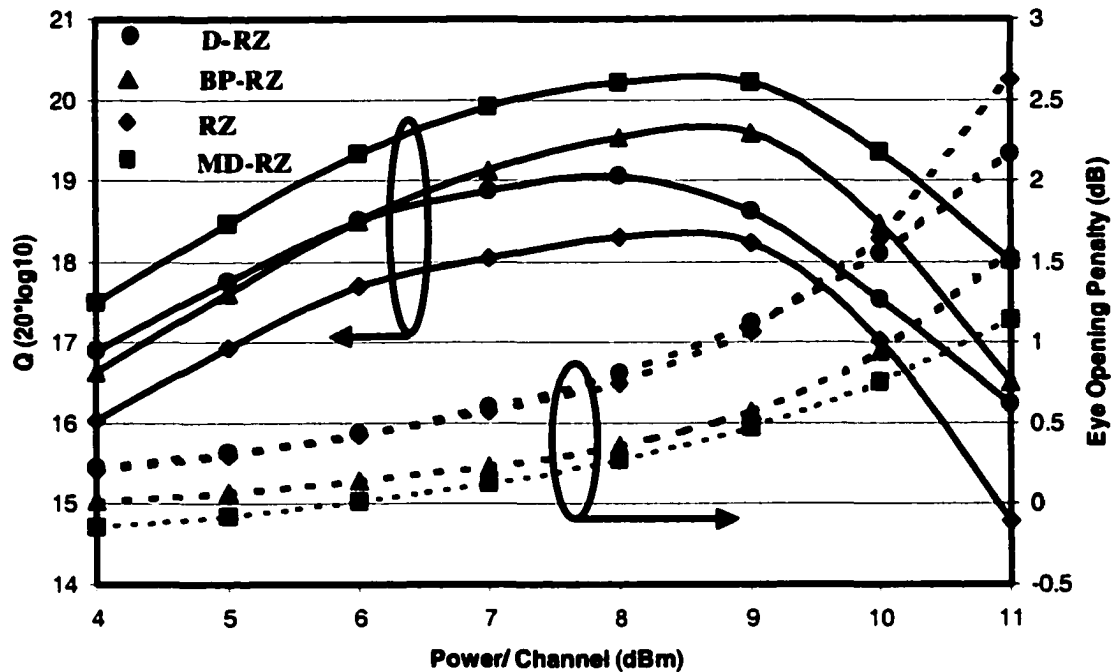


Figure 6.6: Eye Opening Penalty (1 channel, dash lines) and Average Q (8 channels, solid lines) versus Average Launched Channel Power

6.4. Analysis

The performance improvement can be attributed to two factors: the reduction of nonlinear pulse-to-pulse interaction (MD-RZ and BP-RZ) and the suppression of the ghost pulse (MD-RZ and D-RZ). To investigate the reduction of the pulse-to-pulse interaction, the pulse evolution of the optical signals in the first span of SMF, where most nonlinear degradation occurs, was examined. Time traces containing six consecutive ones within the 2^9-1 bit sequences at 2 km, 4 km and 8 km were captured. The traces are shown in **Figure 6.7**. It was found that for a long string of ones (where the major distortion occurs), both the BP-RZ and MD-RZ formats can maintain the pulse shape whereas significant pulse spreading occurs in both the conventional RZ and D-RZ formats. Due to this pulse-shape confinement, there was less nonlinear pulse-to-pulse interaction for consecutive ones in both BP-RZ and MD-RZ and hence less distortion. This pulse-shape confinement effect is the result of the 180° phase shift of the consecutive ones, as mentioned previously, not because of the removal of the optical

carrier or sideband tones. The D-RZ format suppresses all tones in the spectrum, but the distortion at the top of the pulses is still as serious as in the RZ format. The effect of the sideband-tone removal at multiples of the transmission rate, on the other hand, greatly suppresses the generation of the ghost pulses. For both RZ and BP-RZ, there are strong tones at the transmission rate of the signal spectrum; however, no discrete tones are present in both D-RZ and MD-RZ as shown in **Figure 6.4**.

Due to the chromatic dispersion and the nonlinear fiber effect, the original phase and amplitude relationship between two discrete tones at the transmission rate (on each sideband) and the rest of the spectrum is slightly altered (intra-channel FWM). In the time domain, the discrete tones can be viewed as the sinusoidal waves that make up of the Fourier series of the signal. With the distortion, they have different amplitude and relative time delay (this is the reason why the ghost pulses are only approximately located at the center of the zero bit slots) with respect to the rest of the signal Fourier series. Because of this, this sinusoidal wave appears at the signal trace and becomes more prominent at the zero bits, which results in the ghost pulses. **Figure 6.8** shows a portion of the received bit sequence (without electrical filtering) that contains 1 mark followed by 6 spaces. It is clear from the figure that both the RZ and BP-RZ bit sequences contain the ghost pulses. Significantly less power (35 dB lower) appeared in the zeros of both the D-RZ and MD-RZ sequences. The absence of the discrete tones in both D-RZ and MD-RZ simply suppress the process mentioned above, and this greatly reduces the ghost-pulse generation.

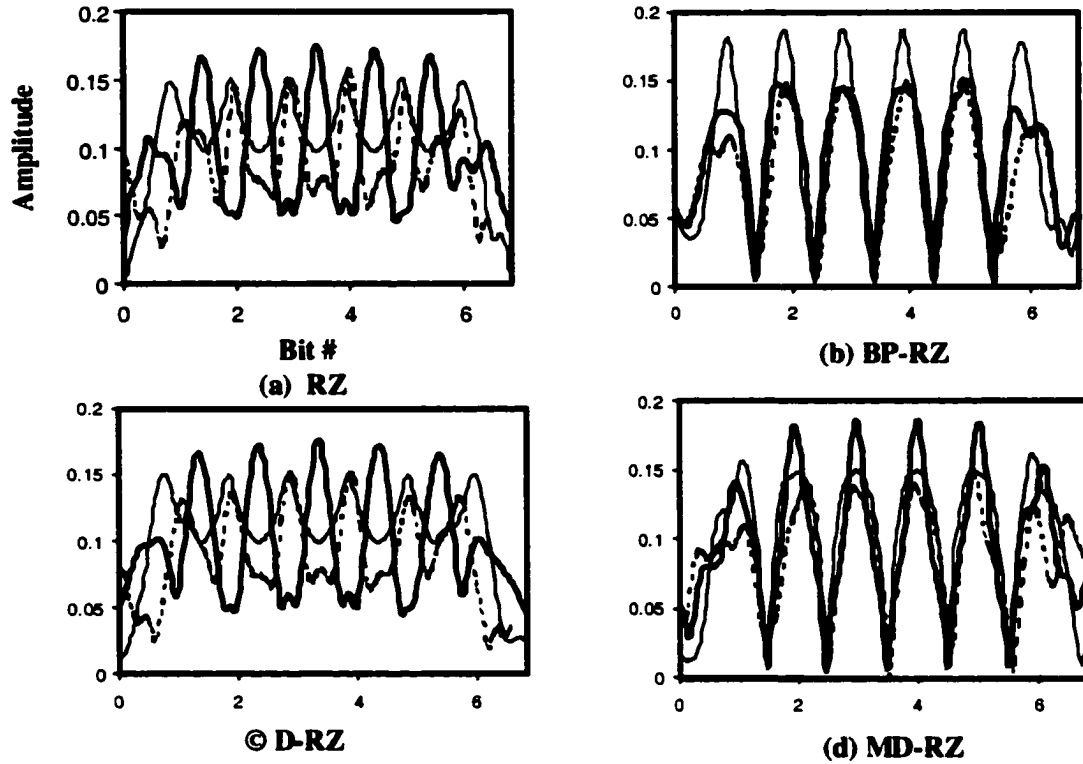


Figure 6.7: Pulse Evolution at 2, 4 and 8 km of SMF (light solid line 2 km, dark solid line 4 km, dark dashed line 8 km)

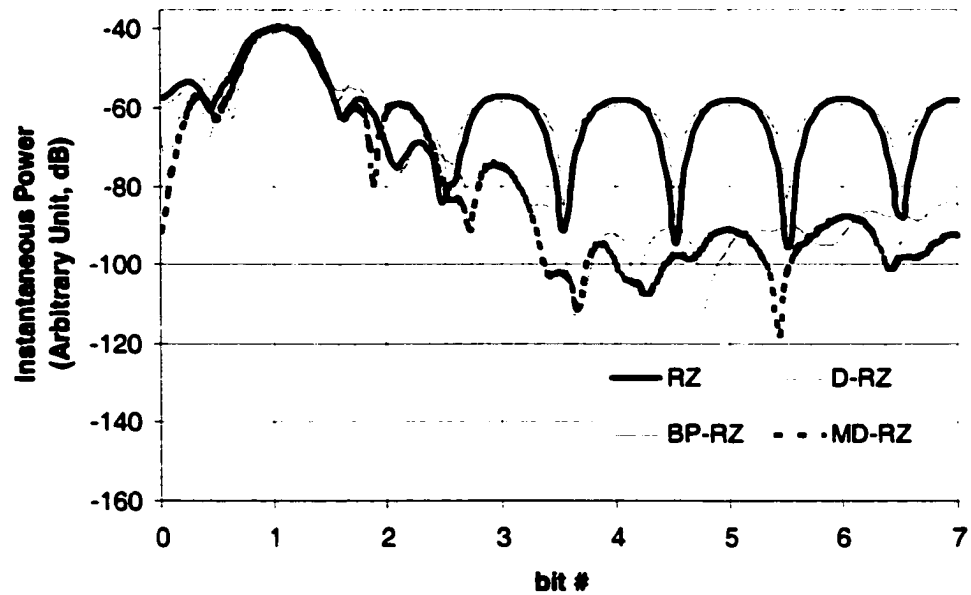


Figure 6.8: Suppression of Ghost Pulses in both D-RZ and MD-RZ

6.5. Summary

For the 40 Gbits/s system studied in this chapter we showed that both the BP-RZ and MD-RZ formats can improve the Q factor by about 2 dB and 3 dB over conventional RZ. Both of these formats can operate at an average channel power 1.3 dB or more greater than the conventional RZ format (2 dB for MD-RZ). We found that this improvement is not simply due to the suppression of the optical carrier, rather the benefit comes from the 180° phase shift between the consecutive ones in the bit sequence. We also showed that the ghost pulses caused by the intra-channel FWM between discrete tones is another significant factor that contributes to the overall performance degradation.

The superior performance of MD-RZ against pulse-to-pulse distortion and intra-channel FWM shows that the MD-RZ format has significant potential as an alternative to the RZ format currently employed in high data-rate fiber-optic communication systems.

7. Conclusion

7.1. Research Summary

There were four main objectives of this research, set out in Chapter 1. The first objective is to modify the existing simulation tool at TRILabs to more accurately model signal propagation in optical fibers. A key sub-objective was to model the essential nonlinear effects exists in optical fiber. Chapter 2 reviewed various fiber nonlinear effects and the nonlinear Schrodinger equation (NLSE) that describes signal propagation. We showed how the simulation algorithm is based on the NLSE. We also discussed various issues that limit the simulation accuracy. The improved simulation tool was verified by comparing the simulation results with some known solutions. The accuracy of the simulation tool was further verified in Chapter 4 (in section 4.4) by directly comparing simulation results with experimental measurements. In every case the experimental measurements agreed well with the simulations.

The second objective of this research was to compare the performance of the OOK, OSSB and duobinary transmission formats in both short-haul and terrestrial systems. Chapter 3 presented the theoretical analyses along with corresponding simulations. For systems without dispersion compensation, the duobinary format has a clear advantage over the other two formats because of its narrower frequency spectrum. However, for commercial systems, dispersion compensation is usually available. The impact of the residual dispersion is not significant for OC-192 systems with 32 channels and 50 GHz spacing. The duobinary format, on the other hand, could have benefits for higher transmission rate systems (where signals are more sensitive to residual dispersion) and systems with more channels. Regarding cross talk, both the duobinary and OSSB formats have a clear disadvantage because of the phase modulation inherent in these formats. The duobinary format does show a benefit over the other two formats for ultra-dense systems (< 18 GHz spacing for OC-192) because of its narrower spectrum. Although the OSSB format can significantly transfer power from one signal sideband to

another one, the residual power left in one sideband still causes significant distortion when the channel spacing is very narrow.

As for robustness against nonlinear fiber effects, the three formats have very similar performance. The impacts of SPM, XPM and FWM to these three systems do not differ much. The OSSB has a slightly higher distortion under the influence of the SPM effect because of the phase modulation from the Hilbert transform. However, this distortion is minimal and does not significantly affect system performance. As for the XPM effect, the duobinary format performs better because it has more carrier power in its 'absolute-squared' spectrum than the other two formats, assuming the same average launched power. The FWM comparison is slightly more complicated. For single-channel systems, both the OSSB and duobinary formats perform worse, again because of signal phase modulation. For multi-channel systems, the discrete phase modulation gives the duobinary format better performance. Overall, the distortion caused by the FWM is similar for all three formats.

For a full-scale system, the duobinary format has a disadvantage because of the initial eye penalty caused by low-pass filtering during the initial duobinary conversion. For OC-192 systems with 50 GHz channel spacing, the duobinary format performs slightly worse than the other two formats simply because the greater resistance to nonlinear fiber effects is offset by the smaller initial eye opening. For OC-192 systems with 25 GHz channel spacing, the duobinary format shows its superiority. Its narrower spectrum reduces channel cross talk and the BER is lower. However, if nonlinear effects are as important as the cross-talk distortion in the ultra-narrow-spacing systems, the duobinary format has performance comparable to the other two formats. For OC-768 systems with 40% spectral efficiency, channel cross talk and ASE noise become the main factors that limit system performance. With only channel cross talk, the duobinary format clearly shows better performance than the other two formats.

Experimental comparisons of the three formats were presented in Chapter 4. The results show that neither the duobinary or OSSB formats appear to have any benefits over the OOK format. In fact, the OSSB format has performance very similar to that of the OOK format. The duobinary format performs worse than the other two formats. The

back-to-back duobinary signal has a smaller eye opening than predicted from simulations. This smaller eye opening leads to greater inter-symbol interference. As a result, the performance of the duobinary format in both single-span and terrestrial systems is worse than the other two formats. Note that due to the unrealistic correlation among channels in our experiments, the measured performance of the three formats in 25-GHz spaced OC192 systems was possibly better than what would be measured in an the actual commercial system setting with uncorrelated channel signals.

The third objective of this research is to investigate the possibility to combine the OSSB and duobinary formats to further reduce the signal bandwidth. Various OSSB formats were discussed in Chapter 5, and their compatibility with duobinary format was also mentioned. It was found that only the conventional OSSB format is compatible with the duobinary format, and an optical SSB-to-DSB converter is required for proper detection at the receiving end. The theory describing the operation of this converter was presented. The results of single-channel simulations for terrestrial systems were presented. It was found that for single-channel system, the eye closure penalty is still acceptable if the average signal power is below 3 dBm. The performance of a multi-channel WDM system depends on the system configurations. Further simulations are required to better explore the potential of specific system configurations. However, with the presence of strong fiber nonlinear effects, it is doubtful that this new combined format can perform well.

The fourth objective of this research is to compare three alternative RZ formats, namely BP-RZ, D-RZ and MD-RZ, with the commonly used RZ format. In Chapter 6, it is shown that for 40 Gbits/s systems, both BP-RZ and MD-RZ can improve the Q factor by about 2 dB and 3 dB over conventional RZ. Both of these formats can operate at an average channel power 1.3 dB or more greater than the conventional RZ format (2 dB for MD-RZ). We found that this improvement is not simply due to the suppression of the optical carrier, rather the benefit comes from the 180° phase shift between the consecutive ones in the bit sequence. We also showed that the ghost pulses caused by the

intra-channel FWM between discrete tones is another significant factor that contributes to the overall performance degradation. The superior performance against pulse-to-pulse distortion and intra-channel FWM shows that the MD-RZ format has significant potential as an alternative RZ format employed in high data-rate fiber-optic communication systems with long fiber spans.

7.2. Future Work

The research relied heavily on computer simulations. The improved simulation tool used in this research can accurately simulate signal propagation in fiber. However, many simulation runs are required to accumulate significant performance statistics. Because of this, simulation times are relatively long. To reduce the simulation time, other researchers have tried to use a semi-analytical method to perform the simulations. In this method, the individual noise contributions from different nonlinear effects are calculated separately using analytical models. By assuming that these noise contributions are independent of each other, they can be summed up at the end of the transmission link to calculate the total noise and hence the Q factor. Much research is still required to perfect these decoupled models.

As mentioned in Chapter 4, the implementation of the filter required for converting OOK format to duobinary format could have been better. Therefore, to further investigate the potential of duobinary format, it will be necessary to improve the implementation of the filter. The filters used in the duobinary experiments were reflective type filters, which require attenuators to be inserted at both the input and output ports for proper functioning. Thus a non-reflective type filter would be preferable. Also, as presented in Chapter 3, the simulation results showed that the duobinary format can perform relatively better than the OOK format in narrow-spaced OC-768 systems. Experiments are needed to verify these simulation results and to explore various implementation options. One of the major difficulties of implementing OC-768

duobinary format is to amplify the electrical duobinary signal to the required voltage to drive the optical modulator. The amplifier needs to drive the signal at about 9 V peak-to-peak (with two switching voltages) and have a gain bandwidth of at least 20 GHz, which is not easy to achieve. Also, the OOK-to-duobinary conversion filter would need to be redesigned to accommodate the frequency response of the amplifier.

In Chapter 6, it was concluded from simulations that the MD-RZ format should out perform the commonly used RZ format. The next step would be to actually implement the MD-RZ format and then directly compare its performance with the RZ format through experimental. The difficulties of implementing the MD-RZ appear similar in magnitude to those for the OC-768 duobinary format.

This research described earlier focused on bare fiber-optic systems that do not have any error correction capability. However, it is becoming more and more common to use error-correction coding to improve the system BER performance. The most commonly used error-correction coding is the Reed-Solomon forward-error correction coding (FEC) [84]. The corresponding FEC encoder can be hardware implemented in a single integrated circuit (IC). Such an IC is inserted before the optical modulator. At the receiver, a FEC decoder is inserted before the decision circuit [84]. With such FEC, it is possible to improve the Q factor by 2.5 dB ($10\log$) [85].

The Reed-Solomon code was designed in general for any type of communication system. There are other codes that are designed specifically for fiber-optic communication systems to suppress nonlinear fiber effects [86]. The development of coding schemes for fiber-optic systems is still not fully mature. Much research is still required to fully understand and develop this useful tool to enhance the fiber system performance. It could be possible to search for codes that not only can correct errors, but are also especially effective at suppressing errors caused by nonlinear effects. Also

certain codes may be suitable for certain transmission formats, but not others. Further research is required to fully explore these issues.

References

1. "Modern Communication: The Laser and Fiber-Optic Revolution", (belongs to a series of articles written for the project: 'Beyond Discovery: The Path from Research to Human Benefit'), *National Academy of Sciences* (<http://www2.nas.edu/bsi>), Dec. 1996.
2. "SONET 101", <http://www.nortelnetworks.com/products/01/sonet/doclib.html>.
3. S. Kano, "The Telecommunications market in Japan: Entering the Digital Era and the Second Phase of Competition", *IEEE Communications Magazine*, vol. 36, no. 11, pp. 38-44, Nov. 1998.
4. Internet Population, http://cyberatlas.internet.com/big_picture/geographics/article/0,1323,5911_151151,00.html
5. "The History of Cable Television", <http://www.ncta.com/glance-body.html>, 1998.
6. Web page of Videotron Telecom, <http://TelecCom.videotron.com/en/reseau.html>.
7. "Long Distance 101", Northern Telecom (www.nortel.com/home/ref_buzz.html), July 1995.
8. S. Walklin, Multilevel Signaling for Increasing the Capacity of High-Speed Optical Communication Systems, Doctoral Thesis, *University of Alberta*, 1997.
9. S. Walklin and J. Conradi, "On the Relationship Between Chromatic Dispersion and Transmitter Filter Response in Duobinary Optical communication Systems", *IEEE Photonics Technology Letters*, vol. 9, no. 7, pp. 1005-1007, July 1997.
10. A. Royset, D. R. Hjelme, "Novel dispersion tolerant optical duobinary transmitter using phase modulator and Bragg grating filter", *ECOC 98*.
11. M. Sieben, J. Conradi and S. Walklin, "10Gbit/s optical single sideband system", *Electronics Letters*, vol. 33, no. 11, p 971, May 1997.
12. G. P. Agrawal, Nonlinear Fiber Optics, 1st Edition, *Academic Press, INC.*, 1989.
13. K. Tanaka, I. Morita, M. Suzuki, N. Edagawa and S. Yamamoto, "400 Gbits/s (20x20 Gbit/s) dense WDM soliton-based RZ signal transmission using dispersion flattened fiber", *Electronics Letters*, vol. 34, no. 23, pp.2257-2258, Nov. 1998.
14. K. Yonenaga and S. Norimatsu, "Dispersion Compensation for Homodyne Detection Systems Using a 10-Gb/s Optical PSK-VSB Signal", *IEEE Photonics Technology Letters*, vol. 7, no. 8, pp. 929-931, Aug. 1995.
15. J. J. Winters, "Equalization in Coherent Lightwave Systems Using Microwave Waveguides", *Journal of Lightwave Technology*, vol. 7, no. 5, pp. 813-815, May 1989.

16. J. C. Cartledge and R. G. Mckay, "Performance of 10 Gb/s Lightwave Systems Using an Adjustable Chirp Optical Modulator and Linear Equalization", *IEEE Photonics Technology Letters*, vol. 4, no. 12, pp. 1394-1397, Dec. 1992.
17. A. H. Gnauck, S. K. Korotky, J. J. Veselka, J. Nagel, C. T. Kemmerer, W. J. Minford and D. T. Moser, "Dispersion Penalty Reduction Using an Optical Modulator with Adjustable Chirp", *IEEE Photonics Technology Letters*, vol. 3, no. 10, pp. 916-918, Oct. 1991.
18. P. P. Iannone, A. H.Gnauck and P. R. Prucnal, "Dispersion-Compensated 333-km 10-Gb/s Transmission Using Mid-Span Spectral Inversion in an Injection-Locked InGaAsP V-Groove Laser", *IEEE Photonics Technology Letters*, vol. 6, no. 8, p. 1046, Aug. 1994 .
19. A. Djupsjobacka and O. Sahlen, "Dispersion Compensation by Differential Time Delay", *Journal of Lightwave Technology*, vol. 12, no. 10, pp. 1849-1853, Oct 1994.
20. M. Sharma, H. Ibe and T. Ozeki, "Optical Circuits for Equalizing Group Delay Dispersion of Optical Fibers", *Journal of Lightwave Technology*, vol. 12, no. 10 , pp. 1759-1765, Oct. 1994.
21. V. A. Semenov, V.Belov, N. N. Vechkanov, "Broadband dispersion-compensating fiber for high-bit-rate transmission network use", *Applied Optics*, vol. 34, no. 24, p. 5331, Aug 1995.
22. W. H. Loh, R. I., Laming, A. D. Ellis and D. Atkinson, "10 Gb/s Transmission over 700 km of Standard Single-Mode fiber with 10-cm Chirped fiber Grating compensator and Duobinary Transmitter", *IEEE Photonics Technology Letters*, vol. 8, no. 9, pp. 1258-1260, Sept. 1996.
23. G. P. Agrawal, Fiber-optic Communication Systems, 2nd Edition, John Wiley & Sons, INC., 1997.
24. <http://www.nortelnetworks.com/products/optical/>.
25. Introduction to Optera, http://www.nortelnetworks.com/products/01/optera/long_haul/index.html.
26. R. C. Alferness, H. Kogelnik, and T. H. Wood, "The Evolution of Optical Systems: Optics Everywhere", *Bell Labs Technical Journal*, pp. 188-202, Jan. - Mar. 2000
27. D. Y. Al-Salameh, M. T. Fatehi, W. J. Gartner, S. Lumish, B. L. Nelson and K. K. Raychaudhuri, "Optical Networking", *Bell Labs Technical Journal*, pp. 39-61, Jan-Mar. 1998.
28. <http://www.convergedigest.com/DWDM/archive/000907alcatelDWDM.htm>
29. <http://www.convergedigest.com/DWDM/archive/001003necDWDM.htm>
30. <http://www.convergedigest.com/DWDM/archive/001004optisphere.htm>
31. <http://www.nortelnetworks.com/products/01/optera/metro/>

32. <http://www.nortelnetworks.com/corporate/pressroom/pressconferences/060600/collateral/qwest.pdf>
33. S. Y. Park, G. J. Pendock, A. K. Srivastava, K. Kantor, J. W. Sulhoff, S. J. Sheih, C. Wolf and Y. Sun, "WDM Transmission over Dispersion Shifted Fiber in L-Band with 25 dB Span Loss", *OFC 2000 Technical Digest*, TuJ2-1
34. T. Ono, Y. Yano, K. Fukuchi, T. Ito, H. Yamazaki, M. Yamaguchi and K. Emura, "Characteristics of Optical "Duobinary Signals in Terabit/s Capacity, High-Spectral Efficiency WDM systems", *Journal of Lightwave Technology*, vol. 16, no. 5, pp. 788-7, 1998.
35. M. I. Hayee, A. E. Willner, *IEEE Photonic Technology Letters* vol. 11, pp. 991-993, 1999.
36. R. Mu, T. Yu, V. S. Grigoryan, and C. R. Menyuk, "Convergence of the CRZ and DMS Formats in WDM Systems Using Dispersion Management", *OFC Technical Digest*, FC1, March 2000
37. T. Ono, and Y. Yano, "Key technologies for terabit/second WDM systems with high spectral efficiency of over 1bits/s/Hz", *IEEE J. Quantum Electron*, 1998, 34, pp. 2080-2088.
38. Y. Miyamoto, A. Hirano, K. Yonenaga, A. Sano, Hi Toba, K. Murata, O. Mitomi, *Electron. Lett.*, 35, 2041 (1999).
39. J. C. Cartledge and A. F. Elrefaie "Effect of Chirping-Induced Waveform Distortion on the Performance of Direct Detection Receivers Using Traveling-Wave Semiconductor Optical Preamplifiers", *Journal of Lightwave Technology*, vol. 9, no. 2, pp. 209-219, Feb. 1991.
40. J. M. Senior, Optical Fiber Communications: Principles and Practice, 2nd Edition, 1992, *Prentice Hall*.
41. B. E. A. Saleh and M. C. Teich, Fundamentals of Photonics, 1st Edition, *John Wiley & Sons, INC.*, 1991.
42. S. Namiki and Y. Emori, "Recent advances in ultra-wideband Raman amplifiers", *OFC 2000 Technical Digest*, FF1-1.
43. A. R. Chraplyvy, "Limitations on Lightwave Communications Imposed by Optical-Fiber Nonlinearities", *Journal of Lightwave Technology*, vol. 8, no. 10, pp. 1548-1557, Oct, 1990.
44. Private Communication, June-Koo Rhee, Corning Inc.
45. J. M. Senior, Optical fiber communications: principles and practice, 2nd Edition, *Prentice Hall*, 1992.
46. R. H. Hardin and F. D. Tappert, *SIAM Rev. Chronicle*, 15, p. 423, 1973.

47. D. G. Schadt and T. D. Stephens, "Power Limitations Due to Four-Wave Mixing Effects in Frequency Division Multiplexed Coherent Systems Using Cascaded Optical Amplifiers", *Journal of Lightwave Technology*, vol. 10, no. 11, pp. 1715-1721, Nov. 1992.
48. R. Tkach, A. Chraplyvy, F. Forghieri, A. Gnauck and R. Derosier, "Four-Photon Mixing and High-Speed WDM Systems", *Journal of Lightwave Technology*, vol. 13, no. 5, pp. 841-849, May 1995.
49. C. Kurtzke, kapazitatsgrenzen digitaler optischer Ubertragungs-systeme, Ph.D Thesis, Berlin, pp. 201-205, 1994.
50. K. Kafadar, "Gaussian White-Noise Generation for Digital Signal Synthesis", *IEEE Transactions on Instrumentation and Measurement*, vol. IM-35, no. 4, pp. 492-495, Dec. 1986.
51. A. Carena, V. Curri, R. Gaudino, P. Poggiolini and S. Benedetto, "New Analytical Results on Fiber Parametric Gain and Its effects on ASE Noise", *IEEE Photonics technology Letters*, vol. 9, no. 4, pp. 535-537, Apr. 1997.
52. C. J. Anderson and J. A. Lyle, "Technique for evaluating system performance using Q in numerical simulations exhibiting intersymbol interference", *Electronics Letters*, vol. 30, no. 1, pp. 71-72, Jan. 1994.
53. J. G. Proakis, Digital communications, McGraw-Hill, Inc. third edition, 1995.
54. M. Sieben, Optical Single Sideband Transmission, Ph.D Thesis, 1998, *University of Alberta*.
55. Y. Xie, .S. Lee, Z. Pan, J.-X. Cai, and A. e. Willner, "Tunable Compensation of the Dispersion Slope Mismatch in Dispersion-Managed systems using a Sampled Nonlinearly-Chirped FBG", *OFC 2000 Technical Digest*, TUS2-1, 2000.
56. K.S. Jepsen, U. Gliese, B.R. Hemenway, S. Yuan, K.S. Cheng, J.E. Hurley, L. Guiziou, J.W. McCamy, N. Boos, D.J. Tebben, B. Dingel, M.J. Li, S. Gray, G.E. Kohnke, L. Jiang, V. Srikant, A.F. Evans and J.M. Jouanno, "Network demonstration of $32\lambda \times 10$ Gb/s across 6 nodes of 640×640 WSXCs with 750 km Raman-amplified fiber", Post deadline paper, *OFC 2000*, Baltimore, USA.
57. P. C. Becker, N. A. Olsson and J. R. Simpson, Erbium-Doped Fiber Amplifiers (Fundamentals and Technology), 1999, *Academic Press*.
58. M. K. Durkin, R. Feced, C. Ramirez and M. N. Zervas, "Advanced Fibre Bragg Gratings for High Performance dispersion Compensation in DWDM Systems", *OFC 2000 Technical Digest*, TuH4-1, 2000.
59. M. Shtaif and M. Eiselt, "Impact of cross phase modulation in WDM systems", *OFC 2000 Technical Digest*, ThM1-1, 2000.

60. R. Hui, K. R. Demarest, and C. T. Allen, "Cross-Phase Modulation in Multispan WDM Optical Fiber Systems", *IEEE Journal of Lightwave Technology*, vol.17, no. 6, pp. 1018-1026, 1999.
61. S. Ten, K. M. Ennser, J. M. Grochocinski, S. P. Burtsev and V.L. da Silva, "Comparison of four-wave mixing and cross phase modulation penalties in dense WDM systems", *OFC 1999 Technical Digest*, vol. 3, pp. 43-45.
62. E. A. Golovchenko, A. N. Pilipetskii, and N. S. Bergano, "Transmission properties of chirped return-to-zero pulses and nonlinear intersymbol interference in 10 Gb/s WDM transmission", *OFC 2000 Technical Digest*, FC3-1
63. M. A. Summerfield, "Comments on "Optical Amplifier Noise Figure Reduction for Optical Single-Sideband Signals", *IEEE Journal of Lightwave Technology*, vol.18, no. 9, pp. 1271-1273, 2000.
64. R. A. Griffin, P. M. Lane, and J. J. O'Reilly, "Optical Amplifier Noise Figure Reduction for Optical Single-Sideband Signals", *IEEE Journal of Lightwave Technology*, vol.17, no. 10, pp. 1793-1796, 1999.
65. <http://www.nortelnetworks.com/products/optical/>.
66. T. Ono, Y. Yano: "Key Technologies for Terabit/Second WDM Systems with High Spectral Efficiency of Over 1bit/s/Hz", *IEEE J. Quantum Electron.*, vol 34, pp 2080-2088, Nov. 1998.
67. S. Aisawa, J. Kani, M. Fukui, T. Sakamoto, M. Jinno, S. Norimatsu, H. Ono, K. Oguchi : "A 1580-nm Band WDM Transmission Technology Employing Optical Duobinary Coding" , *J. Lightwave Technol.*, vol. 17, pp. 191-198, Feb. 1999.
68. H. Suzuki, J. I. Kani and M. Sumida, "1-Tb/s (100x10Gb/s) Super-Dense WDM Transmission with 25-GHz Channel Spacing in the Zero-Dispersion Region Employing Distributed Raman Amplification Technology", *IEEE Photonics Technology Letters*, vol. 12, n. 7, pp. 903-905, Dec. 2000.
69. Y. Yamada, S. I. Nakagawa and K. Goto, "25 GHz spacing ultra-dense WDM transmission experiment of 1 Tbit/s (100 x 10Gbit/s) over 7300 km using non-pre-chirped RZ format", *Electronics Letters*, vol. 35, n. 25, pp. 2212-2213, Dec. 1999.
70. Private Communication, Ulrik Gliese, Corning Inc.
71. Private Communication, Jason Hurley, Corning Inc.
72. B. Chan and J. Conradi, "On the non-Gaussian noise in Erbium-doped fiber amplifiers", *J. Lightwave Technol.*, vol. 17, pp. 680-687, April 1997.
73. Fiber Optic Recirculating Loop, <http://www.o-eland.com/reloop.htm>, 2000.
74. High-Speed WDM Transmission, http://www.ee.ucl.ac.uk/~ong/ong_transmission.html, 2000.

75. G. B. Lockhart, "A Spectral Theory for Hybrid Modulation", *IEEE Transactions on Communications*, vol. COM-21, n. 7, pp.790-800, July 1973.
76. A. Mecozzi, G. Contestabile, F. Mrtelli, L. Graziani, A. D'Ottavi, P. Spano, R. Dall, J. Eckner, F. Gorardin, and G. Gueko, "Optical Spectral Inversion without Frequency Shift by Four-wave Mixing using Two pumps with Orthogonal Polarization", *IEEE Photonic Technology Letters*, vol. 10, n. 3, pp. 355-357, Oct. 1998.
77. L. Y. Lin, J. M. Wiesenfeld, J. S. Perino and A. H. Gnauck, "Polarization-insensitive wavelength conversion up to 10Gb/s based on four-wave mixing in a semiconductor optical amplifier", *IEEE Photonic Technology Letters*, vol. 10, n. 7, pp. 955-957, Oct. 1998
78. M. I. Hayee, A. E. Willner, *IEEE Photon. Technol. Lett.*, vol. 11, pp. 991-993, 1999.
79. Y. Miyamoto, A. Hirano, K. Yonenaga, A. Sano, Hi Toba, K. Murata, O. Mitomi, *Electron. Lett.*, 35, 2041 (1999).
80. P. V. Mamyshev, N. A. Mamysheva, *Optics Lett.*, 24, pp. 1454-1456, June 1999.
81. T. Ono, Y. Yano, K. Fukuchi, T. Ito, H. Yamzaki, M. Yamaguchi, K. Emura, *J. Lightwave Technol.*, 16(5), pp. 788-797, (1998).
82. F. G. Stremler, Introduction to Communication Systems, 3rd Edition, Addison Wesley, 1990.
83. S. Kumar and A. Kasegawa, "Quasi-soliton propagation in dispersion-managed optical fibers", *Optics Letters*, 22(6), pp 372-374, March, 1997.
84. Y. Miyamoto, K. Yonenaga, S. Kuwahara, M. Tomizawa, A. Hirano, H. Toba, K. Murata, Y. Tada, Y. Umeda and H. Miyazawa, "1.2T Tbits/s (30x42.7 Gbit/s ETDM channel) WDM transmission over 3x125 km with forward error correction", *Electronics Letters*, vol. 36, n. 9, pp. 812-813, April 2000.
85. H. Kidorf, N. Ramanujam, I. Hauee, M. Nissov, J. Cai, B. Pedersen, A. Puc and C. Rivers, "Performance improvement in high capacity, ultra-long distance, WDM systems using forward error correction codes", *OFC Technical Digest, THS3*, March, 2000.
86. Y Cai, T. Adalt and C. R. Menyuk, "A line coding scheme for reducing timing jitter in WDM soliton systems", *OFC Technical Digest, THS4*, March 2000.